

Practical Ship Hydrodynamics

Practical Ship Hydrodynamics

Volker Bertram

BUTTERWORTH
HEINEMANN

OXFORD AUCKLAND BOSTON JOHANNESBURG MELBOURNE NEW DELHI

Butterworth-Heinemann
Linacre House, Jordan Hill, Oxford OX2 8DP
225 Wildwood Avenue, Woburn, MA 01801-2041
A division of Reed Educational and Professional Publishing Ltd

 A member of the Reed Elsevier plc group

First published 2000

© Volker Bertram 2000

All rights reserved. No part of this publication may be reproduced in any material form (including photocopying or storing in any medium by electronic means and whether or not transiently or incidentally to some other use of this publication) without the written permission of the copyright holder except in accordance with the provisions of the Copyright, Designs and Patents Act 1988 or under the terms of a licence issued by the Copyright Licensing Agency Ltd, 90 Tottenham Court Road, London, England W1P 9HE. Applications for the copyright holder's written permission to reproduce any part of this publication should be addressed to the publishers

British Library Cataloguing in Publication Data

Bertram, Volker
Practical ship hydrodynamics
1. Ships – Hydrodynamics
I. Title
623.8'12

Library of Congress Cataloguing in Publication Data

Bertram, Volker.
Practical ship hydrodynamics / Volker Bertram.
p. cm.
Includes bibliographical references and index.
ISBN 0 7506 4851 1
1. Ships – Hydrodynamics I. Title.

VM156 .B457 2000
623.8'12–dc21 00-034269

ISBN 0 7506 4851 1

Typeset by Laser Words, Madras, India
Printed in Great Britain by



FOR EVERY TITLE THAT WE PUBLISH, BUTTERWORTH-HEINEMANN
WILL PAY FOR BTCV TO PLANT AND CARE FOR A TREE.

Preface	ix
1 Introduction	1
1.1 Overview of problems and approaches	1
1.2 Model tests similarity laws	4
1.3 Full-scale trials	8
1.4 Numerical approaches (computational fluid dynamics)	9
1.4.1 <i>Basic equations</i>	9
1.4.2 <i>Basic CFD techniques</i>	14
1.4.3 <i>Applications</i>	15
1.4.4 <i>Cost and value aspects of CFD</i>	19
1.5 Viscous flow computations	22
1.5.1 <i>Turbulence models</i>	23
1.5.2 <i>Boundary conditions</i>	26
1.5.3 <i>Free-surface treatment</i>	28
1.5.4 <i>Further details</i>	29
1.5.5 <i>Multigrid methods</i>	31
1.5.6 <i>Numerical approximations</i>	32
1.5.7 <i>Grid generation</i>	34
2 Propellers	37
2.1 Introduction	37
2.2 Propeller curves	39
2.3 Analysis of propeller flows	42
2.3.1 <i>Overview of methods</i>	42
2.3.2 <i>Momentum theory</i>	44
2.3.3 <i>Lifting-line methods</i>	45
2.3.4 <i>Lifting-surface methods</i>	46
2.3.5 <i>Boundary element methods</i>	49
2.3.6 <i>Field methods</i>	50
2.4 Cavitation	51
2.5 Experimental approach	54
2.5.1 <i>Cavitation tunnels</i>	54
2.5.2 <i>Open-water tests</i>	55
2.5.3 <i>Cavitation tests</i>	56
2.6 Propeller design procedure	56
2.7 Propeller-induced pressures	60

3 Resistance and propulsion	62
3.1 Resistance and propulsion concepts	62
3.1.1 <i>Interaction between ship and propeller</i>	62
3.1.2 <i>Decomposition of resistance</i>	65
3.2 Experimental approach	68
3.2.1 <i>Towing tanks and experimental set-up</i>	68
3.2.2 <i>Resistance test</i>	69
3.2.3 <i>Method ITTC 1957</i>	71
3.2.4 <i>Method of Hughes Prohaska</i>	73
3.2.5 <i>Method of ITTC 1978</i>	74
3.2.6 <i>Geosim method of Telfer</i>	75
3.2.7 <i>Propulsion test</i>	75
3.2.8 <i>ITTC 1978 performance prediction method</i>	76
3.3 Additional resistance under service conditions.....	80
3.4 Simple design approaches	83
3.5 CFD approaches for steady flow	83
3.5.1 <i>Wave resistance computations</i>	83
3.5.2 <i>Viscous flow computations</i>	90
3.6 Problems for fast and unconventional ships	91
3.7 Exercises: resistance and propulsion	95
4 Ship seakeeping	98
4.1 Introduction	98
4.2 Experimental approaches (model and full scale)	99
4.3 Waves and seaway	101
4.3.1 <i>Airy waves (harmonic waves of small amplitude)</i>	101
4.3.2 <i>Natural seaway</i>	106
4.3.3 <i>Wind and seaway</i>	109
4.3.4 <i>Wave climate</i>	4.2
4.4 Numerical prediction of ship seakeeping	117

4.4.1 Overview of computational methods	117
4.4.2 Strip method	121
4.4.3 Rankine singularity methods	127
4.4.4 Problems for fast and unconventional ships	130
4.4.5 Further quantities in regular waves	132
4.4.6 Ship responses in stationary seaway	132
4.4.7 Simulation methods	134
4.4.8 Long-term distributions	136
4.5 Slamming	138
4.6 Exercises: seakeeping	146
Discourse: hydrodynamic mass	148
5 Ship manoeuvring	151
5.1 Introduction	151
5.2 Simulation of manoeuvring with known coefficients	152
5.2.1 Introduction and definitions	152
5.2.2 Force coefficients	153
5.2.3 Physical explanation and force estimation	158
5.2.4 Influence of heel	163
5.2.5 Shallow water and other influences	164
5.2.6 Stopping	164
5.2.7 Jet thrusters	165
5.2.8 CFD for ship manoeuvring	166
5.3 Experimental approaches	169
5.3.1 Manoeuvring tests for full-scale ships in sea trials	169
5.3.2 Model tests	175
5.4 Rudders	177
5.4.1 General remarks and definitions ...	177
5.4.2 Fundamental hydrodynamic aspects of rudders and simple estimates	181
5.4.3 Rudder types	188
5.4.4 Interaction of rudder and propeller	190

5.4.5 Interaction of rudder and ship hull.....	193
5.4.6 Rudder cavitation	195
5.4.7 Rudder design.....	200
5.4.8 CFD for rudder flows and conclusions for rudder design	201
5.5 Exercise: manoeuvring.....	203
6 Boundary element methods	207
6.1 Introduction	207
6.2 Source elements	209
6.2.1 Point source	209
6.2.2 Regular first-order panel	211
6.2.3 Jensen panel.....	215
6.2.4 Higher-order panel	218
6.3 Vortex elements	223
6.4 Dipole elements	226
6.4.1 Point dipole	226
6.4.2 Thiart element	227
6.5 Special techniques	229
6.5.1 Desingularization.....	229
6.5.2 Patch method	230
7 Numerical example for BEM	236
7.1 Two-dimensional flow around a body in infinite fluid.....	236
7.1.1 Theory	236
7.1.2 Numerical implementation.....	237
7.2 Two-dimensional wave resistance problem	238
7.2.1 Theory	238
7.2.2 Numerical implementation.....	241
7.3 Three-dimensional wave resistance problem	242
7.3.1 Theory	242
7.3.2 Numerical implementation.....	247
7.4 Strip method module (two dimensional)	250
7.5 Rankine panel method in the frequency domain.....	253
7.5.1 Theory	253

7.5.2 Numerical implementation.....	261
References	265
Index	269

Preface

The first five chapters give an introduction to ship hydrodynamics, which is in my opinion suitable for teaching at a senior undergraduate level or even at a postgraduate level. It is thus also suitable for engineers working in industry. The book assumes that the reader has a solid knowledge of general fluid dynamics. In teaching, general fluid dynamics and specific ship hydrodynamics are often mixed but I believe that universities should first teach a course in general fluid dynamics which should be mandatory to most engineering students. There are many good textbooks on the market for this purpose. Naval architects should then concentrate on the particular aspects of their field and cover material more suited to their needs. This book is organized to support such a strategy in teaching.

The first chapter is an introduction to computational fluid dynamics, and Chapters 2 to 5 cover the four main areas of propeller flows, resistance and propulsion, ship seakeeping and manoeuvring. It is recommended that this sequence be followed in teaching. The first five chapters try to find a suitable balance for practical engineers between facts and minimizing formula work. However, there are still formulae. These are intended to help those tasked with computations or programming. Readers with a practical interest may simply skip these passages. The final two chapters involve more extensive formula work and are more specialized. They may be reserved for graduate and post-graduate teaching and will help understanding and developing boundary element codes. Field methods are not covered in depth here, as my colleague Milovan Peric has already co-authored an excellent book on this particular topic. I tried in vain to find a similar suitable textbook for boundary element methods which would be both easy to understand and address the typical problems encountered in ship flows. As I could not find such a book, I wrote two chapters intended to support me in my teaching and to be of use for many colleagues.

The book is supplemented by some public domain software written in Fortran which is available for downloading in source code on www.bh.com/companions/0750648511. The software consists of small programs or subroutines which may help in developing own codes. Some of the programs have been written by myself, some by Professor Söding, and some by colleagues. Feel free to download the software, but there is no additional documentation available except for the in-program comments. I will not answer questions about the software, but you can comment on which programs you

felt difficult to understand. We may then either update the documentation or take the software off the website. There is no guarantee that the programs are completely debugged and of course neither I nor the publisher will take any responsibility for what happens if you use these programs. Furthermore, the software is public domain and you may not sell it to third parties.

Despite all this, I have worked with most of the software myself without any problems. The website will be updated more often than the book, and there will be a short read.me file on the web with some information on the available software.

This book is based largely on lectures for German students. The nucleus of the book was formed by lectures on ship seakeeping and ship manoeuvring, which I have taught for several years with Professor Heinrich Söding. I always felt that we should have a comprehensive textbook that would also cover resistance and propulsion, as ship seakeeping and manoeuvring are both interwoven strongly with the steady base flow. Many colleagues helped with providing material, allowing me to pick the best from their teaching approaches. A lot of material was written and compiled in a new way, inspired by these sources, but the chapters on ship seakeeping and manoeuvring use extensive existing material.

Thanks are due to Seehafen-Verlag Hamburg for permission to reprint text and figures from the *Manoeuvring Technical Manual*, an excellent book unfortunately no longer in print. Thanks are due to Hansa-Verlag Hamburg for permission to reprint text and figures from German contributions in *Handbuch der Werften XXIV*.

Countless colleagues supported the endeavour of writing this book by supplying material, proof-reading, making comments or just discussing engineering or didactic matters. Among these are (in alphabetical order) Poul Andersen, Kai Graf, Mike Hughes, Hidetsugu Iwashita, Gerhard Jensen, Meinolf Kloppenburg, Jochen Laudan, Maurizio Landrini, Friedrich Mewis, Katsuji Tanizawa, Gerhard Thiart, Michel Visonneau, and Hironori Yasukawa. Most of all, Professor Heinrich Söding has supported this book to an extent that he should have been named as co-author, but, typically for him, he declined the offer. He even refused to allow me to dedicate this book to him.

I then dedicate this book to the best mentor I ever had, a role model as a scientist and a man, so much better than I will ever be. You know who.

Volker Bertram

Models now in tanks we tow.
All of that to Froude we owe.
Will computers, fast and new,
Make us alter Euler's view?

Marshall Tulin

1

Introduction

1.1 Overview of problems and approaches

The prediction of ship hydrodynamic performance can be broken down into the general areas of

- resistance and propulsion
- seakeeping
- manoeuvring

Propeller flows and propeller design can be seen as a subtopic of resistance and propulsion, but it is so important and features special techniques that it is treated as a separate topic in its own right. Morgan and Lin (1998) give a good short introduction to the historical development of these techniques to the state of the art in the late 1990s.

The basic approaches can be roughly classified into:

- *Empirical/statistical approaches*

Design engineers need simple and reasonably accurate estimates, e.g. of the power requirements of a ship. Common approaches combine a rather simple physical model and regression analysis to determine required coefficients either from one parent ship or from a set of ships. The coefficients may be given in the form of constants, formulae, or curves.

Because of the success with model testing, experimental series of hull forms have been developed for varying hull parameters. Extensive series were tested in the 1940s and the subsequent two decades. These series were created around a 'good' hull form as the parent form. The effect of essential hull parameters, e.g. block coefficient, was determined by systematic variations of these parameters. Because of the expense of model construction and testing, there are no recent comparable series tested of modern hull forms and the traditional ship series must be considered as outdated by now.

Although empirical and statistical approaches are still popular in design practice, we will not treat them in detail here, because they are of little relevance to the ship hydrodynamicist. Ship designers are referred to Schneekloth and Bertram (1998) for a review of these empirical approaches.

- *Experimental approaches, either in model tests or in full-scale trials*

The basic idea of model testing is to experiment with a scale model to extract information that can be scaled (transformed) to the full-scale ship.

Despite continuing research and standardization efforts, a certain degree of empiricism is still necessary, particularly in the model-to-ship correlation which is a method to enhance the prediction accuracy of ship resistance by empirical means. The total resistance can be decomposed in various ways. Traditionally, model basins tend to adopt approaches that seem most appropriate to their respective organization's corporate experience and accumulated databases. Unfortunately, this makes various approaches and related aggregated empirical data incompatible.

Although there has been little change in the basic methodology of ship resistance since the days of Froude (1874), various aspects of the techniques have progressed. We now understand better the flow around three-dimensional, appended ships, especially the boundary layer effects. Also non-intrusive experimental techniques like laser-Doppler velocimetry (LDV) allow the measurement of the velocity field in the ship wake to improve propeller design. Another more recent experimental technique is wave pattern analysis to determine the wave-making resistance.

In propulsion tests, measurements include towing speed and propeller quantities such as thrust, torque, and rpm. Normally, open-water tests on the propeller alone are run to aid the analysis process as certain coefficients are necessary for the propeller design. Strictly, open-water tests are not essential for power prediction alone. The model propeller is usually a stock propeller (taken from a large selection/stock of propellers) that approximates the actual design propeller. Propulsion tests determine important input parameters for the actual detailed propeller design, e.g. wake fraction and thrust deduction.

The wake distribution, also needed for propeller design, is measured behind the ship model using pitot tubes or laser-Doppler velocimetry (LDV). For propeller design, measured nominal wakes (for the ship without propeller) for the model must be transformed to effective wakes (for the ship with working propeller) for the full-scale ship. While semi-empirical methods for this transformation work apparently well for most hull forms, for those with considerable flow separation at the stern, i.e. typically full hulls, there are significant scale effects on the wake between model and full scale. To some extent, computational fluid dynamics can help here in estimating the scale effects.

Although the procedures for predicting full-scale resistance from model tests are well accepted, full-scale data available for validation purposes are extremely limited and difficult to obtain. The powering performance of a ship is validated by actual ship trials, ideally conducted in calm seas. The parameters usually measured are torque, rpm, and speed. Thrust is measured only as a special requirement because of the difficulty and extra expense involved in obtaining accurate thrust data. Whenever possible and appropriate, corrections are made for the effects of waves, current, wind, and shallow water. Since the 1990s, the Global Positioning System (GPS) and computer-based data acquisition systems have considerably increased the accuracy and economy of full-scale trials. The GPS has eliminated the need for 'measured miles' trials near the shore with the possible contamination of data due to shallow-water effects. Today trials are usually conducted far away from the shore.

Model tests for seakeeping are often used only for validation purposes. However, for open-top containerships and ro-ro ships model tests are often performed as part of the regular design process, as IMO regulations require

certain investigations for ship safety which may be documented using model tests.

Most large model basins have a manoeuvring model basin. The favoured method to determine the coefficients for the equations of motion is through a planar motion mechanism and rotating arm model tests. However, scaling the model test results to full scale using the coefficients derived in this manner is problematic, because vortex shedding and flow separation are not similar between model and full scale. Appendages generally make scaling more difficult. Also, manoeuvring tests have been carried out with radio-controlled models in lakes and large reservoirs. These tests introduce additional scale effects, since the model propeller operates in a different self-propulsion point than the full-scale ship propeller. Despite these concerns, the manoeuvring characteristics of ships seem generally to be predicted with sufficient accuracy by experimental approaches.

- *Numerical approaches, either rather analytical or using computational fluid dynamics (CFD)*

For ship resistance and powering, CFD has become increasingly important and is now an indispensable part of the design process. Typically inviscid free-surface methods based on the boundary element approach are used to analyse the forebody, especially the interaction of bulbous bow and forward shoulder. Viscous flow codes often neglect wave making and focus on the aftbody or appendages. Flow codes modelling both viscosity and the wave-making are at the threshold of practical applicability. CFD is still considered by industry as too inaccurate for resistance or power predictions. Instead, it is used to gain insight into local flow details and derive recommendation on how to improve a given design or select a most promising candidate design for model testing.

For seakeeping, simple strip methods are used to analyse the seakeeping properties. These usually employ boundary element methods to solve a succession of two-dimensional problems and integrate the results into a quasi-three-dimensional result with usually good accuracy.

A commonly used method to predict the turning and steering of a ship is to use equations of motions with experimentally determined coefficients. Once these coefficients are determined for a specific ship design – by model tests or estimated from similar ships or by empirically enhanced strip methods – the equations of motions are used to simulate the dynamic behaviour of the ship. The form of the equations of motions is fairly standard for most hull designs. The predictions can be used, e.g., to select rudder size and steering control systems, or to predict the turning characteristics of ships. As viscous CFD codes become more robust and efficient to use, the reliance on experimentally derived coefficients in the equations of motions may be reduced. In an intermediate stage, CFD may help in reducing the scaling errors between model tests and full scale.

Although a model of the final ship design is still tested in a towing tank, the testing sequence and content have changed significantly over the last few years. Traditionally, unless the new ship design was close to an experimental series or a known parent ship, the design process incorporated many model tests. The process has been one of design, test, redesign, test etc. sometimes involving more than 10 models each with slight variations. This is no longer feasible due to time-to-market requirements from shipowners and no longer

necessary thanks to CFD developments. Combining CAD (computer-aided design) to generate new hull shapes in concert with CFD to analyse these hull shapes allows for rapid design explorations without model testing. CFD allows the preselection of the most promising design. Then often only one or two models are actually tested to validate the intended performance features in the design and to get a power prediction accepted in practice as highly accurate. As a consequence of this practice, model tests for shipyard customers have declined considerably since the 1980s. This was partially compensated by more sophisticated and detailed tests funded from research projects to validate and calibrate CFD methods.

One of the biggest problems for predicting ship seakeeping is determining the nature of the sea: how to predict and model it, for both experimental and computational analyses. Many long-term predictions of the sea require a Fourier decomposition of the sea and ship responses with an inherent assumption that the sea and the responses are ‘moderately small’, while the physics of many seakeeping problems is highly non-linear. Nevertheless, seakeeping predictions are often considered to be less important or covered by empirical safety factors where losses of ships are shrugged off as ‘acts of God’, until they occur so often or involve such spectacular losses of life that safety factors and other regulations are adjusted to a stricter level. Seakeeping is largely not understood by shipowners and global ‘sea margins’ of, e.g., 15% to finely tuned ($\pm 1\%$) power predictions irrespective of the individual design are not uncommon.

1.2 Model tests – similarity laws

Since the purely numerical treatment of ship hydrodynamics has not yet reached a completely satisfactory stage, model tests are still essential in the design process and for validation purposes. The model tests must be performed such that model and full-scale ships exhibit similar behaviour, i.e. the results for the model can be transferred to full scale by a proportionality factor. We indicate in the following the full-scale ship by the index s and the model by the index m .

We distinguish between

- geometrical similarity
- kinematical similarity
- dynamical similarity

Geometrical similarity means that the ratio of a full-scale ‘length’ (length, width, draft etc.) L_s to a model-scale ‘length’ L_m is constant, namely the model scale λ :

$$L_s = \lambda \cdot L_m$$

Correspondingly we get for areas and volumes: $A_s = \lambda^2 \cdot A_m$; $\nabla_s = \lambda^3 \cdot \nabla_m$.

In essence, the model then ‘appears’ to be the same as the full-scale ship. While this is essential for movie makers, it is not mandatory for naval architects who want to predict the hydrodynamic performance of a full-scale ship. In fact,

there have been proposals to deviate from geometrical similarity to achieve better similarity in the hydrodynamics. However, these proposals were not accepted in practice and so we always strive at least in macroscopic dimensions for geometrical similarity. In microscopic dimensions, e.g. for surface roughness, geometrical similarity is not obtained.

Kinematic similarity means that the ratio of full-scale times t_s to model-scale times t_m is constant, namely the kinematic model scale τ :

$$t_s = \tau \cdot t_m$$

Geometrical and kinematical similarity result then in the following scale factors for velocities and accelerations:

$$V_s = \frac{\lambda}{\tau} \cdot V_m \quad a_s = \frac{\lambda}{\tau^2} \cdot a_m$$

Dynamical similarity means that the ratio of all forces acting on the full-scale ship to the corresponding forces acting on the model is constant, namely the dynamical model scale κ :

$$F_s = \kappa \cdot F_m$$

Forces acting on the ship encompass inertial forces, gravity forces, and frictional forces.

Inertial forces follow Newton's law $F = m \cdot a$, where F denotes force, m mass, and a acceleration. For displacement ships, $m = \rho \cdot \nabla$, where ρ is the density of water and ∇ the displacement. We then obtain for ratio of the inertial forces:

$$\kappa = \frac{F_s}{F_m} = \frac{\rho_s}{\rho_m} \cdot \frac{\nabla_s}{\nabla_m} \cdot \frac{a_s}{a_m} = \frac{\rho_s}{\rho_m} \cdot \frac{\lambda^4}{\tau^2}$$

This equation couples all three scale factors. It is called Newton's law of similarity. We can rewrite Newton's law of similarity as:

$$\kappa = \frac{F_s}{F_m} = \frac{\rho_s}{\rho_m} \cdot \lambda^2 \cdot \left(\frac{\lambda}{\tau} \right)^2 = \frac{\rho_s}{\rho_m} \cdot \frac{A_s}{A_m} \cdot \left(\frac{V_s}{V_m} \right)^2$$

Hydrodynamic forces are often described by a coefficient c as follows:

$$F = c \cdot \frac{1}{2} \rho \cdot V^2 \cdot A$$

V is a reference speed (e.g. ship speed), A a reference area (e.g. wetted surface in calm water). The factor $\frac{1}{2}$ is introduced in analogy to stagnation pressure $q = \frac{1}{2} \rho \cdot V^2$. Combining the above equations then yields:

$$\frac{F_s}{F_m} = \frac{c_s \cdot \frac{1}{2} \rho_s \cdot V_s^2 \cdot A_s}{c_m \cdot \frac{1}{2} \rho_m \cdot V_m^2 \cdot A_m} = \frac{\rho_s}{\rho_m} \cdot \frac{A_s}{A_m} \cdot \left(\frac{V_s}{V_m} \right)^2$$

This results in $c_s = c_m$, i.e. the non-dimensional coefficient c is constant for both ship and model. For same non-dimensional coefficients Newton's similarity law is fulfilled and vice versa.

Gravity forces can be described in a similar fashion as inertial forces:

$$G_s = \rho_s \cdot g \cdot \nabla_s \quad \text{resp.} \quad G_m = \rho_m \cdot g \cdot \nabla_m$$

This yields another force scale factor:

$$\kappa_g = \frac{G_s}{G_m} = \frac{\rho_s}{\rho_m} \cdot \frac{\nabla_s}{\nabla_m} = \frac{\rho_s}{\rho_m} \cdot \lambda^3$$

For dynamical similarity both force scale factors must be the same, i.e. $\kappa = \kappa_g$. This yields for the time scale factor:

$$\tau = \sqrt{\lambda}$$

We can now eliminate the time scale factors in all equations above and express the proportionality exclusively in the length scale factor λ , e.g.:

$$\frac{V_s}{V_m} = \sqrt{\lambda} \longrightarrow \frac{V_s}{\sqrt{L_s}} = \frac{V_m}{\sqrt{L_m}}$$

It is customary to make the ratio of velocity and square root of length non-dimensional with $g = 9.81 \text{ m/s}^2$. This yields the Froude number:

$$F_n = \frac{V}{\sqrt{g \cdot L}}$$

The same Froude number in model and full scale ensures dynamical similarity only if inertial and gravity forces are present (Froude's law). For the same Froude number, the wave pattern in model and full scale are geometrically similar. This is only true for waves of small amplitude where gravity is the only relevant physical mechanism. Breaking waves and splashes involve another physical mechanism (e.g. surface tension) and do not scale so easily. Froude's law is kept in all regular ship model tests (resistance and propulsion tests, seakeeping tests, manoeuvring tests). This results in the following scales for speeds, forces, and powers:

$$\frac{V_s}{V_m} = \sqrt{\lambda} \quad \frac{F_s}{F_m} = \frac{\rho_s}{\rho_m} \cdot \lambda^3 \quad \frac{P_s}{P_m} = \frac{F_s \cdot V_s}{F_m \cdot V_m} = \frac{\rho_s}{\rho_m} \cdot \lambda^{3.5}$$

Frictional forces follow yet another similarity law, and are primarily due to frictional stresses (due to friction between two layers of fluid):

$$R = \mu \cdot \frac{\partial u}{\partial n} \cdot A$$

μ is a material constant, namely the dynamic viscosity. The partial derivative is the velocity gradient normal to the flow direction. A is the area subject to the frictional stresses. Then the ratio of the frictional forces is:

$$\kappa_f = \frac{R_s}{R_m} = \frac{\mu_s (\partial u_s / \partial n_s) A_s}{\mu_m (\partial u_m / \partial n_m) A_m} = \frac{\mu_s}{\mu_m} \frac{\lambda^2}{\tau}$$

Again we demand that the ratio of frictional forces and inertial forces should be the same, $\kappa_f = \kappa$. This yields:

$$\frac{\mu_s}{\mu_m} \frac{\lambda^2}{\tau} = \frac{\rho_s}{\rho_m} \frac{\lambda^4}{\tau^2}$$

If we introduce the kinematic viscosity $\nu = \mu/\rho$ this yields:

$$\frac{\nu_s}{\nu_m} = \frac{\lambda^2}{\tau} = \frac{V_s \cdot L_s}{V_m \cdot L_m} \longrightarrow \frac{V_s \cdot L_s}{\nu_s} = \frac{V_m \cdot L_m}{\nu_m}$$

$R_n = V \cdot L/\nu$ is the Reynolds number, a non-dimensional speed parameter important in viscous flows. The same Reynolds number in model and full scale ensures dynamic similarity if only inertial and frictional forces are present (Reynolds' law). (This is somewhat simplified as viscous flows are complicated by transitions from laminar to turbulent flows, microscopic scale effects such as surface roughness, flow separation etc.) The kinematic viscosity ν of seawater [m/s²] can be estimated as a function of temperature t [°C] and salinity s [%]:

$$\nu = 10^{-6} \cdot (0.014 \cdot s + (0.000645 \cdot t - 0.0503) \cdot t + 1.75)$$

Sometimes slightly different values for the kinematic viscosity of water may be found. The reason is that water is not perfectly pure, containing small organic and inorganic matter which differs regionally and in time.

Froude number and Reynolds number are related by:

$$\frac{R_n}{F_n} = \frac{V \cdot L}{\nu} \cdot \frac{\sqrt{gL}}{V} = \frac{gL^3}{\nu}$$

Froude similarity is easy to fulfil in model tests, as with smaller models also the necessary test speed decreases. Reynolds' law on the other hand is difficult to fulfil as smaller models mean higher speeds for constant kinematic viscosity. Also, forces do not scale down for constant viscosity.

Ships operating at the free surface are subject to gravity forces (waves) and frictional forces. Thus in model tests both Froude's and Reynolds' laws should be fulfilled. This would require:

$$\frac{R_{ns}}{R_{nm}} = \frac{\nu_m}{\nu_s} \cdot \sqrt{\frac{L_s^3}{L_m^3}} = \frac{\nu_m}{\nu_s} \cdot \lambda^{1.5} = 1$$

i.e. model tests should choose model scale and viscosity ratio of the test fluid such that $(\nu_m/\nu_s) \cdot \lambda^{1.5} = 1$ is fulfilled. Such fluids do not exist or at least are not cheap and easy to handle for usual model scales. However, sometimes the test water is heated to improve the viscosity ratio and reduce the scaling errors for viscous effects.

Söding (1994) proposed 'sauna tanks' where the water is heated to a temperature of 90° . Then the same Reynolds number as in cold water can be reached using models of only half the length. Smaller tanks could be used which could be better insulated and may actually require less energy than today's large tanks. The high temperature would also allow similar cavitation numbers as for the full-scale ship. A futuristic towing tank may be envisioned that would also perform cavitation tests on propellers eliminating the need for special cavitation tunnels. However, such 'sauna tanks' have not been established yet and there are doubts concerning the feasibility of such a concept.

For model tests investigating vibrations Froude's similarity law does not automatically also give *similarity in vibrations*. For example, for propeller blade vibrations, model propellers of the same material as the full-scale propeller are too stiff under Froude similarity. Similarity in vibrations follows Cauchy's scaling law, requiring that the Cauchy number is the same in model and full scale:

$$C_n = \frac{E \cdot I \cdot t^2}{\rho \cdot g \cdot L^6}$$

E is the modulus of elasticity, I the moment of inertia, t the time, L a length. The same Cauchy and Froude numbers means that for the same density, the modulus of elasticity is downscaled by λ from full scale to model scale.

1.3 Full-scale trials

Trial tests of the built ship are an important prerequisite for the acceptance of the ship by the shipowner and are always specified in the contract between shipowner and shipyard. The problem is that the trial conditions differ from both model test conditions and design conditions. The contract usually specifies a contract speed at design load at a given percentage of the maximum continuous rating of the engine, this at calm sea without wind and current on deep water. Trial conditions are usually in ballast load, natural seaways, in the presence of currents and often shallow water. Only on rare occasions is it possible to perform trial tests under ideal conditions as specified in the contract. However, upper limits for the wind and sea conditions are usually defined in the contract and test trials are performed only at times or places where the actual conditions are within the specified limits.

The difference between contract and trial conditions requires various corrections to correlate trial results to contract conditions. Apart from the difficulties and margins of uncertainties in the trial measurements, the correlation procedure is plagued by many doubts. The traditional methods are partly empirical, involving curves with manual interpolation etc. It was not uncommon that the results of various consultants, e.g. towing tank experts, differed by several tenths of a knot for the obtainable speed under contract conditions. This

margin may make a difference between paying and not paying considerable penalties! Subsequently, trial evaluation was susceptible to disputes between representatives of shipowners and shipyards. The increasing demand for quality management and clearly documented procedures, preferably on an international standard, led to the formation of various panels of experts. The Japan Marine Standards Association submitted in 1998 a proposal for an ISO standard for the assessment of speed and power in speed trials. Also, the ‘trial and monitoring’ subcommittee of the ITTC (International Towing Tank Conference) was tasked with the development of an international standard.

Test trials were traditionally ‘measured mile trials’, as ships were tested between measured miles near the coast for different ship speeds. The ship speed can be measured ‘over ground’ (relative to the earth) or ‘in water’ (relative to the water). The speed in water includes currents and local flow changes. Historically, various logs have been developed, including devices towed behind the ship, on long rods alongside the ship, electro-acoustic devices, and pitot tubes in the ship bottom. The speed over ground was traditionally determined by electro-acoustic devices, celestial navigation, and radio navigation. The advent of satellite systems, namely GPS (Global Positioning System) and DGPS (Differential GPS), has eliminated many of the previous uncertainties and problems. GPS allows accurate determination of the speed over ground, although the speed of interest is the speed in water. Trials are usually performed by repeatedly testing the ship on opposite courses to eliminate the effects of current. It is best to align the course with the wind and predominant wave propagation direction to make elimination of these effects in the correlation procedure easier.

Seakeeping is usually not measured in detail as a normal procedure in ship deliveries. Full-scale seakeeping tests are sometimes used in research and are discussed in more detail in section 4.2, Chapter 4.

1.4 Numerical approaches (computational fluid dynamics)

1.4.1 Basic equations

For the velocities involved in ship flows, water can be regarded as incompressible, i.e. the density ρ is constant. Therefore we will limit ourselves here to incompressible flows. All equations are given in a Cartesian coordinate system with z pointing downwards.

The continuity equation states that any amount flowing into a control volume also flows out of the control volume at the same time. We consider for the two-dimensional case an infinitely small control volume as depicted in Fig. 1.1. u and v are the velocity components in x resp. y direction. The indices denote partial derivatives, e.g. $u_x = \partial u / \partial x$. Positive mass flux leaves the control volume, negative mass flux enters the control volume. The total mass flux has to fulfil:

$$-\rho \, dy \, du + \rho \, dy (u + u_x \, dx) - \rho \, dx \, dv + \rho \, dx (v + v_y \, dy) = 0$$

$$u_x + v_y = 0$$

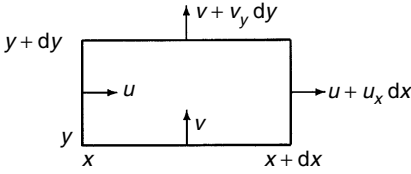


Figure 1.1 Control volume to derive continuity equation in two dimensions

The continuity equation in three dimensions can be derived correspondingly to:

$$u_x + v_y + w_z = 0$$

w is the velocity component in z direction.

The Navier–Stokes equations together with the continuity equation suffice to describe all real flow physics for ship flows. The Navier–Stokes equations describe conservation of momentum in the flow:

$$\rho(u_t + uu_x + vu_y + wu_z) = \rho f_1 - p_x + \mu(u_{xx} + u_{yy} + u_{zz})$$

$$\rho(v_t + uv_x + vv_y + wv_z) = \rho f_2 - p_y + \mu(v_{xx} + v_{yy} + v_{zz})$$

$$\rho(w_t + uw_x + vw_y + ww_z) = \rho f_3 - p_z + \mu(w_{xx} + w_{yy} + w_{zz})$$

f_i is an acceleration due to a volumetric force, p the pressure, μ the viscosity and t the time. Often the volumetric forces are neglected, but gravity can be included by setting $f_3 = g$ ($=9.81 \text{ m/s}^2$) or the propeller action can be modelled by a distribution of volumetric forces f_1 . The l.h.s. of the Navier–Stokes equations without the time derivative describes convection, the time derivative describes the rate of change (‘source term’), the last term on the r.h.s. describes diffusion.

The Navier–Stokes equations in the above form contain on the l.h.s. products of the velocities and their derivatives. This is a non-conservative formulation of the Navier–Stokes equations. A conservative formulation contains unknown functions (here velocities) only as first derivatives. Using the product rule for differentiation and the continuity equation, the non-conservative formulation can be transformed into a conservative formulation, e.g. for the first of the Navier–Stokes equations above:

$$\begin{aligned} (u^2)_x + (uv)_y + (uw)_z &= 2uu_x + u_yv + uv_y + u_zw + uw_z \\ &= uu_x + vu_y + wu_z + u \underbrace{(u_x + v_y + w_z)}_{=0} \\ &= uu_x + vu_y + wu_z \end{aligned}$$

Navier–Stokes equations and the continuity equation form a system of coupled, non-linear partial differential equations. An analytical solution of this system is impossible for ship flows. Even if the influence of the free surface (waves) is neglected, today’s computers are not powerful enough to allow a numerical

solution either. Even if such a solution may become feasible in the future, it is questionable if it is really necessary for engineering purposes in naval architecture.

Velocities and pressure may be divided into a time average and a fluctuation part to bring the Navier–Stokes equations closer to a form where a numerical solution is possible. Time averaging yields the Reynolds-averaged Navier–Stokes equations (RANSE). u , v , w and p are from now on time averages. u' , v' , w' denote the fluctuation parts. For unsteady flows (e.g. manoeuvring), high-frequency fluctuations are averaged over a chosen time interval (assembly average). This time interval is small compared to the global motions, but large compared to the turbulent fluctuations. Most computations for ship flows are limited to steady flows where the terms u_t , v_t , and w_t vanish.

The RANSE have a similar form to the Navier–Stokes equations:

$$\begin{aligned}\rho(u_t + uu_x + vu_y + ww_z) &= \rho f_1 - p_x + \mu(u_{xx} + u_{yy} + u_{zz}) \\ &\quad - \rho((\overline{u'u'})_x + (\overline{u'v'})_y + (\overline{u'w'})_z) \\ \rho(v_t + uv_x + vv_y + vw_z) &= \rho f_2 - p_y + \mu(v_{xx} + v_{yy} + v_{zz}) \\ &\quad - \rho((\overline{u'v'})_x + (\overline{v'v'})_y + (\overline{v'w'})_z) \\ \rho(w_t + uw_x + vw_y + ww_z) &= \rho f_3 - p_z + \mu(w_{xx} + w_{yy} + w_{zz}) \\ &\quad - \rho((\overline{u'w'})_x + (\overline{v'w'})_y + (\overline{w'w'})_z)\end{aligned}$$

They contain as additional terms the derivatives of the Reynolds stresses:

$$\begin{aligned}& - \rho \overline{u'u'} - \rho \overline{u'v'} - \rho \overline{u'w'} \\ & - \rho \overline{u'v'} - \rho \overline{v'v'} - \rho \overline{v'w'} \\ & - \rho \overline{u'w'} - \rho \overline{v'w'} - \rho \overline{w'w'}\end{aligned}$$

The time averaging eliminated the turbulent fluctuations in all terms except the Reynolds stresses. The RANSE require a turbulence model that couples the Reynolds stresses to the average velocities. There are whole books and conferences dedicated to turbulence modelling. Recommended for further studies is, e.g., Ferziger and Peric (1996). Turbulence modelling will not be treated here in detail, except for a brief discourse in section 1.5.1. It suffices to say that none of the present models is universally convincing and research continues to look for better solutions for ship flows. Because we are so far from being able to solve the actual Navier–Stokes equations, we often say ‘Navier–Stokes’ (as in Navier–Stokes solver) when we really mean RANSE.

‘Large-eddy simulations’ (LES) are located between Navier–Stokes equations and RANSE. LES let the grid resolve the large vortices in the turbulence directly and only model the smaller turbulence structures. Depending on what is considered ‘small’, this method lies closer to RANSE or actual Navier–Stokes equations. So far few researchers have attempted LES computations for ship flows and the grid resolution was usually too coarse to allow any real progress compared to RANSE solutions.

Neglecting viscosity – and thus of course all turbulence effects – turns the Navier–Stokes equations (also RANSE) into the Euler equations which still have to be solved together with the continuity equations:

$$\rho(u_t + uu_x + vv_y + ww_z) = \rho f_1 - p_x$$

$$\rho(v_t + uv_x + vv_y + ww_z) = \rho f_2 - p_y$$

$$\rho(w_t + uw_x + vw_y + ww_z) = \rho f_3 - p_z$$

Euler solvers allow coarser grids and are numerically more robust than RANSE solvers. They are suited for computation of flows about lifting surfaces (foils) and are thus popular in aerospace applications. They are not so well suited for ship flows and generally not recommended because they combine the disadvantages of RANSE and Laplace solvers without being able to realize their major advantages: programming is almost as complicated as for RANSE solvers, but the physical model offers hardly any improvements over simple potential flow codes (Laplace solvers).

A further simplification is the assumption of irrotational flow:

$$\nabla \times \vec{v} = \left\{ \begin{array}{c} \partial/\partial x \\ \partial/\partial y \\ \partial/\partial z \end{array} \right\} \times \vec{v} = 0$$

A flow that is irrotational, inviscid and incompressible is called potential flow. In potential flows the components of the velocity vector are no longer independent from each other. They are coupled by the potential ϕ . The derivative of the potential in arbitrary direction gives the velocity component in this direction:

$$\vec{v} = \left\{ \begin{array}{c} u \\ v \\ w \end{array} \right\} = \nabla \phi$$

Three unknowns (the velocity components) are thus reduced to one unknown (the potential). This leads to a considerable simplification of the computation.

The continuity equation simplifies to Laplace's equation for potential flow:

$$\Delta \phi = \phi_{xx} + \phi_{yy} + \phi_{zz} = 0$$

If the volumetric forces are limited to gravity forces, the Euler equations can be written as:

$$\nabla \left(\phi_t + \frac{1}{2}(\nabla \phi)^2 - gz + \frac{1}{\rho} p \right) = 0$$

Integration gives Bernoulli's equation:

$$\phi_t + \frac{1}{2}(\nabla \phi)^2 - gz + \frac{1}{\rho} p = \text{const.}$$

The Laplace equation is sufficient to solve for the unknown velocities. The Laplace equation is linear. This offers the big advantage of combining elementary solutions (so-called sources, sinks, dipoles, vortices) to arbitrarily complex solutions. Potential flow codes are still the most commonly used CFD tools

in naval architecture. Some elementary solutions frequently used for ship flow computations will be discussed later in the book.

Boundary layer equations represent a special branch in the development of hydrodynamics, (see Schlichting (1979)), which are historically important. The boundary layer equations introduce many simplifications in the physical model: diffusion in the predominant flow direction is neglected, the thickness of the boundary layer is taken as small, and the pressure is constant over the thickness. These assumptions are violated near separating boundary layers. Therefore separation cannot be predicted properly. Of course, neither is any evaluation of the separated flow possible. But this is the area of interest for improving aftbodies and designing the propeller. One of the last doctoral theses on boundary layer methods for ship flows concluded in 1993: ‘With the present method the practically interesting velocities at the propeller plane cannot be determined because there is no wall. In order to compute all the velocity components in a thick boundary layer and at the propeller plane, the Navier–Stokes equations have to be solved.’

Boundary layer methods had been substituted almost completely by RANSE solvers by the end of the 1980s. A series of validation workshops demonstrated that the solution of the equations for thin boundary layers failed in the stern region because of the rapid thickening of the boundary layer in this zone. The limited success of generalizations of thin boundary layer equations involving high order corrections was subsequently demonstrated so that the tendency towards computing the full solution of the Navier–Stokes equations became stronger and stronger because increased computer resources became more and more available at continuously decreasing costs.

Basic equations (and flows) are sometimes classified as elliptic, hyperbolic or parabolic. Consider a two-dimensional differential equation of second order:

$$A \frac{\partial^2 f}{\partial x^2} + 2B \frac{\partial^2 f}{\partial x \partial y} + C \frac{\partial^2 f}{\partial y^2} + a \frac{\partial f}{\partial x} + b \frac{\partial f}{\partial y} + c f + d = 0$$

For $\delta = AC - B^2 > 0$ the equation is ‘elliptic’, for $\delta = 0$ ‘parabolic’ and for $\delta < 0$ ‘hyperbolic’. The names are derived from an analogy to the algebraic equation:

$$Ax^2 + 2Bxy + Cy^2 + ax + by + d = 0$$

This equation describes for $\delta = AC - B^2 > 0$ an ellipse, for $\delta = 0$ a parabola, and for $\delta < 0$ a hyperbola. Behind these rather abstract mathematical definitions lies a physical meaning (Fig. 1.2):

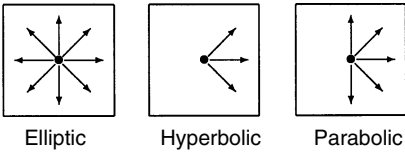


Figure 1.2 A disturbance propagates differently depending on the type of field equation

- *elliptic*:

Disturbances propagate in all directions. RANSE and the Laplace equation are in general elliptic.

- *hyperbolic:*

Disturbances are limited in their propagation to a conical (or in two dimensions a wedge-shaped) region. Supersonic flow with a Mach cone follows a hyperbolic field equation. The Kelvin angle in the wave pattern results in a radiation condition of ‘hyperbolic’ character.

- *parabolic:*

The extreme case of a hyperbolic flow is a parabolic flow. Here the angle of the cone/wedge opens up to 90° . Disturbances propagate only downstream. ‘Parabolic’ RANSE solvers allow faster solution with reduced storage requirements. They start the computation at the upstream end and solve strip after strip marching downstream. Instead of considering the whole domain at one time, only two adjacent strips have to be considered at any time. However, local flow reversals could never be captured by such a method because they violate the assumed parabolic character of the flow. Parabolic RANSE solvers thus appeared only shortly in the 1980s and were replaced by fully elliptic solvers when more computer power became widely available. All unsteady equations are parabolic in time.

1.4.2 Basic CFD techniques

CFD comprises methods that solve the basic field equations subject to boundary conditions by approaches involving a large number of (mathematically simple) elements. These approaches lead automatically to a large number of unknowns. Basic CFD techniques are:

- *Boundary element methods (BEM)*

BEM are used for potential flows. For potential flows, the integrals over the whole fluid domain can be transformed to integrals over the boundaries of the fluid domain. The step from space (3-d) to surface (2-d) simplifies grid generation and often accelerates computations. Therefore practical applications for potential flows about ships (e.g. wave resistance problems) use exclusively BEM which are called panel methods. Panel methods divide the surface of a ship (and often part of the surrounding water surface) into discrete elements (panels). Each of these elements automatically fulfils the Laplace equation. Indirect methods determine the element strengths so that at the collocation points (usually centres of the panels) a linear boundary condition (e.g. zero normal velocity) is fulfilled. This involves the solution of a full system of linear equations with the source strengths as unknowns. The required velocities are computed in a second step, hence ‘indirect’ method. Bernoulli’s equation yields then the pressure field. Direct methods determine the potential directly. They are less suited for boundary conditions involving higher derivatives of the potential, but yield higher accuracy for lifting flows. Most commercially used codes for ship flows are based on indirect methods. BEM cannot be used to solve RANSE or Euler equations. Fundamentals of BEM can be found in, e.g., Hess (1986, 1990).

- *Finite element methods (FEM)*

FEM dominate structural analysis. For ship hydrodynamics they play only a minor role. Unlike in structural analysis, the elementary functions cannot be used also as weight functions to determine the weighted error integrals (residuals) in a Galerkin method. This reduces the elegance of the method considerably. Fundamentals of FEM can be found in, e.g., Chung (1978).

- *Finite difference methods (FDM)*

FDM discretize (like FEM) the whole fluid domain. The derivatives in the field equations are approximated by finite differences. Discretization errors can lead to a violation of conservation of mass or momentum, i.e. in the course of a simulation the amount of water might diminish continuously. While FDM lose popularity and finite volume methods (FVM) gain popularity, FDM give in many cases results of comparable quality.

- *Finite volume methods (FVM)*

FVM also employ finite differences for the spatial and temporal discretization. However, they integrate the equations for mass and momentum conservation over the individual cell before variables are approximated by values at the cell centres. This ensures conservativeness, i.e. mass and momentum are conserved because errors at the exit face of a cell cancel with errors at the entry face of the neighbour cell. Most commercial RANSE solvers today are based on FVM. Fundamentals of FVM can be found in Versteeg and Malalasekera (1995), and Ferziger and Peric (1996).

FEM, FDM, and FVM are called ‘field methods’, because they all discretize the whole fluid domain (field) as opposed to BEM which just discretize the boundaries.

Some textbooks on CFD also include spectral methods which use harmonic functions as elementary solutions. Spectral methods have no practical relevance for ship flows. The interested reader may find some introduction in Peyret and Taylor (1985).

1.4.3 Applications

Practical CFD applications for ship flows concentrate mainly on the ship moving steadily ahead. A 1994 survey at ship model basins showed inviscid BEM computations for wave-resistance and offshore seakeeping as still the most important CFD application for commercial projects (ca. 40–50% of the turnover), followed by RANSE applications (30–40%) and computations for propellers (10–20%). All other applications combined contribute less than 5% of the turnover in the commercial sector. This global decomposition is expected to change slowly as RANSE computation drifts more into commercial applications, but BEM are expected to remain the workhorse of the industry until at least the 2020s. Besides global aspects like resistance, sometimes local flow details are the focus of attention, e.g. the design of shaft brackets, stabilizing fins, or sonar domes (noise reduction), e.g. Larsson *et al.* (1998) and Larsson (1997).

The most important applications are briefly discussed in the following.

- *‘Resistance + Propulsion’*

CFD applications are mainly concerned with steadily advancing ships. For a double-body potential flow, where the wavemaking at the free surface and the effects of viscosity are neglected, the flow computation is relatively simple, quick, and accurate. The name ‘double-body flow’ comes from an interpretation that the ship’s hull is reflected at the waterline at rest. Then the flow in an infinite fluid domain is computed and the lower half of the flow gives automatically the flow about a ship with an undeformed (rigid) water surface. The double-body potential flow is only used as an approximate

solution for other methods (boundary layer, wave resistance, seakeeping). The simultaneous consideration of viscosity and wavemaking was subject to active research in the 1990s reaching the threshold of practical application by the end of the century. Until then, most viscous flow computations in practice still neglected wavemaking (viscous double-body flow). For steady free-surface flows ('wave resistance problem'), inviscid BEM codes were and still are the workhorse. The propeller is almost always neglected in BEM computations for the steady flow ('resistance problem'). RANSE computations included the propeller action ('propulsion problem') usually by applying an equivalent body force in the r.h.s. of the RANSE. The body forces were traditionally prescribed based on experience or experimental results. More sophisticated applications used integrated propeller models. The body forces in both thrust and rotative directions are then estimated, e.g. by a panel method. The distributions obtained by this approach depend on the propeller inflow and are determined iteratively using the RANSE data as input for the propeller computation and vice versa. The approach converges usually quickly.

- *Manoeuvring*

Aspects of manoeuvring properties of ships gain in importance, as public opinion and legislation are more sensitive concerning safety issues after spectacular accidents of tankers and ferries. IMO regulations concerning the (documented) manoeuvrability of ships increased the demand for CFD methods in this field. Model tests as an alternative method are expensive and time consuming. Traditional simple simulation methods with hydrodynamic coefficients gained from analytical approaches or regression analysis (of usually small databases) are often considered as too inaccurate. However, CFD applications to simulate manoeuvring model tests were by 1999 still limited to simplified research applications, e.g. the steady flow about a ship at a yaw angle. Predicting the flow around the hull and appendages (including propellers and rudders) is much more complicated than predicting the steady flow in resistance and propulsion problems. Often, both viscosity and free-surface effects (e.g. dynamic trim and sinkage) play an important role. The rudder is most likely in the hull boundary layer, often operating at high angles of attack and in the propeller wake. The hull forces themselves are also difficult to predict computationally, because sway and yaw motions induce considerable crossflows with shedding of strong vortices. Both BEM and field methods have been employed for selected manoeuvring problems. Selected problems like side forces and moments in steady yaw are well predicted, but longitudinal forces and some flow details still showed considerable errors for real ship geometries. Japanese researchers under Professor Miyata at the University of Tokyo presented the first viscous CFD time simulations of manoeuvring ships, modelling the complete hull of a sailing yacht, but no validation data were available and the required effort surpassed excessively the available resources in usual ship design practice.

- *Ship seakeeping*

The 1990s saw the advent of Rankine panel methods for seakeeping. In the frequency domain, quasi-steady BEMs compute the forces and motions of a ship in regular waves. However, time-domain methods were more versatile and were turned first into commercial flow codes, although development on time-domain codes started several years later. The approaches are similar to those used for the steady wave-resistance problem, but far less mature. What

makes seakeeping problems so much more difficult than the steady wave-resistance problem? BEM discretize the relevant surfaces into elements of finite size. The necessary grid spacing is determined to a large extent by the form of the surface resp. by the rate of change in the flow on this surface. At the water surface, the wavelength determines the necessary grid spacing. The wave-resistance problem has to discretize one dominating wave system and can adjust the grid to this wavelength. Seakeeping problems give in addition several diffraction and radiation wave systems with different wavelengths and propagating directions. If these wavelengths differ by order of magnitudes, one discretization cannot appropriately capture all wave systems. Most properties of practical relevance are calculated accurately enough for most cargo vessels by strip methods, although the underlying physical models are generally considered as crude. The two-dimensional flow calculation for the individual strips are based today almost always on BEM, namely close-fit methods.

- *Slamming/water-entry problems*

Using suitable space–time transformations, the water entry of a two-dimensional wedge can also be used to model the hydrodynamics of planing hulls. We will focus here on the seakeeping aspect of modelling water-entry problems. Slamming involves local loads changing rapidly in time and space. Hydroelastic effects, interaction between trapped air pockets and water, velocities that require consideration of water compressibility with shockwaves forming and the complex shapes of the water surface forming jets, make slamming problems already in two dimensions very challenging. Traditional approaches work well for wedges of suitable deadrise angle and two-dimensional flows. But usually ship cross-sections do not have suitable deadrise angles and the phenomena are three dimensional. CFD is expected to bring substantial progress in this field, but research applications were still in the early stages by 1999. Earlier attempts to employ BEM do not appear to allow substantial progress. Far more can be achieved in principle by employing methods which discretize the fluid volume, not just its boundaries.

- *Zero-speed seakeeping*

For offshore applications, global loads and motions in seakeeping can be computed quite well by BEM. For zero speed, the steady wave system vanishes and various diffraction and radiation wave systems coincide. If the geometry of offshore structure and waves are of the same order of magnitude BEMs can successfully capture three-dimensional effects and complex interactions. The employed three-dimensional BEM determine forces and motions either in the time or the frequency domain. First-order forces and motions are calculated reliably and accurately. Improvements over previous computations are sometimes due to finer grids. For practically required accuracy of first-order quantities, approximately 1000 elements were typically deemed necessary by 1990. Commercial program packages (WAMIT, TIMIT) developed at the MIT for hydrodynamical offshore applications were quickly accepted and are widely used.

- *Propeller flows*

Inviscid flow methods have long been used in propeller design as a standard tool yielding information comparable to experiments. Lifting-surface methods and BEM are equally popular. Lifting-surface methods (quasi-continuous method, vortex-lattice method) allow the three-dimensional

modelling of the propeller. They discretize the mean camber surface of the propeller blade by individual vortex panels. In addition, the free vortices are modelled by elements of given strength. Other than the BEM described below, lifting-surface methods do not fulfil exactly the boundary conditions at the blade's lower and upper surfaces. However, the resulting errors are small for thin blades. BEM represent an improvement concerning the treatment and modelling of the geometry. BEM model both lift and displacement of the propeller blades by surface panels and/or dipoles. They can also model the propeller hub. Despite the theoretical superiority, BEM results were not clearly better than lifting-surface methods results in benchmark tests. BEM codes for propeller applications often use only dipole panels which are distributed over hub, blade surfaces, and the wakes of each blade. Application of viscous flow CFD methods approached the threshold from pure research to practical applications by the mid-1990s.

Further, less frequently found applications of CFD in naval architecture include:

- *Air flow*

Only a few CFD applications are known for the computation of the air flow around the upper hull and superstructure of ships and offshore platforms. Topics of interest are:

- Wind resistance (especially of fast ships)
For fast ships the wind resistance becomes important. For example, for one project of a 50 knot SES (surface effect ship = air-cushion catamaran), the wind resistance constituted ca. 25% of the total resistance. Hull changes limited to the bow decreased the wind resistance by 40%.
- Wind-over-the-deck conditions for helicopter landing
This application concerns both combatants and offshore platforms.
- Wind loads
Wind loads are important for ships with large superstructures and relatively small lateral underwater area, e.g. car transporters, car ferries, container ships, SES, and air-cushion vehicles.
- Tracing of funnel smoke
This is important for passenger vessels (passengers on deck, paintwork) and for offshore platforms (safety of helicopter operation).

The comparison of CFD, wind-tunnel tests, and full-scale measurements shows an overall good agreement, even if large discrepancies appear at some wind directions. The differences between CFD and model-test results are not generally larger than between full-scale and model-scale results. In fact, the differences are not much larger than often found when the same vessel is tested in different wind tunnels. The determination of wind loads on ships and offshore structures by CFD is a realistic alternative to the experimental methods. However, due to the time involved in generating the computational mesh and in computing the solution, CFD was, at least until the year 2000, not economically competitive to routine wind-tunnel model testing.

- *Interior flows*

Inner flow problems are seldomly treated by naval architects. Exceptions are research reports on flow calculations for partially filled tanks in a rolling

ship. Inner flow computations may be coupled to the outer (global) motions of a ship. Related problems are flows in a roll damping tank, sloshing, and water flowing into a damaged ship.

Table 1.1 summarizes an assessment of the maturity of the various CFD applications.

Table 1.1 Maturity of CFD application on a scale from – (not applicable, no applications known) to ●●●● (very mature)

	<i>Viscous</i>	<i>Inviscid</i>
‘Resistance test’	●●	●●●
‘Propulsion test’	●●	–
Manoeuvring	●	●
Ship seakeeping	●	●●
Offshore	–	●●●
Propeller	●	●●●●
Others	●	–

1.4.4 Cost and value aspects of CFD

The value of any product (or service) can be classified according to time, cost and quality aspects. For CFD this means:

- *Time benefits* (How does CFD accelerate processes in ship design?)
In the shipbuilding industry, we see the same trends towards ever decreasing times for product development as in other manufacturing industries. In some cases, delivery time is the key factor for getting the contract. CFD plays a special role in this context. A numerical pre-optimization can save time-consuming iterations in model tests and may thus reduce total development time. The speed of CFD allows applications already in preliminary design. Early use thus reduces development risks for new ships. This is especially important when exploring niche markets for unconventional ships where design cannot be based on experience. In addition, another aspect related to turnover has to be realized: CFD improves chances of successful negotiations by supplying hydrodynamic analyses. It has become almost standard for all high-tech shipbuilders to apply at least inviscid CFD analyses to proposed hull designs when entering negotiations to obtain a contract for building a ship.
- *Quality benefits* (How does CFD enable superior ships or reduce risks in new designs?)
Model tests are still far more accurate for power prognosis than CFD. We see occasionally good agreement of CFD power prediction with measured data, but these cases may just benefit from fortunate error cancellation or tuning of parameters to fit *a posteriori* the experimental data. No ‘blind’ benchmark test has yet demonstrated the ability of CFD codes to predict, at least with 5% accuracy, consistently the power of ship hulls at design speed. I expect this to remain so for some more years. Long-term CFD should outperform model tests, as with growing computational power, accurate simulations at

full-scale will become available overcoming current uncertainties in correlating model tests to full-scale predictions. For some projects, it is only important to ensure that a given installed power will enable the ship to achieve contract speed. In these cases, CFD is of little interest. However, CFD should be considered in cases where model test results show problems or the shipowner is willing to pay a higher price for lower operating costs (due to improved hull). CFD allows insight in flow details not offered by the standard model tests. Insight in flow details is especially important in cases where initial model tests show that power requirements for a given hull are far more than expected. Here CFD also allows the investigation of the flow far below the waterline and modifications can be quickly analysed to see if major improvements are to be expected. The model tests and experience of a towing tank mainly indicate the potential for improvement; CFD indicates where and how to improve the design.

- *Cost benefits* (How does CFD reduce costs in ship designs?)

While the influence of certain decisions and actions on the turnover can be estimated only qualitatively, costs can usually be quantified directly. This explains why management prefers investments with a short payback due to cost reductions even though there is general consent that cost reductions alone do not ensure the economic future of a company. However, CFD's potential for direct cost reductions is small. CFD is still not accurate enough to substitute the model test for power prognosis. Therefore, *one* model test is always performed. In three out of four projects of the Hamburg Ship Model Basin this was sufficient. It reduces the cost saving potential to the additional loops in the towing tank which still account for one-third of all tests. In extreme cases up to 15 additional loops were necessary to achieve the final hull design. In these cases, CFD could have saved considerable costs. The average one additional loop will cost about as much as a CFD computation. Indirect cost savings in other departments are difficult to quantify. Time benefits of CFD will also affect costs. It is possible to determine 40% to 60% of the total production costs of a ship in the first weeks of design. Costs for modifications in later stages are higher by order of magnitudes than those necessary at the conceptual phase. Various decisions concerning production costs can be made earlier and involve lower risks if CFD is employed consistently to determine the final hull form at an earlier time.

The benefits discussed so far only cover one-half of a cost-benefit analysis for a CFD strategy. Understanding the cost structure of CFD is at least as important and some general management guidelines can be deduced. This requires a closer look at the work process in CFD. The work process is split into:

- preprocessing (generation and quality control of grids)
- computation
- postprocessing (graphical displays, documentation)

The individual steps sometimes have to be performed several times in iterations. Cost structures will be discussed separately for each step:

1. *Preprocessing*

Preprocessing requires staff familiar with the special programs for grid generation, especially on the hull. This requires at least a basic understanding of the subsequent CFD computation. Grid generation is best

performed on workstations or fast PCs with high-resolution screens. User experience and a degree of automation mainly determine time (and labour costs) in this step. Experienced staff can expect grid generation to be the major part (30% to 90%) of the man time involved in CFD analyses. Completely automatic procedures for complex geometries such as ships are not available and do not seem realistic for the future. Staff training and software development/adaptation are the main fixed costs which usually surpass depreciation of hardware and software by an order of magnitude.

2. *Computation*

The computation involves almost no man time. Computations for inviscid CFD can usually run on PCs; viscous CFD may prefer more powerful computer environments up to parallel computers/supercomputers depending on the problem size. Often workstations are the preferred choice. Computing costs usually account for less than 1% of total costs. Also software licences for the flow code are often negligible compared to other costs, especially those for generating the grid.

3. *Postprocessing*

The graphics require fast PCs with colour screens, laser printers and colour plotters/printers. The necessary software is commercially available. Post-processing requires some time (typically 10% to 20% of the total time), but can be performed after short training by staff without special qualifications. User friendliness of the programs determines time and thus labour costs in this step. Use of postprocessing programs should be kept as simple as possible minimizing user input. Interpretation of results still requires expertise and is a lengthy process. You pay thus for the interpretation, not the number of colour plots.

The high fixed costs for training and user-defined macros to accelerate the CFD process lead to considerable economies of scale. This is often not realized by management. Experience shows that many shipyards buy CFD software, because the hardware is available or not expensive, and the software licence costs may be as much as a few CFD analyses at a consulting company. The vendors are naturally only too happy to sell the software. Then the problems and the disillusion start. Usually no initial training is given by the vendor (or bought by the shipyard). Typical beginners' mistakes are the consequence:

- Time is lost in program handling.
- Unsuitable grids are used requiring repeated analyses or resulting in useless results.

By the time the management realizes the problems, it is usually too late. The software licences are all bought, the design engineer has now already invested (lost) so much time struggling with the code. Nobody wants to admit defeat. So the CFD analyses are continued in-house with the occasional outsourcing when problems and time pressures become too large. As a general rule, outsourcing is recommended for shipyards and design offices with fewer than five projects per year. In-house CFD makes sense starting from ten projects per year. These numbers may shift if CFD codes become more user-friendly, i.e. run almost automatically. However, for finite-element analyses of structures we have seen a development that after an initial period where shipyards performed the analyses in-house the pendulum swung the other way with shipyards now using almost exclusively outsourcing as the sensible option.

The main part of the variable costs and response time is created in grid generation. There is considerable potential to improve this part of the CFD process:

- *By making grid generation more user-friendly*
Grid generation is largely a matter of experience. The logical deduction would be to incorporate this experience in the grid generation codes to improve user-friendliness. The challenge for research will be to automate human vision ('the grid should look nice') and human decision ('If this problem occurs I change the grid in such a way'). A fundamental dilemma found in grid generation is that the procedures should be flexible to cope with a variety of problems, yet easy to handle with a minimum of input. Existing grid generators (and flow codes) offer a lot of flexibility often at the cost of having many options which in turn leave inexperienced (i.e. occasional) users frustrated and at risk to choose exactly the wrong options for their problems. Incorporation of expert knowledge in the grid generation program offering reasonable default options is a good solution to this dilemma. In the extreme case, a user may choose the 'automatic mode' where the program proceeds completely on its own knowledge. On the other hand, default values may be overruled at any stage by an experienced user.
- *By making the computation more robust*
An easy grid is cheap and fast to generate. Monolithic structured grids are the least flexible and difficult to generate, keeping constraints like orthogonal grid intersections, avoidance of highly skewed cells etc. Therefore we see trends towards:
 - block-structured grids
 - non-matching boundaries between blocks
 - unstructured grids
 - chimera grids (overlapping, non-matching blocks)
- *By generating grids only once*
Time for grid generation means *total* time for all grids generated. The philosophy should be 'Make it right the first time', i.e. the codes should be robust enough or the grid generators good enough that one grid suffices. This may require some sacrifices in accuracy. This should also favour the eventual development of commercial codes with adaptive grid techniques.

Standard postprocessing could save time and would also help customers in comparing results for various ships. However, at present we have at best internal company standards on how to display CFD results.

1.5 Viscous flow computations

Inviscid boundary element methods will be covered in detail in further chapters of this book. Viscous flows will not be treated in similar detail as the fundamentals are covered in an excellent text by my colleague Milovan Peric in Ferziger and Peric (1996). I will therefore limit myself here to a naval architect's view of the most important issues. This is intended to raise the understanding of the matter to a level sufficient to communicate and collaborate with an expert for viscous flows. I deem this sufficient for the purpose of this book as viscous flow codes are still predominantly run by dedicated

experts, while boundary element methods are more widely used. For further studies, the book by Ferziger and Peric is recommended.

1.5.1 Turbulence models

The RANSE equations require external turbulence models to couple the Reynolds stresses (terms from the turbulent fluctuations) to the time-averaged velocities. Turbulence is in general not fully understood. All turbulence models used for ship flows are semi-empirical. They use some theories about the physics of turbulence and supply the missing information by empirical constants. None of the turbulence models used so far for ship flows has been investigated for its suitability at the free surface. On the other hand, it is not clear whether an exact turbulence modelling in the whole fluid domain is necessary for engineering purposes. There are whole books on turbulence models and we will discuss here only the most primitive turbulence models which were most popular in the 1990s, especially as they were standard options in commercial RANSE solvers. ITTC (1990) gives a literature review of turbulence models as applied to ship flows.

Turbulence models may be either algebraic (0-equation models) or based on one or more differential equations (1-equation models, 2-equation models etc.). Algebraic models compute the Reynolds stresses directly by an algebraic expression. The other models require the parallel solution of additional differential equations which is more time consuming, but (hopefully) also more accurate.

The six Reynolds stresses (or more precisely their derivatives) introduce six further unknowns. Traditionally, the Boussinesq approach has been used in practice which assumes isotropic turbulence, i.e. the turbulence properties are independent of the spatial direction. (Detailed measurements of ship models have shown that this is not true in some critical areas in the aftbody of full ships. It is unclear how the assumption of isotropic turbulence affects global properties like the wake in the propeller plane.) The Boussinesq approach then couples the Reynolds stresses to the gradient of the average velocities by an eddy viscosity μ_t :

$$-\rho \begin{bmatrix} \overline{u'u'} & \overline{v'u'} & \overline{w'u'} \\ \overline{u'v'} & \overline{v'v'} & \overline{w'v'} \\ \overline{u'w'} & \overline{v'w'} & \overline{w'w'} \end{bmatrix} = \mu_t \begin{bmatrix} 2u_x & u_y + v_x & u_z + w_x \\ u_y + v_x & 2v_y & w_y + v_z \\ u_z + w_x & w_y + v_z & 2w_z \end{bmatrix} - \begin{bmatrix} \frac{2}{3}\rho k & 0 & 0 \\ 0 & \frac{2}{3}\rho k & 0 \\ 0 & 0 & \frac{2}{3}\rho k \end{bmatrix}$$

k is the (average) kinetic energy of the turbulence:

$$k = \frac{1}{2}(\overline{u^2} + \overline{v^2} + \overline{w^2})$$

The eddy viscosity μ_t has the same dimension as the real viscosity μ , but unlike μ it is not a constant, but a scalar depending on the velocity field. The eddy viscosity approach transforms the RANSE to:

$$\begin{aligned} \rho(u_t + uu_x + vu_y + wu_z) = \rho f_1 - p_x - \frac{2}{3}\rho k_x + (\mu + \mu_t)(u_{xx} + u_{yy} + u_{zz}) \\ + \mu_{tx} 2u_x + \mu_{ty}(u_y + v_x) + \mu_{tz}(u_z + w_x) \end{aligned}$$

$$\begin{aligned}
\rho(v_t + uv_x + vv_y + ww_z) &= \rho f_2 - p_y - \frac{2}{3}\rho k_y + (\mu + \mu_t)(v_{xx} + v_{yy} + v_{zz}) \\
&\quad + \mu_{tx}(u_y + v_x) + \mu_{ty}2v_y + \mu_{tz}(w_y + v_z) \\
\rho(w_t + uw_x + vw_y + ww_z) &= \rho f_3 - p_z - \frac{2}{3}\rho k_z + (\mu + \mu_t)(w_{xx} + w_{yy} + w_{zz}) \\
&\quad + \mu_{tx}(u_z + w_x) + \mu_{ty}(w_y + v_z) + \mu_{tz}2w_z
\end{aligned}$$

Turbulence models generally use a reference length scale and reference velocity scale. Alternatively, the velocity scale can be expressed as the fraction of length scale and a time scale. To obtain the proper dimension, the eddy viscosity is expressed proportional to the product of length scale and velocity scale. The length scale is characteristic for the larger turbulence structures which are mainly contributing to the momentum transfer in the fluid. The velocity scale is characteristic for the intensity of the turbulent fluctuations.

All commonly used turbulence models are plagued by considerable uncertainties. Internationally renowned fluid dynamicists have described turbulence models as follows:

- ‘Turbulence models are voodoo. We still don’t know how to model turbulence.’
- ‘The word “model” is a euphemism for an uncertain, but useful postulated regularity. In the last few decades, scientists have learned to simulate some aspects of turbulence effects by the invention of “turbulence models” which purport to represent the phenomena by postulated laws of conservation, transport and sources for supposed “properties of turbulence” such as its “energy”, its “frequency” or its “length scale”. These “laws” are highly speculative.’

Researchers have succeeded in direct numerical simulation of turbulence for Reynolds numbers several orders of magnitude smaller than ship model Reynolds numbers and for very simple geometries. These simulations allow at best to understand phenomena of turbulence better and to test engineering turbulence models.

The usefulness of a turbulence model for ship flows can only be evaluated in benchmark tests for similar ships. Sometimes simple models work surprisingly well, sometimes the same model fails for the next ship. The most popular turbulence model for ship flow applications in practice in the 1990s was the standard k - ε model, although its results were not convincing in benchmark tests for several ship geometries.

By the late 1990s, k - ω models were proposed for ship flows. These models are like the k - ε models two-equation models and can be seen as a further evolution of them. ω is proportional to ε/k and can be interpreted as a ‘turbulence frequency’. k - ω models yield better agreement with experiments in many cases; however, they react more sensitively to grid quality.

Reynolds stress models calculate the individual Reynolds stresses from their modelled transport equations without recourse to an eddy viscosity hypothesis. These models require more computational effort than, e.g., the two-equation k - ε model, but showed in several ship flow applications superior results. However, it is not yet decided if similarly good results can be obtained by simple turbulence models with properly adjusted coefficients. Large-eddy simulations may eventually solve the current debate over turbulence modelling for engineering applications, but for ship flows we will have to wait at least

two more decades before realistic LES solutions for even model Reynolds numbers become available in practice.

Probably the most widely used turbulence model in engineering applications is the (standard) k - ε model, (Launder and Spalding (1974)). k is the kinetic energy of the turbulence, ε the dissipation rate of k . The k - ε model expresses the eddy viscosity μ_t as a simple function of k and ε :

$$\mu_t = 0.09\rho \frac{k^2}{\varepsilon}$$

0.09 is an empirical constant. k and ε are expressed by two partial differential equations involving further empirical constants:

$$\frac{Dk}{Dt} = \frac{1}{\rho} \left(\left(\frac{\mu_t}{1.0} k_x \right)_x + \left(\frac{\mu_t}{1.0} k_y \right)_y + \left(\frac{\mu_t}{1.0} k_z \right)_z \right) + P_k - \varepsilon$$

$$\frac{D\varepsilon}{Dt} = \frac{1}{\rho} \left(\left(\frac{\mu_t}{1.2} \varepsilon_x \right)_x + \left(\frac{\mu_t}{1.2} \varepsilon_y \right)_y + \left(\frac{\mu_t}{1.2} \varepsilon_z \right)_z \right) + 1.44 \frac{\varepsilon}{k} P_k - 1.92 \frac{\varepsilon^2}{k}$$

P_k is the production rate of k :

$$P_k = \frac{\mu_t}{\rho} (2u_x u_x + (u_y + v_x)u_y + (u_z + w_x)u_z + (v_x + u_y)v_x + 2v_y v_y \\ + (v_z + w_y)v_z + (w_x + u_z)w_x + (w_y + v_z)w_y + 2w_z w_z)$$

The substantial derivative is defined as usual:

$$\frac{D}{Dt} = \frac{\partial}{\partial t} + u \frac{\partial}{\partial x} + v \frac{\partial}{\partial y} + w \frac{\partial}{\partial z}$$

These equations contain four empirical constants (1.0, 1.2, 1.44, and 1.92) which were determined (in a best fit approach) for very simple flows in physical and numerical experiments. The applicability to other turbulent flows (e.g. around ship geometries) was never explicitly validated.

The k - ε model cannot be applied directly at a wall (ship hull) as it assumes inherently high (local) Reynolds numbers. If a no-slip condition (zero relative speed at the hull) is to be enforced directly at the wall, the ε differential equation must be substituted by an algebraic equation near the wall. This is the so-called low-Re k - ε model. However, more popular is the introduction of a wall function coupled to the standard k - ε model. The wall function is empirically determined for two-dimensional flows. One assumes that the velocity increases logarithmically with distance from the wall:

$$\frac{u}{u_\tau} = \begin{cases} y^+ & y^+ \leq y_m^+ \\ \frac{1}{0.42} \ln(9.0 y^+) & y^+ > y_m^+ \end{cases}$$

where y_m^+ is implicitly given by:

$$y_m^+ = \frac{1}{0.42} \ln(9.0 y_m^+)$$

0.42 and 9.0 are empirical constants. $y^+ = y\rho u_\tau/\mu$ is a non-dimensional distance from the wall, u the velocity in longitudinal (parallel to the wall) direction, $u_\tau = \sqrt{\tau_w/\rho}$ with τ_w the wall shear stress.

The centres of the innermost cells should lie within a distance from the wall where the logarithmic law of the wall function applies, i.e. $100 < y^+$, 1000. However, y^+ contains the wall shear stress which is part of the solution and not *a priori* known. It is thus only possible to judge *a posteriori* if a chosen wall distance was appropriate. Higher Reynolds numbers require generally smaller y^+ .

The fundamental assumptions for the wall function are:

- velocity gradient in normal direction much larger than in other directions
- pressure gradient and gravity influence so small that shear stresses in the boundary layer are constant
- shear stresses and velocity vectors have the same direction in the whole boundary layer
- equilibrium of turbulence generation and dissipation
- linear variation of the reference length for turbulence

These assumptions are questionable for complex flows as found in the aftbodies of ships. The standard $k-\varepsilon$ model usually overpredicts the turbulent kinetic energy in the stern region. Also, the model cannot properly account for the reduction of the turbulent kinetic energy near the wall when the viscous layer becomes thick over the stern. The wall function approach usually yields worse results for the wall shear stresses than turbulence models that apply a no-slip condition directly at the wall. However, the wall function saves many cells (and thus computational time).

The $k-\varepsilon$ model appears suitable for flows with a predominant boundary-layer character. Problems with defining a reference length, as in many algebraic models, are avoided and at least the important physical aspect of turbulence transport is explicitly reflected in the model. The wall function makes the approach numerically efficient, but the model is in principle not capable of predicting flow separation for curved surfaces (e.g. ships!).

1.5.2 Boundary conditions

The computational grid can only cover part of the real fluid domain. This introduces artificial boundaries of the computational domain in addition to the physical boundaries of the hull and the free surface. In the 1990s computations often neglected the wavemaking of the free surface and treated it as a rigid plane of symmetry.

For ships moving straight ahead (as in simulations of resistance or propulsion tests), the midship plane is also treated as a symmetry plane. The usual symmetry of the ship would intuitively suggest that this indeed reflects physical reality. However, viscous flows with symmetric inflow to symmetric bodies do not automatically result in symmetric flow patterns at all times. Vortex shedding results in asymmetric flow patterns which only in the time average are symmetric again. This may result in considerable differences in the resistance. The following example may illustrate the problem (Fig. 1.3). Behind a circular cylinder in uniform inflow one would assume intuitively a symmetrical flow which would hardly be disturbed by a flat plate behind the cylinder. However, experiments yield a considerably smaller resistance coefficient for the cylinder with a flat plate. The reason is vortex shedding behind the cylinder with large

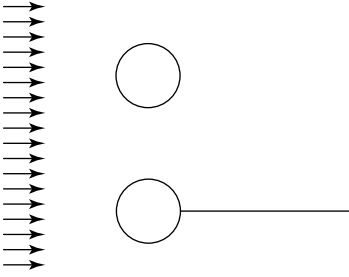


Figure 1.3 A cylinder with a flat plate in the wake has a considerable lower resistance coefficient than a cylinder without a plate. Care is required when assuming symmetry planes for viscous flow computations

vortices oscillating from one side to the other. These large vortex oscillations are blocked by the flat plate.

This leaves the inlet, outlet, and side/bottom boundaries. The side and bottom boundaries may correspond to an actual physical boundary as in a model tank. In this case, the boundaries may be treated similar to the ship hull with a no-slip condition. However, one should remember that the outer boundaries then have a relative velocity to the ship. Usually, the physical boundaries would be too far away to be considered. Then the side and bottom boundaries should be sufficiently removed from the ship. Often the side and bottom boundary forms part of a cylinder (quarter for double-body flow with symmetry in y), as a cylinder leads usually to better grids (for single-block grids) than a block-type grid. A typical cylinder radius would be between 0.5 and 1 ship length.

The boundary condition on the hull is a no-slip condition (zero relative speed) which is either enforced directly or via a wall function depending on the turbulence model employed.

At the inlet all unknowns are specified. If the inlet is chosen sufficiently upstream of the ship, uniform flow with corresponding hydrostatic pressure can be assumed. If the k - ε model is employed, the distribution of k and ε at the inlet also have to be specified. The influence of the specified values for k and ε decays rapidly downstream, such that errors have decayed by some orders of magnitude after several cells. One may then simply specify zero k and ε . A slightly more sophisticated approach estimates the turbulence intensity I (turbulent fluctuation component of a velocity component made non-dimensional with the ship speed V) at the inlet. For isotropic turbulence we then get:

$$k = \frac{3}{2}(VI)^2$$

In the absence of experimental data for I in a specific case, $I = 5\%$ has often been assumed. The dissipation rate is typically assumed as:

$$\varepsilon = 0.164 \frac{k^{1.5}}{\ell}$$

0.164 is an empirical constant and ℓ a reference length. For ship flows, there are few indications as to how to choose this reference length. Own computations have used 1/100 of the radius of the cylinder forming the computational domain. However, the initial choice of the quantities does not influence the final result, but 'only' the required number of iterations to obtain this result. If only the aftbody is considered, then the inlet may be placed, e.g., amidships. In this

case all unknowns must be specified from experiments (for validation studies) or simpler computations (e.g. coarse grid computations for the whole domain, inviscid flow computations coupled with boundary layer computations etc.).

At the outlet usually the derivatives in longitudinal direction are set for all unknowns to zero and the flow leaving the domain is determined such that continuity is preserved for the whole fluid domain. The longitudinal derivatives are in reality not really zero, but this boundary condition prevents upstream propagation of any reflections of disturbances created by the numerical method. Numerical experiments show that these boundary conditions affect results only in a small local region near the outlet.

At symmetry planes normal velocity and all derivatives in the normal direction are set zero. Since the normal derivatives of the tangential velocities vanish, the shear stresses are zero. The outer boundary of the computational domain (side and bottom) may be treated as ‘symmetry plane’, i.e. on each outer cell face normal velocity and all normal derivatives are set zero. In this case, the outer boundary must be far away from the ship such that virtually uniform flow is encountered. Another possibility is to specify values computed by inviscid codes at the outer boundary which allows much smaller computational domains, but not much fewer cells as most cells are concentrated near the ship hull.

If a propeller is modelled in RANSE computations for ship flows (propulsion test condition), the propeller is generally simplified by specifying the propeller effect as body forces. Often, only the longitudinal body forces are specified in the cells covering the location of the propeller. This simulates the acceleration of the flow by the propeller. The sum of all body forces yields the thrust. The distribution is often assumed to be parabolic in the radial direction and constant in the circumferential direction. Alternatively, the distribution of the body forces for the propeller may be specified from:

- experience with similar ships
- experiments for the actual ship
- alternating computations for the propeller loading with non-uniform inflow from the RANSE computation. The propeller loading is then computed every 10 or 20 iterations in the RANSE computation as the propeller loading converges much faster than the other properties of the RANSE computation (Bertram and Ishikawa (1996)). Convergence for the propeller loading is usually obtained with five or seven iterations.

1.5.3 Free-surface treatment

Most viscous flow computations for ships in design projects in the 1990s still assumed the free surface to be a symmetry plane. In reality this is not true. The free surface forms waves which break locally at the bow, and the ship changes trim and sinkage (squat) due to the free surface. By the late 1990s only few research applications included trim and sinkage, while many included the wavemaking of the free surface. The problem of turbulence models (and their specific boundary conditions) near the free surface has not been addressed in ship flows and generally the same conditions as for symmetry planes are used.

A variety of methods exists to capture wavemaking with various degrees of success. Eventually, only methods also capable of modelling breaking waves should survive. The difficulty with the unknown free surface position is usually

resolved by considering the problem transient, starting from rest. The hull is thus accelerated to the requested Froude number and the time integration is continued until steady state conditions have been achieved. (This procedure corresponds to usual practice in towing tank experiments.) The free surface position is updated as part of the iterative process.

The methods for computing flows with a free surface can be classified into two major groups:

- Interface-tracking methods define the free surface as a sharp interface which motion is followed. They use moving grids fitted to the free surface and compute the flow of liquid only. Problems are encountered when the free surface starts folding or when the grid has to be moved along walls of a complicated shape (like a real ship hull geometry).
- Interface-capturing methods do not define a sharp boundary between liquid and gas and use grids which cover both liquid- and gas-filled regions. Either marker particles or a transport equation for the void fraction of the liquid phase are used to capture the free surface.

Interface tracking is bound to dominate in the long term for ship flow as the ability to model complex geometries of hull and water surface is essential for real ship flows. Interface-tracking methods may also solve the flow in the air above the water, but for most ship flows this is not necessary. Ferziger and Peric (1996) present results for a Wigley hull, comparing an interface-capturing method with an interface-tracking method.

A typical approach uses a volume-of-fluid (VOF) formulation introducing an additional scalar function, which describes the volume concentration of water, to identify the position of the free surface.

So far problems persist with numerical damping of the ship wave propagation. This minor blemish – for practical purposes it suffices to know the wave profile close to the hull – should be overcome in time by better spatial resolution or by using higher-order schemes.

1.5.4 Further details

The vector equations for conservation of momentum yield three scalar equations for three-dimensional computations. These determine the three velocity components for a given pressure. Usually these velocities do not fulfil the continuity equation. The introduction of a pressure correction equation derived from the continuity equation allows a correction of pressure and velocities. Popular methods for such pressure–velocity coupling are:

- SIMPLE (*semi-implicit pressure linked equations*) and related methods
- PISO (*pressure implicit with splitting of operators*)

In the 1990s most RANSE codes used for ship flows employed SIMPLE or related pressure–velocity coupling. The SIMPLE method is fast, but tends to slow convergence for suboptimal grids. Figure 1.4 gives a simple flow chart for the SIMPLE algorithm. PISO like SIMPLE is based on a predictor–corrector method, but employs several corrector steps while SIMPLE uses only one. This makes the PISO method more stable, but less efficient. In personal experience, the computation time for one tanker was increased by a factor of 5 switching from SIMPLE to PISO. For unsteady problems, however, the PISO

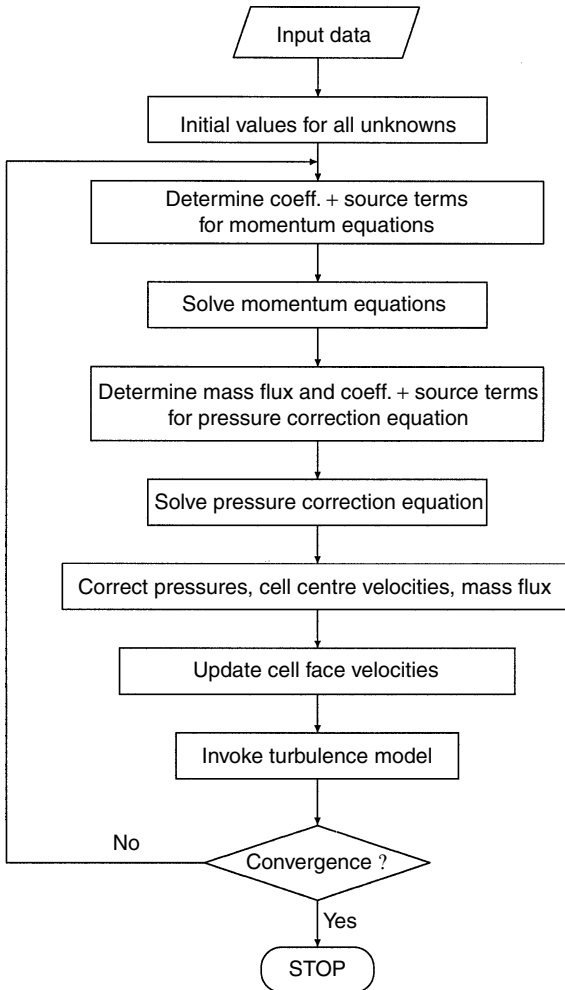


Figure 1.4 Flow chart for SIMPLE algorithm

method is generally preferred to the SIMPLE method due to its better stability. The discretization of the fundamental differential equations leads to very large systems of linear equations which are usually sparse, i.e. most of the elements of the matrix are zero. (This is fundamentally different from boundary element methods where full matrices with an often not dominant main diagonal need to be solved.) Direct solvers like Gauss elimination or matrix inversion have prohibitively excessive computational time and storage requirements. In addition, the solution of the system of equations is embedded in an outer iteration which requires only an approximate solution, because the coefficients due to the non-linearity of the differential equations and the pressure-velocity coupling require further corrections. Therefore field methods generally employ iterative solvers:

- Gauss-Seidel method (point iterative)

- LSOR (line successive overrelaxation), ADI (alternating direction implicit) (line iterative)
- ILU (incomplete lower upper) decomposition, e.g. SIP (strong implicit procedure)
- CG (conjugate gradient) method

The various iterative methods differ in their prerequisite (dominant main diagonal, symmetry etc.), convergence properties, and numerical effort per iteration. Strongly implicit schemes such as SIP feature high convergence rates. The convergence is especially high for multigrid acceleration which today is almost a standard choice.

1.5.5 Multigrid methods

Multigrid methods use several grids of different grid size covering the same computational fluid domain. Iterative solvers determine in each iteration (relaxation) a better approximation to the exact solution. The difference between the exact solution and the approximation is called residual (error). If the residuals are plotted versus the line number of the system of equations, a more or less wavy curve appears for each iterative step. A Fourier analysis of this curve then yields high-frequency and low-frequency components. High-frequency components of the residual are quickly reduced in all solvers, but the low-frequency components are reduced only slowly. As the frequency is defined relative to the number of unknowns, respectively the grid fineness, a given residual function is highly frequent on a coarse grid, and low frequent on a fine grid. Multigrid methods use this to accelerate overall convergence by the following general procedure:

1. Iteration (relaxation) of the initial system of equations until the residual is a smooth function, i.e. only low-frequent components are left.
2. ‘Restriction’: transforming the residuals to a coarser grid (e.g. double the grid space).
3. Solution of the residual equation on the coarse grid. Since this grid contains for three-dimensional flow and grid space halving only 1/8 of the unknowns and the residual is relatively high frequent now, only a fraction of the computational time is needed because a further iteration on the original grid would have been necessary for the same accuracy.
4. ‘Prolongation’: interpolation of the residuals from the coarse grid to the fine grid.
5. Addition of the interpolated residual function to the fine-grid solution.

This procedure describes a simple two-grid method and is recursively repeated to form a multigrid method. If the multigrid method restricts (stepwise) from the finest grid to the coarsest grid and afterwards back to the finest grid, a V-cycle is formed. If the prolongation is only performed to an intermediate level, again before restriction is used, this forms a W-cycle (Fig. 1.5).

The multigrid method accelerates the overall solutions considerably, especially for grids with many unknowns. Multigrid algorithms obtain computational times which are almost proportional to the number of cells, while single-grid solvers yield computational times proportional approximately to the square of the number of cells. Multigrid methods are relatively easy to combine with all major iterative solvers. The considerable speed-up of

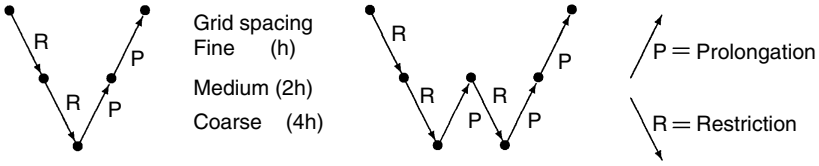


Figure 1.5 Multigrid cycles: V-cycle (left), W-cycle (right), h : grid spacing

computations more than justifies the additional expense of programming and storage requirements. Therefore most newer developments for RANSE codes for ship flows include multigrid methods.

1.5.6 Numerical approximations

Finite-volume methods require values (and derivatives) of various variables at the cell faces, when they are originally only known at the cell centres. The flow direction is often considered when these quantities are determined for convective terms. Time derivatives are also numerically approximated.

Consider, e.g., the convective fluxes in the x direction. One determines in general the value of a variable (e.g. pressure or velocity) at the location x by employing an interpolation polynomial through the neighbouring cell centres x_i :

$$f(x) = a_1 + a_2(x - x_1) + a_3(x - x_1)(x - x_2) + \dots$$

The coefficients a_i are determined by inserting the known function values $f_i = f(x_i)$. The most simple case uses just the value of the next cell centre upstream (*upwind differencing scheme, UDS*):

$$f(x) = f_{i-1} \quad u > 0$$

$$f(x) = f_i \quad u < 0$$

u is the flow velocity in the x direction. This is a first-order approximation, i.e. for fine grids halving the grid size should halve the error in approximating the derivative. The order of an approximation is derived from a Taylor expansion for equidistant grids. For non-equidistant grids, an additional error appears that depends on the ratio of adjacent cell lengths. This error may dominate for coarse to moderately coarse grids, but vanishes in the theoretical limit of infinitely fine grids. The approximation depends thus on the direction of the velocity in the cell centre. UDS is unconditionally stable, but plagued by large numerical diffusion. Numerical diffusion smoothes the derivatives (gradients) and may thus easily lead to wrong results. The numerical diffusion becomes maximum for an angle of 45° between grid lines and flow direction. Grid refinement reduces the numerical diffusion, but increases of course the computational effort.

The *central differencing scheme (CDS)* uses the adjacent upstream and downstream points:

$$f(x) = \frac{f_{i-1} + f_i}{2}$$

This is a second-order approximation, i.e. halving the grid size will reduce the error by $1/4$ for fine grids. The approximation is independent of the sign of the

flow direction. CDS tends to numerical instabilities and is therefore for usual discretizations and speeds unsuited for the approximation of the convective fluxes; the diffusive terms are usually approximated by CDS.

The *linear upwind differencing scheme (LUDS)* uses the cell centres of the next two upstream points:

$$f(x) = \frac{f_{i-2} - f_{i-1}}{x_{i-2} - x_{i-1}}(x - x_{i-1}) + f_{i-1} \quad u > 0$$

$$f(x) = \frac{f_i - f_{i+1}}{x_i - x_{i+1}}(x - x_i) + f_i \quad u < 0$$

This second-order approximation considers again the flow direction. LUDS is more stable than CDS, but can yield unphysical results. This is sometimes referred to as 'numerical dispersion'.

Three points allow quadratic interpolation. The *QUICK (quadratic upstream interpolation for convective kinematics)* uses two adjacent points upstream and one downstream:

$$f(x) = \frac{f_i + f_{i-1}}{2} - \frac{1}{8}(f_{i-2} + f_i - 2f_{i-1}) \quad u > 0$$

$$f(x) = \frac{f_i + f_{i-1}}{2} - \frac{1}{8}(f_{i+1} + f_{i-1} - 2f_i) \quad u < 0$$

This third-order approximation may also produce unphysical results due to overshoots and requires of course a higher computational effort than the other schemes presented so far.

Blended schemes combine the basic schemes in weighted averages. Optimum weight factors depend on the problem. Blending combines the advantages (stability, accuracy) of the individual schemes, but requires more effort in each iteration. For an optimum weight the reduced number of iterations should more than compensate for this. However, for ship flows our experience is still insufficient to give general recommendations for blending schemes. Ideally, the weighting factors are chosen depending on the local flow. This usually involves the Peclet number, i.e. a local Reynolds number based on the local velocity and the grid size. Even more sophisticated techniques use a basic scheme (e.g. CDS) unless local instabilities (wiggles) are diagnosed automatically. These instabilities are then smoothed or filtered. These schemes do not require (error-prone) user input as do the simpler blending schemes. However, no applications of such sophisticated schemes to ship flows were known in the 1990s.

For the approximation of time derivatives implicit or explicit schemes may be used. In explicit schemes, the variables (e.g. derivatives of velocities) depend in each point in space only on known values of previous time steps. They can thus be computed directly (explicitly). Implicit schemes couple the unknowns to neighbouring values (in time) and require the solution of a system of equations. Explicit schemes can usually not be employed for ship flows, because they require very small time steps for the necessary very fine spatial discretization. A popular implicit scheme is the Crank–Nicholson scheme.

1.5.7 Grid generation

Grid generation for CFD computations, especially RANSE computations, accounts for the major part of the total time needed in a CFD project. For complex three-dimensional simulations it is not uncommon for more than 80% of the man-hours required to perform a simulation to be spent on model generation. Grids must capture the changes in the geometries of hull and free surface (if included), but also all changes in the flow, with sufficient accuracy. For reasons of computational accuracy and efficiency (convergence rate), one should try to avoid extreme side ratios of cells and skewed angles in individual cells. However, for ship flows the flow changes drastically in the normal direction to the hull and little in the tangential longitudinal direction. One would like to have a similar good resolution for all changes in the flow direction. This automatically forces us to use cells with extreme side ratios, e.g. 1:1000.

The numerical (non-physical) diffusion can be reduced by aligning grid lines along streamlines. However, flow separation and flow recirculation in ship flows allow this only to a limited extent.

Cartesian grids consist of elements with cell edges parallel to the axes of a Cartesian coordinate system. They are thus easy to generate, but unsuited for capturing complex geometries like ship hulls.

Therefore in practice *curvilinear grids* (body-fitted grids) are generally employed. These grids may be orthogonal or non-orthogonal. *Orthogonal grids* employ grid lines which intersect orthogonally. Since real ship geometries do not intersect the water surface orthogonally, at least some non-orthogonal grid lines have to be accepted. Otherwise, orthogonal grids are preferred since they facilitate the description of the discretized equations.

Curvilinear orthogonal grids require considerable effort in grid generation, but keep the complexity of the discretized equations relatively low. The velocity components may be grid oriented (local) or Cartesian (global). A general trend or preference is not yet apparent, but a formulation in Cartesian coordinates seems to react less sensitively to small deviations from smoothness in the grid.

Grid generation starts with specifying the cell faces on the boundaries (hull, water surface, inlet, outlet, outer boundary). Then the internal cell nodes are interpolated. Various techniques exist for this interpolation:

- *Algebraic grid generation* uses algebraic transformation and interpolation functions to create the grid geometry. For complex geometries (like real ship hulls), the resulting grid is often not smooth enough.
- *Conformal mapping* has been used for ships where the original mapping was enhanced by additional transformations to ensure that for real ship geometries the grids (within each two-dimensional section) were (nearly) orthogonal. However, this technique is fundamentally limited to two dimensions, i.e. for cross-sections. Smoothness and orthogonality in the longitudinal direction cannot be ensured automatically. Therefore, these grid generation techniques have been replaced largely by methods that solve (a simple) three-dimensional differential equation.
- *Grid generation based on differential equations* solve first a (relatively simple) differential equation subject to certain user-specified control functions or boundary conditions. The most popular choice is the Poisson

equation, i.e. the Laplace equation with a specified non-zero function on the r.h.s. Thompson *et al.* (1985) describe such a method in detail which allows the user to control distance and orientation of the grid lines by specifying control functions. However, the process involves trial and error requiring either patience or experience from the user. Poisson solvers create automatically smooth and orthogonal grids. Subsequent algebraic interpolation may speed up the process to find an appropriate grid. Solving the Poisson equation can be interpreted physically as determining lines of constant temperature in the fluid where the ship is a heat source with heat distribution specified by the control functions.

Staggered grids specify, e.g., the pressure at the cell centre and the velocities at the cell faces. This improves automatically the numerical stability of the scheme, but is particularly unsuited for multigrid acceleration. Therefore staggered grids are becoming increasingly unpopular. Instead, other numerical techniques are employed to avoid pressure oscillations from cell to cell.

Grid generation is vital for the economic success of a CFD method. Grid techniques have successively developed to allow more flexibility and faster grid generation:

- *Single-block structured grids*

Structured grids arrange cells in a simple $n_x \cdot n_y \cdot n_z$ array where each cross-section has the same number of cells, even though the cell shape and size may differ arbitrarily. Structured grids allow easy automation of grid generation and can easily be coupled with multigrid methods. They were traditionally employed because they allow simple program structures. Neighbouring cells can be determined by a simple mathematical formula avoiding the necessity for storing this information. However, this approach to grid generation does not allow the arrangement of additional cells in areas where the flow is changing rapidly. The choice is then either to accept insufficient accuracy in some areas or unnecessarily many cells (and thus computational effort) for areas where the flow is of little interest. In addition, complex ship geometries involving appendages are virtually impossible to model with such a grid. At least, the resulting grid is usually not smooth or involves highly skewed cells. As a result convergence problems are frequent.

- *Block-structured grids*

Block-structured grids combine various single-block grids. Each block is then structured and easily generated. But the block-structured approach allows some areas to discretize finer and others coarser. Blocks are also more easily adapted to local geometries allowing smoother grids with largely block-like cells which improve convergence. The interpolation of results at each block requires some care, but techniques have been developed that allow accurate interpolation even for non-matching block interfaces, i.e. block interfaces where grid lines do not coincide.

- *Chimera grids*

Chimera was a fire-breathing (female) mythological monster that had a lion's head, a goat's body, and a serpent's tail. Chimera grids are arbitrarily assembled blocks of grids that overlap. They thus pose even fewer restrictions on grid generation and appear to be a very good choice for grid generation in ships, even though the interpolation between blocks is more complicated than for block-structured grids.

- *Unstructured grids*

Unstructured grids allow the largest flexibility in grid generation, but require far more effort and are therefore not popular for ship flows. However, unstructured grid programs can also handle structured or block-structured grids. One may then generate a simple grid and use adaptive grid techniques which automatically generate unstructured grids in the computation.

Grids should be rather fine in regions of high velocity or pressure gradients. The curvature of the ship hull and the experience with similar ship hull forms give some indications where such regions are to be expected, but often one identifies only after computations regions where the grid should have been finer. Ideally the computation should refine the grid in these regions automatically during a computation. Such adaptive grid techniques are subject to research for ship flows. They should bring considerable progress in accuracy without increasing computational effort excessively, but require usually unstructured grid capabilities of the code.

Propellers

2.1 Introduction

Ships are predominantly equipped with ‘simple’ screw propellers. Special means of propulsion include:

- nozzled propellers
- waterjets
- surface-piercing propellers
- contra-rotating propellers (almost exclusively for torpedoes)
- azimuthing propellers
- Voith–Schneider propellers

These are discussed in more detail by Schneekluth and Bertram (1998). In the past, paddle-wheels played a large role for river boats, but have been largely replaced now by propellers or waterjets. We will limit ourselves here to ships equipped with propellers. Waterjets as alternative propulsive systems for fast ships, or ships operating in extremely shallow water are discussed by, e.g., Allison (1993), Kruppa (1994), and Terswiga (1996). The Royal Institution of Naval Architects has in addition hosted dedicated conferences on waterjet propulsion in 1994 and 1998 and the ITTC has a subcommittee reviewing the continuing progress on waterjets.

Propellers turning clockwise seen from aft are ‘right-handed’. In twin-screw ships, the starboard propeller is usually right-handed and the port propeller left-handed. The propellers are then turning outwards.

The propeller geometry is given in technical drawings following a special convention, or in thousands of offset points or spline surface descriptions, similar to the ship geometry. The complex propeller geometry is usually characterized by a few parameters. These include (Fig. 2.1):

- propeller diameter D
- boss (or hub) diameter d
- propeller blade number Z
- propeller pitch P

A propeller may be approximated by a part of a helicoidal surface which in rotation screws its way through the water. A helicoidal surface is generated as follows. Consider a line AB perpendicular to a line AA' as shown in Fig. 2.2. AB rotates around the axis of AA' with uniform angular velocity

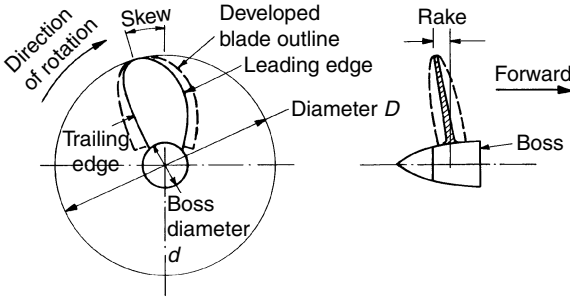


Figure 2.1 Propeller geometry

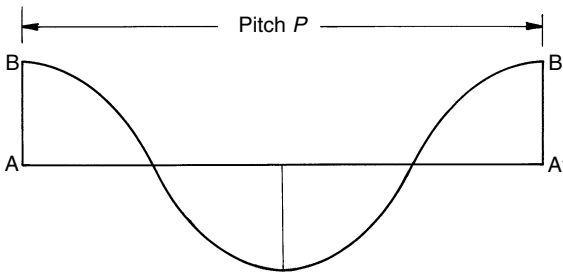


Figure 2.2 Helicoidal surface defining pitch

while moving along AA' with uniform speed. AB then forms a helicoidal surface. Its pitch is the distance AA' . A propeller with a flat face and radially constant pitch would trace out a helicoidal surface. In reality, ship propellers often have neither a radially constant pitch nor a flat face. Then averaging in a circumferential direction creates a flat reference line to define the pitch as a function of the radius. Again averaging in a radial direction may define an average pitch P used to describe the propeller globally. Alternatively, the pitch at one radial position, typically $0.7R = 0.35D$, is taken as a single value to represent the radial pitch distribution.

- disc area $A_0 = \pi \cdot D^2/4$

- projected area A_p

The blade area can be projected on to a plane normal to the shaft yielding the projected outline. Usually the area of the boss is not included.

- expanded blade area A_E

The expanded outline is obtained if the circumferential chord of the blade is set out against the radius. The area of the formed outline is A_E .

- skew (back)

The line of the half chord length of each radial cross-section of the propeller is usually not a straight line, but curved back relative to the rotation of the blade. Skew is usually expressed as the circumferential displacement of the propeller tip made non-dimensional by the propeller diameter. Skew back evens out to some extent the influence of a highly non-uniform wake field and reduces peak values of propeller-induced vibrations. Modern ship propellers always have some skew back.

- rake i_G
The face of the propeller may be tilted versus the normal plane on the propeller shaft. The tilt is usually backwards to increase the clearance between the blade tip and the hull.
- profile shape
A propeller section at a given radius is the intersection between the blade and a circular cylinder of that radius. The section is then laid out flat (developed) and displayed as a two-dimensional profile. Historically, the early propeller designs had a flat face and circular cross-sections which were then completely described by the blade width and maximum thickness. Today's profiles are far more complicated, but again usually characterized by a few parameters. The camber line is the line through the mid-thickness of the profile. If this line is curved, the profile is 'cambered'. The chord is the line joining the leading edge and the trailing edge. The camber is the maximum distance between the camber line and the chord. Profile sections are often defined by specifying the ordinates of the face and back as measured from the camber line.

Some of these data are often given as non-dimensional ratios:

- d/D
- A_E/A_0
- P/D
- i_G

The blade number Z is an important parameter for propeller-induced vibration. In general, odd numbers Z feature better vibration characteristics than even numbers. High blade numbers reduce vibration problems (due to less pronounced pressure peaks), but increase manufacturing costs. For large ships, blade numbers of 4 to 7 are typical. For small boats, blade numbers of 2 to 4 are typical. The propellers for large ships are always tailored towards the specific ship and involve extensive hydrodynamic analyses. The propellers for boats are often mass-produced.

Typical extended blade area ratios are $0.3 < A_E/A_0 < 1.5$. Area ratios above 1 mean overlapping blades which are expensive to manufacture. A_E/A_0 is chosen such that the blade load is kept low enough to avoid unacceptable cavitation. Therefore A_E/A_0 increases with propeller load (thrust per propeller area A_0). The propeller efficiency decreases with A_E/A_0 since the increased area also increases frictional losses. Larger A_E/A_0 also often demand higher blade numbers to avoid too small side ratios for the blades.

2.2 Propeller curves

Thrust T and torque Q are usually expressed as functions of rpm n in non-dimensional form as:

$$K_T = \frac{T}{\rho \cdot n^2 \cdot D^4}$$

$$K_Q = \frac{Q}{\rho \cdot n^2 \cdot D^5}$$

The force T is made non-dimensional by the propeller disk area times the stagnation pressure based on the circumferential speed, omitting a factor $\pi^2/8$. The moment Q is made non-dimensional by the additional length D , i.e. the propeller diameter.

The advance number J is defined as $J = V_A/(nD)$. V_A is the average inflow speed to the propeller. The propeller open-water efficiency is derived from thrust and torque coefficients and the advance number:

$$\eta_0 = \frac{T \cdot V_A}{2\pi \cdot n \cdot Q} = \frac{K_T \cdot \rho \cdot n^2 \cdot D^4}{K_Q \cdot \rho \cdot n^2 \cdot D^5} \cdot \frac{V_A}{2\pi \cdot n} = \frac{K_T}{K_Q} \cdot \frac{J}{2\pi}$$

K_T , K_Q , and η_0 are displayed over J . The curves are mainly used for propeller optimization and to determine the operation point (rpm, thrust, torque, power) of the ship. While the use of diagrams in education is still popular, in practice computer programs are almost exclusively used in propeller design. These represent traditionally the curves as polynomials in the form:

$$K_T = \sum C_T \cdot J^s \cdot \left(\frac{P}{D}\right)^t \cdot \left(\frac{A_E}{A_0}\right)^u \cdot Z^v$$

with tables of coefficients:

C_T	s	t	u	v
0.00880496	0	0	0	0
-0.20455403	1	0	0	0
...
-0.00146564	0	3	2	2

For standard Wageningen propellers the table consists of 49 coefficients for K_T and 56 coefficients for K_Q . While this may appear tedious, it is easy to program and fast to evaluate either by higher programming languages or spreadsheets. Diagrams are still popular in practice for documentation and visualization of tendencies.

Another important open-water parameter is the thrust loading coefficient:

$$C_{Th} = \frac{T}{\rho \cdot V_A^2 \cdot D^2 \cdot \frac{\pi}{8}}$$

This coefficient makes the thrust non-dimensional with the propeller disk area times stagnation pressure based on the propeller inflow velocity. Sometimes C_{Th} is also plotted explicitly in propeller characteristics diagrams, but sometimes it is omitted as it can be derived from the other quantities.

Figure 2.3 shows a typical propeller diagram. K_T and K_Q decrease monotonously with J . The efficiency η_0 has one maximum.

The open-water diagrams are based on stationary flow. They are only suited for the case when the ship moves steadily ahead. For cases where the speed is changed, so-called four-quadrant diagrams are used. The name derives from a classification into four possible combinations:

- ship has forward speed, propeller delivers forward thrust
- ship has forward speed, propeller delivers reverse thrust

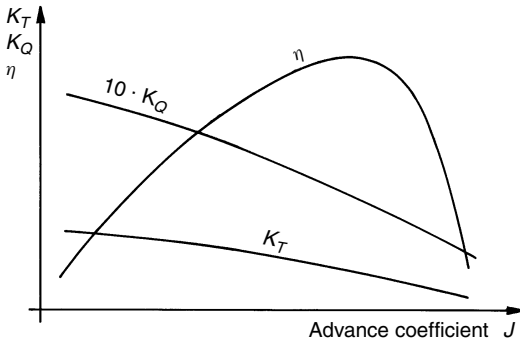


Figure 2.3 Propeller diagram

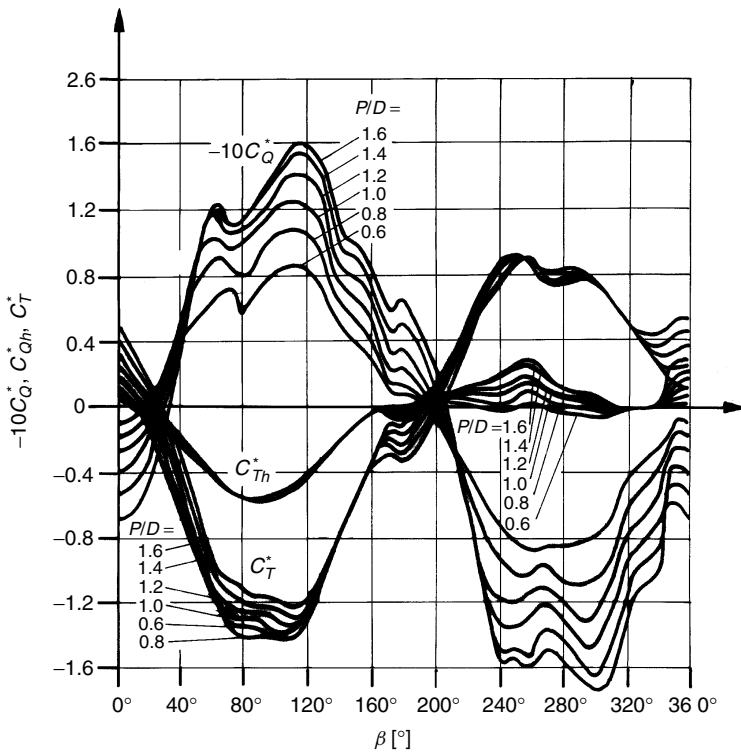


Figure 2.4 Four-quadrant diagram for propellers

- ship has reverse speed, propeller delivers forward thrust
- ship has reverse speed, propeller delivers reverse thrust

The results of corresponding open-water tests are displayed in diagrams as shown in Fig. 2.4. The abscissa is the effective advance angle β defined by:

$$\tan \beta = \frac{V_A}{0.7 \cdot \pi \cdot n \cdot D}$$

Displayed are non-dimensional modified thrust and torque coefficients:

$$C_{Th}^* = \frac{T}{\rho V_R^2 \pi D^2 / 8}$$

$$C_Q^* = \frac{Q}{\rho V_R^2 \pi D^3 / 8}$$

four-quadrant diagrams require considerably higher experimental effort than regular open-water diagrams. They are only available for some selected propellers. Four-quadrant diagrams are mainly used in computer simulations of ship manoeuvres.

2.3 Analysis of propeller flows

2.3.1 Overview of methods

Propellers create thrust as each of the blades is subject to local lift forces. Ideally, this lift is created with minimum drag losses. This basic goal is the same for other foil flows, e.g. airfoils, ship rudders etc. Each propeller section resembles a cross-section of a foil. However, unlike aeronautical foils, ship propellers feature short and stubby blades with a much smaller span-to-chord ratio than in aeronautical foils. The reason is that the limited diameter and the danger of cavitation impose more severe restrictions on ship propellers.

The small span-to-chord ratio of a ship propeller blade is one of the reasons why ship propeller flows are so complex. All two-dimensional approaches to model the flow around a propeller blade (like lifting-line theories) introduce considerable errors that must be corrected afterwards. Lifting-line approaches are still popular in propeller design as a preliminary step, before more powerful, but also more expensive, three-dimensional methods are employed. Many lifting-line codes in use today can be traced back to a fundamental formulation given by Lerbs (1952, 1955).

The advent of high-skew propellers necessitated truly three-dimensional theories to model the flow around the propeller. Empirical corrections for the lifting-line method could no longer be applied satisfactorily to the new and more complex propeller geometries. The approach was then to use lifting-line methods for an initial design serving as a starting point for more sophisticated methods which could then serve to answer the following questions:

- Will the propeller deliver the design thrust at the design rpm?
- What will be the propeller (open-water) efficiency?
- How will the propeller perform at off-design conditions?
- Will the pressure distribution be such that the propeller features favourable cavitation characteristics?
- What are the time-dependent forces and moments from the propeller on the propeller shaft and ultimately the shaft bearings?
- What are the propeller-induced pressures at the ship hull (exciting vibrations and noise)?

These more sophisticated three-dimensional propeller theories used in practical propeller design today are lifting-surface methods, namely vortex-lattice methods, which do not consider the blade thickness, and boundary element

methods or panel methods, which do consider the blade thickness. Field methods were still subject to research by the end of the 1990s.

The main methods in increasing complexity are listed below with their respective advantages and disadvantages:

- *Momentum theory*

The propeller is reduced to an actuator disk which somehow creates a pressure jump in the flow. Thrust and corresponding delivered power are expressed by increased velocities in the propeller plane and the contracted wake downstream of this plane. This simple model is unsuited for propeller design, but popular as a simple propeller model in RANSE ship computations and useful in understanding, some basic concepts of propeller flows.

- + Simple and fast; yields ideal efficiency η_i
- Rotative and viscous losses not modelled; momentum theory is no method to design propellers or analyse given propeller designs

- *Lifting-line method*

Propeller blade is reduced to radially aligned straight vortices (lifting lines). The vortex strength varies over the radius. Free vortices are shed in the flow.

- + Proven in practice; suitable for initial design of propellers, rotative losses reflected in model; viscous losses incorporated by empirical corrections
- Does not yield complete propeller geometry; cross-sections found, but angle of incidence and camber require corrections; no simple way to consider skew

- *Lifting-surface method, especially vortex-lattice method*

Propeller blade is reduced to a grid of horseshoe vortices; pressure distribution on the blade follows from Bernoulli's law from the induced velocities; pressure distribution yields forces and moments for the whole propeller.

- + Blade modelled three dimensionally; corrections only necessary for viscous effects; good convergence to grid-independent solutions with grid refinement
- More complex programming; pressure distribution must be corrected at the propeller hub

- *Boundary element method/panel method*

Exact formulation of the potential theory problem with source or dipole panels.

- + No simplifications besides the potential flow assumption; finite velocities in the hub region
- Programming complex, especially for the Kutta condition; relatively large number of dipole and/or source panels necessary; flow near propeller tip still not well captured

- *RANSE method*

Field method formulation of the three-dimensional viscous flow.

- + Effective wake easily incorporated; viscous effects decreasing propeller efficiency directly captured; flow well captured also near hub and tip of propeller
- Grid generation expensive; computation expensive; turbulence model questionable

Dedicated treatment of propeller flow analysis methods, predominantly based on lifting-surface and panel methods, can be found in, e.g., Breslin and Andersen (1993), Kinnas (1996), and Streckwall (1993, 1999).

2.3.2 Momentum theory

Momentum theory models the propeller as a simple actuator disk accelerating the flow in the axial direction by somehow creating a pressure jump in the propeller plane. The propeller is then seen as a continuous circular disk with infinite blades and $A_E/A_0 = 1$. The model is too crude to be of any value in propeller design, but allows some valuable insight into the global mechanisms of a propeller. The momentum theory regards inflow and outflow of the propeller plane as the flow through a tube of varying cross-section, but always of circular shape. Only the longitudinal velocity component is considered, i.e. the velocity is a scalar quantity.

The inflow to the propeller is given by $\rho \cdot u_A \cdot A_A$ where A_A is the cross-sectional area of the considered propeller plane. The propeller induces a velocity jump to the outflow velocity u_j and the cross-sectional area of the ‘flow tube’ is A_j . The thrust T is the change in the momentum:

$$T = \rho \cdot u_A \cdot A_A \cdot (u_j - u_A)$$

Continuity requires $A_j \cdot u_j = A_A \cdot u_A$, i.e. the flow contracts after the propeller due to the higher velocity (Fig. 2.5).

The velocity in the propeller plane is the average between the velocities far upstream and far downstream of the propeller in this model. Bernoulli’s law couples the pressure to the velocity yielding qualitatively the distribution shown in Fig. 2.5.

The actuator disk yields an ideal efficiency for the propeller of:

$$\eta_i = \frac{2u_A}{u_j + u_A}$$

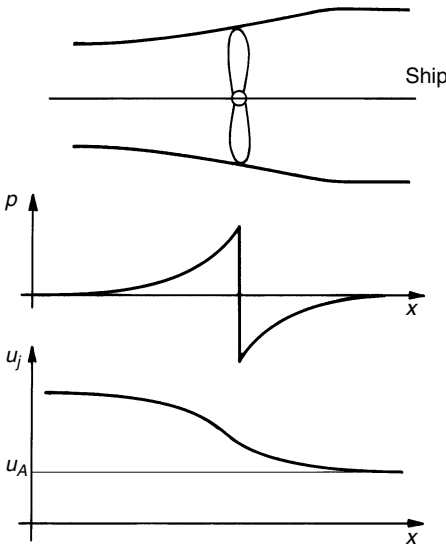


Figure 2.5 Momentum theory considers propeller flow as one-dimensional flow with sudden pressure jump accelerating velocity from u_A to u_j

This formula can be interpreted as follows. The smaller increase in velocity due to the propeller, the better is the efficiency. If the velocity downstream is the same as the velocity upstream, the efficiency would be an ideal $\eta_i = 1$. (But no thrust would be produced.) The ideal efficiency can also be expressed in terms of the thrust loading coefficient c_{Th} as:

$$\eta_i = \frac{2}{1 + \sqrt{1 + c_{Th}}}$$

Thus a large thrust loading coefficient decreases the efficiency.

The conclusion for practical propeller design is that usually the propeller diameter should be chosen as large as possible to increase the efficiency.

2.3.3 Lifting-line methods

Lifting-line methods still form a vital part of practical propeller design. They find the radial distribution of loading optimum with respect to efficiency as a first step to determine the corresponding blade geometry. Alternatively, the radial distribution of loading may be specified to determine the corresponding blade geometry (Lerbs (1952, 1954)). Of course, this approach works only within limits. If unrealistic or too demanding pressure distributions are specified, either no solution is found or the error in framework of the theory is so large that the solution does not reflect reality.

Lifting-line methods for propellers were adapted from lifting-line theory for straight foils. We shall therefore briefly review the lifting-line theory for straight foils.

A straight line of vorticity creates lift orthogonal to the direction of the vortex line and the direction of the inflow, (Fig. 2.6). Helmholtz's first and second laws state:

1. The strength of a vortex line is constant along its length.
2. A vortex line must be closed, it cannot end in the fluid.

As a consequence, the vortex lines on a foil are bent downstream at the end of the foil. Far downstream these vortex lines are closed again, but often 'far

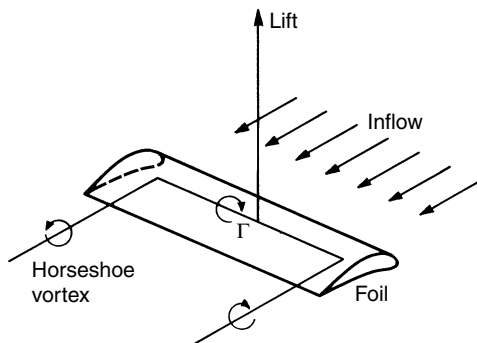


Figure 2.6 Lifting-line theory is based on representing the foil by bound vortex and trailing vortices

downstream' is interpreted as 'at infinity', i.e. the vortex line forms a semi-infinite horseshoe vortex. The vortex segment representing the foil is called the 'bound' vortex, as it stays always with the foil. The two vortex segments swept downstream are the 'trailing vortices', also denoted as axial vortices or tip vortices. The closing vortex segment far downstream is the 'starting' vortex.

In reality, the lift and thus the vorticity (vortex strength) are not constant over the foil span. This can be considered by approximating the continuous lift by a number of discrete, piecewise constant vortex segments. Each of these will then produce trailing vortices (Fig. 2.7). In sum, the vortex segments form a 'lifting line' of (stepwise) variable vorticity. The trailing vortices induce a flow at the foil which is downward for positive lift. This velocity is therefore called downwash and changes the effective inflow angle experienced by each section of the foil.

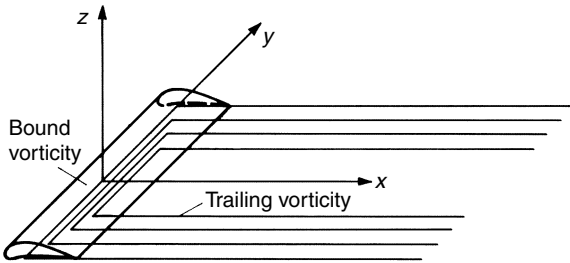


Figure 2.7 A better model represents the foil by a distribution of horseshoe vortices

The strengths of the individual vortex elements (each forming a closed or semi-infinite loop) are determined by requiring that there is no flow through the foil at a corresponding number of collocation points. This results in a system of linear equations which is solved numerically. Once all vortex strengths are known, the velocities and pressures can be evaluated everywhere. Lift and drag can then be computed.

For propellers, each blade is represented by one lifting line extending from hub to blade tip. Typically the lifting lines are straight with skew and rake being neglected at this point in the analysis. The proper end condition for the lifting line at the hub is unclear. Usually, the hub is neglected and the vorticity is required to go to zero as at the blade tip. This is called the 'hubless propeller assumption'. Lerbs has argued that near the hub, the blades are close enough together such that the positive pressure on the face of one blade is cancelled by the negative pressure on the back of the adjacent blade. However, in practice the lifting-line results near the hub, but also often near the blade, are unrealistic and are then manually corrected (smooth connection to the rest of the lift distribution based on human insight).

2.3.4 Lifting-surface methods

The discussion to substitute the lifting-line approach by lifting-surface theories dates back to the 1950s, but the realization of this goal was initially impossible for real ship propeller geometries due to insufficient computing

power. The earliest lifting-surface attempts were based on mode functions which prescribed continuous distributions of surface singularities. At that time, the mode function approach was the ordinary procedure for solving lifting-line or two-dimensional wing section problems and naturally it was tried first. For lifting surfaces that had to fit propeller blades these mode functions needed a careful and complicated mathematical treatment. Their ability to describe arbitrary blade geometries was poor. The second generation of lifting-surface methods was developed around the late 1970s when sufficient computer power became widely available (Kerwin (1978)). These methods used vortex lattices. Vortex-lattice methods are characterized by comparably simple mathematics. They can handle arbitrary blade geometries, but neither consider the true blade thickness, nor the propeller hub. This makes the theory of vortex-lattice methods more complicated than panel methods, but reduces the number of unknowns and thus the computational effort considerably. Despite the theoretical inferiority, vortex-lattice methods gave in benchmark tests of the ITTC for propellers with moderate skew-back results of comparable quality as panel methods. Figure 2.8 shows a typical discretization of the propeller blades and the wake. The hub is not modelled which leads to completely unrealistic results in the immediate vicinity of the hub.

Vortex-lattice methods were in the 1990s extended to rather complicated propeller geometries, e.g. contra-rotating propellers, and unsteady propeller inflow (nominal wake computations). Cavitation may be simulated by additional singularities of both source and vortex type, but this remains a rather coarse approximation of the real phenomenon.

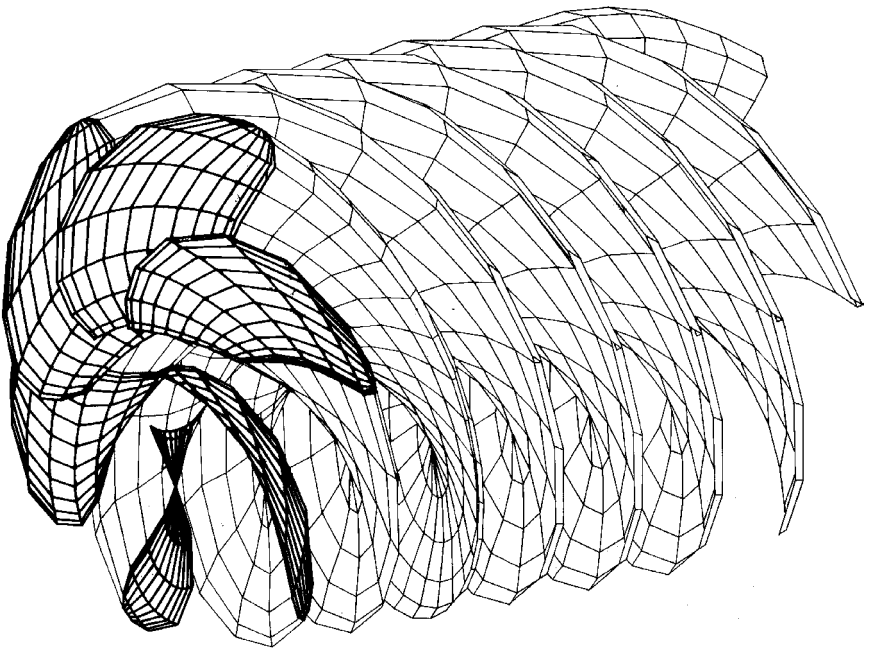


Figure 2.8 Vortex-lattice model of a propeller and trailing wakes

A complete vortex-lattice method (VLM) can be established on the basis of the lifting-line method just described. The lifting-line model was used to find a circulation Γ that corresponds to a given resultant flow direction at the lifting line and is able to provide the predetermined (design) thrust. With a vortex lattice instead of a lifting line, a model for the material blade is inserted. One can now really investigate whether a given geometry corresponds to a desired thrust, a task that is beyond the scope of a lifting-line theory.

Figure 2.9 shows a vortex-lattice system. The flow is generated by spanwise and (dependent) streamwise line vortices. Control points are positioned inside the loops of the vortex system. For steady flow, the vortex elements in the wake have the same strength in each spanwise segment. The vertical vortex lines then cancel each other and a semi-infinite horseshoe vortex results. The most downstream control point is located at the trailing edge behind the last streamwise vortex which is a very robust measure to enforce the Kutta condition.

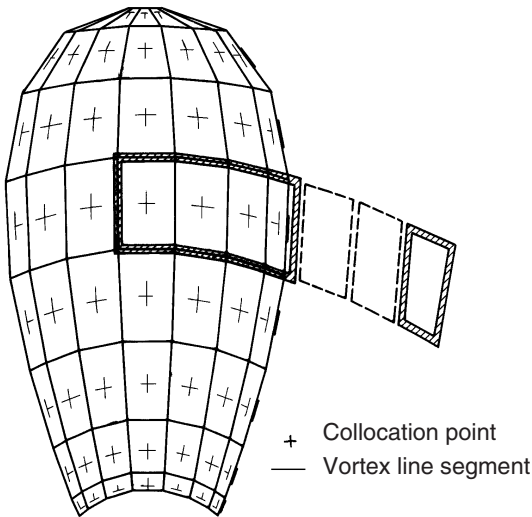


Figure 2.9 Allocation of vortex-lattice elements on propeller blade

The kinematic boundary condition (zero normal velocity in a blade-fixed coordinate system) together with some basic relations between blade vortices and trailing vortices is sufficient to calculate blade surface pressures and thus propeller thrust and torque. Although the kinematic condition is fulfilled on a zero thickness blade, the influence of the blade thickness is not excluded. The thin wing theory provides a simple formula to derive a source system from the slope of the section contours. This source system already enters the kinematic conditions and serves to correct the angle of attack of the blade sections for the displacement effect of the neighbouring blades.

In most applications a 'frozen' vortex wake is used, i.e. the trailing vortex geometry is fixed from the start. A more or less empirical relation serves to prescribe the pitch of the helical lines. Since surface friction effects are not part of the solution, the forces and moments from the vortex lattice must be

corrected subsequently. This is usually achieved by local section drag coefficients using empirical relations to express the Reynolds number dependence.

Figure 2.10 shows a typical pressure distribution for a propeller blade cross-section. The pressure coefficient can be decomposed into a mean value between both sides of the profile and a difference Δc_p . The pressure on the suction side is then obtained by subtracting Δc_p from the mean value; the pressure on the other side by adding Δc_p . Lifting-surface methods arrange the vortex and source elements on the mean chord surface of the blade. Following Bernoulli's law, the pressure can be computed from the velocities. This yields pressure distributions which usually reproduce the actual pressure distributions quite well except for a narrow region at the leading edge which may extend to a length of approximately twice the nose radius. The sources yield the average pressure distribution and the vortex elements induce the pressure difference Δc_p . As the source strengths are explicitly derived from the change of the profile thickness in longitudinal direction, the main problem is to determine the vortex strengths.

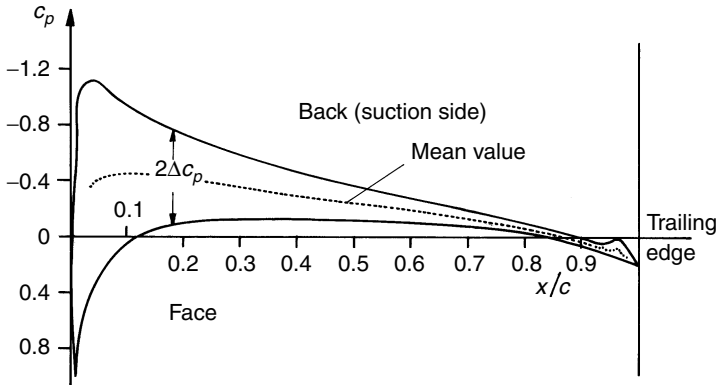


Figure 2.10 Pressure distribution on a propeller blade profile

2.3.5 Boundary element methods

Panel methods were developed to overcome the disadvantage of an incomplete geometry model. Panel methods also model the blade thickness and include the hub in the numerical model. The development of panel methods for propellers was apparently not an easy task. After the ship hull flow could be treated by panel methods it took another decade until in the late 1980s before the first successful panel approaches were established for propellers. The implementation of a robust Kutta condition is a decisive element of each propeller panel code, since it controls torque and thrust. In principle, there exist many possibilities to create panel codes, depending on panel type and the formulation of the problem, e.g. Kerwin *et al.* (1987). The following panel types are found:

- dipole panels
- source panels
- mix of dipole panels and source panels

The problem may be formulated as

- direct formulation (potential formulation); potential itself is the unknown
- indirect formulation (velocity formulation); source or dipole strength is unknown

For indirect formulations, Kerwin *et al.* (1987) show how a dipole-based formulation can be transformed to an equivalent vortex-based formulation.

The majority of the panel codes used for propellers follows Morino's approach (Morino and Kuo (1974), Morino (1975)). Morino's approach is a direct formulation, i.e. it solves directly for the potential and determines velocities by numerical differentiation. The approach uses exclusively dipole panels which discretize the surfaces of the propeller blades, the hub, and part of the wakes of each blade. The Kutta condition demands that at the trailing edge the pressure difference between face and back should vanish. This couples the dipoles on the wake to the dipoles on the propeller. The panels in the wake all have the same strength for steady flow conditions. The pitch of the wake is either specified by largely empirical relations or determined iteratively as part of the solution. The Kutta condition enforcing a vanishing pressure jump at the trailing edge is a non-linear condition requiring an iterative solution. The numerical implementation of the Kutta condition requires great care, since simplifications or conceptual errors in the physical model may strongly affect the computed lift forces.

The main problems of these methods lie in:

- numerical realization of the Kutta condition (stagnation point at the trailing edge)
- numerical (accurate) determination of velocity and pressure fields

In the 1990s, panel methods were presented that were also capable of solving the problem for time-dependent inflow and ducted propellers, e.g. Kinnas (1996).

2.3.6 Field methods

The common procedure to run unsteady propeller vortex-lattice or panel methods contains an inherent weakness. The ship is usually represented by the velocity field measured without the propeller at the propeller plane, i.e. the nominal wake. But in a real ship, the propeller rearranges the streamlines that reach the propeller plane, i.e. the propeller operates in the effective wake. There are measures to correct the nominal wake, but it is at least doubtful if these treat the details of the wake correctly.

No such complications arise in theory if viscous flow computations are employed. It is possible to interactively couple viscous flow computations for the ship based on RANSE solvers with potential flow computations for the propeller, e.g. vortex-lattice or panel methods, and research is active to solve also the flow around propellers using RANSE solvers. The flow can then be specified once at an inlet area upstream of the propeller and from there to the propeller plane the flow develops in agreement with the equations for mass and momentum. The viscous flow representation for the propeller may ultimately be embedded in a viscous model for the ship, so that all problems from decoupling ship flow and propeller flow will vanish. Viscous

flow computations are able to deliver accurate flow details in the tip region of the propeller blade.

Typical propeller geometries require careful grid generation to assure converged solutions. The warped propeller geometry makes grid generation particularly difficult especially for high-skew propellers. By the late 1990s, most RANSE applications for propellers were still for steady flow (open-water case), but first unsteady computations in the ship wake appeared. However, the excessive effort in grid generation limited the calculations to research projects.

2.4 Cavitation

High velocities result in low pressures. If the pressure falls sufficiently low, cavities form and fill up with air coming out of solution and by vapour. This phenomenon is called cavitation. The cavities disappear again when the pressure increases. They grow and collapse extremely rapidly, especially if vapour is filling them. Cavitation involves highly complex physical processes with highly non-linear multi-phase flows which are subject to dedicated research by specialized physicists. We will cover the topic only to the extent that any naval architect should know. For a detailed treatment of cavitation for ship propellers, the reader is referred to the book of Isay (1989).

For ship propellers, the velocities around the profiles of the blade may be sufficiently high to decrease the local pressures to trigger cavitation. Due to the hydrostatic pressure, the total pressure will be higher on a blade at the 6 o'clock position than at the 12 o'clock position. Consequently, cavitating propellers will then have regions on a blade where alternately cavitation bubbles are formed (near the 12 o'clock position) and collapse again. The resulting rapid succession of explosions and implosions on each blade will have various negative effects:

- vibration
- noise (especially important for navy ships like submarines)
- material erosion at the blade surface (if the bubble collapse occurs there)
- thrust reduction (Fig. 2.11)

Cavitation occurs not only at propellers, but everywhere where locally high velocities appear, e.g. at rudders, shaft brackets, sonar domes, hydrofoils etc.

Cavitation may be classified by:

- Location
tip cavitation, root cavitation, leading edge or trailing edge cavitation, suction side (back) cavitation, face cavitation etc.
- Cavitation form
sheet cavitation, cloud cavitation, bubble cavitation, vortex cavitation
- Dynamic properties of cavitation
stationary, instationary, migrating

Since cavitation occurs in regions of low pressures, it is most likely to occur towards the blade tips where the local inflow velocity to the cross-sections is highest. But cavitation may also occur at the propeller roots near the hub, as the angle of incidence for the cross-sections is usually higher there than at the tip. The greatest pressure reduction at each cross-section profile occurs

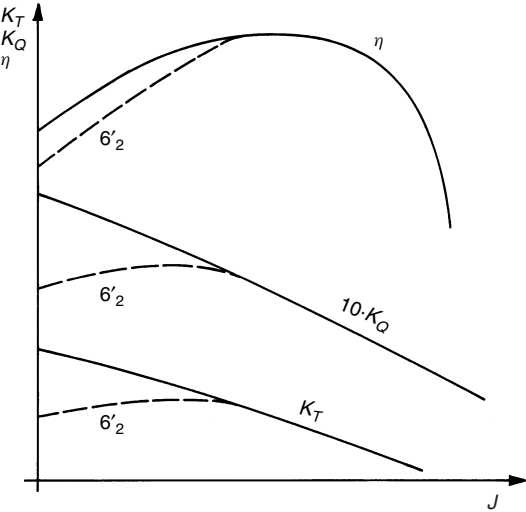


Figure 2.11 Influence of cavitation on propeller characteristics

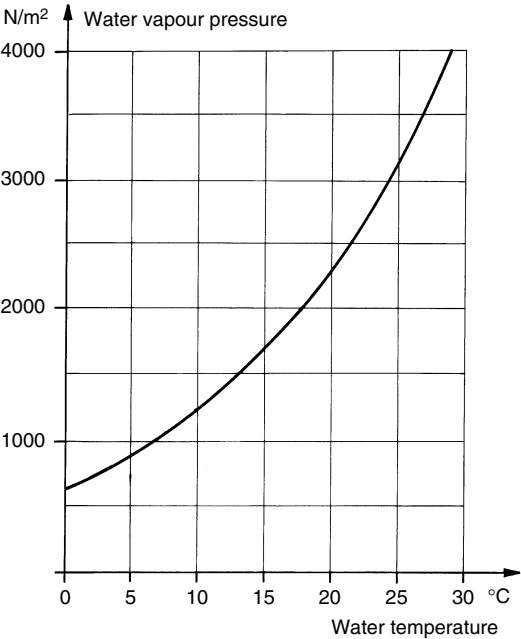


Figure 2.12 Vapour pressure as function of temperature

usually between the leading edge and mid-chord, so bubbles are likely to form there first.

In ideal water with no impurities and no dissolved air, cavitation will occur when the local pressure falls below vapour pressure. Vapour pressure depends on the temperature (Fig. 2.12). For 15° it is 1700 Pa. In real water, cavitation

occurs earlier, as cavitation nuclei like microscopic particles and dissolved gas facilitate cavitation inception. The cavitation number σ is a non-dimensional parameter to estimate the likelihood of cavitation in a flow:

$$\sigma = \frac{p_0 - p}{\frac{1}{2}\rho V_0^2}$$

p_0 is an ambient reference pressure and V_0 a corresponding reference speed. p is the local pressure. For $\sigma < \sigma_v$ (the cavitation number corresponding to vapour pressure p_v) the flow will be free of cavitation in an ideal fluid. In reality, one introduces a safety factor and sets a higher pressure than vapour pressure as the lower limit.

Cavitation is predominantly driven by the pressure field in the water. Cavitation avoidance consequently strives to control the absolute pressure minimum in a flow. This is achieved by distributing the thrust on a larger area, either by increasing the diameter or the blade area ratio A_E/A_0 .

The most popular approach to estimate the danger of cavitation at a propeller uses Burill diagrams. These diagrams can only give a rough indication of cavitation danger. For well-designed, smooth propeller blades they indicate a lower limit for the projected area. Burill uses the coefficient τ_c :

$$\tau_c = \frac{T}{q_{0.7R}^2 A_p}$$

$$q_{0.7R} = \frac{1}{2}\rho V_R^2$$

$$V_R = \sqrt{V_A^2 + (0.7\pi nD)^2}$$

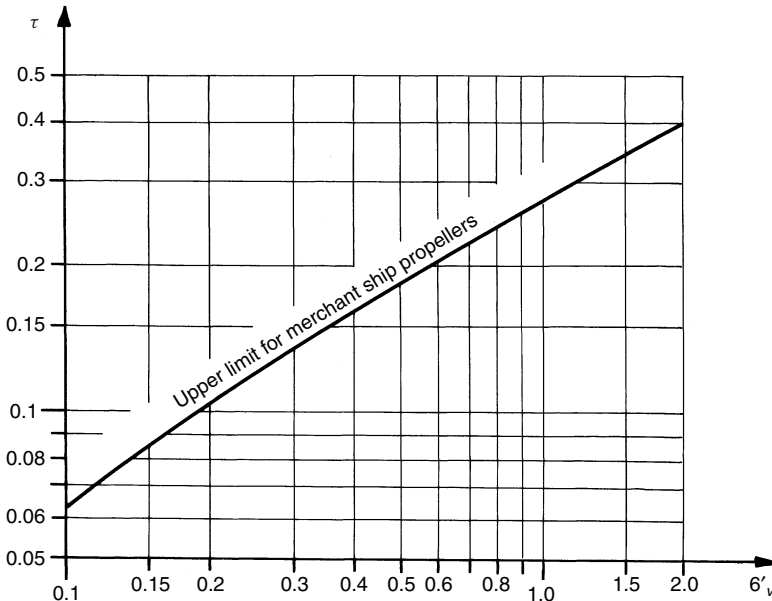


Figure 2.13 Burill diagram

V_R is the absolute value of the local velocity at 0.7 of the propeller radius. V_A is the inflow velocity to the propeller plane. A_p is the projected propeller area. Burill uses as reference pressure the atmospheric pressure plus the hydrostatic pressure at the propeller shaft:

$$p_0 = p_{\text{atm}} + \rho gh$$

The Burill diagram then yields limiting curves (almost straight) to avoid cavitation (Fig. 2.13). The curves have been transformed into algebraic expressions and are also included in propeller design programs. The upper limit for τ_c yields indirectly a minimum A_p which yields (for Wageningen B-series propellers) approximately the expanded blade area:

$$A_E \approx \frac{A_p}{1.067 - 0.229(P/D)}$$

2.5 Experimental approach

2.5.1 Cavitation tunnels

Propeller tests (open-water tests, cavitation tests) are usually performed in cavitation tunnels. A cavitation tunnel is a closed channel in the vertical plane recirculating water by means of an impeller in the lower horizontal part. This way the high hydrostatic pressure ensures that even for reduced pressure in the tunnel, the impeller itself will not cavitate. The actual test section is in the upper horizontal part. The test section is provided with observation glass ports. The tunnels are designed to give (almost) uniform flow as inflow to the test section. If just the propeller is tested (with the driving shaft downstream), it is effectively tested in open water. Larger circulation tunnels also include ship models and thus testing the propeller in the ship wake. The ship models are sometimes shortened to obtain a thinner boundary layer in the aftbody (which thus resembles more the boundary layer in a large-scale model). Alternatively, sometimes grids are installed upstream to generate a flow similar to that of a full-scale ship wake. This requires considerable experience and is still at best a good guess at the actual wake field.

Vacuum pumps reduce the pressure in the tunnel and usually some devices are installed to reduce the amount of dissolved air and gas in the water. Wire screens may be installed to generate a desired amount of turbulence.

Cavitation tunnels are equipped with stroboscopic lights that illuminate the propeller intermittently such that propeller blades are seen always at the same position. The eye then perceives the propeller and cavitation patterns on each blade as stationary.

Usual cavitation tunnels have too much background noise to observe or measure the noise making or hydro-acoustic properties of a propeller which are of great interest for certain propellers, especially for submarines or anti-submarine combatants. Several dedicated hydro-acoustic tunnels have been built worldwide to allow acoustical measurements. The HYKAT (hydro-acoustic cavitation tunnel) of HSVA is one of these.

2.5.2 Open-water tests

Although in reality the propeller operates in the highly non-uniform ship wake, a standard propeller test is performed in uniform flow yielding the so-called open-water characteristics, namely thrust, torque, and propeller efficiency.

The model scale λ for the model propeller should be the same as for the ship model in the propulsion tests. For many propulsion tests, the ship model scale is determined by the stock propeller, i.e. the closest propeller to the optimum propeller on stock at a model basin. The similarity laws (see section 1.2, Chapter 1) determine for geometrical and Froude similarity:

$$\left(\frac{V_A}{n \cdot D} \right)_s = \left(\frac{V_A}{n \cdot D} \right)_m$$

In other words, the advance number $J = V_A/(nD)$ is the same for model and full scale. J has thus a similar role for the propeller as the Froude number F_n has for the ship. V_A is the average inflow speed to the propeller, n the propeller rpm, and D the propeller diameter. $\pi \cdot n \cdot D$ is the speed of a point at the tip of a propeller blade in circumferential direction.

The Reynolds number for a propeller is usually based on the chord length of one blade at 0.7 of the propeller radius and the absolute value of the local velocity V_R at this point. V_R is the absolute value of the vector sum of inflow velocity V_A and circumferential velocity:

$$V_R = \sqrt{V_A^2 + (0.7\pi n D)^2}$$

Propeller model tests are performed for geometrical and Froude similarity. It is not possible to keep Reynolds similarity at the same time. Therefore, as in ship model tests, corrections for viscous effects are necessary in scaling to full scale. ITTC 1978 recommends the following empirical corrections:

$$K_{Ts} = K_{Tm} - 0.3 \cdot Z \cdot \left(\frac{c}{D} \right)_{r=0.7} \cdot \frac{P}{D} \cdot \Delta C_D$$

$$K_{Qs} = K_{Qm} + 0.25 \cdot Z \cdot \left(\frac{c}{D} \right)_{r=0.7} \cdot \Delta C_D$$

c is the propeller blade chord length at $0.7R$, R the propeller radius, $\Delta C_D = C_{Dm} - C_{Ds}$ is a correction for the propeller resistance coefficient with:

$$C_{Dm} = 2 \cdot \left(1 + 2 \frac{t}{c} \right) \cdot \left(\frac{0.044}{R_n^{1/6}} - \frac{5}{R_n^{2/3}} \right)$$

$$C_{Ds} = 2 \cdot \left(1 + 2 \frac{t}{c} \right) \cdot \left(1.89 + 1.62 \log \left(\frac{c}{k_p} \right) \right)^{-2.5}$$

Here t is the (maximum) propeller blade thickness, R_n is the Reynolds number based on V_R , both taken at $0.7R$. k_p is the propeller surface roughness, taken as $3 \cdot 10^{-5}$ if not known otherwise.

2.5.3 Cavitation tests

Cavitation tests investigate the cavitation properties of propellers. Experiments usually observe the following similarity laws:

- Geometrical similarity making the propeller as large as possible while still avoiding tunnel wall effects.
- Kinematical similarity, i.e. same advance number in model and ship $J_m = J_s$.
- Dynamical similarity would require that model and full-scale ship have the same Froude and Reynolds numbers. Reynolds similarity is difficult to achieve, but the water speed is chosen as high as possible to keep the Reynolds number high and reduce scaling effects for the friction on the blades. Gravity effects are negligible in propeller flows, i.e. waves usually play no role. Thus the Froude number may be varied.
- Cavitation similarity requires same cavitation numbers in model and full-scale ships. The tunnel pressure is adjusted to give the same cavitation number at the propeller shaft axis to approximate this condition.
- For similarity in bubble formation in cavitation, the Weber number should also be the same in model and ship:

$$\left(\frac{\rho \cdot V^2 \cdot l}{T_e} \right)_m = \left(\frac{\rho \cdot V^2 \cdot l}{T_e} \right)_s$$

T_e is the surface tension. This similarity law is usually violated.

The cavitation tests are performed for given inflow velocity and cavitation number, varying the rpm until cavitation on the face and back of the propeller is observed. This gives limiting curves $\sigma = \sigma(J)$ for cavitation-free operation. The tests are often performed well beyond the first inception of cavitation and then the extent and type of cavitation is observed, as often designers are resigned to accept some cavitation, but individual limits of accepted cavitation differ and are often subject to debate between shipowners, ship designers and hydrodynamic consultants. The tests are usually completely based on visual observation, but techniques have been developed to automatically detect and visualize cavitation patterns from video recordings. These techniques substitute the older practice of visual observation and manual drawings, making measurements by various persons at various times more objectively comparable.

2.6 Propeller design procedure

Traditionally, propeller design was based on design charts. These charts were created by fitting theoretical models to data derived from actual model or full size tests and therefore their number was limited. By and large, propeller design was performed manually. In contrast, contemporary propeller design relies heavily on computer tools. Some of the traditional propeller diagrams, such as for the Wageningen B-series of propellers, have been transformed into polynomial expressions allowing easy interpolation and optimization within

the traditional propeller geometries. This is still a popular starting point for modern propeller design. Then, a succession of ever more sophisticated analysis programs is employed to modify and fine-tune the propeller geometry.

Propeller design is an iterative process to optimize the efficiency of a propeller subject to more or less restrictive constraints concerning cavitation, geometry, strength etc. The severeness of constraints depends on the ship type. For example, submarine propellers have strict constraints concerning cavitation-induced noise. Subsequently the efficiencies of these propellers are lower than for cargo ships, but the primary optimization goal is still efficiency. A formal optimization is virtually impossible for modern propellers as the description of the final geometry involves typically some hundred offsets and the evaluation of the efficiency based on numerical hydrodynamics codes requires considerable time. Thus, while the word ‘optimization’ is often used, the final design is rather ‘satisficing’, i.e. a good solution satisfying the given constraints.

Additional constraints are inherently involved in the design process, but often not explicitly formulated. These additional constraints reflect the personal ‘design philosophy’ of a designer or company and may lead to considerably different ‘optimal’ propellers for the same customer requirements. An example for such a ‘design philosophy’ could be the constraint that no cavitation should occur on the pressure side of the propeller. The following procedure will reflect the design philosophy of HSVA as detailed in Reich *et al.* (1997). The overall procedure will, however, be similar to any other state-of-the-art propeller design process. The main engine influences the propeller design primarily through the propeller rpm and delivered power. Modern turbo-charged diesels, almost exclusively used for cargo ships today, are imposing a rather narrow bandwidth for the operating point (rpm/power combination) of the propeller. We limit ourselves therefore to such cases where the rpm, the ship’s speed, and an estimated delivered power P_D are specified by requirement. This covers more than 90% of the cases in practice.

The procedure follows a few main steps which involve model tests, analytical tools of successive sophistication and power, and some experience in deciding trade-offs in conflict situations:

1. Preparation of model experiments

Known at this stage: rpm of the full-scale propeller n_s
 ship speed V_s
 estimate of delivered power for the ship P_D
 ship hull form (lines plan)
 classification society
 often: number of blades Z
 often: diameter of propeller D

Generally, the customer specifies within small margins what power P_D has to be delivered at what speed V_s and what is the rpm of the (selected) main engine. While in theory such a combination may be impossible to realize, in practice the shipyard engineers (i.e. the customers) have sufficient experience to estimate a realistic power for a shipowner specified speed and rpm. The shipyard or another department in the model basin will specify a first proposal for the ship lines. Often, the customer will also already determine the number of blades for the propeller. A few simple rules gained from experience will guide this selection, e.g. if the engine has an even

number of cylinders, the propeller should have an odd number of blades. The propeller of optimal efficiency can then be automatically determined based on the Wageningen-B-Series by computer codes. The performance of these older propellers is insufficient for today's expectations and the propeller thus determined will only be used as a starting point for the actual design. This procedure yields the average (or representative) pitch-to-diameter ratio P_m/D and the diameter D . An upper limit for the diameter is specified from the ship geometry. Sometimes the customer already specifies the diameter, otherwise it is a result of the optimization. The expanded area ratio A_E/A_0 is usually part of the optimization result, but may be restricted with respect to cavitation if problems are foreseen. In this case, a limiting value for A_E/A_0 is derived from Burill diagrams.

Then, from a database of stock propellers, the most suitable propeller is selected. This is the propeller with the same number of blades, closest in P_m/D to the optimized propeller. If several stock propellers coincide with the desired P_m/D , the propeller closest in A_E/A_0 among these is selected. A selection constraint comes from upper and lower limits for the diameter of the stock propeller which are based on experience for the experimental facilities. For example, for HSVA, the ship models may not exceed 11 metres in length to avoid the influence of canal restrictions, but should be larger than 4 metres to avoid problems with laminar flow effects. As the ship length is specified and the model scale for propeller and ship must be the same, this yields one of the constraints for upper and lower values of the diameter of the stock propeller. Usually, the search of the database is limited to the last 300 stock propellers, i.e. the most recent designs.

The selected stock propeller then determines the model scale and the ship model may be produced and tested. The output of the model tests relevant for the propeller designer is:

- nominal wake distribution (axial, tangential and radial velocities in the propeller plane)
- thrust deduction fraction t
- effective wake fraction w
- relative rotative efficiency η_R
- delivered power P_D

The delivered power P_D is of secondary importance (assuming that it is close to the customer's estimate). It indicates how much the later propeller design has to strive for a high efficiency. If the predicted P_D is considerably too high, then the ship form has to be changed and the tests repeated.

2. Estimate effective wake distribution full scale

Known at this stage: all of the above and ...

- number of blades Z
- diameter of propeller D
- blade area ratio A_E/A_0
- thrust deduction fraction t
- effective wake fraction w
- relative rotative efficiency η_R
- nominal wake field (axial, tangential, radial velocity components)

Ship-propeller interaction is difficult to capture. The inflow is taken from experiments and based on experience modified to account for scale effects

(model/full-scale ship). The radial distribution of the axial velocity component is transformed from the nominal (without propeller action) value for the model to an effective (with propeller) value for the full-scale ship. The other velocity components are assumed to be not affected. Several methods have been proposed to perform this transformation. To some extent, the selection of the 'appropriate' method follows usually rational criteria, e.g. one method is based on empirical data for full ships such as tankers, another method for slender ships such as container ships. But still the designer expert usually runs several codes, looks at the results and selects the 'most plausible' based on 'intuition'. The remaining interaction effects such as thrust deduction fraction t and relative rotative efficiency η_R are usually taken as constant with respect to the results of ship model tests with propellers.

3. *Determine profile thickness according to classification society*

Known at this stage: all of the above

Classification societies have simple rules to determine the minimum thickness of the foils. The rules of all major classification societies are usually implemented in programs that adjust automatically the (maximum) thickness of all profiles to the limit value prescribed by the classification society.

4. *Lifting-line and lifting-surface calculations*

Known at this stage: all of the above and ...

max. thickness at few radii

As additional input, default values are taken for profile form (NACA series), distribution of chord length and skew. If this step is repeated at a later stage, the designer may deviate from the defaults. At this stage, the first analytical methods are employed. A lifting-line method computes the flow for a two-dimensional profile, i.e. the three-dimensional flow is approximated by a succession of two-dimensional flows. This is numerically stable and effective. The method needs an initial starting value for the circulation distribution. This is taken as a semi-elliptical distribution. The computation yields then the optimal radial distribution of the circulation. These results are directly used for a three-dimensional lifting-surface program. The lifting-surface code yields as output the radial distribution of profile camber and pitch.

5. *Smoothing results of Step 4*

Known at this stage: all of the above and ...

radial distribution of profile camber (estimate)

radial distribution of pitch (estimate)

The results of the three-dimensional panel code are generally not smooth and feature singularities at the hub and tip of the propeller. The human designer deletes 'stray' points (point-to-point oscillations) and specifies values at hub and tip based on experience.

6. *Final hydrodynamic analysis*

Known at this stage: all of the above (updated)

The propeller is analysed in all operating conditions using a lifting-surface analysis program and taking into account the complete wake distribution. The output can be broadly described as the cavitation and vibrational characteristics of the propeller. The work sometimes involves the inspection of plots by the designer. Other checks are already automated. Based on his 'experience' (sometimes resembling a trial-and-error process), the designer modifies the geometry (foil length, skew, camber, pitch, profile

form and even, as a last resort, diameter). However, the previous steps are not repeated and this step can be treated as a self-contained module.

7. *Check against classification society rules*

Known at this stage: all of the above (updated)

A finite-element analysis is used to calculate the strength of the propeller under the pressure loading. The von-Mises stress criterion is plotted and inspected. As the analysis is still limited to a radially averaged inflow, a safety margin is added to account for the real inflow. In most cases, there is no problem. But if the stress is too high in some region (usually the trailing edge), the geometry is adjusted and Step 6 is repeated. The possible geometry modifications at this stage are minor and local; they have no strong influence on the hydrodynamics and therefore one or two iterations usually suffice to satisfy the strength requirements.

2.7 Propeller-induced pressures

Due to the finite number of blades the pressure field of the propeller is unsteady if taken at a fixed point on the hull. The associated forces induce vibrations and noise. An upper limit for the maximum pressure amplitude that arises on the stern (usually directly above the propeller) is often part of the contract between shipyard and owner.

For many classes of ships the dominant source for unsteady hull pressures is the cavitation on the propeller-blades. The effect of cavitation in computations of propeller-induced pressures is usually modelled by a stationary point source positioned in the propeller plane. To assure similarity with the propeller cavitation, the source must be given an appropriate volume amplitude, a frequency of oscillation, and a suitable position in the propeller plane specified by a radius and an angle. As the propeller frequency is rather high, the dominant term in the Bernoulli equation is the time-derivative term. If mainly fluctuating forces from propeller-induced hull pressures are of interest, the pressure is therefore usually sufficiently well approximated by the term $-\rho\phi_t$, where ϕ denotes the potential on the hull due to the perturbations from the propeller.

If pressures and forces induced by a fluctuating source on solid boundaries are to be considered, the point source may be positioned underneath a flat plate to arrive at the simplest problem of that kind. The kinematic boundary condition on the plate is ensured via an image source of the same sign at the opposite side of the plate. For the pressure field on a real ship, this model is too coarse, as a real ship aftbody does not look like a flat plate and the influence of the free surface is neglected. Potential theory is still sufficient to solve the problem of a source near a hull of arbitrary shape with the free surface present. A panel method (BEM) easily represents the hull, but the free surface requires special treatment. The high frequency of propeller rpm again allows a simplification of the treatment of the free surface. It is sufficient to specify then:

$$\phi(x, y, z = \zeta, t) = 0$$

at the free surface $z = \zeta$. If the free surface is considered plane ($\zeta = 0$), $\phi = 0$ can be achieved by creating a hull image above the free surface and changing the sign for the singularities on the image panels. An image for the source that

represents the cavity (again of opposite sign in strength) has to be introduced as well. The free surface can be considered in good approximation as a plane for low Froude numbers, such as typically encountered for tankers and bulkers, but it is questionable for moderate and high Froude numbers. A pronounced stern wave will have a significant effect on the wetted areas at the stern.

The main problem of the above procedure is the reliability of calculated cavity volumes.

Resistance and propulsion

3.1 Resistance and propulsion concepts

3.1.1 Interaction between ship and propeller

Any propulsion system interacts with the ship hull. The flow field is changed by the (usually upstream located) hull. The propulsion system changes, in turn, the flow field at the ship hull. However, traditionally naval architects have considered propeller and ship separately and introduced special efficiencies and factors to account for the effects of interaction. While this decomposition is seen by many as an important aid in structuring the complex problems of ship hydrodynamics, it also hinders a system approach in design and can confuse as much as it can help. Since it is still the backbone of our experimental procedures and ingrained in generations of naval architects, the most important concepts and quantities are covered here. The hope is, however, that CFD will in future allow a more comprehensive optimization of the ship interacting with the propeller as a whole system.

The general definition ‘power = force · speed’ yields the effective power

$$P_E = R_T \cdot V_s$$

R_T is the total calm-water resistance of the ship excluding resistance of appendages related to the propulsive organs. Sometimes the rudder is also excluded and treated as part of the propulsion system. (This gives a glimpse of the conceptual confusion likely to follow from different conventions concerning the decomposition. Remember that in the end the installed power is to be minimized. Then ‘accounting’ conventions for individual factors do not matter. What is lost in one factor will be gained in another.) V_s is the ship speed. P_E is the power we would have to use to tow the ship without propulsive system.

Following the same general definition of power, we can also define a power formed by the propeller thrust and the speed of advance of the propeller, the so-called thrust power:

$$P_T = T \cdot V_A$$

The thrust T measured in a propulsion test is higher than the resistance R_T measured in a resistance test (without propeller). So the propeller induces an additional resistance:

1. The propeller increases the flow velocities in the aftbody of the ship which increases frictional resistance.
2. The propeller decreases the pressure in the aftbody, thus increasing the inviscid resistance.

The second mechanism dominates for usual propeller arrangements. The thrust deduction fraction t couples thrust and resistance:

$$t = 1 - \frac{R_T}{T} \quad \text{or} \quad T(1 - t) = R_T$$

t is usually assumed to be the same for model and ship, although the friction component introduces a certain scale effect. Empirical formulae for t can be found in Schneekluth and Bertram (1998), but are all plagued by large margins of uncertainty.

The propeller inflow, i.e. the speed of advance of the propeller V_A , is generally slower than the ship speed due to the ship's wake. The wake is usually decomposed into three components:

- *Friction wake*

Due to viscosity, the flow velocity relative to the ship hull is slowed down in the boundary layer, leading in regions of high curvature (especially in the aftbody) to flow separation.

- *Potential wake*

In an ideal fluid without viscosity and free surface, the flow velocity at the stern resembles the flow velocity at the bow, featuring lower velocities with a stagnation point.

- *Wave wake*

The steady wave system of the ship changes locally the flow as a result of the orbital velocity under the waves. A wave crest above the propeller increases the wake fraction, a wave trough decreases it.

For usual single-screw ships, the frictional wake dominates. Wave wake is only significant for $F_n > 0.3$. The measured wake fraction in model tests is larger than in full scale as boundary layer and flow separation are relatively larger in model scale. Traditionally, correction formulae try to consider this overprediction, but the influence of separation can only be estimated and this introduces a significant error margin. So far CFD also largely failed to reproduce the wake even in model scale probably due to insufficient turbulence modelling. The errors in predicting the required power remain nevertheless small, as the energy loss due to the wake is partially recovered by the propeller. However, the errors in predicting the wake propagate completely when computing optimum propeller rpm and pitch.

The wake behind the ship without propeller is called the nominal wake. The propeller action accelerates the flow field by typically 5–20%. The wake behind the ship with operating propeller is called the effective wake. The wake distribution is either measured by laser-Doppler velocimetry or computed by CFD. While CFD is not yet capable of reproducing the wake with sufficient accuracy, the integral of the wake over the propeller plane, the wake fraction w , is predicted well. The wake fraction is defined as:

$$w = 1 - \frac{V_A}{V_s}$$

Schneekluth and Bertram (1998) give several empirical formulae to estimate w in simple design approaches. All these formulae consider only a few main parameters, but actually the shape of the ship influences the wake considerably. Other important parameter like propeller diameter and propeller clearance are also not explicitly represented in these simple design formulae.

The ratio of the effective power to the thrust power is called the hull efficiency:

$$\eta_H = \frac{P_E}{P_T} = \frac{R_T \cdot V_s}{T \cdot V_A} = \frac{1 - t}{1 - w}$$

The hull efficiency can thus be expressed solely by thrust deduction factor t and wake fraction w . η_H can be less or greater than 1. It is thus not really an efficiency which by definition cannot be greater than 100%.

The power delivered at the propeller can be expressed by the torque and the rpm:

$$P_D = 2\pi \cdot n \cdot Q$$

This power is less than the 'brake power' directly at the ship engine P_B due to losses in shaft and bearings. These losses are comprehensively expressed in the shafting efficiency η_S : $P_D = \eta_S \cdot P_B$. The ship hydrodynamicist is not concerned with P_B and can consider P_D as the input power to all further considerations of optimizing the ship hydrodynamics. We use here a simplified definition for the shafting efficiency. Usually marine engineers decompose η_S into a shafting efficiency that accounts for the losses in the shafting only and an additional mechanical efficiency. For the ship hydrodynamicist it suffices to know that the power losses between engine and delivered power are typically 1.5–2%.

The losses from delivered power P_D to thrust power P_T are expressed in the (propeller) efficiency behind ship η_B : $P_T = \eta_B \cdot P_D$.

The open-water characteristics of the propeller are relatively easy to measure and compute. The open-water efficiency η_0 of the propeller is, however, different to η_B . Theoretically, the relative rotative efficiency η_R accounts for the differences between the open-water test and the inhomogeneous three-dimensional propeller inflow encountered in propulsion conditions: $\eta_B = \eta_R \cdot \eta_0$. In reality, the propeller efficiency behind the ship cannot be measured and all effects not included in the hull efficiency, i.e. wake and thrust deduction fraction, are included in η_R . η_R again is not truly an efficiency. Typical values for single-screw ships range from 1.02 to 1.06. Schneekluth and Bertram (1998) give again simple empirical formulae for design purposes.

The various powers and efficiencies can be expressed as follows:

$$P_B > P_D > P_T > P_E$$

$$\begin{aligned} P_E &= \eta_H \cdot P_T = \eta_H \cdot \eta_B \cdot P_D = \eta_H \cdot \eta_0 \cdot \eta_R \cdot P_D = \eta_H \cdot \eta_0 \cdot \eta_R \cdot \eta_S \cdot P_B \\ &= \eta_D \cdot \eta_S \cdot P_B \end{aligned}$$

The propulsive efficiency η_D collectively expresses the hydrodynamic efficiencies: $\eta_D = \eta_H \cdot \eta_0 \cdot \eta_R$. Schneekluth and Bertram (1998) again give simple design estimates for η_D .

3.1.2 Decomposition of resistance

As the resistance of a full-scale ship cannot be measured directly, our knowledge about the resistance of ships comes from model tests. The measured calm-water resistance is usually decomposed into various components, although all these components usually interact and most of them cannot be measured individually. The concept of resistance decomposition helps in designing the hull form as the designer can focus on how to influence individual resistance components. Larsson and Baba (1996) give a comprehensive overview of modern methods of resistance decomposition (Fig. 3.1).

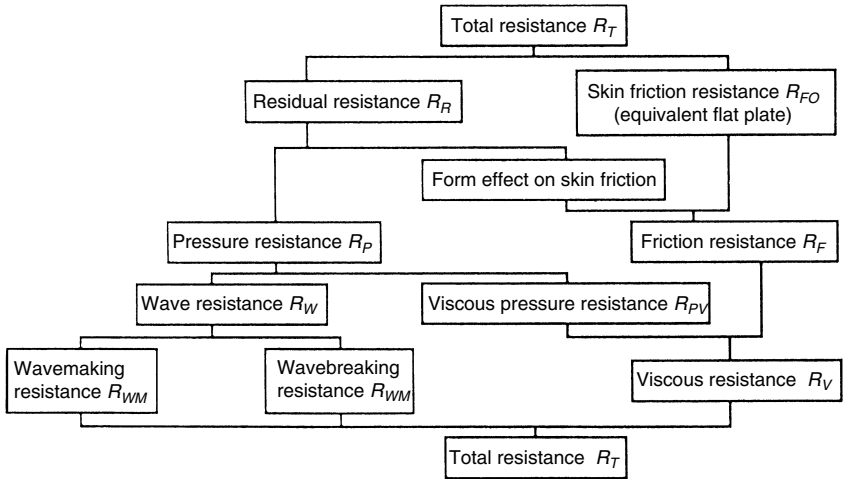


Figure 3.1 Resistance decomposition

The total calm-water resistance of a new ship hull can be decomposed into:

- *Friction resistance*

Due to viscosity, directly at the ship hull water particles ‘cling’ to the surface and move with ship speed. A short distance away from the ship, the water particles already have the velocity of an outer, quasi-inviscid flow. The region between the ship surface and the outer flow forms the boundary layer. In the aftbody of a container ship with $R_n \approx 10^9$, the boundary layer thickness may be 1 m. The rapid velocity changes in normal direction in the boundary layer induce high shear stresses. The integral of the shear stresses over the wetted surface yield the friction resistance.

- *Viscous pressure resistance*

A deeply submerged model of a ship will have no wave resistance, but its resistance will be higher than just the frictional resistance. The form of the ship induces a local flow field with velocities that are sometimes higher and sometimes lower than the average velocity. The average of the resulting shear stresses is then higher. Also, energy losses in the boundary layer, vortices and flow separation prevent an increase to stagnation pressure in the aftbody as predicted in an ideal fluid theory. Full ship forms have a higher viscous pressure resistance than slender ship forms.

- *Wave resistance*

The ship creates a typical wave system which contributes to the total resistance. In the literature, the wave system is often (rather artificially) decomposed into a primary and a secondary wave system:

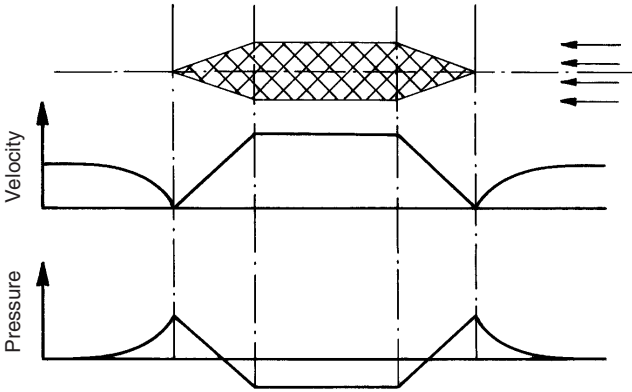


Figure 3.2 'Primary' wave system

1. *Primary wave system (Fig. 3.2)*

In an ideal fluid with no viscosity, a deeply submerged body would have zero resistance (D'Alembert's paradoxon). The flow would be slower at both ends of the body and faster in the middle. Correspondingly at each end the pressure will be higher than average, reaching at one point stagnation pressure, and the pressure in the middle will be lower than average. Now imagine a body consisting of the ship hull below the calm-water surface and its mirror image at the calm-water surface (Fig. 3.3). This double body would create a certain pressure distribution at the symmetry plane (calm-water surface) in an infinite ideal fluid. Following Bernoulli's equation, we could express a corresponding surface elevation (wave height) distribution for this pressure distribution, yielding wave crests at the ship ends and a long wave trough along the middle. This is called the primary wave system. The shape of the primary wave system is speed independent, e.g. the locations of maxima, minima, and zero crossings are not affected by the speed. The vertical scale (wave height) depends quadratically on the speed.

2. *Secondary wave system (Fig. 3.4)*

At the free surface, a typical wave pattern is produced and radiated downstream. Even if we assume an ideal fluid with no viscosity, this wave pattern will result in a resistance. The wave pattern consists of transverse and divergent waves. In deep water, the wave pattern is limited to a wedge-shaped region with a half-angle of 19.5° . This angle is independent of the actual shape of the ship. On shallow water, the half-angle widens to 90° (for depth Froude number $F_{nh} = 1.0$) and then becomes more and more narrow for supercritical speeds above $F_{nh} = 1$. The ship

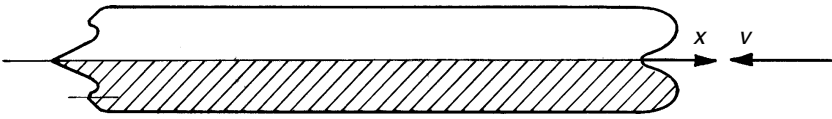


Figure 3.3 Double-body flow

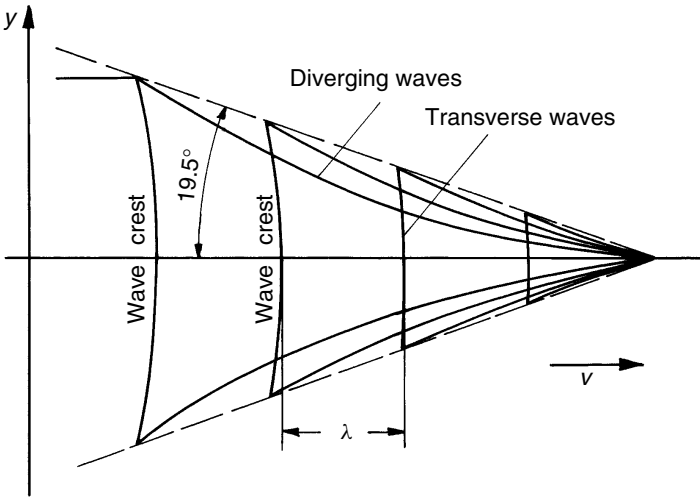


Figure 3.4 'Secondary' wave system

produces various wave patterns which interfere with each other. The main wave patterns are created where strong changes in the geometry near the water surface occur, i.e. at the bulbous bow, the bow, the forward shoulder, the aft shoulder, and the stern. The wave length λ depends quadratically on the ship speed. Unfavourable Froude numbers with mutual reinforcement between major wave systems, e.g. bow and stern waves, should be avoided. This makes, e.g., $F_n = 0.4$ an unfavourable Froude number. The interference effects result in a wave resistance curve with humps and hollows. If the wave resistance coefficient is considered, i.e. the wave resistance made non-dimensional by an expression involving the square of the speed, the humps and hollows become very pronounced.

In reality, the problem is more complex:

- The steepness of waves is limited. The pressure in the 'primary wave system' changes rapidly at the ship ends enforcing unrealistically steep waves. In reality, waves break here and change the subsequent 'secondary wave pattern'. At Froude numbers around 0.25 usually considerable wavebreaking starts, making this Froude number in reality often unfavourable although many textbooks recommend it as favourable based on the above interference argument for the 'secondary wave pattern'.

- The free surface results also in a dynamic trim and sinkage. This also changes the wave pattern. Even if the double-body flow around the dynamically trimmed and sunk ship is computed, this is not really the ship acting on the fluid, as the actually wetted surface (wave profile) changes the hull. The double-body flow model breaks down completely, if a transom stern is submerged, but dry at the ship speed. This is the case for many modern ship hulls.

The wave resistance cannot be properly estimated by simple design formulae. It is usually determined in model tests. Although efforts to compute the wave resistance by theoretical methods date back more than 100 years, the problem is still not completely solved satisfactorily. The beginning of computational methods is usually seen with the work of the Australian mathematician Michell who in 1898 proposed an integral expression to compute the wave resistance. Today, boundary element methods have become a standard tool to compute the ‘wave resistance problem’, but the accurate prediction of the wave resistance came only close to a satisfactory solution by the end of the 1990s. Even then, problems remained with breaking waves and the fundamental dilemma that in reality ship resistance exists only as a whole quantity. Its separation into components is merely a hypothesis to facilitate analysis, but the theoretically cleanly divided resistance components interact and require a comprehensive approach for a completely satisfactory treatment.

Computational methods for the analysis of the wave resistance will be discussed in detail in section 3.5.1.

3.2 Experimental approach

3.2.1 Towing tanks and experimental set-up

Despite the ever increasing importance of numerical methods for ship hydrodynamics, model tests in towing tanks are still seen as an essential part in the design of a ship to predict (or validate) the power requirements in calm water which form a fundamental part of each contract between shipowner and shipyard.

We owe the modern methodology of predicting a ship’s resistance to William Froude, who presented his approach in 1874 to the predecessor of the RINA in England. His hypothesis was that the ship resistance is divisible into frictional and wavemaking resistance, with the wavemaking resistance following his ‘law of comparison’ (Froude similarity). This ingenious concept allowed Froude to show, for the first time, how the resistance of a full-scale ship may be determined by testing scale models. His success motivated building the first model basin in 1879 in Torquay, England. Soon further model basins followed in Europe and the USA.

Tests are usually performed in towing tanks, where the water is still and the model is towed by a carriage. (Alternatively, tests can also be performed in circulating tanks, where the model is still and the water moves.) The carriage in a towing tank keeps its speed with high precision. The model is kept on

course by special wires at the ship ends. Usually, models are free to trim and sink. After the initial acceleration, some time has to pass before a stationary state is reached. Then the remaining measuring time is determined by the remaining towing tank distance and the deceleration time of the carriage. Therefore, towing tanks are usually several hundred metres long to allow sufficient measuring time (in most cases).

The model size is determined by a number of boundary conditions:

- The model should be as large as possible to minimize viscosity scale effects, especially concerning laminar/turbulent flow and flow separation.
- The model should be small enough to avoid strength problems (both internal strength of the model and loads on the test carriage).
- The model should be small enough such that the corresponding test speed can be achieved by the carriage.
- The model should be small enough to avoid noticeable effects of restricted water in the test basin.

This leads to a bandwidth of acceptable model sizes. Typically models for resistance and propulsion tests have a size $4\text{ m} \leq L_m \leq 10\text{ m}$. Model scales range between $15 \leq \lambda \leq 45$. In practice, often the selected stock propeller decides the exact model scale.

Tests are performed keeping Froude similarity, i.e. Froude number of model and full scale are the same. The Reynolds numbers differ typically by two orders of magnitude. The scale effect (error of not keeping the Reynolds similarity) is then compensated by empirical corrections.

The models are made of special paraffin wax or special tropical wood that hardly changes volume and shape with time or temperature. Wax models are cheaper, but less robust. Wooden models receive a smooth finish of paint. Yellow is the preferred colour for regular models as this colour contrasts nicely with the (blackish) water which is important for visual observations, e.g., of the wave profile. For icebreakers, often for similar purposes red is the preferred colour as it appears to be a good compromise for contrasts of water and ice.

Models operate at considerably lower Reynolds numbers. (Typically for models $R_n \approx 10^7$ and for full-scale ships $R_n \approx 10^9$.) This means that in the model the transition from laminar to turbulent flow occurs relatively further aft. As a consequence, the resistance would be more difficult to scale. Therefore, the model is equipped with artificial turbulence stimulators (sand strip, studs, or trip wire) in the forebody. One assumes that the transition from laminar to turbulent flow occurs at a length corresponding to $R_n = 0.5 \cdot 10^6$ from the stem. In practice, often the turbulence stimulators are located somewhat further aft. Then the reduced resistance due to the longer laminar flow compensates (at least partially) the additional resistance of the turbulence stimulators.

3.2.2 Resistance test

Resistance tests determine the resistance of the ship without propeller (and often also without other appendages; sometimes resistance tests are performed

for both the ‘naked’ hull and the hull with appendages). Propulsion tests are performed with an operating propeller and other relevant appendages. A problem is that the forces on appendages are largely driven by viscosity effects with small to negligible gravity effects. As Reynolds similarity is violated, the forces cannot be scaled easily to full scale. For ships with large and unusual appendages, the margins of errors in prediction are thus much larger than for usual hulls where experience helps in making appropriate corrections.

The model is towed by weights and wires (Fig. 3.5). The main towing force comes from the main weight G_1 . The weight G_2 is used for fine tuning:

$$R_T = G_1 \pm G_2 \sin \alpha$$

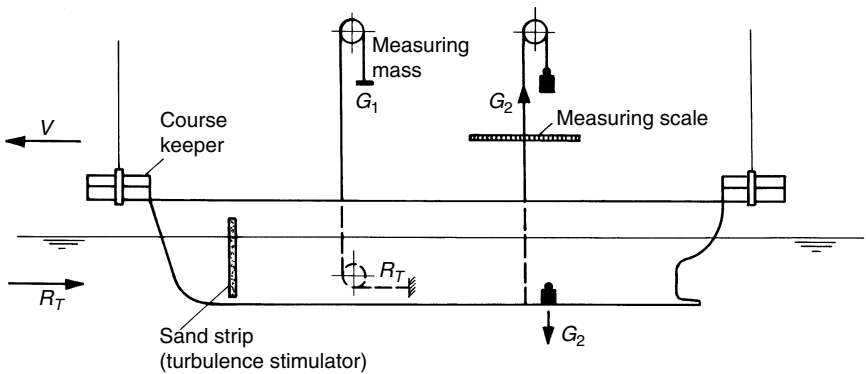


Figure 3.5 Experimental set-up for resistance test

The sign is positive if the vertical wire moves aft. The angle α is determined indirectly by measuring the distance on the length scale. Alternatively, modern experimental techniques also use strain gauges as these do not tend to oscillate as the wire-weight systems.

The model test gives the resistance (and power) for towing tank conditions:

- (usually) sufficiently deep water
- no seaway
- no wind
- fresh water at room temperature

This model resistance has to be converted for a prediction of the full-scale ship. To do this conversion several methods are outlined in the following chapters, namely:

- Method ITTC 1957
- Method of Hughes/Prohaska
- Method ITTC 1978
- Geosim method of Telfer

The most important of these methods in practice is the method ITTC 1978.

Resistance tests are also used to measure the nominal wake, i.e. the wake of the ship without propeller. Measurements of the nominal wake are usually

limited to the propeller plane. The local velocities were traditionally measured by pitot tubes. Currently, Laser-Doppler velocimetry also allows non-intrusive measurements of the flow field. The results are usually displayed as contour lines of the longitudinal component of the velocity (Fig. 3.6). These data play an important role in the design of a propeller. For optimizing the propeller pitch as a function of the radial distance from the hub, the wake fraction is computed as a function of this radial distance by integrating the wake in the circumferential direction:

$$w(r) = \frac{1}{2\pi} \int 2\pi_0 w(r, \phi) d\phi$$

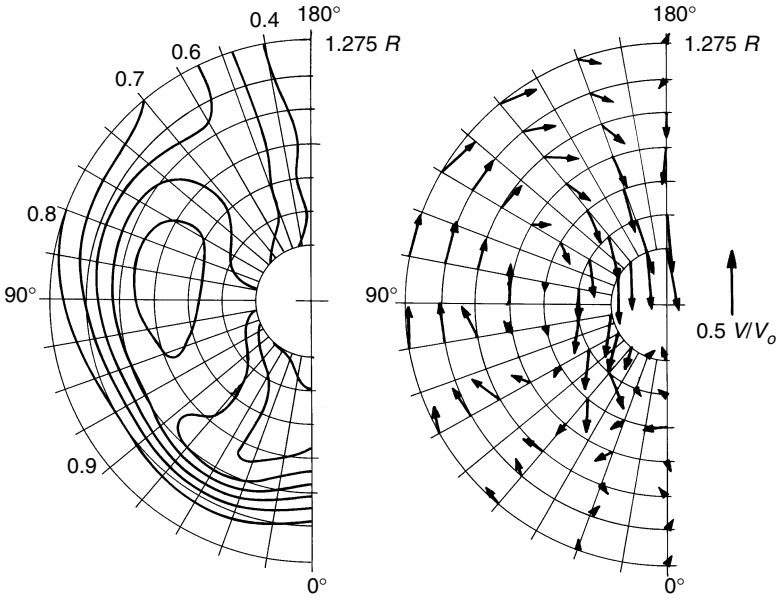


Figure 3.6 Results of wake measurement

The wake field is also used in evaluating propeller-induced vibrations.

3.2.3 Method ITTC 1957

The resistance of the hull is decomposed as:

$$R_T = R_F + R_R$$

R_F is the frictional resistance, R_R the residual resistance. Usually the resistance forces are expressed as non-dimensional coefficients of the form:

$$c_i = \frac{R_i}{\frac{1}{2} \rho V_s^2 S}$$

S is the wetted surface in calm water, V_s the ship speed. The resistance coefficient of the ship is then determined as:

$$c_{Ts} = c_{Fs} + c_R + c_A = c_{Fs} + (c_{Tm} - c_{Fm}) + c_A$$

The index s again denotes values for the full-scale ship, the index m values for the model. c_R is assumed to be independent of model scale, i.e. c_R is the same for model and full scale. The model test serves primarily to determine c_R . The procedure is as follows:

1. Determine the total resistance coefficient in the model test:

$$c_{Tm} = \frac{R_{Tm}}{\frac{1}{2}\rho_m \cdot V_m^2 \cdot S_m}$$

2. Determine the residual resistance, same for model and ship:

$$c_R = c_{Tm} - c_{Fm}$$

3. Determine the total resistance coefficient for the ship:

$$c_{Ts} = c_R + c_{Fs} + c_A$$

4. Determine the total resistance for the ship:

$$R_{Ts} = c_{Ts} \cdot \frac{1}{2}\rho_s V_s^2 S_s$$

The frictional coefficients c_F are determined by the ITTC 1957 formula:

$$c_F = \frac{0.075}{(\log_{10} R_n - 2)^2}$$

This formula already contains a global form effect increasing the value of c_F by 12% compared to the value for flat plates (Hughes formula).

Historically c_A was a roughness allowance coefficient which considered that the model was smooth while the full-scale ship was rough, especially when ship hulls were still riveted. However, with the advent of welded ships c_A sometimes became negative for fast and big ships. Therefore, c_A is more appropriately termed the correlation coefficient. c_A encompasses collectively all corrections, including roughness allowance, but also particularities of the measuring device of the model basin, errors in the model–ship correlation line and the method. Model basins use c_A not as a constant, but as a function of the ship size, based on experience. The correlation coefficient makes predictions from various model basins difficult to compare and may in fact be abused to derive overly optimistic speed prediction to please customers.

Formulae for c_A differ between various model basins and shipyards. Examples are Table 3.1 and:

$$c_A = 0.35 \cdot 10^{-3} - 2 \cdot L_{pp} \cdot 10^{-6}$$

$$c_A = 0.11 \cdot (R_n \cdot 10^{-9} - 2.1 - a)^2 - a + 0.62 \quad \text{with}$$

$$a = \max(0.6, \min(C_B, 0.8))$$

Table 3.1 Recommended values for C_A

L_{pp} (m)	c_A
50–150	0.00035–0.0004
150–210	0.0002
210–260	0.0001
260–300	0
300–350	–0.0001
350–4000	–0.00025

3.2.4 Method of Hughes–Prohaska

This approach decomposes the total resistance (coefficient) as follows:

$$c_T = (1 + k) \cdot c_{F0} + c_w$$

Both form factor $(1 + k)$ and wave resistance coefficient c_w are assumed to be the same for model and full scale, i.e. independent of R_n . The model test serves primarily to determine the wave resistance coefficient. The procedure is as follows:

1. Determine the total resistance coefficient in the model test as for the ITTC 1957 method:

$$c_{Tm} = \frac{R_{Tm}}{\frac{1}{2} \rho_m \cdot V_m^2 \cdot S_m}$$

2. Determine the wave resistance coefficient, same for model and ship:

$$c_w = c_{Tm} - c_{F0m} \cdot (1 + k)$$

3. Determine the total resistance coefficient for the ship:

$$c_{Ts} = c_w + c_{F0s} \cdot (1 + k) + c_A$$

4. Determine the total resistance for the ship:

$$R_{Ts} = c_{Ts} \cdot \frac{1}{2} \rho_s V_s^2 S_s$$

The frictional coefficients c_{F0} for flat plates are determined by Hughes' formula:

$$c_{F0} = \frac{0.067}{(\log_{10} R_n - 2)^2}$$

The correlation coefficient c_A differs fundamentally from the correlation coefficient for the ITTC 1957 method. Here c_A does not have to compensate for scaling errors of the viscous pressure resistance. ITTC recommends universally $c_A = 0.0004$.

The Hughes–Prohaska method is a form factor method. The form factor $(1 + k)$ is assumed to be independent of F_n and R_n and the same for model and ship. The form factor is determined by assuming:

$$\frac{c_T}{c_{F0}} = (1 + k) + \alpha \frac{F_n^4}{c_{F0}}$$

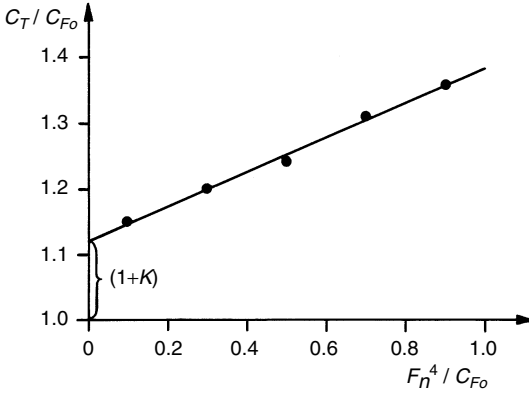


Figure 3.7 Extrapolation of form factor

Model test results for several Froude numbers (e.g. between 0.12 and 0.24) serve to determine α in a regression analysis (Fig. 3.7).

3.2.5 Method of ITTC 1978

This approach is a modification of the Hughes–Prohaska method. It is generally more accurate and also considers the air resistance. The total resistance (coefficient) is again written in a form factor approach:

$$C_{TS} = (1 + k)C_{Fs} + c_w + c_A + c_{AA}$$

c_w is the wave resistance coefficient, assumed to be the same for model and ship, i.e. independent of R_n . C_{Fs} is the frictional coefficient, following the ITTC 1957 formula. c_A is the correlation coefficient which depends on the hull roughness:

$$c_A \cdot 10^3 = 105 \cdot \sqrt[3]{\frac{k_s}{L_{oss}}} - 0.64$$

k_s is the roughness of the hull, L_{oss} is the wetted length of the full-scale ship. For new ships, a typical value is $k_s/L_{oss} = 10^{-6}$, i.e. $c_A = 0.00041$.

c_{AA} considers globally the air resistance as follows:

$$c_{AA} = 0.001 \cdot \frac{A_T}{S}$$

A_T is the frontal area of the ship above the waterline, S the wetted surface.

The model test serves primarily to determine the wave resistance coefficient. The procedure is similar to the procedure for Hughes–Prohaska, but the frictional coefficient is determined following the ITTC 1957 formula instead of Hughes' formula. The form factor is also determined slightly differently:

$$\frac{C_T}{C_F} = (1 + k) + \alpha \cdot \frac{F_n^n}{C_F}$$

Both n and α are determined in a regression analysis.

3.2.6 Geosim method of Telfer

Telfer proposed in 1927 to perform model tests with families of models which are *geometrically similar*, but have different model scale. This means that tests are performed at the same Froude number, but different Reynolds numbers. The curve for the total resistance as a function of the Reynolds number is then used to extrapolate to the full-scale Reynolds number.

Telfer plotted the total resistance coefficient over $\log R_n^{-1/3}$. For each model, a curve of the resistance is obtained as a function of F_n . Points of same Froude number for various model scales are connected by a straight line which is easily extrapolated to full scale.

Telfer's method is regarded as the most accurate of the discussed prediction methods and avoids theoretically questionable decomposition of the total resistance. However, it is used only occasionally for research purposes as the costs for the model tests are too high for practical purposes.

3.2.7 Propulsion test

Propulsion tests are performed to determine the power requirements, but also to supply wake and thrust deduction, and other input data (such as the wake field in the propeller plane) for the propeller design. The ship model is then equipped with a nearly optimum propeller selected from a large stock of propellers, the so-called stock propeller. The actual optimum propeller can only be designed after the propulsion test. The model is equipped with a propulsive drive, typically a small electro-motor (Fig. 3.8).

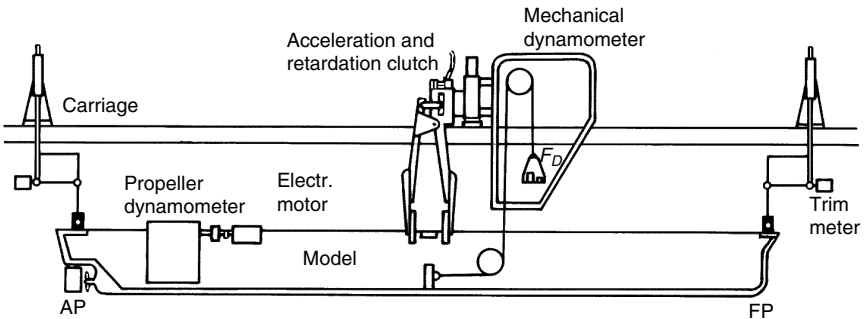


Figure 3.8 Experimental set-up for propulsion test

The tests are again performed for Froude similarity. The total resistance coefficient is then higher than for the full-scale ship, since the frictional resistance coefficient decreases with increasing Reynolds number. This effect is compensated by applying a 'friction deduction' force. This compensating force is determined as follows (see section 3.2.5):

$$F_D = \frac{1}{2} \rho \cdot V_m^2 \cdot S_m \cdot ((1 + k)(C_{Fm} - C_{Fs}) - C_A - C_{AA})$$

The propeller then has to produce a thrust that has to compensate the total resistance R_T minus the compensating force F_D . The propulsion test is conducted with constant speed. The rpm of the propeller is adjusted such that the model

is in self-propelled equilibrium. Usually the speed of the towing tank carriage is kept constant and the rpm of the propeller varied until an equilibrium is reached. A propeller dynamometer then measures thrust and torque of the propeller as a function of speed. In addition, dynamical trim and sinkage of the model are recorded. The measured values can be transformed from model scale to full scale by the similarity laws: speed $V_s = \sqrt{\lambda} \cdot V_m$, rpm $n_s = n_m / \sqrt{\lambda}$, thrust $T_s = T_m \cdot (\rho_s / \rho_m) \cdot \lambda^3$, torque $Q_s = Q_m \cdot (\rho_s / \rho_m) \cdot \lambda^4$. A problem is that the propeller inflow is not geometrically similar for model and full scale due to the different Reynolds number. Thus the wake fraction is also different. Also, the propeller rpm should be corrected to be appropriate for the higher Reynolds number of the full-scale ship.

The scale effects on the wake fraction are attempted to be compensated by the empirical formula:

$$w_s = w_m \cdot \frac{C_{Fs}}{C_{Fm}} + (t + 0.04) \cdot \left(1 - \frac{C_{Fs}}{C_{Fm}}\right)$$

t is the thrust deduction coefficient. t is assumed to be the same for model and full scale.

The evaluation of the propulsion test requires the resistance characteristics and the open-water characteristics of the stock propeller. There are two approaches:

1. ‘Thrust identity’ approach

The propeller produces the same thrust in a wake field of wake fraction w as in open-water with speed $V_s(1 - w)$ for the same rpm, fluid properties etc.

2. ‘Torque identity’ approach

The propeller produces the same torque in a wake field of wake fraction w as in open-water with speed $V_s(1 - w)$ for the same rpm, fluid properties etc.

ITTC standard is the ‘thrust identity’ approach. It will be covered in more detail in the next chapter on the ITTC 1978 performance prediction method.

The results of propulsion tests are usually given in diagrams as shown in Fig. 3.9. Delivered power and propeller rpm are plotted over speed. The results of the propulsion test prediction are validated in the sea trial of the ship introducing necessary corrections for wind, seaway, and shallow water. The diagrams contain not only the full-load design condition at trial speed, but also ballast conditions and service speed conditions. Service conditions feature higher resistance reflecting the reality of the ship after some years of service: increased hull roughness due to fouling and corrosion, added resistance in seaway and wind.

3.2.8 ITTC 1978 performance prediction method

The ITTC 1978 performance prediction method (IPPM78) has become a widely accepted procedure to evaluate model tests. It combines various aspects of resistance, propulsion, and open-water tests. These are comprehensively reviewed here. Further details may be found in section 3.2.5, section 3.2.7 and section 2.5, Chapter 2. The IPPM78 assumes that the following tests have

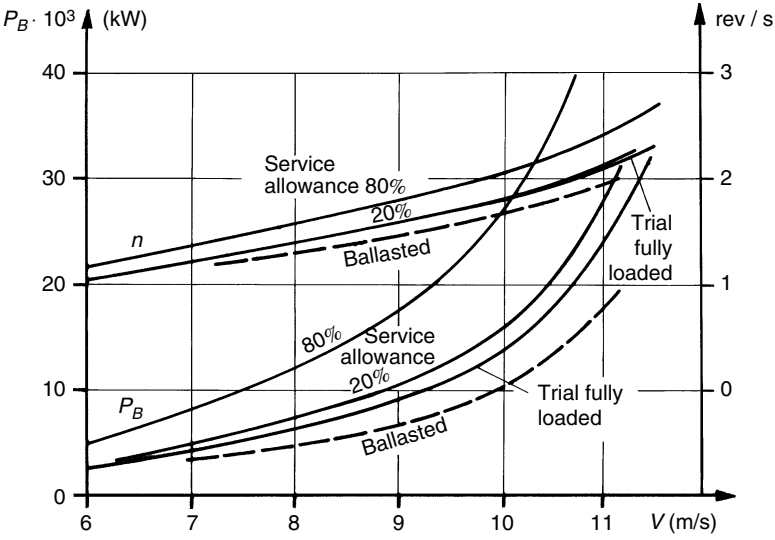


Figure 3.9 Result of propulsion test

been performed yielding the corresponding results:

resistance test $R_{Tm} = f(V_m)$

open-water test $T_m = f(V_{Am}, n_m)$

$$Q_m = f(V_{Am}, n_m)$$

propulsion test $T_m = f(V_m, n_m)$

$$Q_m = f(V_m, n_m)$$

R_T is the total resistance, V the ship speed, V_A the average inflow speed to the propeller, n the propeller rpm, K_T the propeller thrust coefficient, K_Q the propeller torque coefficient. Generally, m denotes model, s full scale.

The resistance is evaluated using the ITTC 1978 method (for single-screw ships) described in section 3.2.5:

1. Determine the total resistance coefficient in the model test:

$$c_{Tm} = \frac{R_{Tm}}{\frac{1}{2} \rho_m \cdot V_m^2 \cdot S_m}$$

2. Determine the frictional resistance coefficient for the model following ITTC 1957:

$$c_{Fm} = \frac{0.075}{(\log_{10} R_{nm} - 2)^2}$$

The Reynolds number of the model is $R_{nm} = V_m L_{osm} / \nu_m$, where L_{os} is the wetted length of the model. L_{os} is the length of the overall wetted surface, i.e. usually the length from the tip of the bulbous bow to the trailing edge of the rudder.

3. Determine the wave resistance coefficient, same for model and ship:

$$c_w = c_{Tm} - (1 + k)c_{Fm}$$

The determination of the form factor $(1 + k)$ is described below.

4. Determine the total resistance coefficient for the ship:

$$c_{Ts} = c_w - (1 + k)c_{Fs} + c_A + c_{AA}$$

c_{Fs} is the frictional resistance coefficient following ITTC 1957, but for the full-scale ship. c_A is a correlation coefficient (roughness allowance). c_{AA} considers the air resistance:

$$c_A = \left(105 \sqrt[3]{\frac{k_s}{L_{oss}}} - 0.64 \right) \cdot 10^{-3}$$

k_s is the roughness ($= 1.5 \cdot 10^{-4}$ m) and L_{oss} the wetted length of the ship.

$$c_{AA} = 0.001 \frac{A_T}{S_s}$$

A_T is the frontal area of the ship above the water, S_s the wetted surface.

5. Determine the total resistance for the ship:

$$R_{Ts} = c_{Ts} \cdot \frac{1}{2} \rho_s V_s^2 S_s$$

The form factor is determined in a least square fit of α and n in the function:

$$\frac{c_{Tm}}{c_{Fm}} = (1 + k) + \alpha \cdot \frac{F_n^n}{c_{Fm}}$$

The open-water test gives the thrust coefficient K_T and the torque coefficient K_Q as functions of the advance number J :

$$K_{Tm} = \frac{T_m}{\rho_m n_m^2 D_m^4} \quad K_{Qm} = \frac{Q_m}{\rho_m n_m^2 D_m^5} \quad J = \frac{V_{Am}}{n_m D_m}$$

D_m is the propeller diameter. The model propeller characteristics are transformed to full scale (Reynolds number correction) as follows:

$$K_{Ts} = K_{Tm} + 0.3Z \frac{c}{D_s} \frac{P_s}{D_s} \cdot \Delta C_D$$

$$K_{Qs} = K_{Qm} - 0.25Z \frac{c}{D_s} \cdot \Delta C_D$$

Z is the number of propeller blades, P_s/D_s the pitch-diameter ratio, D_s the propeller diameter in full scale, c the chord length at radius $0.7D$.

$$\Delta C_D = C_{Dm} - C_{Ds}$$

This is the change in the profile resistance coefficient of the propeller blades. These are computed as:

$$C_{Dm} = 2 \left(1 + 2 \frac{t_m}{c_m} \right) \left(\frac{0.044}{R_{nco}^{1/6}} - \frac{5}{R_{nco}^{2/3}} \right)$$

t is the maximum blade thickness, c the maximum chord length. The Reynolds number $R_{nco} = V_{co}c_m/v_m$ at $0.7D_m$, i.e. $V_{co} = \sqrt{V_{Am}^2 + (0.7\pi n_m D_m)^2}$.

$$C_{Ds} = 2 \left(1 + 2 \frac{t_s}{c_s} \right) \left(1.89 + 1.62 \log_{10} \frac{c_s}{k_p} \right)^{-2.5}$$

k_p is the propeller blade roughness, taken as $3 \cdot 10^{-5}$ if not otherwise known.

The evaluation of the propulsion test requires the resistance and open-water characteristics. The open-water characteristics are denoted here by the index fv . The results of the propulsion test are denoted by pv :

$$K_{Tm,pv} = \frac{T_m}{\rho_m \cdot D_m^4 \cdot n_m^2}$$

$$K_{Qm,pv} = \frac{Q_m}{\rho_m \cdot D_m^5 \cdot n_m^2}$$

Thrust identity is assumed, i.e. $K_{Tm,pv} = K_{Tm,fv}$. Then the open-water diagram can be used to determine the advance number J_m . This in turn yields the wake fraction of the model:

$$w_m = 1 - \frac{J_m D_m n_m}{V_m}$$

The thrust deduction fraction is:

$$t = 1 + \frac{F_D - R_{Tm}}{T_m}$$

F_D is the force compensating for the difference in resistance similarity between model and full-scale ship:

$$F_D = \frac{1}{2} \rho \cdot V_m^2 \cdot S \cdot ((1+k)(c_{Fm} - c_{Fs}) - c_A - c_{AA})$$

With known J_m the torque coefficient $K_{Qm,fv}$ can also be determined. The propeller efficiency behind the ship is then:

$$\eta_{bm} = \frac{K_{Tm,pv}}{K_{Qm,pv}} \cdot \frac{J_m}{2\pi}$$

The open-water efficiency is:

$$\eta_{0m} = \frac{K_{Tm,fv}}{K_{Qm,fv}} \cdot \frac{J_m}{2\pi}$$

This determines the relative rotative efficiency:

$$\eta_R = \frac{\eta_{bm}}{\eta_{0m}} = \frac{K_{Qm,fv}}{K_{Qm,pv}}$$

While t and η_R are assumed to be the same for ship and model, the wake fraction w has to be corrected:

$$w_s = w_m \frac{c_{Fs}}{c_{Fm}} + (t + 0.04) \left(1 - \frac{c_{Fs}}{c_{Fm}} \right)$$

A curve for the parameter K_T/J^2 as function of J is introduced in the open-water diagram for the full-scale ship. The design point is defined by:

$$\left(\frac{K_T}{J^2}\right)_s = \frac{T_s}{\rho_s \cdot D_s^2 \cdot V_{As}^2} = \frac{S_s}{2D_s^2} \cdot \frac{c_{Ts}}{(1-t)(1-w_s)^2}$$

The curve for K_T/J^2 can then be used to determine the corresponding J_s . This in turn determines the torque coefficient of the propeller behind the ship $K_{Qs} = f(J_s)$ and the open-water propeller efficiency $\eta_{0s} = f(J_s)$. The propeller rpm of the full-scale propeller is then:

$$n_s = \frac{(1-w_s) \cdot V_s}{J_s D_s}$$

The propeller torque in full scale is then:

$$Q_s = \frac{K_{Qs}}{\eta_R} \rho_s \cdot n_s^2 \cdot D_s^2$$

The propeller thrust of the full-scale ship is:

$$T_s = \left(\frac{K_T}{J^2}\right)_s \cdot J_s^2 \cdot \rho_s \cdot n_s^2 \cdot D_s^4$$

The delivered power is then:

$$P_{Ds} = Q_s \cdot 2\pi \cdot n_s$$

The total propulsion efficiency is then:

$$\eta_{Ds} = \eta_0 \cdot \eta_R \cdot \eta_{Hs}$$

3.3 Additional resistance under service conditions

The model test conditions differ in certain important points from trial and service conditions for the real ship. These include effects of

- Appendages
- Shallow water
- Wind
- Roughness
- Seaway

Empirical corrections (based on physically more or less correct assumptions) are then used to estimate these effects and to correlate measured values from one state (model or trial) to another (service). The individual additional resistance components will be briefly discussed in the following.

- *Appendages*

Model tests can be performed with geometrically properly scaled appendages. However, the flow around appendages is predominantly governed by viscous forces and would require Reynolds similarity. Subsequently, the measured forces on the appendages for Froude similarity

are not properly scaled up to the real ship. Appendages may be tested separately and often the resistance of the appendages is scaled separately and added in a prediction for the full-scale ship. Unfortunately, this procedure does not account for interaction between hull and appendages and also introduces considerable error margins. Fortunately, most ships have only a few appendages and errors in estimating their resistance can be accepted. For unconventional ships with many and complex appendages, the difficulties in estimating the resistance of the appendages properly leads to a larger margin of uncertainty for the global full-scale prediction.

Schneekluth and Bertram (1998) compile some data from shipbuilding experience: properly arranged bilge keels contribute only 1–2% to the total resistance of ships. However, trim and ship motions in seastates increase the resistance more than for ships without bilge keels. Thus, in evaluation of model tests, a much higher increase of resistance should be made for ships in ballast condition. Bow thrusters, if properly designed and located, do not significantly increase resistance. Transverse thrusters in the aftbody may increase resistance by 1–6%. Shaft brackets and bossings increase resistance by 5–12%. For twin-screw ships with long propeller shafts, the resistance increase may be more than 20%. Rudders increase resistance little ($\sim 1\%$) if in the neutral position and improve propulsion. But moderate rudder angles may increase resistance already by 2–6%.

- *Shallow water*

Shallow water increases friction resistance and usually also wave resistance. Near the critical depth Froude number $F_{nh} = V/\sqrt{gH} = 1$, where H is the water depth, the resistance is strongly increased. Figure 3.10 allows one to estimate the speed loss for weak shallow-water influence. The figure

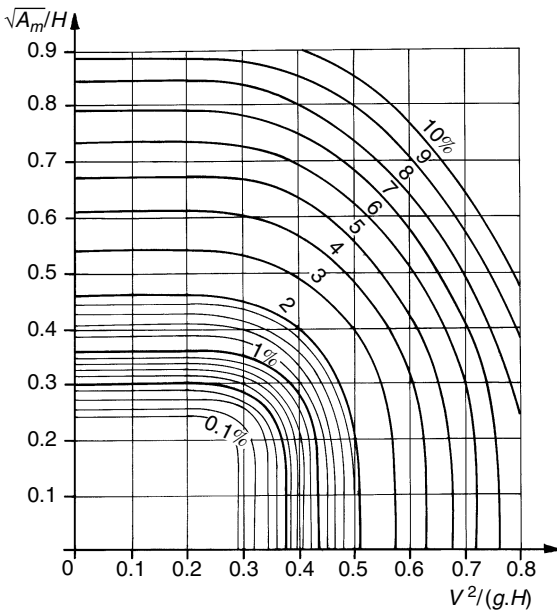


Figure 3.10 Percentage loss of speed in shallow water (Lackenby (1963))

follows Schlichting's hypothesis that the wave resistance is the same if the wave lengths of the transversal waves are the same. Similar, but more sophisticated, diagrams are still popular in practice. For strong shallow-water influence a simple correction is impossible as wavebreaking, squat and deformation of the free surface introduce complex physical interactions. In this case, only model tests or CFD may help.

In numerical simulations (CFD), the inclusion of shallow water is relatively simple. Boundary element methods based on Rankine elements use mirror images of the elements with respect to the water bottom. The image elements have the same strength as the original elements. This automatically yields zero normal velocity on the water bottom due to symmetry. The analytical inclusion of the bottom in Green function methods is more difficult, but also feasible. Field methods discretize the fluid domain to the water bottom and enforce a suitable boundary condition there. However, shallow-water flows feature often stronger non-linearities than deep-water flows making them in turn more difficult to solve numerically. Nevertheless, in future CFD may be used to convert shallow-water results to deep-water results capturing more of the actual physics and thus reducing some of the inherent uncertainties introduced by assuming, e.g., that the form factor is not affected by the water depth.

- *Wind*

Wind resistance is important for ships with large lateral areas above the water level, e.g. containerships and car ferries. Fast and unconventional ships, e.g. air-cushioned vehicles, also require the contribution of wind or air resistance. Schneekluth and Bertram (1998) give simple design estimates with empirical formulae. Usually wind tunnel tests are the preferred choice for a more accurate estimate, as they are fast and cheap to perform. CFD is not yet competitive, as grid generation is so far too time consuming and expensive for most applications. However, several prototype applications have shown the capability of CFD to compute air flow about complex ship and offshore geometries with good results. As cost for grid generation will decrease, CFD may also substitute increasingly wind tunnel tests.

- *Roughness*

The friction resistance can increase considerably for rough surfaces. For new ships, the effect of roughness is included in the ITTC line or the correlation constant. A rough hull surface (without fouling) increases the frictional resistance by up to 5%. Fouling can increase the resistance by much more. However, modern paints prevent fouling to a large extent and are also self-polishing, i.e. the paint will not become porous as did old paints in use before the 1970s. The problem of correlating roughness and resistance is insufficiently understood. Model tests try to produce a hull surface as smooth as possible. As a rule, CFD does not consider roughness at all.

- *Seaway*

The added resistance of a ship in a seaway is generally determined by computational methods and will be discussed in more detail in the chapters treating ship seakeeping. Such predictions for a certain region or route depend on the accuracy of seastate statistics which usually introduce a larger error than the actual computational simulation. Ship size is generally more important than ship shape. Schneekluth and Bertram (1998) give simple design estimates for the speed loss due to added resistance in waves.

3.4 Simple design approaches

In early design stages, the power requirements have to be estimated to judge the weight and volume requirements of the main engine and fuel. As this has to be done repeatedly in design loops, model tests are no suitable solution for reasons of time and costs. Instead, simple, largely empirical methods are employed which only require a few global design parameters. These methods are discussed in more detail by Schneekluth and Bertram (1998).

The main approaches are:

- estimate from parent ship, e.g. by admiralty or similar formulae
- systematical series, e.g. Taylor–Gertler, Series-60, SSPA
- regression analysis of many ships, e.g. Lap–Keller, Holtrop–Mennen, Hollenbach

The estimate from a parent ship may give good estimates if the parent ship is close enough (in geometrical properties and speed parameters) to the design ship. The admiralty formula is very coarse and not recommended, but an estimate based on a form factor approach is popular in practice. Here, it is usually assumed that the parameter c_w/F_n^4 and the form factor remain constant in the conversion from parent ship to design ship. Such a more or less sophisticated plus/minus conversion from a parent ship is currently the preferred choice for a quick estimate.

All of the systematical series and most of the regression analysis approaches are outdated. They often underestimate the actual resistance of modern ship hulls. It may come as a surprise that older ships were apparently better in terms of resistance. There are several explanations:

- suitability for container stowage plays a larger role in modern ships;
- modern ships often have a higher propulsive efficiency compensating partially for the higher resistance;
- more severe safety regulations, e.g. concerning stability, pose additional constraints on the hydrodynamic optimization.

Nevertheless, some of the old estimation methods are still popular as they are easy to program. Thus they are embedded in naval architectural CAD systems or more recently in design expert systems. However, they are fundamentally limited to global predictions, as they represent the hull shape by few global parameters.

3.5 CFD approaches for steady flow

3.5.1 Wave resistance computations

The wave resistance problem considers the steady motion of a ship in initially smooth water assuming an ideal fluid, i.e. especially neglecting all viscous effects. The ship will create waves at the freely deformable water surface. The computations involve far more information than the mere resistance which is of minor importance in many applications and usually computed quite inaccurately. But the expression ‘wave resistance problem’ is easier than ‘steady, inviscid straight-ahead course problem’, and thus more popular.

The work of the Australian mathematician J. H. Michell in 1898 is seen often as the birth of modern theoretical methods for ship wave resistance predictions. While Michell's theory cannot be classified as computational fluid dynamics in the modern sense, it was a milestone at its time and is still inspiring mathematicians today. Michell expressed the wave resistance of a thin wall-sided ship as:

$$R_w = \frac{4}{\pi} \rho V^2 \nu^2 \int_1^\infty \frac{\lambda^2}{\sqrt{\lambda^2 - 1}} |A(\lambda)|^2 d\lambda$$

with:

$$A(\lambda) = -i\nu\lambda \int_S e^{\nu\lambda^2 z + i\nu\lambda x} f(x, z) dz dx$$

V is the ship speed, ρ water density, $\nu = g/V^2$, g gravity acceleration, $f(x, z)$ halfwidth of ship, x longitudinal coordinate (positive forward), z vertical coordinate (from calm waterline, positive upwards), S ship surface below the calm waterline. The expression gives realistic results for very thin bodies (width/length ratio very small) for arbitrary Froude number, and for slender ships (width/length ratio and depth/length ratio very small) for high Froude numbers. Michell's theory (including all subsequent refinements) is in essence unacceptable for real ship geometries and ship speeds. However, on occasion it is still useful. An example may be the prediction of the wave resistance of a submarine near the free surface with a streamlined snorkel piercing the free surface. While CFD can discretize the main submarine, it will neglect all appendages of much smaller scale. Then Michell's theory can be applied to analyse the additional influence of the snorkel which will have a very large Froude number based on the chord length of its profile cross-section. Söding (1995) gives a Fortran routine to compute Michell's integral.

The classical methods (thin ship theories, slender-body theories) introduce simplifications which imply limitations regarding the ship's geometry. Real ship geometries are generally not thin or slender enough. The differences between computational and experimental results are consequently unacceptable. Practical applications in industry are based almost exclusively on boundary element methods. These remain the most important tools for naval architects despite the recently increased application of viscous flow tools.

These boundary element methods represent the flow as a superposition of Rankine sources and sometimes also dipoles or vortices. Classical methods using so-called Kelvin or Havelock sources fulfil automatically a crude approximation of the dynamical and kinematical free surface conditions. Kelvin sources are complicated and require great care in their numerical evaluation. Rankine sources on the other hand are quite simple. The potential of a Rankine point source is a factor divided by the distance between the point source and the considered point in the fluid domain. The factor is called the source strength. The derivative of the potential in arbitrary spatial direction gives the velocity in this direction. This mathematical operation is simple to perform for Rankine sources. Chapter 6 will discuss Rankine elements in detail.

Boundary element methods discretize surfaces into a finite number of elements and corresponding number of collocation points. A desired (linear) condition is fulfilled exactly at these collocation points by proper adjustment

of the initially unknown source strengths. One hopes/claims that between these points the boundary condition is fulfilled at least in good approximation. Laplace's equation and the decay condition (far away the ship does not disturb the flow) are automatically fulfilled. Mirror images of the panels at the bottom of the fluid domain walls may enforce a no-penetration condition there for shallow-water cases. Repeated use of mirror images at vertical canal walls can enforce in similar fashion the side-wall condition. For numerical reasons, this is preferable to a treatment of the side walls as collocation points similar as for the ship hull.

In the wave resistance problem, we consider a ship moving with constant speed V in water of constant depth and width. For inviscid and irrotational flow, this problem is equivalent to a ship being fixed in an inflow of constant speed. The following simplifications are generally assumed:

- Water is incompressible, irrotational, and inviscid.
- Surface tension is negligible.
- There are no breaking waves.
- The hull has no knuckles which cross streamlines.
- Appendages and propellers are not included in the model. (The inclusion of a propeller makes little sense as long as viscous effects are not also included.)

The governing field equation is Laplace's equation. A unique description of the problem requires further conditions on all boundaries of the modelled fluid domain:

- Hull condition: water does not penetrate the ship's surface.
- Transom stern condition: for ships with a transom stern, we generally assume that the flow separates and the transom stern is dry. Atmospheric pressure is then enforced at the edge of the transom stern. The condition is usually linearized assuming that the water flows only in the longitudinal direction. This can only approximately reflect the real conditions at the stern, but apparently works well as long as the transom stern is moderately small as for most container ships. For fast ships which have a very large transom stern, several researchers report problems. For submerged transom sterns at low speed, the potential flow model is inapplicable and only field methods are capable of an appropriate analysis.
- Kinematic condition: water does not penetrate the water surface.
- Dynamic condition: there is atmospheric pressure at the water surface. Beneath an air cushion, this conditions modifies to the air cushion pressure. The inclusion of an air cushion in wave resistance computations has been reported in various applications. However, these computations require the user to specify the distribution of the pressure, especially the gradual decline of the pressure at the ends of the cushion. In reality, this is a difficult task as the dynamics of the air cushion and the flexible skirts make the problem more complicated. Subsequently, the computations must be expected to be less accurate than for conventional displacement hulls.
- Radiation condition: waves created by the ship do not propagate ahead. (This condition is not valid for shallow water cases when the flow becomes unsteady and soliton waves are pulsed ahead. For subcritical speeds with depth Froude number $F_{nh} < 1$, this poses no problem.)
- Decay condition: the flow is undisturbed far away from the ship.

- Open-boundary condition: waves generated by the ship pass unreflected any artificial boundary of the computational domain.
- Equilibrium: the ship is in equilibrium, i.e. trim and sinkage are changed in such a way that the dynamical vertical force and the trim moment are counteracted.
- Bottom condition (shallow-water case): no water flows through the sea bottom.
- Side-wall condition (canal case): no water flows through the side walls.
- Kutta condition (for catamaran/SWATH): at the stern/end of the strut the flow separates. The Kutta condition describes a phenomenon associated with viscous effects. Potential flow methods use special techniques to ensure that the flow separates. However, the point of separation has to be determined externally 'by higher insight'. For geometries with sharp aftbodies (foils), this is quite simple. For twin-hull ships, the disturbance of the flow by one demi-hull induces a slightly non-uniform inflow at the other demi-hull. This resembles the flow around a foil at a very small angle of incident. A simplified Kutta condition suffices usually to ensure a realistic flow pattern at the stern: Zero transverse flow is enforced. This is sometimes called the 'Joukowski condition'.

The decay condition substitutes the open-boundary condition if the boundary of the computational domain lies at infinity. The decay condition also substitutes the bottom and side wall condition if bottom and side wall are at infinity, which is the usual case.

Hull, transom stern, and Kutta condition are usually enforced numerically at collocation points. Also a combination of kinematic and dynamic condition is numerically fulfilled at collocation points. Combining dynamic and kinematic boundary conditions eliminates the unknown wave elevation, but yields a non-linear equation to be fulfilled at the *a priori* unknown free surface elevation.

Classical methods linearize the differences between the actual flow and uniform flow to simplify the non-linear boundary condition to a linear condition fulfilled at the calm-water surface. This condition is called the Kelvin condition. For practical purposes this crude approximation is nowadays no longer accepted.

Dawson proposed in 1977 to use the potential of a double-body flow and the undisturbed water surface as a better approximation. Double-body linearizations were popular until the early 1990s. The original boundary condition of Dawson was inconsistent. This inconsistency was copied by most subsequent publications following Dawson's approach. Sometimes this inconsistency is accepted deliberately to avoid evaluation of higher derivatives, but in most cases and possibly also in the original it was simply an oversight. Dawson's approach requires the evaluation of terms on the free surface along streamlines of the double-body flow. This required either more or less elaborate schemes for streamline tracking or some 'courage' in simply applying Dawson's approach on smooth grid lines on the free surface which were algebraically generated.

Research groups in the UK and Japan proposed in the 1980s non-linear approximations for the correct boundary condition. These non-linear methods should not be confused with 'fully non-linear' methods that fulfil the correct

non-linear boundary condition iteratively. They are not much better than Dawson's approach and no longer considered state of the art.

The first consistently linearized free surface condition for arbitrary approximations of the base flow and the free surface elevation was developed in Hamburg by Söding. This condition is rather complicated involving up to third derivatives of the potential, but it can be simply repeated in an iterative process which is usually started with uniform flow and no waves. Section 7.3, Chapter 7, will derive this expression for the wave resistance problem.

Fully non-linear methods were first developed in Sweden and Germany in the late 1980s. The success of these methods quickly motivated various other research groups to copy the techniques and apply the methods commercially. The most well-known codes used in commercial applications include SHIPFLOW-XPAN, SHALLO, RAPID, SWIFT, and FSWAVE/VSAERO. The development is very near the limit of what potential flow codes can achieve. The state of the art is well documented in two PhD theses, Raven (1996) and Janson (1996). Despite occasional other claims, all 'fully non-linear' codes have similar capabilities when used by their designers or somebody well trained in using the specific code. Everybody loves his own child best, but objectively the differences are small. All 'fully non-linear' codes in commercial use share similar shortcomings when it comes to handling breaking waves, semi-planing or planing boats or extreme non-linearities. It is debatable if these topics should be researched following an inviscid approach in view of the progress that viscous free-surface CFD codes have made.

Once the unknown velocity potential is determined, Bernoulli's equation determines the wave elevation. In principle, a linearized version of Bernoulli's equation might be used. However, it is computationally simpler to use the non-linear equation. Once the potential is determined, the forces can also be determined by direct pressure integration on the wetted hull. The wave resistance may also be determined by an analysis of the wave pattern (wave cut analysis) which is reported to be often more accurate. The z -force and y -moment are used to adjust the position of the ship in fully non-linear methods.

Waves propagate only downstream (except for rare shallow-water cases). This radiation condition has to be enforced by numerical techniques. Most methods employ special finite difference (FD) operators to compute second derivatives of the potential in the free surface condition. Dawson proposed a four-point FD operator for second derivatives along streamlines. Besides the considered collocation point, the FD operator uses the next three points upstream. Dawson's method automatically requires grids oriented along streamlines of the double-body flow approximate solution. Dawson determined his operator by trial and error for a two-dimensional flow with a simple Kelvin condition. His criteria were that the wave length should correspond to the analytically predicted wave length and the wave amplitude should remain constant some distance behind the disturbance causing the waves.

Dawson approximated the derivative of any function H with respect to ℓ at the point i numerically by:

$$H_{\ell i} \approx CA_i H_i + CB_i H_{i-1} + CC_i H_{i-2} + CD_i H_{i-3}$$

$H_{\ell i}$ is the derivative with respect to ℓ at point P_i . H_i to H_{i-3} are the values of the function H at points P_i to P_{i-3} , all lying on the same streamline of the double-body flow upstream of P_i . The coefficients CA_i to CD_i are determined

from the arc lengths L_j ($j = 1$ to $i - 3$) of the streamline between point P_i and point P_j :

$$L_j = \int_{P_i}^{P_j} d\ell \quad \text{on the streamline}$$

$$CA_i = -(CB_i + CC_i + CD_i)$$

$$CB_i = L_{i-2}^2 L_{i-3}^2 (L_{i-3} - L_{i-2})(L_{i-3} + L_{i-2})/D_i$$

$$CC_i = -L_{i-1}^2 L_{i-3}^2 (L_{i-3} - L_{i-1})(L_{i-3} + L_{i-1})/D_i$$

$$CD_i = L_{i-1}^2 L_{i-2}^2 (L_{i-2} - L_{i-1})(L_{i-2} + L_{i-1})/D_i$$

$$D_i = L_{i-1}L_{i-2}L_{i-3}(L_{i-3} - L_{i-1})(L_{i-2} - L_{i-1})(L_{i-3} - L_{i-2}) \\ \times (L_{i-3} + L_{i-2} + L_{i-1})$$

This four-point FD operator dampens the waves to some extent and gives for usual discretizations (about 10 elements per wave length) wave lengths which are about 5% too short. Strong point-to-point oscillations of the source strength occur for very fine grids. Various FD operators have been subsequently investigated to overcome these disadvantages. Of all these, only the spline interpolation developed at MIT was really convincing as it overcomes all the problems of Dawson (Nakos (1990), Nakos and Sclavounos (1990)).

An alternative approach to FD operators involves ‘staggered grids’ as developed in Hamburg. This technique adds an extra row of source points (or panels) at the downstream end of the computational domain and an extra row of collocation points at the upstream end (Fig. 3.11). For equidistant grids this can also be interpreted as shifting or staggering the grid of collocation points vs. the grid of source elements. This technique shows absolutely no numerical damping or distortion of the wave length, but requires all derivatives in the formulation to be evaluated numerically.

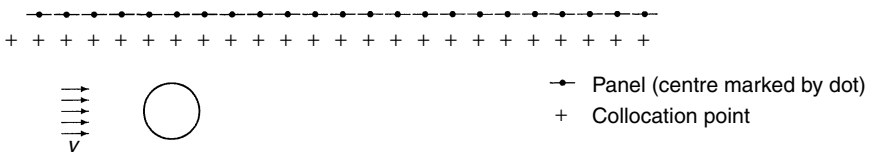


Figure 3.11 ‘Shifting’ technique (in 2d)

Only part of the water surface can be discretized. This introduces an artificial boundary of the computational domain. Disturbances created at this artificial boundary can destroy the whole solution. Methods based on FD operators use simple two-point operators at the downstream end of the grid which strongly dampen waves. At the upstream end of the grid, where waves should not appear, various conditions can be used, e.g. the longitudinal component of the disturbance velocity is zero. Nakos (1990) has to ensure in his MIT method (SWAN code) based on spline interpolation that waves do not reach the side boundary. This leads to relatively broad computational domains. Time-domain versions of the SWAN code use a 'numerical beach'. For the wave

resistance problem, the time-domain approach seems unnecessarily expensive and is rarely used in practice. Norwegian researchers tried to reduce the computational domain by matching the panel solution for the near-field to a thin-ship-theory solution in the far-field. However, this approach saved only little computational time at the expense of a considerably more complicated code and was subsequently abandoned. The 'staggered grid' technique is again an elegant alternative. Without further special treatment, waves leave the computational domain without reflection.

Most methods integrate the pressure on the ship's surface to determine the forces (especially the resistance) and moments. 'Fully non-linear' methods integrate over the actually wetted surface while older methods often take the CWL as the upper boundary for the integration. An alternative to pressure integration is the analysis of the wave energy behind the ship (wave cut analysis). The wave resistance coefficients should theoretically tend to zero for low speeds. Pressure integration gives usually resistance coefficients which remain finite for small Froude numbers. However, wave cut analysis requires larger grids behind the ship leading to increased computational time and storage. Most developers of wave resistance codes have at some point tried to incorporate wave cut analysis to determine the wave resistance more accurately. So far the evidence has not yet been compelling enough to abandon the direct pressure integration.

Most panel methods give as a direct result the source strengths of the panels. A subsequent computation determines the velocities at the individual points. Bernoulli's equation then gives pressures and wave elevations (again at individual points). Integration of pressures and wave heights finally yields the desired forces and moments which in turn are used to determine dynamical trim and sinkage ('squat').

Fully non-linear state of the art codes fulfil iteratively an equilibrium condition (dynamical trim and sinkage) and both kinematic and dynamic conditions on the actually deformed free surface. The differences in results between 'fully non-linear' and linear or 'somewhat non-linear' computations are considerable (typically 25%), but the agreement of computed and measured resistances is not better in 'fully non-linear' methods. This may in part be due to the computational procedure or inherent assumptions in computing a wave resistance from experimental data (usually using a form factor method), but also due to computational errors in determining the resistance which are of similar magnitude as the actual resistance. One reason for the unsatisfactory accuracy of the numerical procedures lies in the numerical sensitivity of the pressure integration. The pressure integration involves basically subtracting forces of same magnitude which largely cancel. The relative error is strongly propagated in such a case. Initial errors stem from the discretization. For example, integration of the hydrostatic pressure for the ship at rest should give zero longitudinal force, but usual discretizations show forces that may lie within the same order of magnitude as the wave resistance. Still, there is consensus that panel methods capture the pressure distribution at the bow quite accurately. The vertical force is not affected by the numerical sensitivity. Predictions for the dynamical sinkage differ usually by less than 5% for a large bandwidth of Froude numbers. Trim moment is not predicted as well due to viscous effects and numerical sensitivity. This tendency is amplified by shallow water.

Panel methods are still the most important CFD instrument for form improvement of ships. Worldwide research aims at faster methods, wider applications, and higher accuracy:

- *Faster methods*

Cluster or multigrid techniques could make existing methods faster by one order of magnitude (Söding (1996)). The price is a more complicated program code. At present, the actual computation in practice accounts for less than 10% of the total response time (from receiving the hull description to delivering the CFD report) and even less of the cost. So the incentive to introduce these techniques is low in practice.

- *Wider applications*

Non-Linear solutions are limited today to moderate non-linearities. Ships with strong section flare close to the waterline and fast ships still defy most attempts to obtain non-linear solutions. Planing boats feature complex physics including spray. Panel methods as described here will not be applied successfully to these ships for some years, although first attempts in this direction appeared in the early 1990s. State of the art computations for planing boats are based on special non-CFD methods, e.g. slender-body approaches.

- *Higher accuracy*

The absolute accuracy of the predicted resistance is unsatisfactory. Patch methods as proposed by Söding and discussed briefly in section 6.5.2, Chapter 6, may overcome this problem to some extent. But the intersection between water surface and ship will remain a problem zone, because the problem is ill-posed here within a potential flow model. The immediate vicinity of the bow of a ship always features to some extent breaking waves and spray not included by the currently used methods. The exact simulation of plunging waves is impossible for panel methods. Ad-hoc solutions are subject to research, but no convincing solution has been published yet. One approach of overcoming these limitations lies in methods discretizing the fluid volume rather than boundary element methods. Such methods can simulate flows with complicated free surface geometries (breaking waves, splashes) allowing the analyses of problems beyond the realm of BEM applications.

3.5.2 Viscous flow computations

RANSE solvers are state of the art for viscous ship flows. A computational prediction of the total calm-water resistance using RANSE solvers to replace model tests would be desirable, but so far the accuracy of the RANSE predictions is largely perceived as still insufficient. Nevertheless, RANSE solvers are widely applied to analyse:

- the flow around aftbodies of ships
- the flow around appendages

The first research applications for RANSE solutions with wavemaking for ships appeared in the late 1980s. By the late 1990s various research groups also presented results for ships free to trim and sink. However, most computations for actual ship design projects in practice still neglected all free-surface effects

(double-body flow). Most computations, especially those for practical design applications, were limited to Reynolds numbers corresponding to model tests. Sometimes, potential flow computations were used as preprocessors to determine trim and sinkage and the wave elevation, before RANSE computations started with fixed boundaries.

The basic techniques of RANSE codes have been discussed in section 1.5, Chapter 1. Various applications to ship design and research applications are found in the literature. Representative for the state of the art for ship design applications are surveys by leading companies in the field such as Flowtech (Larsson (1997, 1998)), or HSVA (Bertram and Jensen (1994)), Bertram (1998a). The state of the art in research is documented in validation workshops like the Tokyo 1994 workshop and the Gothenborg 2000 workshop. RANSE computations require considerable skill and experience in grid generation and should therefore as a rule be executed by experts usually found in special consulting companies or by using modern towing tanks.

3.6 Problems for fast and unconventional ships

Model testing has a long tradition for the prediction and optimization of ship performance of conventional ships. The scaling laws are well established and the procedures correlate model and ship with a high level of accuracy. The same scaling laws generally apply to high-speed craft, but two fundamental problems may arise:

1. Physical quantities may have major effects on the results which cannot be deduced from classical model tests. The physical quantities in this context are: surface tension (spray), viscous forces and moments, aerodynamic forces, cavitation.
2. Limitations of the test facilities do not allow an optimum scale. The most important limitations are generally water depth and carriage speed.

Fast and unconventional ships are often ‘hybrid’ ships, i.e. they produce the necessary buoyancy by more than one of the three possible options: buoyancy, dynamic lift (foils or planing), aerostatic lift (air cushion). For the propulsion of fast ships, subcavitating, cavitating, and ventilated propellers as well as waterjets with flush or pitot-type inlets are used. Due to viscous effects and cavitation, correlation to full-scale ships causes additional problems.

Generally we cannot expect the same level of accuracy for a power prediction as for conventional ships. The towing tank should provide an error estimate for each individual case. Another problem arises from the fact that the resistance curves for fast ships are often quite flat near the design point as are the curves of available thrust for many propulsors. For example, errors in predicted resistance or available thrust of 1% would result in an error of the attainable speed of also about 1%, while for conventional cargo ships the error in speed would often be only 1/3%, i.e. the speed prediction is more accurate than the power prediction.

The main problems for model testing are discussed individually:

- *Model tank restrictions*

The physics of high-speed ships are usually highly non-linear. The positions of the ship in resistance (without propeller) and propulsion (with propeller)

conditions differ strongly. Viscosity and free surface effects, including spray and overturning waves, play significant roles making both experimental and numerical predictions difficult.

Valid predictions from tank tests for the resistance of the full-scale ship in unrestricted water are only possible if the tank is sufficiently large as compared to the model to allow similarity in flow. Blockage, i.e. the ratio of the submerged cross-section of the model to the tank cross-section, will generally be very low for models of high-speed ships. However, shallow-water effects depend mainly on the model speed and the tank water depth. The depth Froude number F_{nh} should not be greater than 0.8 to be free of significant shallow-water effects.

The frictional resistance is usually computed from the frictional resistance of a flat plate of similar length as the length of the wetted underwater body of the model. This wetted length at test speed differs considerably from the wetted length at zero speed for planing or semi-planing hull forms. In addition the correlation requires that the boundary layer is fully turbulent. Even when turbulence stimulators are used, a minimum Reynolds number has to be reached. We can be sure to have a turbulent boundary layer for $R_n > 5 \cdot 10^6$. This gives a lower limit to the speeds that can be investigated depending on the used model length.

Figure 3.12 illustrates, using a towing tank with water depth $H = 6$ m and a water temperature 15° , how an envelope of possible test speeds evolve from these two restrictions. A practical limitation may be the maximum carriage speed. However, at HSVA the usable maximum carriage speed exceeds the maximum speed to avoid shallow-water effects.

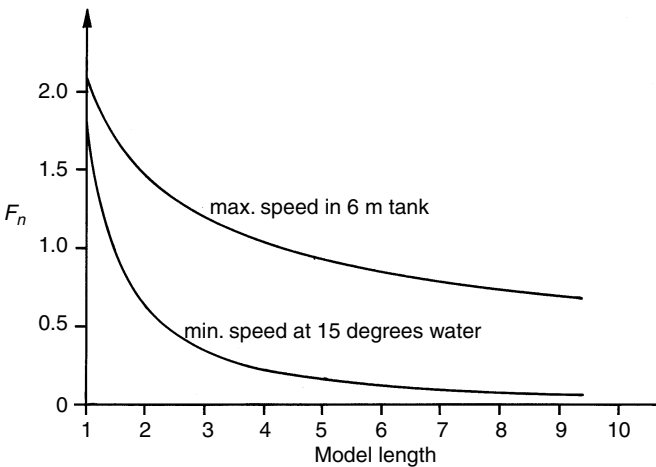


Figure 3.12 Possible speed range to be safely investigated in a 6 m deep towing tank at 15° water temperature

- *Planing hulls*

In the planing condition a significant share of the resistance is frictional and there is some aerodynamic resistance. At the design speed, the residual resistance, i.e. the resistance component determined from model tests, may

only be 25% to 30% of the total resistance. In model scale, this part is even smaller. Therefore the measurements of the model resistance must be very accurate. Resistance of planing hulls strongly depends on the trim of the vessel. Therefore a careful test set-up is needed to ensure that the model is towed in the correct direction. The most important problem, however, is the accurate determination of the wetted surface and the wetted length which is needed to compute the frictional resistance for both the model and the ship. The popular use of side photographs are not adequate. Preferably underwater photographs should be used. In many cases, the accurate measurement of trim and sinkage may be adequate in combination with hydrostatic computation of wetted surface and length. As the flotation line of such vessels strongly depends on speed, proper arrangement of turbulence stimulation is needed as well.

Depending on the propulsion system, planing vessels will have appendages like rudders and shafts. For typical twin-screw ships with shafts, one pair of I-brackets and one pair of V-brackets, the appendage resistance could account for 10% of the total resistance of the ship. As viscous resistance is a major part in the appendage resistance and as the Reynolds number of the appendages will be small for the model in any case or the appendage may be within the boundary layer of the vessel, only a crude correlation of the appendage resistance is possible: the resistance of the appendage is determined in model scale by comparing the resistance of the model with and without appendages. Then an empirical correction for transferring the appendage resistance to the full-scale ship is applied. In many cases, it may be sufficient to perform accurate measurements without any appendages on the model and then use an empirical estimate for the appendage resistance.

- *Craft with hydrofoils*

Hydrofoils may be used to lift the hull out of the water to reduce resistance. Besides classical hydrofoils which are lifted completely out of the water and are fully supported by foil lift, hybrid hydrofoils may be used which are partially supported by buoyancy and partially by foil lift, e.g. catamarans with foils between the two hulls. When performing and evaluating resistance and propulsion tests for such vessels, the following problems have to be kept in mind:

- The Reynolds number of the foils and struts will always be very low. Therefore the boundary layer on the foil may become partially laminar. This will influence the lift and the frictional resistance of the foils in a way requiring special correlation procedures to compensate at least partially these scaling errors. The uncertainty level is still estimated as high as 5% which is definitely higher than for conventional craft.
- Cavitation may occur on the full-scale hydrofoil. This may not only cause material erosion, but it will also influence the lift and drag of the foils. Significant cavitation will certainly occur if the foil loading exceeds 10^5 N/m^2 . With configurations not fully optimized for cavitation avoidance, significant cavitation is expected for foil loadings in excess of $6 \cdot 10^4 \text{ N/m}^2$ already. Another important parameter is the vessel's speed. Beyond 40 knots, cavitation has to be expected on joints to struts, flaps, foil tips and other critical parts. At speeds beyond 60 knots, cavitation on the largest part of the foil has to be expected. When model testing

these configurations in model tanks, no cavitation will occur. Therefore similarity of forces cannot be expected. To overcome this problem, resistance and propulsion tests could be performed in a free surface cavitation tunnel. However, due to the usually small cross-sections of these tunnels, shallow-water effects may be then unavoidable. Therefore HSVA recommends the following procedure:

1. Perform tests in the towing tank using non-cavitating foils from stock, varying angle of attack, and measure the total resistance and the resistance of the foils.
2. Test the foils (including struts) in a cavitation tunnel varying angle of attack, observe cavitation and measure forces.
3. Combine the results of both tests by determining the angle of attack for similar lift of foils and summing the resistance components.

In the preliminary design phase, the tests in the cavitation tunnel may be substituted by corresponding flow computations.

- *Surface effect ships (SES)*

SES combine aerostatic lift and buoyancy. The wave resistance curve of SES exhibits humps and hollows as in conventional ships. The magnitude of the humps and hollows in wave resistance depends strongly on the cushion L/B ratio. Wavemaking of the submerged hulls and the cushion can simply be scaled according to Froude similarity as long as the tank depth is sufficient to avoid shallow-water effects. Otherwise a correction based on the potential flow due to a moving pressure patch is applied. Due to the significant influence of trim, this method has some disadvantages. To determine the wetted surface, observations inside the cushion are required with a video camera. The frictional resistance of the seals cannot be separated out of the total resistance. The pressure distribution between seals and cushion has to be controlled and the air flow must be determined. Also the model aerodynamic resistance in the condition under the carriage has to be determined and used for separating the wave resistance. Generally separate wind tunnel tests are recommended to determine the significant aerodynamic resistance of such ships.

- *Propulsion with propellers*

- *Conventional propellers*

Most of the problems concerning the scaling of resistance also appear in the propulsion test, as they determine the propeller loading. The use of a thrust deduction fraction is formally correct, but the change in resistance is partially due to a change of trim with operating propellers. For hydrofoils, the problem is that cavitation is not present at model scale. Therefore, for cases with propeller loading where significant cavitation is expected, additional cavitation tests are used to determine the thrust loss due to cavitation. Z-drives which may even be equipped with contra-rotating propellers are expensive to model and to equip with accurate measuring devices. Therefore propulsion tests with such units are rarely performed. Instead the results of resistance and open-water tests of such units in a proper scale are numerically combined.

- *Cavitating propellers*

Certain high-speed propellers are designed to operate with a controlled extent of cavitation on the suction side of the blades. They are called super-cavitating or partially cavitating (Newton–Rader) propellers. These propulsors cannot be tested in a normal towing tank. Here again either

resistance tests or propulsion tests with non-cavitating stock propellers are performed and combined with open-water tests in a cavitation tunnel.

– *Surface-piercing propellers*

Surface-piercing or ventilated propellers operate directly at the free surface. Thus the suction side is ventilated and therefore the collapse of cavitation bubbles on the blade surface is avoided. Due to the operation at the free surface, Froude similarity has to be maintained in model tests. On the other hand, thrust and torque, but more important also the side and vertical forces, strongly depend on the cavitation number. The vertical force may amount up to 40% of the thrust and therefore will strongly influence the resistance of planing vessels or SES, ships where this type of propeller is typically employed.

• *Waterjet propulsion*

A common means of propulsion for high-speed ships is the waterjet. Through an inlet in the bottom of the craft water enters into a bent duct to the pump, where the pressure level is raised. Finally the water is accelerated and discharged in a nozzle through the transom. Power measurements on a model of the complete system cannot be properly correlated to full scale. Only the inlet and the nozzle are built to scale and an arbitrary model pump with sufficient capacity is used. The evaluation of waterjet experiments is difficult and involves usually several special procedures involving a combination of computations, e.g. the velocity profile on the inlet by boundary layer or RANSE computations, and measured properties, e.g. pressures in the nozzle. The properties of the pump are determined either in separate tests of a larger pump model, taken from experience with other pumps, or supplied by the pump manufacturer. A special committee of the ITTC was formed to cover waterjet propulsion and latest recommendation and literature references may be found in the ITTC proceedings.

3.7 Exercises: resistance and propulsion

Solutions to the exercises will be posted on the internet (www.bh.com/companions/0750648511)

1. A 6 m model of a 180 m long ship is towed in a model basin at a speed of 1.61 m/s. The towing pull is 20 N. The wetted surface of the model is 4 m². Estimate the corresponding speed for the ship in knots and the effective power P_E using simple scaling laws, i.e. assuming resistance coefficients to be independent of scale.
2. A ship model with scale $\lambda = 23$ was tested in fresh water with: $R_{T,m} = 104.1$ N, $V_m = 2.064$ m/s, $S_m = 10.671$ m², $L_m = 7.187$ m.
Both model and ship are investigated at a temperature of 15°.
 - (a) What is the prediction for the total calm-water resistance in sea water of the full-scale ship following ITTC'57? Assume $c_A = 0.0002$.
 - (b) What would be the prediction following ITTC'78 with a form factor $k = 0.12$? Assume standard surface roughness. Neglect air resistance.
3. A base ship (Index O) has the following main dimension: $L_{pp,O} = 128.0$ m, $B_O = 25.6$ m, $T_O = 8.53$ m, $C_B = 0.565$ m. At a speed $V_O = 17$ kn, the ship has a total calm-water resistance of $R_{T,O} = 460$ kN. The viscosity of water is $\nu = 1.19 \cdot 10^{-6}$ m²/s and $\rho = 1025.9$ kg/m³.

What is the resistance of a ship with $L_{pp} = 150$ m if the ship is geometrically and dynamically similar to the base ship and the approach of ITTC'57 is used (essentially resistance decomposition following Froude's approach)?

The wetted surface may be estimated by (Schneekluth and Bertram (1998), p. 185):

$$S = (3.4\nabla^{1/3} + 0.5L_{wl})\nabla^{1/3}$$

L_{wl} may be estimated by $L_{wl} = 1.01L_{pp}$.

The Reynolds number shall be based on L_{pp} . The correlation coefficient can be neglected.

4. A sailing yacht has been tested. The full-scale dimensions are $L_{pp} = 9.00$ m, $S = 24.00$ m², $\nabla = 5.150$ m³. The yacht will operate in sea water of $\rho = 1.025$ t/m³, $\nu = 1.19 \cdot 10^{-6}$ m²/s.

The model was tested with scale $\lambda = 7.5$ in fresh water with $\rho = 1000$ kg/m³, $\nu = 1.145 \cdot 10^{-6}$ m²/s.

The experiments yield for the model:

V_m (m/s)	0.5	0.6	0.75	0.85	1.0	1.1	1.2
$R_{T,m}$ (N)	0.402	0.564	0.867	1.114	1.584	2.054	2.751

(a) Determine the form factor following Hughes–Prohaska.

(b) Determine the form factor following ITTC'78. For simplification assume the exponent n for F_n to be 4 and determine just the α and k in regression analysis.

5. A container ship shall be lengthened by adding a parallel midship section of 12.50 m length (40' container and space between stacks). At full engine power (100% MCR = maximum continuous rating), the ship is capable of $V = 15.6$ knots.

Ship data (original):

L_{pp}	117.20 m
L_{wl}	120.00 m
B	20.00 m
T	6.56 m
r_{bilge}	1.5 m
C_B	0.688
lcb	0.0

Wake fraction and thrust deduction shall be given by:

$$w = 0.75 \cdot C_B - 0.24 \quad t = 0.5 \cdot C_B - 0.15$$

$$\nu = 1.19 \cdot 10^{-6} \text{ m}^2/\text{s}, \rho = 1025 \text{ kg/m}^3.$$

The ship is equipped with a propeller with $\eta_0 = 0.55$. The relative rotative efficiency is $\eta_R = 1$.

What is the power requirement after the conversion, if the propeller is assumed to remain unchanged? Base your prediction on Lap–Keller (Lap (1954), Keller (1973)) with a correlation coefficient $c_A = 0.35 \cdot 10^{-3}$.

6. A ship of 150 m length sails with 15 kn on water of 12 m depth. It experiences a dynamic sinkage amidships of 1 m and a trim (bow immerses) of

1°. Slender-body theories give the relation that both trim and sinkage are proportional to:

$$\frac{F_{nh}^2}{\sqrt{1 - F_{nh}^2}}$$

How much is then according to this theory the dynamic sinkage at the bow for 12 kn on 13 m water depth?

Ship seakeeping

4.1 Introduction

Seakeeping of ships is investigated with respect to the following issues:

- Maximum speed in a seaway: ‘involuntary’ speed reduction due to added resistance in waves and ‘voluntary’ speed reduction to avoid excessive motions, loads etc.
- Route optimization (routing) to minimize, e.g., transport time, fuel consumption, or total cost.
- Structural design of the ship with respect to loads in seaways.
- Habitation comfort and safety of people on board: motion sickness, danger of accidental falls, man overboard.
- Ship safety: capsizing, large roll motions and accelerations, slamming, wave impact on superstructures or deck cargo, propeller racing resulting in excessive rpm for the engine.
- Operational limits for ships (e.g. for offshore supply vessels or helicopters landing on ships).

Tools to predict ship seakeeping are:

- Model tests.
- Full-scale measurements on ships at sea.
- Computations in the frequency domain: determination of the ship reactions to harmonic waves of different wave lengths and wave directions.
- Computations in the time domain (simulation in time): computation of the forces on the ship for given motions at one point in time; based on that information the computation of the motions at a following point in time etc.
- Computations in the statistical domain: computation of statistically significant seakeeping values in natural (irregular) seaways, e.g. average frequency (occurrence per time) of events such as exceeding certain limits for motions or loads in a given seaway or ocean region.

For many seakeeping issues, seakeeping is determined as follows:

1. Representation of the natural seaway as superposition of many regular (harmonic) waves (Fourier decomposition).
2. Computation (or sometimes measurement in model tests) of the ship reactions of interest in these harmonic waves.

3. Addition of the reactions in all these harmonic waves to a total reaction (superposition).

This procedure assumes (respectively requires) that the reaction of one wave on the ship is not changed by the simultaneous occurrence of another wave. This assumption is valid for small wave heights for almost all ship reactions with the exception of the added resistance.

This procedure is often applied also for seaways with large waves. However, in these cases it can only give rough estimates requiring proper corrections. One consequence of the assumed independence of the individual wave reactions is that all reactions of the ship are proportional to wave height. This is called linearization with respect to wave height.

The computations become considerably more expensive if this simplification is not made. Non-linear computations are usually necessary for the treatment of extreme motions (e.g. for capsizing investigations); here simulation in the time domain is the proper tool. However, for the determination of maximum loads it often suffices to apply corrections to initially linearly computed loads. The time-averaged added resistance is in good approximation proportional to the square of the wave height. Here the effect of harmonic waves of different lengths and direction can be superimposed as for the linear ship reactions.

To determine global properties (e.g. ship motions and accelerations) with sufficient accuracy, simpler methods suffice than for the determination of local properties (pressures, relative motions between water and ship).

Further recommended reading includes Faltinsen (1993) and Lewis (1990).

4.2 Experimental approaches (model and full scale)

Seakeeping model tests usually employ self-propelled models in narrow towing tanks or broad, rectangular seakeeping basins. The models are sometimes completely free being kept on course by a rudder operated in remote control or by an autopilot. In other cases, some degrees of freedom are suppressed (e.g. by wires). If internal forces and moments are to be determined, the model is divided into a number of sections. The individual watertight sections are coupled to each other by gauges. These gauges consist of two rigid frames connected by rather stiff flat springs with strain gauges. Model motions are determined either directly by or by measuring the accelerations and integrating them twice in time. Waves and relative motions of ships and waves are measured using two parallel wires penetrating the water surface. The change in the voltage between the wires is then correlated to the depth of submergence in water. The accuracy of ultrasonic devices is slightly worse. The model position in the tank can be determined from the angles between ship and two or more cameras at the tank side. Either lights or reflectors on the ship give the necessary clear signal.

The waves are usually created by flaps driven by hydraulical cylinders. The flaps are inclined around a horizontal axis lying at the height of the tank bottom or even lower. Traditionally, these flaps were controlled mechanically by shaft mechanisms which created a (nearly) sinusoidal motion. Modern wavemakers are computer controlled following a prescribed time function. Sinusoidal flap motion creates harmonic waves. The superposition of many sinusoidal waves of different frequency creates irregular waves similar to natural wind seas.

Some wavemakers use heightwise segmented flaps to simulate better the exponential decay of waves with water depth. Sometimes, but much less frequently, vertically moved bodies or air cushions are also used to generate waves. These facilities create not only the desired wave, but also a near-field disturbance which decays with distance from the body or the air cushion. More harmful is the generation of higher harmonics (waves with an integer multiple of the basic wave frequency), but these higher harmonics can be easily filtered from the measured reactions if the reactions are linear. In computer controlled wavemakers they can be largely eliminated by proper adjustment of the flap motions.

In towing tanks, waves are generated usually by one flap at one tank end spanning the complete tank width. The other tank end has a 'beach' to absorb the waves (ideally completely) so that no reflected waves influence the measurements and the water comes to rest after a test as soon as possible. If several, independently controlled flaps are used over the tank width waves with propagation direction oblique to the tank longitudinal axis can be generated. These waves will then be reflected at the side walls of the tank. This is unproblematic if a superposition of many waves of different direction ('short-crested sea') is created as long as the distribution of the wave energy over the propagation direction is symmetrical to the tank longitudinal axis. In natural wind seas the energy distribution is similarly distributed around the average wind direction.

Rectangular wide seakeeping basins have typically a large number of wave-making flaps at two adjacent sides. An appropriate phase shift in the flap motions can then create oblique wave propagation. The other two sides of such a basin are then equipped with 'beaches' to absorb waves.

Seakeeping model tests are usually only performed for strongly non-linear seakeeping problems which are difficult to compute. Examples are roll motion and capsizing, slamming and water on deck. Linear seakeeping problems are only measured for research purposes to supply validation data for computational methods. In these cases many different frequencies can be measured at the same time. The measured data can then be decomposed (filtered) to obtain the reactions to the individual wave frequencies.

Seakeeping tests are expensive due to the long waiting periods between tests until the water has come to rest again. The waiting periods are especially long in conventional towing tanks. Also, the scope of the experiments is usually large as many parameters need to be varied, e.g. wave length, wave height, angle of encounter, ship speed, draught and trim, metacentric height etc. Tests keep Froude similarity just as in resistance and propulsion tests. Gravity and inertia forces then correspond directly between model and full-scale ship. However, scale effects (errors due to the model scale) occur for forces which are due to viscosity, surface tension, compressibility of the water, or model elasticity. These effects are important, e.g., for slamming pressure, water on deck, or sway, roll and yaw motions of catamarans. However, in total, scale effects play a lesser role for seakeeping tests than for resistance and propulsion tests or manoeuvring tests.

Seakeeping can also be measured on ships in normal operation or during special trial tests. Ship motions (with accelerometers and gyros) and sometimes also global and local loads (strain gauges), loss of speed, propeller rpm and torque are all measured. Recording the seaway is difficult in full-scale measurements. The options are:

1. No recording of actual seaway during trial; instead measurements of seaway over many years such that, e.g., the expected maximum values during the lifetime of the ship can be extrapolated from the recorded distribution of long-term measured values (long-term measurement). The random variation of the actual seastate encountered by the ship introduces considerable inaccuracies for the predicted extreme values even if several years of measurements are available.
2. Computation of the seaway from the ship motions based on computed or model-test measured response amplitude operators for the motions. This allows only a rather rough estimate of the seaway. In following seas this method is hardly applicable. Nevertheless, averaging over, e.g., 10 to 100 half-hour measurements yields usually good estimates for the correlation of loads and seaway (medium-term measurement) for example.
3. Parallel measurement of the seaway. Options are:
 - Using seastate measuring buoys (brought by the ship).
 - Performing the sea trials near a stationary seaway measuring installation.
 - Measuring the ship motions (by accelerometers) and the relative motion between water and ship (by pressure measurements at the hull or water level measurements using a special radar device); based on these data indirect determination of the absolute motion of the water surface is possible.
 - Measuring the wave spectrum (energy distribution over frequency and propagation direction) by evaluating radar signals reflected by the waves.
 - Computation or estimation of the seaway from the wind field before and during the experiments.
 - Estimation of significant wave height and period from ‘experienced’ seamen. This common practice is to be rejected as far too inaccurate: the correlation coefficient between measured (actual) and estimated wave period is typically <50%! This holds also if the estimates are used to derive statistical distributions. For most extreme values of interest the errors in the estimates do not cancel, but are rather concentrated around the extreme values.

4.3 Waves and seaway

4.3.1 Airy waves (harmonic waves of small amplitude)

Wind-induced seaways can be approximated by the superposition of regular waves of small wave height (elementary waves, Airy waves). Each elementary wave has a sinusoidal profile with an infinite number of wave troughs and wave crests (Fig. 4.1). The wave troughs and crests are perpendicular to the direction of wave propagation. Such elementary waves are an important building block for all computational methods for linear seakeeping problems. Steep regular waves can be computed by, e.g., Stokes’ theory or panel methods. However, the superposition principle no longer applies to these waves. Therefore they play virtually no role at all for the prediction of ship seakeeping and are rather of academical interest for naval architects. Unfortunately, in using the superposition principle for elementary waves, all properties of the seaway which are non-linear with wave steepness (=wave height/wave length) are lost.

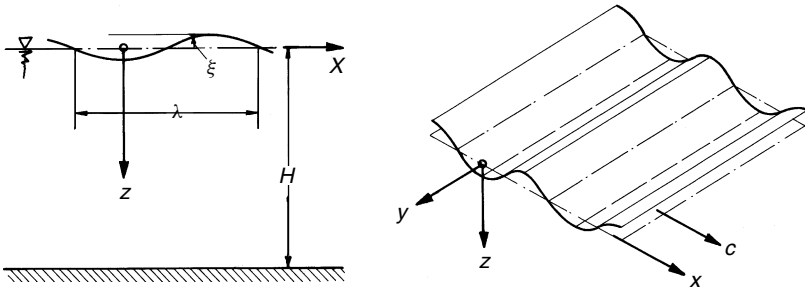


Figure 4.1 Elementary waves

These are, e.g., the broader wave troughs and steeper wave crests, the higher celerity of steeper waves which results in a tendency to form wave groups in natural wind seas: groups of waves with low wave height are followed by groups of waves with larger wave heights.

For ship seakeeping, the relevant waves are dominated by gravity effects and surface tension, water compressibility and (for deep and moderately shallow water) viscosity can be neglected. Computations can then assume an ideal fluid (incompressible, inviscid) without surface tension. Consequently potential theory can be applied to describe the waves.

Generally, regular waves are described by a length parameter (wave length λ or wave number k) and a time parameter (wave period T or (circular) frequency ω). k and ω are defined as follows:

$$k = \frac{2\pi}{\lambda}; \quad \omega = \frac{2\pi}{T}$$

The celerity c denotes the speed of wave propagation, i.e. the speed of an individual wave crest or wave trough:

$$c = \frac{\lambda}{T} = \frac{\omega}{k}$$

For elementary waves, the following (dispersion) relation holds:

$$k = \frac{\omega^2}{g} \quad \text{on deep water} \quad k \tanh(kH) = \frac{\omega^2}{g} \quad \text{on finite depth}$$

$g = 9.81 \text{ m/s}^2$ and H is the water depth (Fig. 4.1).

The above equations can then be combined to give the following relations (for deep water):

$$c = \sqrt{\frac{g}{k}} = \frac{g}{\omega} = \sqrt{\frac{g\lambda}{2\pi}} = \frac{gT}{2\pi}$$

The potential ϕ of a wave travelling in the $+x$ direction is:

$$\begin{aligned} \phi &= \text{Re}(-i\hat{c}h e^{-kz} e^{i(\omega t - kx)}) \quad \text{for deep water} \\ &= \text{Re}\left(\frac{-i\hat{c}h}{\sinh(kH)} \cosh(k(z - H)) e^{i(\omega t - kx)}\right) \quad \text{for finite depth} \end{aligned}$$

Re denotes the real part of a complex quantity; $i = \sqrt{-1}$; z as in Fig. 4.1; \hat{h} denotes as usual a complex amplitude; \hat{h} = the complex amplitude of the wave. $h = |\hat{h}|$ is the (real-valued) wave amplitude, i.e. half the wave height (from wave trough to wave crest). The real part of \hat{h} gives the distance of the wave trough from the calm-water level at time $t = 0$ at $x = 0$; the imaginary part gives the same value at $\frac{1}{4}$ period earlier. The deep-water formulae are applicable with errors of $< \frac{1}{2}\%$ if the water depth is larger than half a wave length.

The velocity is obtained by differentiation of the potential, e.g. for deep water:

$$v_x = \frac{\partial \phi}{\partial x} = \phi_x = \text{Re}(-\omega \hat{h} e^{-kz} e^{i(\omega t - kx)})$$

$$v_z = \frac{\partial \phi}{\partial z} = \phi_z = \text{Re}(i\omega \hat{h} e^{-kz} e^{i(\omega t - kx)})$$

The complex amplitudes of the velocities have the same absolute value and a phase shift of 90° . A water particle thus follows a circular track or orbital motion (from Latin *orbis* = circle). In water of finite depth, the motion of a water particle follows an ellipse. The vertical axis of each ellipse decreases with depth until at the water bottom $z = H$ the motion is only in the horizontal direction.

If we excite a group of waves (not elementary waves, but, e.g., 10 wave crests and troughs) in initially calm water we will notice that the front of the wave crests decay while at the end of the wave packet new wave crests are formed (Fig. 4.2). The wave packet thus moves slower than the wave crests,

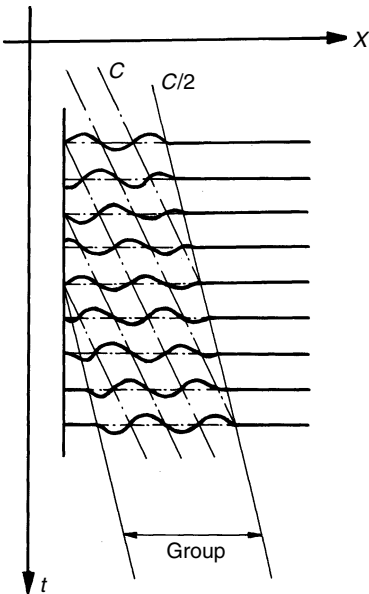


Figure 4.2 Celerity and group velocity

i.e. with a speed slower than celerity c , namely with group velocity c_{gr} :

$$c_{\text{gr}} = \frac{1}{2}c \quad \text{for deep water}$$

$$c_{\text{gr}} = c \left(\frac{1}{2} + \frac{kH}{\sinh(2kH)} \right) \quad \text{for finite depth}$$

The linearized Bernoulli equation

$$p + \rho \frac{\partial \phi}{\partial t} - \rho g z = p_0$$

and the wave potential give the difference pressure to atmospheric pressure at a point below the water surface (for deep water):

$$p - p_0 = \rho g z - \rho g \operatorname{Re}(\hat{h} e^{-kz} e^{i(\omega t - kx)})$$

p_0 is the atmospheric pressure, ρ the water density, z the depth of the point below the calm-water surface. The first term represents the hydrostatic pressure in calm water. The second term represents the pressure change due to the wave. As with all wave effects, it decays exponentially with depth. The pressure gradient $\partial p / \partial z$ is for the hydrostatic case equal to the specific weight of the fluid and causes a buoyant lifting force on the immersed body that equals the weight of the displaced water. This lifting force changes in a wave! The lifting force is lower in a wave crest, higher in a wave trough. This is called the Smith effect.

The mechanical energy E per area of the water surface is composed of potential and kinetic energy. Let ζ be the momentary elevation of the free surface. Then the potential energy (per area) is:

$$E_{\text{pot}} = -\frac{\zeta}{2} \rho g (-\zeta) = \frac{1}{2} \rho g \zeta^2$$

The potential energy is positive both in wave troughs and wave crests and oscillates in time and space between 0 and $\rho g |\hat{h}|^2$. The time average is

$$\overline{E}_{\text{pot}} = \frac{1}{4} \rho g |\hat{h}|^2$$

The kinetic energy per area is:

$$E_{\text{kin}} = \int_{\zeta}^{\infty} \frac{1}{2} \rho (v_x^2 + v_z^2) dz = \int_{\zeta}^{\infty} \frac{1}{2} \rho \omega^2 |\hat{h}|^2 e^{-2kz} dz \approx \int_0^{\infty} \dots dz = \frac{1}{4} \rho g |\hat{h}|^2$$

Here the formulae for v_x and v_z have been used and in a linearization the wave elevation ζ was substituted by 0. The kinetic energy is constant in time and space. The time-averaged total energy per area for a deep-water wave is then:

$$\overline{E} = \frac{1}{2} \rho g |\hat{h}|^2$$

The average energy travels with c_{gr} in the same direction as the wave. For finite-depth water the average energy remains the same but the kinetic energy oscillates also in time and space.

The elementary wave was so far described in an earth-fixed coordinate system. In a reference system moving with ship speed V in the direction of

the ship axis x_s under an angle of encounter μ (Fig. 4.3), the wave seems to change its frequency. The (circular) frequency experienced by the ship is denoted encounter frequency:

$$\omega_e = |\omega - kV \cos \mu| = \left| \omega - \frac{\omega^2 V}{g} \cos \mu \right|$$

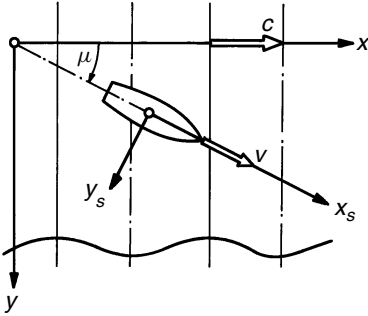


Figure 4.3 Definition of angle of encounter

Figure 4.4 illustrates this phenomenon. For course against the sea ($\mu > 90^\circ$) the encounter frequency is higher than the incident wave frequency ω . For course with the sea ($\mu < 90^\circ$) the encounter frequency is usually lower than

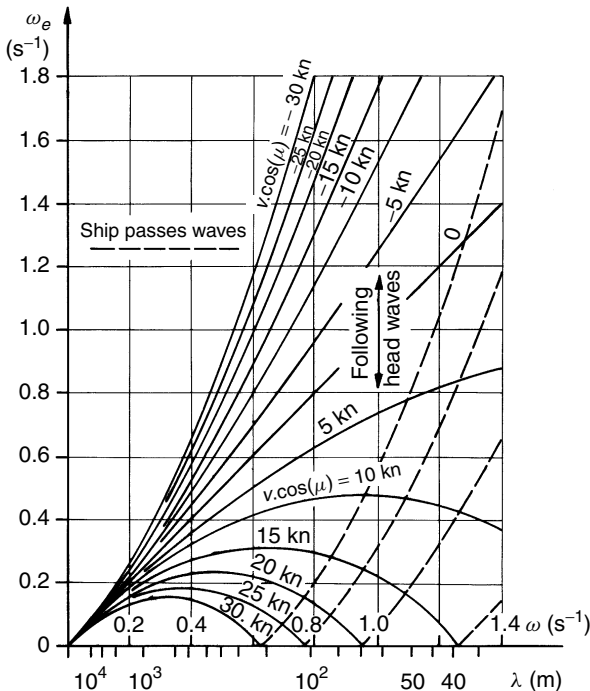


Figure 4.4 Relation between wave frequency, wave length and encounter frequency

the incident wave frequency ω . An exception are short following seas which are passed by the ship. The condition for the ship passing the waves is:

$$F_n > \frac{0.4}{\cos \mu} \sqrt{\frac{\lambda}{L}}$$

An important parameter in this context is:

$$\tau = \frac{\omega_e V}{g} = \frac{\omega V}{g} - \left(\frac{\omega V}{g} \right)^2 \cos \mu$$

For following sea for cases with $\tau \cos \mu < 0.25$, for given speed V , encounter angle μ , and encounter frequency ω_e three possible ω values exist:

$$\omega_1 = \frac{g}{2V \cos \mu} (1 + \sqrt{1 + 4\tau \cos \mu})$$

$$\omega_2 = \frac{g}{2V \cos \mu} (1 + \sqrt{1 - 4\tau \cos \mu})$$

$$\omega_3 = \frac{g}{2V \cos \mu} (1 - \sqrt{1 - 4\tau \cos \mu})$$

The potential of a deep-water wave in a coordinate system moving with ship speed is:

$$\phi = \text{Re}(-i\hat{c}he^{-kz}e^{-ik(x_s \cos \mu - y_s \sin \mu)}e^{i\omega_e t})$$

The above formulae for velocities and pressures can correspondingly be derived in the coordinate system moving with ship speed.

4.3.2 Natural seaway

Wind-excited seaway can be approximated with good accuracy as the superposition of many elementary waves of different wave lengths and propagation directions. The phase shifts between these elementary waves change with time and location and are taken as random quantities for the origin and time $t = 0$. The randomness of the phases – which corresponds to the randomness (irregularity) of the natural seaway – means that only statistical statements can be made, e.g. what the probability is that the wave height exceeds a given limit.

The initial assumptions are:

1. The seaway is stationary, i.e. its statistical properties (e.g. average wave height, average wave period etc.) do not change within the considered time frame.
2. The seaway is not too steep so that linearized equations are still accurate enough. Then any linear superposition of two or more waves with the same or differing frequency or propagation direction will again be a possible form of the water surface.

Only those seaway properties which do not change for small variations of the registration location or the registration time are of interest for ship seakeeping.

The procedure to obtain these properties is as follows: Assume we have a record of the wave elevation $\zeta(t)$ at a given point for the time interval $t = 0$ to T . Then ζ is decomposed in a Fourier analysis, i.e. the complex constants \hat{A}_j are determined in a finite series:

$$\zeta(t) = A_0 + \sum_{j=1}^J \operatorname{Re}(\hat{A}_j e^{i\omega_j t}) \quad \text{with} \quad \omega_j = j\Delta\omega, \quad \Delta\omega = 2\pi/T$$

The average wave elevation A_0 is of no interest here. The phase angle ε_j of the complex amplitudes $\hat{A}_j = |\hat{A}_j|e^{i\varepsilon_j}$ would be different at a different (near-by) location and are therefore also of no interest here. The absolute value of \hat{A}_j depends on the registration time T . Only the sea spectrum remains as constant and of interest in the above sense:

$$S_\zeta(\omega_j) = \frac{\text{Average value of } |\hat{A}_j|^2}{2\Delta\omega_j}$$

The averaging can be done:

- over many records of statistically equivalent seaways (e.g. at various locations spaced by a few kilometres at the same time), or
- over many records of time intervals of the total registration time T , or
- over several (10 to 30) ‘neighbouring’ $|\hat{A}_j|^2$ (preferred choice in practice); e.g. for $j = 1$ to 10, 11 to 20, 21 to 30 etc., an average $|\hat{A}|^2$ can be found as the arithmetic average of ten $|\hat{A}_j|^2$ in each case.

The ω_j in the argument of the sea spectrum S_ζ is the (circular) frequency (in the last case the average frequency) on which the average is based.

The wave energy per horizontal area in an elementary wave is:

$$E = \frac{1}{2}\rho g |\hat{A}|^2$$

$\rho g S_\zeta$ is thus the average seaway energy per frequency interval and area. Therefore S_ζ is also called the energy spectrum of a seaway. It describes the distribution of wave energy over the frequency ω . Its dimension is, e.g., $\text{m}^2 \cdot \text{s}$.

The spectrum can be used to reconstruct the time function $\zeta(t)$ given earlier in this section:

$$\zeta(t) = \sum_{j=1}^J \sqrt{2S_\zeta(\omega_j)\Delta\omega_j} \cdot \cos(\omega_j t + \varepsilon_j)$$

(Instead of $\operatorname{Re} e^{i\alpha}$ we simply write here $\cos \alpha$.) We substituted here $|\hat{A}_j|^2$ by its average value; this usually has no significant effect. As the phase angle information is no longer contained in the spectrum (and we usually only have the spectrum information to reconstruct a seaway) the phase angles ε_j are chosen as random quantities equally distributed in the interval $[0, 2\pi]$. This creates various functions $\zeta(t)$ depending on the actual choice of ε_j , but all these functions have the same spectrum, i.e. the same characteristic (non-random) properties as the original seaway.

If all phase angles are chosen to zero the extremely unlikely (but not impossible) case results that all elementary waves have a wave trough at the considered location at time $t = 0$. The number of terms in the sum for $\zeta(t)$ in the above equation is taken as infinite in theoretical derivations. In practical simulations, usually 30 to 100 terms are taken.

Each elementary wave in a Fourier decomposition of natural seaway depends on time and space. The superposition of many elementary waves all propagating in the x direction, but having different frequencies, yields long-crested seaways as depicted in Fig. 4.5 (left). Long-crested seaway is described by:

$$\zeta(t) = \sum_{j=1}^J \sqrt{2S_{\zeta}(\omega_j)\Delta\omega_j} \cdot \cos(\omega_j t + k_j x + \varepsilon_j)$$

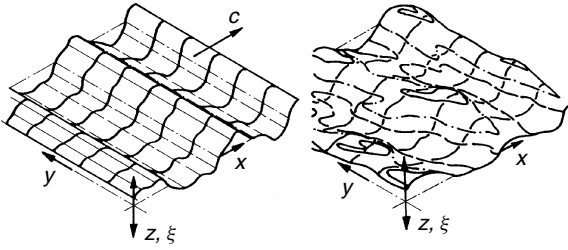


Figure 4.5 Long-crested (left) and short-crested (right) seaways

$k_j = \omega_j^2/g$ is the wave number corresponding to frequency ω_j .

Short-crested seaway, Fig. 4.5 (right), is a better approximation to wind-excited seaway. Short-crested seaway is described if the wave energy is distributed not only over frequency, but also over wave propagation direction μ . The corresponding description is:

$$\begin{aligned} \zeta(t) = & \sum_{j=1}^J \sum_{l=1}^L \sqrt{2S_{\zeta}(\omega_j, \mu_l)\Delta\omega_j\Delta\mu_l} \\ & \times \cos[\omega_j t - k_j(x \cos \mu_l - y \sin \mu_l) + \varepsilon_{jl}] \end{aligned}$$

$S_{\zeta}(\omega_j, \mu_l)$ is the directional or two-dimensional spectrum as opposed to the one-dimensional spectrum $S_{\zeta}(\omega_j)$.

At a ship, the wave elevation oscillates in a regular wave with encounter frequency ω_e . The encounter spectrum $S_{\zeta_e}(\omega_e)$ describes the distribution of the wave energy in a seaway over ω_e instead of ω . The energy must be independent of the reference system:

$$S_{\zeta}(\omega) \cdot |\Delta\omega| = S_{\zeta_e}(\omega_e) \cdot |\Delta\omega_e|$$

This yields:

$$S_{\zeta_e}(\omega_e) = \frac{S_{\zeta}(\omega)}{d\omega_e/d\omega} = S_{\zeta}(\omega) \left/ \left| 1 - \frac{2\omega}{g} V \cos \mu \right| \right|$$

If several ω result in the same ω_e the contributions of all three frequencies are added on the r.h.s. of this equation (Fig. 4.6). Correspondingly an encounter directional spectrum can also be determined. Because of the several possible contributions on the r.h.s. and the singularity at $S_{\zeta e}$ – where the denominator on the r.h.s. in the above equation becomes zero – the encounter spectrum is not used in seakeeping computations. However, it is needed for the analysis of data if these were measured from a ship with forward speed.

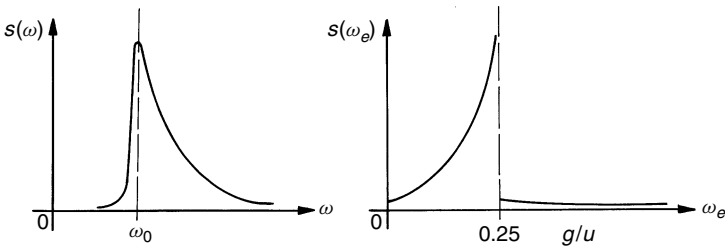


Figure 4.6 Sea spectrum and corresponding encounter spectrum

4.3.3 Wind and seaway

We distinguish between swell and wind sea. Swell waves have a celerity higher than the present wind speed (e.g. measured in 10 m height above mean sea level; only the component in wave propagation direction is considered). Swell has been excited originally by some stronger winds at some other location and propagates without significant damping or excitation until it is damped in shallow-water regions or excited again to wind sea in stronger winds. By definition, wind sea has celerity less or equal to the wind speed. Due to the gustiness of wind and other factors, the distinction between swell and wind sea is not sharp.

Swell, sometimes also wind sea (for winds changing rapidly in time or space), can change the form of the spectrum considerably. On the other hand, a rather uniform form of a wind sea spectrum is achieved within $\frac{1}{2}$ to 1 hour if the wind is constant in time and space. The relevant area in this context extends over a distance of $(\frac{1}{2}$ to 1 hour)/group velocity of waves in a downwind direction. In the following, we will consider only spectra developed in constant wind. The spectrum parameters, especially wave height and period, converge only after many hours or several days to constant values. The form of the spectrum is determined by the physical processes of:

- wave generation (e.g. the wind resistance of wave crests)
- dissipation (wavebreaking; in shallow water also friction at the ocean bottom)
- convection (transport of wave energy with group velocity)
- non-linear interaction between waves of different frequencies and direction

The directional spectrum is described as the product of a one-dimensional spectrum $S_{\zeta}(\omega)$ with a function f . f describes the distribution of the wave energy over the propagation direction μ assumed to be symmetrical to a main

propagation direction μ_0 :

$$S_\zeta(\omega, \mu) = S_\zeta(\omega) \cdot f(\mu - \mu_0)$$

Söding and Bertram (1998) give a more modern form than the often cited Pierson–Moskowitz and JONSWAP spectra. The older spectra assume a stronger decay of the wave energy at higher frequencies (proportional to ω^{-5} , while more recent measurements indicate a decay proportional to ω^{-4}).

The one-dimensional spectrum $S_\zeta(\omega)$ must be zero for small frequencies (where the wave celerity is much higher than the wind speed) and converge to zero for high frequencies, because high frequency means short waves which in turn can only have small height as the wave steepness before breaking is limited. In between, there must be a maximum. The (circular) frequency where the spectrum assumes its maximum is called modal frequency or peak frequency ω_p . The function $S_\zeta(\omega)$ contains as an important parameter U_c/c_p . U_c is the component of the wind velocity in the main direction of wave propagation, measured in 10 m height. c_p is the celerity of elementary waves of frequency ω_p . c_p is computed using the formula $c_p = g/\omega_p$ which is valid for elementary waves. In reality, waves of frequency ω_p travel some 5 to 10% faster due to their larger steepness. The ratio U_c/c_p lies usually between 1 (fully developed seaway) and 5 (strongly increasing seaway).

$S_\zeta(\omega)$ is written as the product of three factors:

- an initial factor $\alpha g^2/\omega_p^5$
- a ‘base form’ containing the ω dependency (corresponding to the Pierson–Moskowitz spectrum widely used previously)
- a peak enhancement factor γ^Γ independent of U_c/c_p :

$$S_\zeta(\omega) = \frac{\alpha g^2}{\omega_p^5} \cdot \left(\frac{\omega_p}{\omega}\right)^4 \exp\left[-\left(\frac{\omega_p}{\omega}\right)^4\right] \cdot \gamma^\Gamma$$

with:

$$\alpha = 0.006(U_c/c_p)^{0.55}$$

Figure 4.7 illustrates α , Fig. 4.8 the base form, and Fig. 4.9 the peak enhancement for three representative values of U_c/c_p . The peak enhancement makes the maximum of the spectrum very pointed for a not fully developed seaway ($U_c/c_p > 1$), while fully developed seaways feature broader and less pronounced maxima. γ describes the maximum of the peak enhancement over ω . It occurs at ω_p and increases the ‘base form’ by a factor of:

$$\gamma = 1.7 + \max[0, 6 \log_{10}(U_c/c_p)]$$

Γ describes how the enhancement factor decays left and right of the model frequency ω_p ; for this purpose a formula corresponding to a normal (Gaussian) distribution is chosen (but without a forefactor; thus the maximum of Γ is 1):

$$\Gamma = \exp\left(-\frac{(\omega/\omega_p - 1)^2}{2\sigma^2}\right) \quad \text{with}$$

$$\sigma = 0.08[1 + 4/(U_c/c_p)^3]$$

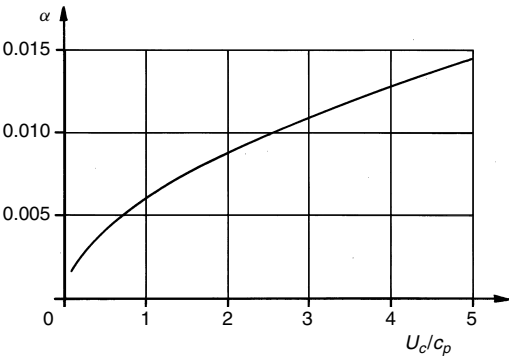


Figure 4.7 Spectrum factor

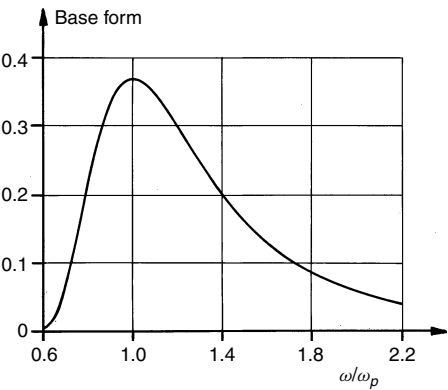


Figure 4.8 Spectrum base form

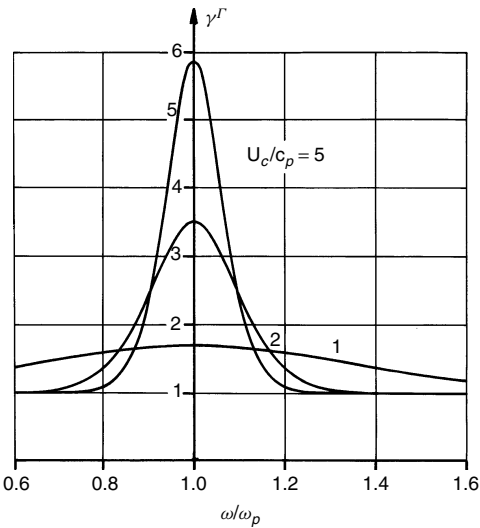


Figure 4.9 Peak enhancement factor

The distribution of the wave energy over the propagation direction $f(\mu - \mu_0)$ is independent of U_c/c_p . Instead, it depends on the non-dimensional frequency ω/ω_p :

$$f(\mu - \mu_0) = 0.5\beta/\cosh^2[\beta(\mu - \mu_0)] \quad \text{with}$$

$$\beta = \max(1.24, 2.61(\omega/\omega_p)^{1.3}) \quad \text{for } \omega/\omega_p < 0.95$$

$$\beta = \max(1.24, 2.28(\omega/\omega_p)^{-1.3}) \quad \text{for } \omega/\omega_p \geq 0.95$$

Figure 4.10 illustrates $f(\mu - \mu_0)$. Figure 4.11 illustrates $\beta(\omega/\omega_p)$.

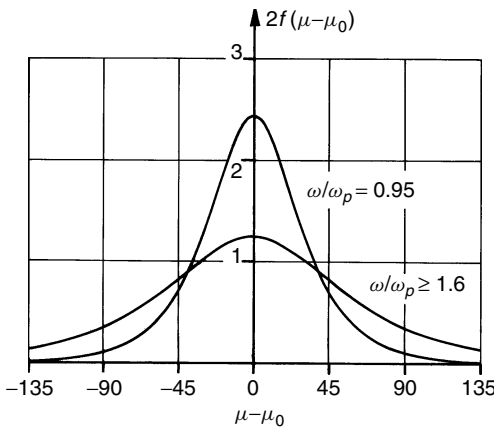


Figure 4.10 Angular distribution of seaway energy

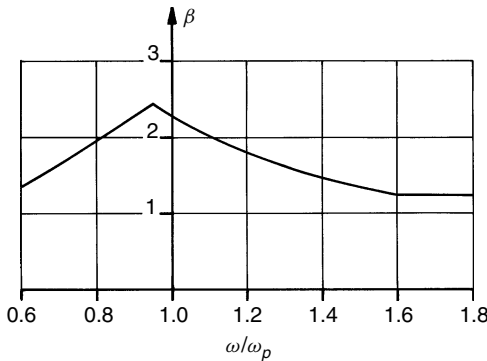


Figure 4.11 Angular spreading β

Since short waves adapt more quickly to the wind than long waves, a changing wind direction results in a frequency-dependent main propagation direction μ_0 . Frequency-dependent μ_0 are also observed for oblique offshore wind near the coast. The wave propagation direction here is more parallel to the coast than the wind direction, because this corresponds to a longer fetch.

The (only statistically defined) wave steepness = wave height/wave length does not depend strongly on the wind velocity, U_c/c_p , or ω/ω_p . The wave steepness is so large that the celerity deviates noticeably from the theoretical values for elementary waves (of small amplitude) as described above. Also, the average shape of the wave profiles deviates noticeably from the assumed sinusoidal wave forms of elementary waves. However, non-linear effects in the waves are usually much weaker than the non-linear effects of ship seakeeping in the seaway.

The significant wave height $H_{1/3}$ of a seaway is defined as the mean of the top third of all waves, measured from wave crest to wave trough. $H_{1/3}$ is related to the area m_0 under the sea spectrum:

$$H_{1/3} = 4\sqrt{m_0} \quad \text{with} \quad m_0 = \int_0^\infty \int_0^{2\pi} S_\xi(\omega, \mu) d\mu d\omega$$

For the above given wind sea spectrum, $H_{1/3}$ can be approximated by:

$$H_{1/3} = 0.21 \frac{U_c^2}{g} \left(\frac{U_c}{c_p} \right)^{-1.65}$$

The modal period is:

$$T_p = 2\pi/\omega_p$$

The periods T_1 and T_2 , which were traditionally popular to describe the seaway, are much shorter than the modal period. T_1 corresponds to the frequency ω where the area under the spectrum has its centre. T_2 is the average period of upward zero crossings.

If we assume that water is initially calm and then a constant wind blows for a duration t and over a distance x , the seaway parameter U_c/c_p becomes approximately:

$$\frac{U_c}{c_p} = \max(1, 18\xi^{-3/10}, 110\theta^{-3/7})$$

ξ is the non-dimensional fetch x , θ the non-dimensional wind duration t :

$$\xi = gx/U_c^2; \quad \theta = gt/U_c$$

The fetch is to be taken downwind from the point where the seaway is considered, but of course at most to the shore. In reality, there is no sudden and then constant wind. But the seakeeping parameters are not very sensitive towards x and t . Therefore it is possible to estimate the seaway with practical accuracy in most cases when the wind field is given.

Table 4.1 shows how the above formulae estimate the seaway parameters $H_{1/3}$ and T_p for various assumed wind durations t for an exemplary wind velocity $U_c = 20$ m/s. The fetch x was assumed to be so large that the centre term in the 'max'-bracket in the above formula for U_c/c_p is always smaller than one of the other two terms. That is, the seaway is not fetch-limited, but either time-limited (for $110\theta^{-3/7} > 1$) or fully developed.

Figure 4.12 shows wind sea spectra for $U_c = 20$ m/s for various fetch values. Figure 4.13 shows the relation between wave period T_p and significant wave

Table 4.1 Sea spectra for various wind duration times for $U_c = 20\text{ m/s}$

Quantity	Case 1	Case 2	Case 3
Assumed wind duration time t (h)	5	20	50
Non-dimensional duration time θ	8 830	35 000	88 000
Maturity parameter U_c/c_p	2.24	1.24	1
Significant wave higher $H_{1/3}$ (m)	2.26	6.00	8.56
$\omega_p = g/c_p = g/U_c \cdot U_c/c_p$ (s ⁻¹)	1.10	0.61	0.49
Modal period $2\pi/\omega_p$ (s)	5.7	10.3	12.8

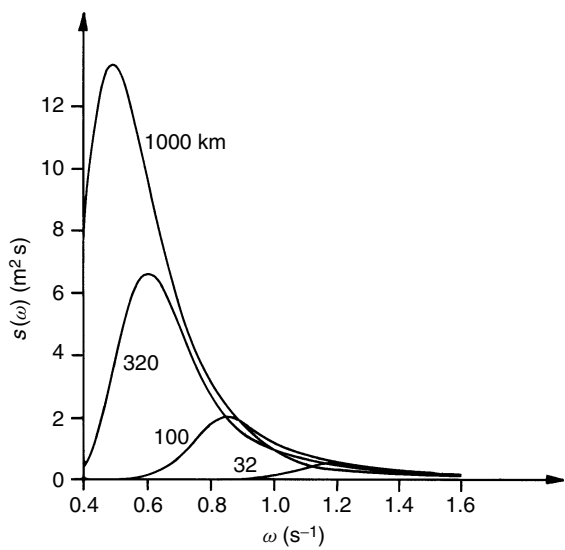


Figure 4.12 Wind sea spectra for $u_c = 20\text{ m/s}$ for various fetch values

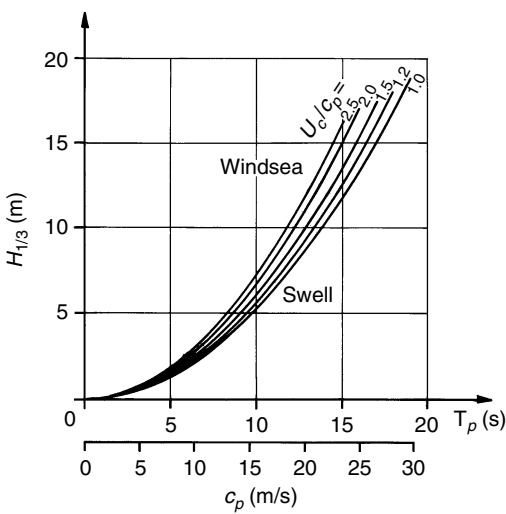


Figure 4.13 Correlation between significant wave height $H_{1/3}$, modal period T_p , wind speed U_c and wave celerity at modal frequency c_p

height $H_{1/3}$ for various values of U_c/c_p . c_p (lower scale) and U_c/c_p together yield the wind velocity U_c that has excited the wind sea characterized by $H_{1/3}$ and T_p . For swell, we can assume $U_c \approx c_p$. Figure 4.14 shows the relation between various seaway parameters, the 'wind force' and the wind velocity U_c .

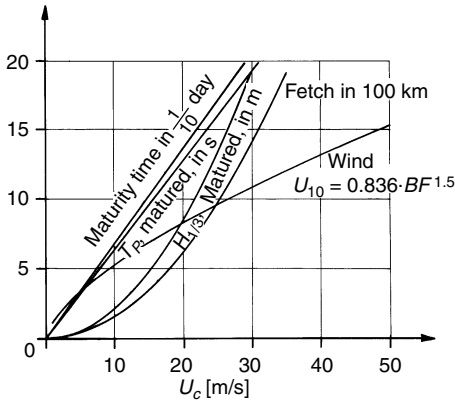


Figure 4.14 Key wind sea parameters depending on the wind speed U_c (component in wave propagation direction in 10 m height)

Programs to compute the given wind sea spectrum from either U_c , t and x or $H_{1/3}$ and T_p are given by Söding (1997).

4.3.4 Wave climate

Predictions of maximum loads, load collectives for fatigue strength analyses etc. require distributions of the significant seaway properties in individual ocean areas. The best sources for such statistics are computations of the seaway based on measured wind fields. ANEP-II (1983) gives such statistical data extensively for North Atlantic, North Sea, Baltic Sea, Mediterranean Sea and Black Sea. Based on these data, Germanischer Lloyd derived distributions for $H_{1/3}$ and T_1 for all of the Atlantic between 50 and 60 longitudinal and the western Atlantic between 40 and 50 longitudinal (Table 4.2). The table is based on data for a period of 10 years. T_1 is the period corresponding to the centre of gravity of the area under the sea spectrum. The modal period is for this table:

$$T_p = T_1/0.77$$

The values in the table give 10^6 the time share when T_1 was in the given time interval and $H_{1/3}$ in the interval denoted by its mean value, at an arbitrary point in the sea area. FCUM denotes the cumulated share in per cent. Similar tables can be derived from ANEP-II and other publications for special seaway directions, seasons and other ocean areas.

Table 4.2 can also be used to approximate other ocean areas by comparing the wind field in the North Atlantic with the wind field in another ocean area,

Table 4.2 Relative occurrence $\cdot 10^6$ of combinations of $H_{1/3}$ and T_1 in the North Atlantic

T_1 (s)			$H_{1/3}$ (m)																
from	to	FCUM	0.5	1.5	2.5	3.5	4.5	5.5	6.5	7.5	8.5	9.5	11.0	13.0	15.0	17.0	19.0	21.0	24.0
1.9	3.1	0.2	2 040	0	0	0	0	0	0	0	0	0	0	0	0	0	0	0	0
3.1	4.3	0.6	2 343	1 324	0	0	0	0	0	0	0	0	0	0	0	0	0	0	0
4.3	5.3	5.3	21 165	25 562	306	0	0	0	0	0	0	0	0	0	0	0	0	0	0
5.3	6.2	14.3	17 770	51 668	20 543	308	0	0	0	0	0	0	0	0	0	0	0	0	0
6.2	7.1	26.4	14 666	38 973	58 152	8 922	0	0	0	0	0	0	0	0	0	0	0	0	0
7.1	7.9	41.6	15 234	29 453	52 102	49 055	6 093	304	0	0	0	0	0	0	0	0	0	0	0
7.9	9.0	57.0	9 918	21 472	33 742	43 660	36 809	7 464	715	0	0	0	0	0	0	0	0	0	0
9.0	10.1	75.9	7 894	21 221	26 655	37 214	39 675	36 189	17 120	2 768	307	0	0	0	0	0	0	0	0
10.1	11.1	85.4	3 062	8 167	11 945	14 497	15 621	15 314	13 579	9 188	3 369	714	0	0	0	0	0	0	0
11.1	12.1	91.3	1 672	4 094	6 034	7 374	8 208	8 467	8 121	6 955	4 845	2 120	822	0	0	0	0	0	0
12.1	13.2	95.2	981	2 185	3 140	3 986	4 659	4 948	4 947	4 726	4 117	3 062	2 318	215	0	0	0	0	0
13.2	14.6	97.7	547	1 038	1 527	2 122	2 418	2 633	2 788	2 754	2 632	2 385	3 043	784	78	0	0	0	0
14.6	16.4	99.1	269	412	719	942	1 069	1 259	1 312	1 374	1 358	1 325	2 246	1 303	378	44	0	0	0
16.4	18.6	99.8	110	124	290	314	424	451	516	534	559	557	1 072	908	544	197	43	3	0
18.6	21.0	100.0	32	32	71	86	106	126	132	151	154	162	327	314	268	187	86	27	5
FCUM			9.8	30.3	51.9	68.7	80.2	87.9	92.9	95.7	97.4	98.5	99.5	99.8	99.9	100.0	100.0	100.0	100.0

using data of Blendermann (1998), and employing the relation between wind and sea as given in the previous chapter.

4.4 Numerical prediction of ship seakeeping

4.4.1 Overview of computational methods

If the effect of the wave amplitude on the ship seakeeping is significantly non-linear, there is little sense in investigating the ship in elementary waves, since these waves do not appear in nature and the non-linear reaction of the ship in natural seaways cannot be deduced from the reaction in elementary waves. In these non-linear cases, simulation in the time domain is the appropriate tool for numerical predictions.

However, if the non-linearity is weak or moderate the seakeeping properties of a ship in natural seaways can be approximated by superposition of the reactions in elementary waves of different frequency and direction. In these cases, the accuracy can be enhanced by introducing some relatively simple corrections of the purely linear computations to account for force contributions depending quadratically on the water velocity or considering the time-dependent change of position and wetted surface of the ship, for example. Even if iterative corrections are applied the basic computations of the ship seakeeping is still based on its reaction in elementary waves, expressed by complex amplitudes of the ship reactions. The time dependency is then always assumed to be harmonic, i.e. sinusoidal.

The Navier–Stokes equation (conservation of momentum) and the continuity equation (conservation of mass) suffice in principle to describe all phenomena of ship seakeeping flows. However, we neither can nor want to resolve all little turbulent fluctuations in the ship's boundary layer and wake. Therefore we average over time intervals which are long compared to the turbulent fluctuations and short compared to the wave periods. This then yields the Reynolds-averaged Navier–Stokes equations (RANSE). By the late 1990s RANSE computations for ship seakeeping were subject to research, but were still limited to selected simplified problems.

If viscosity is neglected the RANSE turn into the Euler equations. Euler solvers do not have to resolve the boundary layers (no viscosity = no boundary layer) and allow thus coarser grids and considerably shorter computational times. By the late 1990s, Euler solvers were also still limited to simplified problems in research applications, typically highly non-linear free surface problems such as slamming of two-dimensional sections.

In practice, potential flow solvers are used almost exclusively in seakeeping predictions. The most frequent application is the computation of the linear seakeeping properties of a ship in elementary waves. In addition to the assumption for Euler solvers potential flow assumes that the flow is irrotational. This is no major loss in the physical model, because rotation is created by the water adhering to the hull and this information is already lost in the Euler flow model. Relevant for practical applications is that potential flow solvers are much faster than Euler and RANSE solvers, because potential flows have to solve only one linear differential equation instead of four non-linear coupled differential equations. Also potential flow solvers are usually based on boundary element methods and need only to discretize the boundaries of the domain, not the

whole fluid space. This reduces the effort in grid generation (the main cost item in most analyses) considerably. On the other hand, potential flow methods require a simple, continuous free surface. Flows involving breaking waves and splashes can hardly be analysed properly by potential flow methods.

In reality, viscosity is significant in seakeeping, especially if the boundary layer separates periodically from the hull. This is definitely the case for roll and yaw motions. In practice, empirical corrections are introduced. Also, for flow separation at sharp edges in the aftbody (e.g. vertical sterns, rudder, or transoms) a Kutta condition is usually employed to enforce a smooth detachment of the flow from the relevant edge.

The theoretical basics and boundary conditions of linear potential methods for ship seakeeping are treated extensively in the literature, e.g. by Newman (1978). Therefore, we can limit ourselves here to a short description of the fundamental results important to the naval architect.

The ship flow in elementary waves is described in a coordinate system moving with ship speed in the x direction, but not following its periodic motions. The derivatives of the potential give the velocity of water relative to such a coordinate system. The total velocity potential is decomposed:

$$\phi^t = (-Vx + \phi^s) + (\phi^w + \phi^I)$$

with ϕ^t potential of total flow

$-Vx$ potential of (downstream) uniform flow with ship speed V

ϕ^s potential of the steady flow disturbance

ϕ^w potential of the undisturbed wave as given at the end of section 4.3.1

ϕ^I remaining unsteady potential

The first parenthesis describes only the steady (time-independent) flow, the second parenthesis the periodic flow due to sea waves. The potentials can be simply superimposed, since the fundamental field equation (Laplace equation, describing continuity of mass) is linear with respect to ϕ^t :

$$\Delta\phi^t = \left(\frac{\partial^2}{\partial x^2} + \frac{\partial^2}{\partial y^2} + \frac{\partial^2}{\partial z^2} \right) \phi^t = 0$$

Various approximations can be used for ϕ^s and ϕ^I which affect computational effort and accuracy of results. The most important linear methods can be classified as follows:

- *Strip method*

Strip methods are the standard tool for ship seakeeping computations. They omit ϕ^s completely and approximate ϕ^I in each strip $x = \text{constant}$ independently of the other strips. Thus in essence the three-dimensional problem is reduced to a set (e.g. typically 10 to 30) of two-dimensional boundary value problems. This requires also a simplification of the actual free surface condition. The method originated in the late 1950s with work of Korvin-Kroukovsky and Jacobs. Most of today's strip methods are variations of the strip method proposed by Salvesen, Tuck and Faltinsen (1970). These are sometimes also called STF strip methods where the first letter of each author is taken to form the abbreviation. The two-dimensional problem

for each strip can be solved analytically or by panel methods, which are the two-dimensional equivalent of the three-dimensional methods described below. The analytical approaches use conform mapping to transform semi-circles to cross-sections resembling ship sections (Lewis sections). Although this transformation is limited and, e.g., submerged bulbous bow sections cannot be represented in satisfactory approximation, this approach still yields for many ships results of similar quality as strip methods based on panel methods (close-fit approach). A close-fit approach (panel method) to solve the two-dimensional problem will be described in section 7.4, Chapter 7. Strip methods are – despite inherent theoretical shortcomings – fast, cheap and for most problems sufficiently accurate. However, this depends on many details. Insufficient accuracy of strip methods often cited in the literature is often due to the particular implementation of a code and not due to the strip method in principle. But at least in their conventional form, strip methods fail (as most other computational methods) for waves shorter than perhaps $\frac{1}{3}$ of the ship length. Therefore, the added resistance in short waves (being considerable for ships with a blunt waterline) can also only be estimated by strip methods if empirical corrections are introduced. Section 4.4.2 describes a linear strip method in more detail.

- *Unified theory*

Newman (1978) and Sclavounos developed at the MIT the ‘unified theory’ for slender bodies. Kashiwagi (1997) describes more recent developments of this theory. In essence, the theory uses the slenderness of the ship hull to justify a two-dimensional approach in the near field which is coupled to a three-dimensional flow in the far field. The far-field flow is generated by distributing singularities along the centreline of the ship. This approach is theoretically applicable to all frequencies, hence ‘unified’. Despite its better theoretical foundation, unified theories failed to give significantly and consistently better results than strip theories for real ship geometries. The method therefore failed to be accepted by practice.

- *‘High-speed strip theory’ (HSST)*

Several authors have contributed to the high-speed strip theory after the initial work of Chapman (1975). A review of work since then can be found in Kashiwagi (1997). HSST usually computes the ship motions in an elementary wave using linear potential theory. The method is often called $2\frac{1}{2}$ dimensional, since it considers the effect of upstream sections on the flow at a point x , but not the effect of downstream sections. Starting at the bow, the flow problem is solved for individual strips (sections) $x = \text{constant}$. The boundary conditions at the free surface and the hull (strip contour) are used to determine the wave elevation and the velocity potential at the free surface and the hull. Derivatives in longitudinal direction are computed as numerical differences to the upstream strip which has been computed in the previous step. The computation marches downstream from strip to strip and ends at the stern resp. just before the transom. HSST is the appropriate tool for fast ships with Froude numbers $F_n > 0.4$. For lower Froude numbers, it is inappropriate.

- *Green function method (GFM)*

ISSC (1994) gives a literature review of these methods. GFM distribute panels on the average wetted surface (usually for calm-water floating position neglecting dynamical trim and sinkage and the steady wave profile) or

on a slightly submerged surface inside the hull. The velocity potential of each panel (Green function) fulfils automatically the Laplace equation, the radiation condition (waves propagate in the right direction) and a simplified free-surface condition (omitting the ϕ^s completely). The unknown (either source strength or potential) is determined for each element by solving a linear system of equations such that for each panel at one point the no-penetration condition on the hull (zero normal velocity) is fulfilled. The various methods, e.g. Ba and Guilbaud (1995), Iwashita (1997), differ primarily in the way the Green function is computed. This involves the numerical evaluation of complicated integrals from 0 to ∞ with highly oscillating integrands. Some GFM approaches formulate the boundary conditions on the ship under consideration of the forward speed, but evaluate the Green function only at zero speed. This saves a lot of computational effort, but cannot be justified physically and it is not recommended.

As an alternative to the solution in the frequency domain (for excitation by elementary waves), GFM may also be formulated in the time domain (for impulsive excitation). This avoids the evaluation of highly oscillating integrands, but introduces other difficulties related to the proper treatment of time history of the flow in so-called convolution integrals. Both frequency and time domain solutions can be superimposed to give the response to arbitrary excitation, e.g. by natural seaway, assuming that the problem is linear.

All GFMs are fundamentally restricted to simplifications in the treatment of ϕ^s . Usually ϕ^s is completely omitted which is questionable for usual ship hulls. It will introduce, especially in the bow region, larger errors in predicting local pressures.

- *Rankine singularity method (RSM)*

Bertram and Yasukawa (1996) give an extensive overview of these methods covering both frequency and time domains. RSM, in principle, capture ϕ^s completely and also more complicated boundary conditions on the free surface and the hull. In summary, they offer the option for the best approximation of the seakeeping problem within potential theory. This comes at a price. Both ship hull and the free surface in the near field around the ship have to be discretized by panels. Capturing all waves while avoiding unphysical reflections of the waves at the outer (artificial) boundary of the computational domain poses the main problem for RSM. Since the early 1990s, various RSM for ship seakeeping have been developed. By the end of the 1990s, the time-domain SWAN code (SWAN = Ship Wave ANALysis) of MIT was the first such code to be used commercially.

- *Combined RSM–GFM approach*

GFM are fundamentally limited in the capturing the physics when the steady flow differs considerably from uniform flow, i.e. in the near field. RSM have fundamental problems in capturing the radiation condition for low τ values. Both methods can be combined to overcome the individual shortcomings and to combine their strengths. This is the idea behind combined approaches. These are described as ‘Combined Boundary Integral Equation Methods’ by the Japanese, and as ‘hybrid methods’ by Americans. Initially only hybrid methods were used which matched near-field RSM solutions directly to far-field GFM solutions by introducing vertical control surfaces at the outer boundary of the near field. The solutions are matched by requiring that the potential and its normal derivative are continuous at the control surface

between near field and far field. In principle methods with overlapping regions also appear possible.

4.4.2 Strip method

This section presents the most important formulae for a linear frequency-domain strip method for slender ships in elementary waves. The formulae will be given without derivation. For a more extensive coverage of the theoretical background, the reader is referred to Newman (1978).

Two coordinate systems are used:

- The ship-fixed system x, y, z , with axes pointing from amidships forward, to starboard and downwards. In this system, the ship's centre of gravity is time independent x_g, y_g, z_g .
- The inertial system ξ, η, ζ . This system follows the steady forward motion of the ship with speed V and coincides in the time average with the ship-fixed system.

The main purpose of the strip method is to compute the ship's rigid-body motions, i.e. the three translations of the origin of ship-fixed system in the ξ, η, ζ direction and the three rotations around these axes. We denote, (Fig. 4.15):

u_1 surge u_4 roll
 u_2 sway u_5 pitch
 u_3 heave u_6 yaw

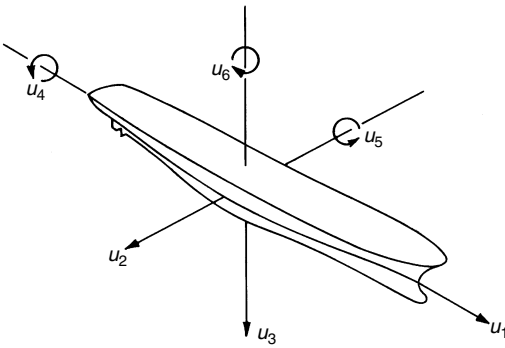


Figure 4.15 Six degrees of freedom for motions

The motions are combined in a six-component vector \vec{u} . The forces and moments acting on the ship are similarly combined in a six-component vector \vec{F} . \vec{u} and \vec{F} are harmonic functions of time t oscillating with encounter frequency ω_e :

$$\vec{F} = \text{Re}(\hat{F}e^{i\omega_e t})\vec{u} = \text{Re}(\hat{u}e^{i\omega_e t})$$

The fundamental equation of motion is derived from $\vec{F} = M \cdot \ddot{\vec{u}}$:

$$[-\omega_e^2(M + A) + i\omega_e N + S]\hat{\vec{u}} = \hat{\vec{F}}_e$$

Here M , A , N and S are real-valued 6×6 matrices. For mass distribution symmetrical to $y = 0$ the mass matrix M is:

$$M = \begin{bmatrix} m & 0 & 0 & 0 & mz_g & 0 \\ 0 & m & 0 & -mz_g & 0 & mx_g \\ 0 & 0 & m & 0 & -mx_g & 0 \\ 0 & -mz_g & 0 & \theta_{xx} & 0 & -\theta_{xz} \\ mz_g & 0 & -mx_g & 0 & \theta_{yy} & 0 \\ 0 & mx_g & 0 & -\theta_{xz} & 0 & -\theta_{zz} \end{bmatrix}$$

The mass moments of inertia θ are related to the origin of the ship-fixed coordinate system:

$$\theta_{xx} = \int (y^2 + z^2) dm; \quad \theta_{xz} = \int xz dm; \quad \text{etc.}$$

If we neglect contributions from a dry transom stern and other hydrodynamic forces due to the forward speed of the ship, the restoring forces matrix S is:

$$S = \begin{bmatrix} 0 & 0 & 0 & 0 & 0 & 0 \\ 0 & 0 & 0 & 0 & 0 & 0 \\ 0 & 0 & \rho g A_w & 0 & -\rho g A_w x_w & 0 \\ 0 & 0 & 0 & gm\overline{GM} & 0 & 0 \\ 0 & 0 & -\rho g A_w x_w & 0 & gm\overline{GM}_L & 0 \\ 0 & 0 & 0 & 0 & 0 & \theta_{zz}\omega_g^2 \end{bmatrix}$$

Here A_w is the waterline area, x_w the x coordinate of the centre of the waterline, \overline{GM} the metacentric height, \overline{GM}_L the longitudinal metacentric height, ω_g the circular eigenfrequency of yaw motions. ω_g is determined by the control characteristics of the autopilot and usually has little influence on the yaw motions in seaways. In computing \overline{GM}_L , the moment of inertia is taken with respect to the origin of the coordinate system (usually amidships) and not, as usual, with respect to the centre of the waterline. For corrections for dry transoms and unsymmetrical bodies reference is made to Söding (1987).

N is the damping matrix; it contains mainly the effect of the radiated waves. A is the added mass matrix. (Readers unfamiliar with the concept of added mass should now read the discourse on added mass.) The decomposition of the force into hydrostatic (S) and hydrodynamic (A) components is somewhat arbitrary, especially for the ship with forward speed. Therefore, comparisons between computations and experiments often are based on the term $-\omega_e^2 A + S$.

\vec{F}_e is the vector of exciting forces which a wave would exert on a ship fixed on its average position (diffraction problem). The exciting forces can be decomposed into a contribution due to the pressure distribution in the undisturbed incident wave (Froude–Krilov force) and the contribution due to the disturbance by the ship (diffraction force). Both contributions are of similar order of magnitude.

To determine A and N , the flow due to the harmonic ship motions \vec{u} must be computed (radiation problem). For small frequency of the motion (i.e. large

wave length of the radiated waves), the hydrostatic forces dominated and the hydrodynamic forces are almost negligible. Therefore large relative errors in computing A and N are acceptable. For high frequencies, the crests of the waves radiated by the ship motions are near the ship almost parallel to the ship hull, i.e. predominantly in longitudinal direction. Therefore the longitudinal velocity component of the radiated waves can be neglected. Then only the two-dimensional flow around the ship sections (strips) must be determined. This simplifies the computations a great deal.

For the diffraction problem (disturbance of the wave due to the ship hull), which determines the exciting forces \bar{F}_e , a similar reasoning does not hold: unlike radiation waves (due to ship motions), diffraction waves (due to partial reflection at the hull and distortion beyond the hull) form a similar angle (except for sign) with the hull as the incident wave. Therefore, for most incident waves, the diffraction flow will feature also considerable velocities in longitudinal direction. These cannot be considered in a regular strip method, i.e. if we want to consider all strips as hydrodynamically independent. This error is partially compensated by computing the diffraction flow for wave frequency ω instead of encounter frequency ω_e , but a residual error remains. To avoid also these residual errors, sometimes \bar{F}_e is determined indirectly from the radiation potential following formulae of Newman (1965). However, these formulae are only valid if the waterline is also streamline. This is especially not true for ships with submerged transom sterns.

For the determination of the radiation and (usually also) diffraction (=exciting) forces, the two-dimensional flow around an infinite cylinder of same the cross-section as the ship at the considered position is solved, (Fig. 4.16). The flow is generated by harmonic motions of the cylinder (radiation) or an incident wave (diffraction). Classical methods used analytical

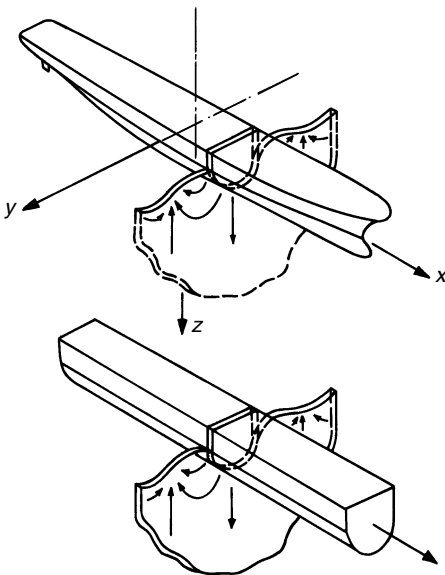


Figure 4.16 Principle of strip method

solutions based on multipole methods. Today, usually two-dimensional panel methods are preferred due to their (slightly) higher accuracy for realistic ship geometries. These two-dimensional panel methods can be based on GFM or RSM, see previous chapter.

The flow and thus the pressure distribution depends on

- for the radiation problem:
hull shape, frequency ω_e , and direction of the motion (vertical, horizontal, rotational)
- for the diffraction problem:
hull shape, wave frequency ω , and encounter angle μ

For the radiation problem, we compute the pressure distributions for unit amplitude motions in one degree of freedom and set all other motions to zero and omit the incident wave. For the diffraction problem, we set all motions to zero and consider only the incident wave and its diffraction. We denote the resulting pressures by:

- \hat{p}_2 for horizontal unit motion of the cylinder
- \hat{p}_3 for vertical unit motion of the cylinder
- \hat{p}_4 for rotational unit motion of the cylinder around the x axis
- \hat{p}_0 for the fixed cylinder in waves (only the pressure in the undisturbed wave)
- \hat{p}_7 for the fixed cylinder in waves (only the disturbance of the pressure due to the body)

Let the actual motions of the cylinder in a wave of amplitude \hat{h}_x be described by the complex amplitudes $\hat{u}_{2,0x}$, $\hat{u}_{3,0x}$, $\hat{u}_{4,0x}$. Then the complex amplitude of the harmonic pressure is:

$$\hat{p}_i = \hat{p}_2 \hat{u}_{2,0x} + \hat{p}_3 \hat{u}_{3,0x} + \hat{p}_4 \hat{u}_{4,0x} + (\hat{p}_0 + \hat{p}_7) \hat{h}_x$$

The amplitudes of the forces per length on the cylinder are obtained by integrating the pressure over the wetted surface of a cross-section (wetted circumference):

$$\begin{aligned} \begin{Bmatrix} \hat{f}_2 \\ \hat{f}_3 \\ \hat{f}_4 \end{Bmatrix} &= \int_0^l \begin{Bmatrix} n_2 \\ n_3 \\ yn_3 - zn_2 \end{Bmatrix} \cdot \hat{p}_i d\ell \\ &= \int_0^l \begin{Bmatrix} n_2 \\ n_3 \\ yn_3 - zn_2 \end{Bmatrix} \cdot (\hat{p}_2, \hat{p}_3, \hat{p}_4, \hat{p}_0 + \hat{p}_7) d\ell \cdot \begin{Bmatrix} \hat{u}_{2,0x} \\ \hat{u}_{3,0x} \\ \hat{u}_{4,0x} \\ \hat{h}_x \end{Bmatrix} \end{aligned}$$

$\{0, n_2, n_3\}$ is here in the inward unit normal on the cylinder surface. The index x in the last vector indicates that all quantities are taken at the longitudinal coordinate x at the ship, i.e. the position of the strip under consideration. ℓ is the circumferential length coordinate of the wetted contour. We can write the above equation in the form:

$$\hat{\vec{f}} = \hat{H} \cdot \{\hat{u}_{2,0x}, \hat{u}_{3,0x}, \hat{u}_{4,0x}, \hat{h}_x\}^T$$

The elements of the matrix \hat{H} , obtained by the integrals over the wetted surface in the above original equation, can be interpreted as added masses a_{ij} , damping n_{ij} and exciting forces per wave amplitude \hat{f}_{ei} :

$$\hat{H} = \begin{bmatrix} \omega_e^2 a_{22} - i\omega_e n_{22} & 0 & \omega_e^2 a_{24} - i\omega_e n_{24} & \hat{f}_{e2} \\ 0 & \omega_e^2 a_{33} - i\omega_e n_{33} & 0 & \hat{f}_{e3} \\ \omega_e^2 a_{42} - i\omega_e n_{42} & 0 & \omega_e^2 a_{44} - i\omega_e n_{44} & \hat{f}_{e4} \end{bmatrix}$$

For example, a_{22} is the added mass per cylinder length for horizontal motion.

The added mass tends towards infinity as the frequency goes to zero. However, the effect of the added mass also goes to zero for small frequencies, as the added mass is multiplied by the square of the frequency.

The forces on the total ship are obtained by integrating the forces per length (obtained for the strips) over the ship length. For forward speed, the harmonic pressure according to the linearized Bernoulli equation contains also a product of the constant ship speed $-V$ and the harmonic velocity component in the x direction. Also, the strip motions denoted by index x have to be converted to global ship motions in 6 degrees of freedom. This results in the global equation of motion:

$$[S - \omega_e^2(M + \hat{B})]\hat{u} = \hat{E}h$$

\hat{B} is a complex matrix. Its real part is the added mass matrix A . Its imaginary part is the damping matrix N :

$$\omega_e^2 \hat{B} = \omega_e^2 A - i\omega_e N = \int_L V(x) \cdot \left(1 + \frac{iV}{\omega_e} \frac{\partial}{\partial x}\right) (\hat{H}_B \cdot W(x)) dx$$

This equation can be used directly to compute \hat{B} , e.g. using the trapezoidal rule for the integrals and numerical difference schemes for the differentiation in x . Alternatively, partial integration can remove the x derivatives. The new quantities in the above equations are defined as:

$$\hat{\hat{E}} = \frac{\hat{\hat{F}}_E}{h} = \int_L V(x) \left(\hat{H}_E + \frac{iV}{\omega} \frac{\partial \hat{H}_{E7}}{\partial x} \right) e^{ikx \cos \mu} dx$$

$$W(x) = \begin{bmatrix} 0 & 1 & 0 & t_x & 0 & x - V/(i\omega_e) \\ 0 & 0 & 1 & 0 & -x + V/(i\omega_e) & 0 \\ 0 & 0 & 0 & 1 & 0 & 0 \end{bmatrix}$$

t_x is the z coordinate (in the global ship system) of the origin of the reference system for a strip. (Often a strip reference system is chosen with origin in the waterline, while the global ship coordinate system may have its origin on the keel.)

$$V(x) = \begin{bmatrix} 1 & 0 & 0 & 0 & 0 \\ 0 & 1 & 0 & 0 & 0 \\ 0 & 0 & 1 & 0 & 0 \\ 0 & t_x & 0 & 1 & 0 \\ -t_x & 0 & -x & 0 & 1 \\ 0 & x & 0 & 0 & 0 \end{bmatrix}$$

$$\hat{H}_B = \begin{bmatrix} 0 & 0 & 0 \\ \omega_e^2 a_{22} - i\omega_e n_{22} & 0 & \omega_e^2 a_{24} - i\omega_e n_{24} \\ 0 & \omega_e^2 a_{33} - i\omega_e n_{33} & 0 \\ \omega_e^2 a_{42} - i\omega_e n_{42} & 0 & \omega_e^2 a_{44} - i\omega_e n_{44} \\ 0 & 0 & 0 \end{bmatrix}$$

$$\hat{H}_E = \begin{Bmatrix} -i\rho g k A_x \cos \mu \\ \hat{f}_{e2} \\ \hat{f}_{e3} \\ \hat{f}_{e4} \\ -i\rho g k A_x s_x \cos \mu \end{Bmatrix}$$

A_x is the submerged section area at x ; s_x is the vertical coordinate of the centre of the submerged section area in the global system. \hat{H}_E contains both the Froude–Krilov part from the undisturbed wave (Index 0) and the diffraction part (Index 7), while \hat{H}_{E7} contains only the diffraction part.

The formulae for \hat{B} and \hat{E} contain x derivatives. At locations x , where the ship cross-section changes suddenly (propeller aperture, vertical stem, submerged transom stern), this would result in extremely high forces per length. To a large extent, this is actually true at the bow, but not at the stern. If the cross-sections decrease rapidly there, the streamlines separate from the ship hull. The momentum (which equals added mass of the cross-section times velocity of the cross-section) remains then in the ship's wake while the above formulae would yield in strict application zero momentum behind the ship as the added mass \hat{H} is zero there. Therefore, the integration of the x derivatives over the ship length in the above formulae has to end at such locations of flow separation in the aftbody.

The global equation of motion above yields the vector of the response amplitude operators (RAOs) (=complex amplitude of reaction/wave amplitude) for the ship motions:

$$\frac{\hat{u}}{h} = (S - \omega_e^2 [M + \hat{B}])^{-1} \cdot \hat{E}$$

The effect of rudder actions due to course deviations (yaw oscillations) was already considered in the matrix S . In addition, there are forces on the rudder (and thus the ship) due to ship motions (for centrally located rudders only due to sway, yaw, and roll) and due to the incident wave. Here it is customary to incorporate the rudder in the model of the rigid ship filling the gaps between rudder and ship. (While this is sufficient for the computation of the ship motions, it is far too crude if the forces on the rudder in a seaway are to be computed.)

Accurate computation of the motions, pressures, internal forces etc. requires further additions and corrections, e.g. to capture the influence of non-linear effects especially for roll motion, treatment of low encounter frequencies, influence of bilge keels, stabilizing fins etc. The special and often empirical treatment of these effects differs in various strip methods. Details can be found in the relevant specialized literature.

4.4.3 Rankine singularity methods

Bertram and Yasukawa (1996) give an extensive survey of these methods. A linear frequency-domain method is described briefly here to exemplify the general approach. Section 7.5, Chapter 7, treats this panel method in more detail.

In principle, RSM can completely consider ϕ^s . If ϕ^s is completely captured the methods are called ‘fully three dimensional’ to indicate that they capture both the steady and the harmonic flow three dimensionally. In this case, first the ‘fully non-linear’ wave resistance problem is solved to determine ϕ^s and its derivatives, including second derivatives of ϕ^s on the hull. The solution yields also all other steady flow effects, namely dynamic trim and sinkage, steady wave profile on the hull, steady and the wave pattern on the free surface. Then the actual seakeeping computations can be performed considering the interaction between steady and harmonic flow components. The boundary conditions for ϕ^l are linearized with regard to wave amplitude h and quantities proportional to h , e.g. ship motions. The Laplace equation (mass conservation) is solved subject to the boundary conditions:

1. Water does not penetrate the hull.
2. Water does not penetrate the free surface.
3. At the free surface there is atmospheric pressure.
4. Far away from the ship, the flow is undisturbed.
5. Waves generated by the ship radiate away from the ship.
6. Waves generated by the ship are not reflected at the artificial boundary of the computational domain.
7. For antisymmetric motions (sway, roll, yaw), a Kutta condition is enforced on the stern.
8. Forces (and moments) not in equilibrium result in ship motions.

For $\tau = \omega_e V/g > 0.25$ waves generated by the ship travel only downstream, similar to the steady wave pattern. Thus also the same numerical techniques as for the steady wave resistance problem can be used to enforce proper radiation, e.g. shifting source elements relative to collocation points downstream. Values $\tau < 0.25$ appear especially in following waves. Various techniques have been proposed for this case, as discussed in Bertram and Yasukawa (1996). However, there is no easy and accurate way in the frequency domain. In the time domain, proper radiation follows automatically and numerical beaches have to be introduced to avoid reflection at the outer boundary of the computational domain.

We split here the six-component motion vector of the chapter for the strip method approach into two three-component vectors. $\vec{u} = \{u_1, u_2, u_3\}^T$ describes the translations, $\vec{\alpha} = \{u_4, u_5, u_6\}^T = \{\alpha_1, \alpha_2, \alpha_3\}^T$ the rotations. The velocity potential is again decomposed as in section 4.4.1:

$$\phi^l = (-Vx + \phi^s) + (\phi^w + \phi^l)$$

The steady potential ϕ^s is determined first. Typically, a ‘fully non-linear’ wave resistance code employing higher-order panels is used also to determine second derivatives of the potential on the hull. Such higher-order panels are described

in the section on boundary elements. ϕ^w is the incident wave as in section 4.3:

$$\phi^w = \text{Re}(-i\hat{c}\hat{h}e^{-kz}e^{-ik(x\cos\mu - y\sin\mu)}e^{i\omega_e t})$$

The wave amplitude is chosen to $\hat{h} = 1$.

The remaining unknown potential ϕ^I is decomposed into diffraction and radiation components:

$$\phi^I = \phi^d + \sum_{i=1}^6 \phi^i u_i$$

The boundary conditions 1–3 and 7 are numerically enforced in a collocation scheme, i.e. at selected individual points. The remaining boundary conditions are automatically fulfilled in a Rankine singularity method. Combining 2 and 3 yields the boundary condition on the free surface, to be fulfilled by the unsteady potential $\phi^{(1)} = \phi^w + \phi^I$:

$$\begin{aligned} &(-\omega_e^2 + Bi\omega_e)\hat{\phi}^{(1)} + ([2i\omega_e + B]\nabla\phi^{(0)} + \vec{a}^{(0)} + \vec{a}^g)\nabla\hat{\phi}^{(1)} \\ &+ \nabla\phi^{(0)}(\nabla\phi^{(0)}\nabla)\nabla\hat{\phi}^{(1)} = 0 \end{aligned}$$

With:

$$\begin{aligned} \phi^{(0)} &= -Vx + \phi^s && \text{steady potential} \\ \vec{a} &= (\nabla\phi^{(0)}\nabla)\nabla\phi^{(0)} && \text{steady particle acceleration} \\ \vec{a}^g &= \vec{a} - \{0, 0, g\}^T \\ B &= -(1/a_3^g)\partial(\nabla\phi^{(0)}\vec{a}^g)/\partial z \\ \nabla &= \{\partial/\partial x, \partial/\partial y, \partial/\partial z\}^T \end{aligned}$$

The boundary condition 1 yields on the ship hull

$$\vec{n}\nabla\hat{\phi}^{(1)} + \hat{u}(\vec{m} - i\omega_e\vec{n}) + \hat{\alpha}[\vec{x} \times (\vec{m} - i\omega_e\vec{n}) + \vec{n} \times \nabla\phi^{(0)}] = 0$$

Here the m terms have been introduced:

$$\vec{m} = (\vec{n}\nabla)\nabla\phi^{(0)}$$

Vectors \vec{n} and \vec{x} are to be taken in the ship-fixed system.

The diffraction potential ϕ^d and the six radiation potentials ϕ^i are determined in a panel method that can employ regular first-order panels. The panels are distributed on the hull and on (or above) the free surface around the ship. The Kutta condition requires the introduction of additional dipole (or alternatively vortex) elements. The preferred choice here are Thiert elements, see section 6.4.2, Chapter 6.

Test computations for a container ship (standard ITTC test case S-175) have shown a significant influence of the Kutta condition for sway, yaw and roll motions for small encounter frequencies.

To determine ϕ^d , all motions ($u_i, i = 1$ to 6) are set to zero. To determine the ϕ^i , the corresponding u_i is set to 1, all other motion amplitudes, ϕ^d and ϕ^w

to zero. Then the boundary conditions form a system of linear equations for the unknown element strengths which is solved, e.g., by Gauss elimination. Once the element strengths are known, all potentials and derivatives can be computed.

For the computation of the total potential ϕ^t , the motion amplitudes u_i remain to be determined. The necessary equations are supplied by the momentum equations:

$$m(\ddot{\vec{u}} + \ddot{\vec{\alpha}} \times \vec{x}_g) = -\vec{\alpha} \times \vec{G} + \int (p^{(1)} - \rho[\vec{u}\vec{a}^g + \vec{\alpha}(\vec{x} \times \vec{a}^g)]) \vec{n} dS$$

$$m(\vec{x}_g \times \ddot{\vec{u}}) + I\ddot{\vec{\alpha}} = -\vec{x}_g \times (\vec{\alpha} \times \vec{G}) + \int (p^{(1)} - \rho[\vec{u}\vec{a}^g + \vec{\alpha}(\vec{x} \times \vec{a}^g)]) \times (\vec{x} \times \vec{n}) dS$$

$G = gm$ is the ship's weight, \vec{x}_g its centre of gravity and I the matrix of the moments of inertia of the ship (without added masses) with respect to the coordinate system. I is the lower-right 3×3 sub-matrix of the 6×6 matrix M given in the section for the strip method.

The integrals extend over the average wetted surface of the ship. The harmonic pressure $p^{(1)}$ can be decomposed into parts due to the incident wave, due to diffraction, and due to radiation:

$$p^{(1)} = p^w + p^d + \sum_{i=1}^6 p^i u_i$$

The pressures p^w , p^d and p^i , collectively denoted by p^j , are determined from the linearized Bernoulli equation as:

$$p^j = -\rho(\phi_t^j + \nabla\phi^{(0)}\nabla\phi^j)$$

The two momentum vector equations above form a linear system of equations for the six motions u_i which is easily solved.

The explicit consideration of the steady potential ϕ^s changes the results for computed heave and pitch motions for wave lengths of similar magnitude as the ship length – these are the wave lengths of predominant interest – by as much as 20–30% compared to total neglect. The results for standard test cases such as the Series-60 and the S-175 agree much better with experimental data for the ‘fully three-dimensional’ method. For the standard ITTC test case of the S-175 container ship, in most cases good agreement with experiments could be obtained (Fig. 4.17). Only for low encounter frequencies, the antisymmetric motions are overpredicted, probably because viscous effects and autopilot were not modelled at all in the computations.

If ϕ^s is approximated by double-body flow, similar results are obtained as long as the dynamic trim and sinkage are small. However, the computational effort is nearly the same.

Japanese experiments at a tanker model indicate that for full hulls the diffraction pressures in the forebody for short head waves ($\lambda/L = 0.3$ and 0.5) are predicted with errors of up to 50% if ϕ^s is neglected (as typically in GFM or strip methods). Computations with and without consideration of ϕ^s yield large

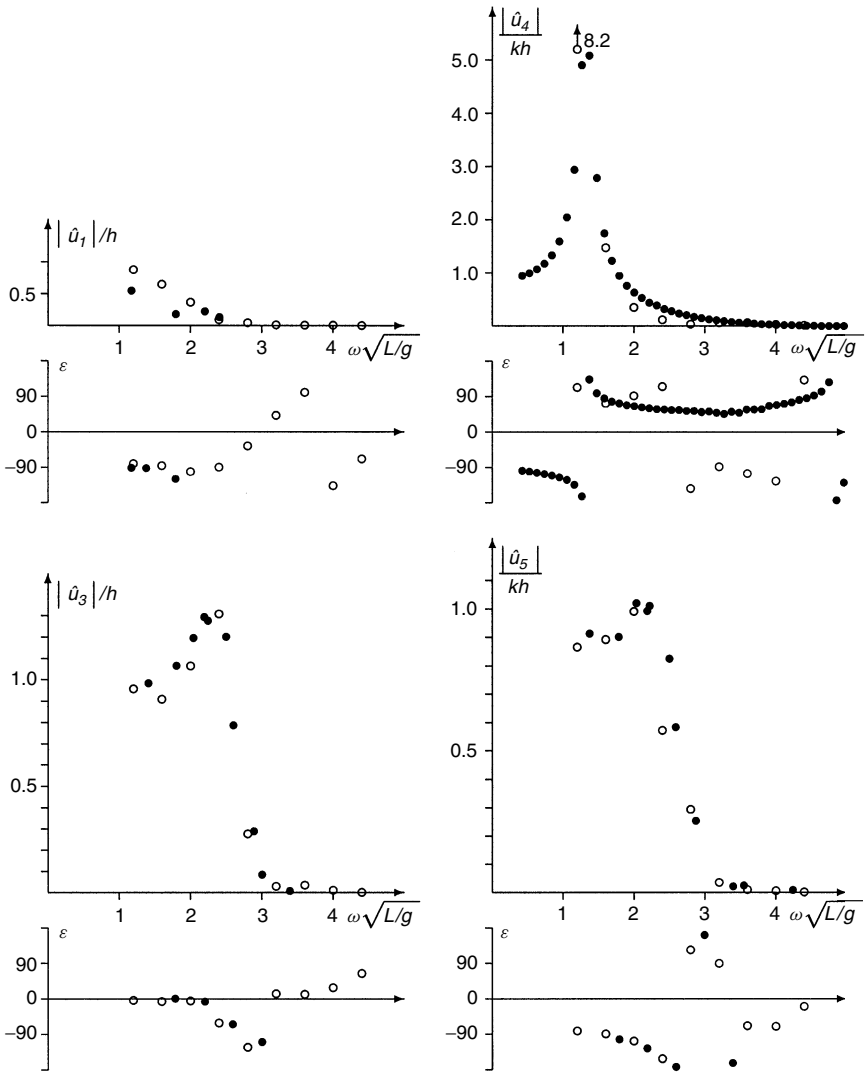


Figure 4.17 Selected response amplitude operators of motions for the container ship S-175 at $f_n = 0.275$; experiment, computation surge (top left) for $\mu = 180^\circ$; roll (top right) for $\mu = 120^\circ$; heave (bottom left) for $\mu = 150^\circ$; pitch (bottom right) for $\mu = 150^\circ$

differences in the pressures in the bow region for radiation in short waves and for diffraction in long waves.

4.4.4 Problems for fast and unconventional ships

Seakeeping computations are problematic for fast and unconventional ships. Seakeeping plays a special role here, as fast ships are often passenger ferries, which need good seakeeping characteristics to attract passengers. This is the reason why, e.g., planing boats with their bad seakeeping are hardly ever used

for commercial passenger transport. For fast cargo ships, the reduced speed in seaways can considerably influence transport efficiency. A hull form, which is superior in calm water, may well become inferior in moderate seaways. Warships also often require good seakeeping to supply stable platforms for weapon systems, helicopters, or planes.

Unfortunately, computational methods for conventional ships are usually not at all or only with special modifications suitable for fast and unconventional ships. The special ‘High-speed strip theory’, see section 4.4.1, has been successfully applied in various forms to both fast monohulls and multihulls. Japanese validation studies showed that for a fast monohull with transom stern the HSST fared much better than both conventional strip methods and three-dimensional GFM and RSM. However, the conventional strip methods and the three-dimensional methods did not use any special treatment of the large transom stern of the test case. This impairs the validity of the conclusions. Researchers at the MIT have shown that at least for time-domain RSM the treatment of transom sterns is possible and yields good results also for fast ships, albeit at a much higher computational effort than the HSST. In most cases, HSST should yield the best cost-benefit ratio for fast ships.

It is claimed often in the literature that conventional strip methods are only suitable for low ship speeds. However, benchmark tests show that strip methods can yield good predictions of motion RAOs up to Froude numbers $F_n \approx 0.6$, provided that proper care is taken and the dynamic trim and sinkage and the steady wave profile at the hull is included to define the average submergence of the strips. The prediction of dynamic trim and sinkage is relatively easy for fast displacement ships, but difficult for planing boats. Neglecting these effects, i.e. computing for the calm-water wetted surface, may be a significant reason why often in the literature a lower Froude number limit of $F_n \approx 0.4$ is cited.

For catamarans, the interaction between the hulls plays an important role especially for low speeds. For design speed, the interaction is usually negligible in head seas. Three-dimensional methods (RSM, GFM) capture automatically the interaction as both hulls are simultaneously modelled. The very slender form of the demihulls introduces smaller errors for GFM catamaran computations than for monohulls. Both RSM and GFM applications to catamarans can be found in the literature, usually for simplified research geometries. Strip methods require special modifications to capture, at least in good approximation, the hull interaction, namely multiple reflection of radiation and diffraction waves. Simply using the hydrodynamic coefficients for the two-dimensional flow between the two cross-sections leads to strong overestimation of the interaction for $V > 0$.

Seakeeping computations for air-cushioned vehicles and surface effect ships are particularly difficult due to additional problems:

- The flexible skirts deform under the changing air cushion pressure and the contact with the free surface. Thus the effective cushion area and its centre of gravity change.
- The flow and the pressure in the cushion contain unsteady parts which depend strongly on the average gap between free surface and skirts.
- The dynamics of fans (and their motors) influences the ship motions.

Especially the narrow gaps between skirts and free surface result in a strongly non-linear behaviour that so far excludes accurate predictions.

4.4.5 Further quantities in regular waves

Within a linear theory, the velocity and acceleration RAOs can be directly derived, once the motion RAOs are determined. The relative motion between a point on the ship and the water surface is important to evaluate the danger of slamming or water on deck. The RAOs for relative motion should incorporate the effect of diffraction and radiation, which is again quite simple once the RAOs for the ship motions are determined. However, effects of flared hull shape with outward forming spray for heave motion cannot be modelled properly within a linear theory, because these depend non-linearly on the relative motion. In practice, the section flare is important for estimating the amount of water on deck.

Internal forces on the ship hull (longitudinal, transverse, and vertical forces, torsional, transverse, and longitudinal bending moment) can also be determined relatively easily for known motions. The pressures are then only integrated up to a given cross-section instead of over the whole ship length. (Within a strip method approach, this also includes the matrix of restoring forces S , which contains implicitly many hydrostatic pressure terms.) Also, the mass forces (in matrix M) should only be considered up to the given location x of the cross-section. Stresses in the hull can then be derived from the internal forces. However, care must be taken that the moments are transformed to the neutral axis of the ‘beam’ ship hull. Also, stresses in the hull are of interest often for extreme loads where linear theory should no longer be applied.

The longitudinal force on the ship in a seaway is to first order within a linear theory also a harmonically oscillating quantity. The time average of this quantity is zero. However, in practice the ship experiences a significantly non-zero added resistance in seaways. This added resistance (and similarly the transverse drift force) can be estimated using linear theory. Two main contributions appear:

- Second-order pressure contributions are integrated over the average wetted surface.
- First-order pressure contributions are integrated over the difference between average and instantaneous wetted surface; this yields an integral over the contour of the waterplane.

If the steady flow contribution is completely retained (as in some three-dimensional BEM), the resulting expression for the added resistance is rather complicated and involves also second derivatives of the potential on the hull. Usually this formula is simplified assuming

- uniform flow as the steady base flow
- dropping a term involving x -derivatives of the flow
- considering only heave and pitch as main contributions to added resistance

4.4.6 Ship responses in stationary seaway

Here the issue is how to get statistically significant properties in natural seaways from a response amplitude operator $Y_r(\omega, \mu)$ in elementary waves for an arbitrary response r depending linearly on wave amplitude. The seaway is assumed to be stationary with known spectrum $S_\zeta(\omega, \mu)$.

Since the spectrum is a representation of the distribution of the amplitude squared over ω and μ , and the RAO \hat{Y}_r is the complex ratio of r_A/ζ_A , the spectrum of r is given by:

$$S_r(\omega, \mu) = |Y_r(\omega, \mu)|^2 S_\zeta(\omega, \mu)$$

Values of r , chosen at a random point in time, follow a Gaussian distribution. The average of r is zero if we assume $r \sim \zeta_A$, i.e. in calm water $r = 0$. The probability density of randomly chosen r values is:

$$f(r) = \frac{1}{\sqrt{2\pi}\sigma_r} \exp\left(-\frac{r^2}{2\sigma_r^2}\right)$$

The variance σ_r^2 is obtained by adding the variances due to the elementary waves in which the natural seaway is decomposed:

$$\sigma_r^2 = \int_0^\infty \int_0^{2\pi} S_r(\omega, \mu) d\mu d\omega$$

The sum distribution corresponding to the frequency density $f(r)$ above is:

$$F(r) = \int_{-\infty}^r f(\rho) d\rho = \frac{1}{2}[1 + \phi(r/\sigma_r)]$$

The probability integral ϕ is defined as:

$$\phi = 2/\sqrt{2\pi} \cdot \int_{-\infty}^x \exp(-t^2/2) dt$$

$F(r)$ gives the percentage of time when a response (in the long-term average) is less or equal to a given limit r . $1 - F(r)$ is then the corresponding percentage of time when the limit r is exceeded.

More often the distribution of the amplitudes of r is of interest. We define here the amplitude of r (differing from some authors) as the maximum of r between two following upward zero crossings (where $r = 0$ and $\dot{r} > 0$). The amplitudes of r are denoted by r_A . They have approximately (except for extremely 'broad' spectra) the following probability density:

$$f(r_A) = \frac{r_A}{\sigma_r^2} \exp\left(-\frac{r_A^2}{2\sigma_r^2}\right)$$

The corresponding sum distribution is:

$$F(r_A) = 1 - \exp\left(-\frac{r_A^2}{2\sigma_r^2}\right)$$

σ_r follows again the formula given above. The formula for $F(r_A)$ describes a so-called Rayleigh distribution. The probability that a randomly chosen amplitude of the response r exceeds r_A is:

$$1 - F(r_A) = \exp\left(-\frac{r_A^2}{2\sigma_r^2}\right)$$

The average frequency (occurrences/time) of upward zero crossings and also as the above definition of amplitudes of r is derived from the r spectrum to:

$$f_0 = \frac{1}{2\pi\sigma_r} \sqrt{\int_0^\infty \int_0^{2\pi} \omega_e^2 S_r(\omega, \mu) d\mu d\omega}$$

Together with the formula for $1 - F(r_A)$ this yields the average occurrence of r amplitudes which exceed a limit r_A during a period T :

$$z(r_A) = T f_0 \exp\left(-\frac{r_A^2}{2\sigma_r^2}\right)$$

Often we are interested in questions such as, ‘How is the probability that during a period T a certain stress is exceeded in a structure or an opening is flooded?’ Generally, the issue is then the probability $P_0(r_A)$ that during a period T the limit r_A is never exceeded. In other words, $P_0(r_A)$ is the probability that the maximum amplitude during the period T is less than r_A . This is given by the sum function of the distribution of the maximum or r during T . We make two assumptions:

- $z(r_A) \ll T f_0$; this is sufficiently well fulfilled for $r_A \geq 2\sigma_r$.
- An amplitude r_A is statistically nearly independent of its predecessors. This is true for most seakeeping responses, but not for the weakly damped amplitudes of elastic ship vibration excited by seaway, for example.

Under these assumption we have:

$$P_0(r_A) = e^{-z(r_A)}$$

If we insert here the above expression for $z(r_A)$ we obtain the ‘double’ exponential distribution typical for the distribution of extreme values:

$$P_0(r_A) = e^{-T f_0 \exp(-r_A^2/(2\sigma_r^2))}$$

The probability of exceedence is then $1 - P_0(r_A)$. Under the (far more limiting) assumption that $z(r_A) \ll 1$ we obtain the approximation:

$$1 - P_0(r_A) \approx z(r_A)$$

The equations for $P_0(r_A)$ assume neither a linear correlation of the response r from the wave amplitude nor a stationary seaway. They can therefore also be applied to results of non-linear simulations or long-term distributions.

4.4.7 Simulation methods

The appropriate tool to investigate strongly non-linear ship reactions are simulations in the time domain. The seaway itself is usually linearized, i.e. computed as superposition of elementary waves. The frequencies of the individual elementary waves ω_j may not be integer multiples of a minimum frequency ω_{\min} . In this case, the seaway would repeat itself after $2\pi/\omega_{\min}$ unlike a real natural seaway. Appropriate methods to chose the ω_j are:

- The ω_j are chosen such that the area under the sea spectrum between ω_j and ω_{j+1} is the same for all j . This results in constant amplitudes for all elementary waves regardless of frequency.
- The frequency interval of interest for the simulation is divided into intervals. These intervals are larger where S_ζ or the important RAOs are small and vice versa. In each interval a frequency ω_j is chosen randomly (based on constant probability distribution). One should not choose the same ω_j for all the L encounter angles under consideration. Rather each combination of frequency ω_j and encounter angle μ_l should be chosen anew and randomly.

The frequencies, encounter angles, and phase angles chosen before the simulation must be kept during the whole simulation.

Starting from a realistically chosen start position and velocity of the ship, the simulation computes in each time step the forces and moments acting from the moving water on the ship. The momentum equations for translations and rotations give the translatory and rotational accelerations. Both are three-component vectors and are suitably expressed in a ship-fixed coordinate system. The momentum equations form a system of six scalar, coupled ordinary second-order differential equations. These can be transformed into a system of 12 first-order differential equations which can be solved by standard methods, e.g. fourth-order Runge–Kutta integration. This means that the ship position and velocity at the end of a small time interval, e.g. one second, are determined from the corresponding data at the beginning of this interval using the computed accelerations.

The forces and moments can be obtained by integrating the pressure distribution over the momentary wetted ship surface. Three-dimensional methods are very, and usually too, expensive for this purpose. Therefore modified strip methods are most frequently used. A problem is that the pressure distribution depends not only on the momentary position, velocity, and acceleration, but also from the history of the motion which is reflected in the wave pattern. This effect is especially strong for heave and pitch motions. In computations for the frequency domain, the historical effect is expressed in the frequency dependency of the added mass and damping. In time-domain simulations, we cannot consider a frequency dependency because there are many frequencies at the same time and the superposition principle does not hold. Therefore, the historical effect on the hydrodynamic forces and moments \vec{F} is either expressed in convolution integrals (\vec{u} contains here not only the ship motions, but also the incident waves):

$$\vec{F}(t) = \int_{-\infty}^t K(\tau) \vec{u}(\tau) d\tau$$

or one considers 0 to n time derivatives of the forces \vec{F} and 1 bis $(n + 1)$ time derivatives of the motions \vec{u} :

$$B_0 \vec{F}(t) + B_1 \dot{\vec{F}}(t) + B_2 \ddot{\vec{F}}(t) + \dots = A_0 \dot{\vec{u}}(t) + A_1 \ddot{\vec{u}}(t) + A_2 \ddot{\vec{u}}(t) \dots$$

The matrix $K(\tau)$ in the first alternative and the scalars A_i, B_i in the second alternative are determined in potential flow computations for various sinkage and heel of the individual strips.

The second alternative is called state model and appears to be far superior to the first alternative. Typical values for n are 2 to 4; for larger n problems occur

in the determination of the constants A_i and B_i resulting, e.g., in numerically triggered oscillations. Pereira (1988) gives details of such a simulation method. The simulation method has been extended considerably in the mean time and can also consider simultaneously the flow of water through a damaged hull, sloshing of water in the hull, or water on deck.

A far simpler and far faster approach is described, e.g., in Söding (1987). Here only the strongly non-linear surge and roll motions are determined by a direct solution of the equations of motion in the time-domain simulation. The other four degrees of freedom are linearized and then treated similarly as the incident waves, i.e. they are computed from RAOs in the time domain. This is necessary to couple the four linear motions to the two non-linear motions. (Roll motions are often simulated as independent from the other motions, but this yields totally unrealistic results.) The restriction to surge and roll much simplifies the computation, because the history effect for these degrees of freedom is negligible. Extensive validation studies for this approach with model tests gave excellent agreement for capsizing of damaged ro-ro vessels drifting without forward speed in transverse waves (Chang and Blume (1998)).

Simulations often aim to predict the average occurrence $z(r_A)$ of incidents where in a given period T a seakeeping response $r(t)$ exceeds a limit r_A . A new incident is then counted when after a previous incident another zero crossing of r occurred. The average occurrence is computed by multiple simulations with the characteristic data, but other random phases ϵ_{ji} for the superposition of the seaway. Alternatively, the simulation time can be chosen as nT and the number of occurrences can be divided by n . Both alternatives yield the same results except for random fluctuations.

Often seldom (extremely unlikely) incidents are of interest which would require simulation times of weeks to years to determine $z(r_A)$ directly if the occurrences are determined as described above. However, these incidents are expected predominantly in the presence of one or several particularly high waves. One can then reduce the required simulation time drastically by substituting the real seaway of significant wave height H_{real} by a seaway with larger significant wave height H_{sim} . The periods of both seaways shall be the same. The following relation between the incidents in the real seaway and in the simulated seaway exists (Söding (1987)):

$$\frac{H_{\text{sim}}^2}{H_{\text{real}}^2} = \frac{\ln[z_{\text{real}}(r_A)/z(0)] + 1.25}{\ln[z_{\text{sim}}(r_A)/z(0)] + 1.25}$$

This equation is sufficiently accurate for $z_{\text{sim}}/z(0) < 0.03$. In practice, one determines in simulated seaway, e.g. with 1.5 to 2 times larger significant wave height, the occurrences $z_{\text{sim}}(r_A)$ and $z(0)$ by direct counting; then the above equation is solved for the unknown $z_{\text{real}}(r_A)$:

$$z_{\text{real}}(r_A) = z(0) \exp \left(\frac{H_{\text{sim}}^2}{H_{\text{real}}^2} \{ \ln[z_{\text{sim}}(r_A)/z(0)] + 1.25 \} - 1.25 \right)$$

4.4.8 Long-term distributions

Section 4.4.6 treated ship reactions in stationary seaway. This chapter will cover probability distributions of ship reactions r during periods T with

changing sea spectra. A typical example for T is the total operational time of a ship. A quantity of interest is the average occurrence $z_L(r_A)$ of cases when the reaction $r(t)$ exceeds the limit r_A . The average can be thought of as the average over many hypothetical realizations, e.g. many equivalently operated sister ships.

First, one determines the occurrence $z(r_A; H_{1/3}, T_p, \mu_0)$ of exceeding the limit in a stationary seaway with characteristics $H_{1/3}$, T_p , and μ_0 during total time T . (See section 4.4.6 for linear ship reactions and section 4.4.7 for non-linear ship reactions.) The weighted average of the occurrences in various seaways is formed. The weighing factor is the probability $p(H_{1/3}, T_p, \mu_0)$ that the ship encounters the specific seaway:

$$z_L(r_A) = \sum_{\text{all } H_{1/3}} \sum_{\text{all } T_p} \sum_{\text{all } \mu_0} z(r_A; H_{1/3}, T_p, \mu_0) p(H_{1/3}, T_p, \mu_0)$$

Usually, for simplification it is assumed that the ship encounters seaways with the same probability under n_μ encounter angles μ_0 :

$$z_L(r_A) = \frac{1}{n_\mu} \sum_{\text{all } H_{1/3}} \sum_{\text{all } T_p} \sum_{i=1}^{n_\mu} z(r_A; H_{1/3}, T_p, \mu_{0i}) p(H_{1/3}, T_p)$$

The probability $p(H_{1/3}, T_p)$ for encountering a specific seaway can be estimated using data as given in Table 4.2. If the ship would operate exclusively in the ocean area for Table 4.2, the table values (divided by 10^6) could be taken directly. This is not the case in practice and requires corrections. A customary correction then is to base the calculation only on 1/50 or 1/100 of the actual operating time of the ship. This correction considers, e.g.:

- The ship usually operates in areas with not quite so strong seaways as given in Table 4.2.
- The ship tries to avoid particularly strong seaways.
- The ship reduces speed or changes course relative to the dominant wave direction, if it cannot avoid a particularly strong seaway.
- Some exceedence of r_A is not important, e.g. for bending moments if they occur in load conditions when the ship has only a small calm-water bending moment.

The sum distribution of the amplitudes r_A , i.e. the probability that an amplitude r is less than a limit r_A , follows from z_L :

$$P_L(r_A) = 1 - \frac{z_L(r_A)}{z_L(0)}$$

$z_L(0)$ is the number of amplitudes during the considered period T . This distribution is used for seakeeping loads in fatigue strength analyses of the ship structure. It is often only slightly different from an exponential distribution, i.e. it has approximately the sum distribution:

$$P_L(r_A) = 1 - e^{-r_A/r_0}$$

where r_0 is a constant describing the load intensity. (In fatigue strength analyses, often the logarithm of the exceedence probability $\log(1 - P_L)$ is plotted

over r_A ; since for an exponential distribution the logarithm results in a straight line, this is called a log-linear distribution.)

The probability distribution of the largest loads during the period T can be determined from (see section 4.4.6 for the underlying assumptions):

$$P_0(r_A) = e^{-z(r_A)}$$

The long-term occurrence $z_L(r_A)$ of exceeding the limit r_A is inserted here for $z(r_A)$.

4.5 Slamming

In rough seas with large relative ship motion, slamming may occur with large water impact loads. Usually, slamming loads are much larger than other wave loads. Sometimes ships suffer local damage from the impact load or large-scale buckling on the deck. For high-speed ships, even if each impact load is small, frequent impact loads accelerate fatigue failures of hulls. Thus, slamming loads may threaten the safety of ships. The expansion of ship size and new concepts in fast ships have decreased relative rigidity causing in some cases serious wrecks.

A rational and practical estimation method of wave impact loads is thus one of the most important prerequisites for safety design of ships and ocean structures. Wave impact has challenged many researchers since von Karman's work in 1929. Today, mechanisms of wave impacts are correctly understood for the 2-d case, and accurate impact load estimation is possible for the deterministic case. The long-term prediction of wave impact loads can be also given in the framework of linear stochastic theories. However, our knowledge on wave impact is still far from sufficient.

A fully satisfactory theoretical treatment has been prevented so far by the complexity of the problem:

- Slamming is a strongly non-linear phenomenon which is very sensitive to relative motion and contact angle between body and free surface.
- Predictions in natural seaways are inherently stochastic; slamming is a random process in reality.
- Since the duration of wave impact loads is very short, hydro-elastic effects are large.
- Air trapping may lead to compressible, partially supersonic flows where the flow in the water interacts with the flow in the air.

Most theories and numerical applications are for two-dimensional rigid bodies (infinite cylinders or bodies of rotational symmetry), but slamming in reality is a strongly three-dimensional phenomenon. We will here briefly review the most relevant theories. Further recommended literature includes:

- Tanizawa and Bertram (1998) for practical recommendations translated from the Kansai Society of Naval Architects, Japan.
- Mizoguchi and Tanizawa (1996) for stochastic slamming theories.
- Korobkin (1996) for theories with strong mathematical focus.
- SSC (1995) for a comprehensive compilation (more than 1000 references) of slamming literature.

The wave impact caused by slamming can be roughly classified into four types (Fig. 4.18):

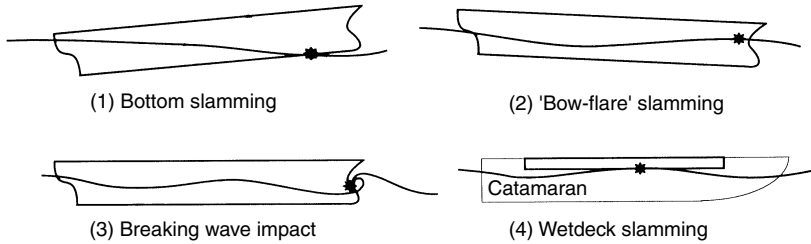


Figure 4.18 Types of slamming impact of a ship

1. Bottom slamming occurs when emerged bottoms re-enter the water surface.
2. Bow-flare slamming occurs for high relative speed of bow-flare to the water surface.
3. Breaking wave impacts are generated by the superposition of incident wave and bow wave hitting the bow of a blunt ship even for small ship motion.
4. Wet-deck slamming occurs when the relative heaving amplitude is larger than the height of a catamaran's wet-deck.

Both bottom and bow-flare slamming occur typically in head seas with large pitching and heaving motions. All four water impacts are 3-d phenomena, but have been treated as 2-d for simplicity. For example, types 1 and 2 were idealized as 2-d wedge entry to the calm-water surface. Type 3 was also studied as 2-d phenomenon similar to wave impact on breakwaters. We will therefore review 2-d theories first.

- *Linear slamming theories based on expanding thin plate approximation*

Classical theories approximate the fluid as inviscid, irrotational, incompressible, free of surface tension. In addition, it is assumed that gravity effects are negligible. This allows a (predominantly) analytical treatment of the problem in the framework of potential theory.

For bodies with small deadrise angle, the problem can be linearized. Von Karman (1929) was the first to study theoretically water impact (slamming). He idealized the impact as a 2-d wedge entry problem on the calm-water surface to estimate the water impact load on a seaplane during landing (Fig. 4.19). Mass, deadrise angle, and initial penetrating velocity of the wedge are denoted as m , β and V_0 . Since the impact is so rapid, von Karman assumed very small water surface elevation during impact and negligible gravity effects. Then the added mass is approximately $m_v = (\frac{1}{2})\pi\rho c^2$. ρ is the water density and c the half width of the wet area implicitly computed from $dc/dt = V \cot \beta$. The momentum before the impact mV_0 must be equal to the sum of the wedge momentum mV and added mass momentum $m_v V$, yielding the impact load as:

$$P = \frac{V_0^2 / \tan \beta}{\left(1 + \frac{\rho \pi c^2}{2m}\right)^3} \cdot \rho \pi c$$

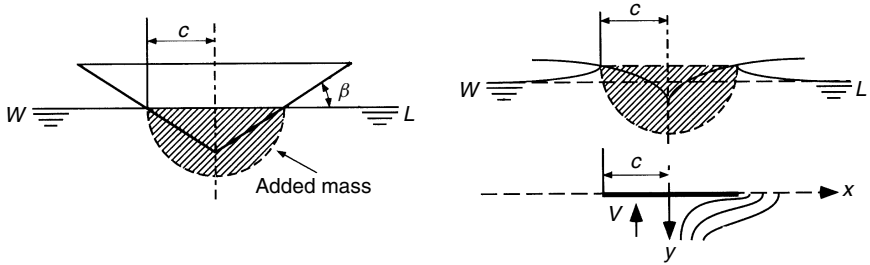


Figure 4.19 Water impact models of von Karman (left) and Wagner (right)

Since von Karman's impact model is based on momentum conservation, it is usually referred to as momentum impact, and because it neglects the water surface elevation, the added mass and impact load are underestimated, particularly for small deadrise angle.

Wagner derived a more realistic water impact theory in 1932. Although he assumed still small deadrise angles β in his derivation, the theory was found to be not suitable for $\beta < 3^\circ$, since then air trapping and compressibility of water play an increasingly important role. If β is assumed small and gravity neglected, the flow under the wedge can be approximated by the flow around an expanding flat plate in uniform flow with velocity V (Fig. 4.19). Using this model, the velocity potential ϕ and its derivative with respect to y on the plate $y = 0^+$ is analytically given as:

$$\phi = \begin{cases} V\sqrt{c^2 - x^2} & \text{for } x < c \\ 0 & \text{for } x > c \end{cases}$$

$$\partial\phi/\partial y = \begin{cases} 0 & \text{for } x < c \\ V/\sqrt{1 - c^2/x^2} & \text{for } x > c \end{cases}$$

The time integral of the last equation gives the water surface elevation and the half width of the wetted area c . The impact pressure on the wedge is determined from Bernoulli's equation as:

$$\frac{p(x)}{\rho} = \frac{\partial\phi}{\partial t} - \frac{1}{2}(\nabla\phi)^2 = \sqrt{c^2 - x^2} \frac{dV}{dt} + V \frac{c}{\sqrt{c^2 - x^2}} \frac{dc}{dt} - \frac{1}{2} \frac{V^2 x^2}{c^2 - x^2}$$

Wagner's theory can be applied to arbitrarily shaped bodies as long as the deadrise angle is small enough not to trap air, but not so small that air trapping plays a significant role. Wagner's theory is simple and useful, even if the linearization is sometimes criticized for its inconsistency as it retains a quadratic term in the pressure equation. This term is indispensable for the prediction of the peak impact pressure, but it introduces a singularity at the edge of the expanding plate ($x = \pm c$) giving negative infinite pressure there. Many experimental studies have checked the accuracy of Wagner's theory. Measured peak impact pressures are typically a little lower than estimated. This suggested that Wagner's theory gives conservative estimates for practical use. However, a correction is needed on the peak pressure measured by

pressure gauges with finite gauge area. Special numerical FEM analyses of the local pressure in a pressure gauge can be used to correct measured data. The corrected peak pressures agree well with estimated values by Wagner's theory. Today, Wagner's theory is believed to give accurate peak impact pressure for practical use.

The singularity of Wagner's theory can be removed taking spray into account. An 'inner' solution for the plate is asymptotically matched to an 'outer' solution of the spray region, as, e.g., proposed by Watanabe in Japan in the mid-1980s (Fig. 4.20). The resulting equation for constant falling velocity is consistent and free from singularities. Despite this theoretical improvement, Watanabe's and Wagner's theories predict basically the same peak impact pressure (Fig. 4.21).

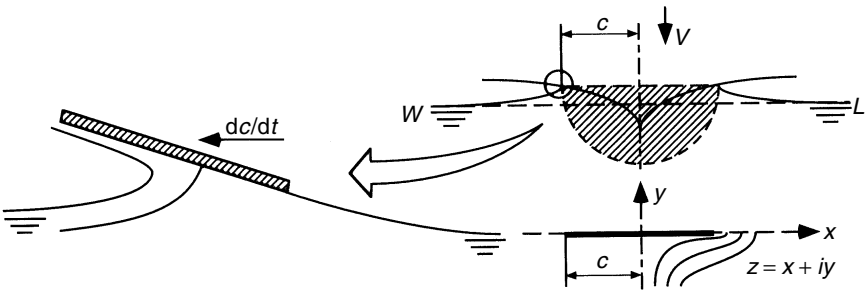


Figure 4.20 Water impact model of Watanabe

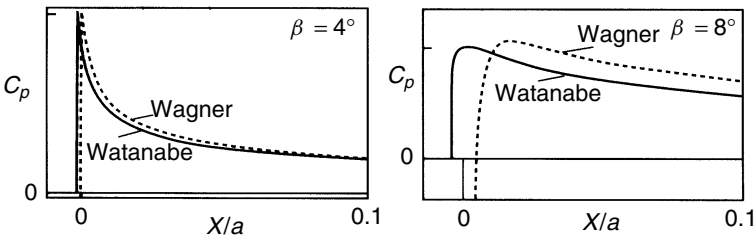


Figure 4.21 Spatial impact pressure distribution

- *Simple non-linear slamming theories based on self-similar flow*

We consider the flow near the vertex of a 2-d body immediately after water penetration. We can assume:

- Near the vertex, the shape of the 2-d body can be approximated by a simple wedge.
- Gravity accelerations are negligible compared to fluid accelerations due to the impact.
- The velocity of the body v_0 is constant in the initial stage of the impact. Then the flow can be considered as self-similar depending only on x/v_0t and y/v_0t , where x, y are Cartesian coordinates and t is time. Russian scientists have converted the problem to a 1-d integral equation for $f(t)$. The resulting integral equation is so complicated that it cannot be solved analytically.

However, numerically it has been solved by Faltinsen in Norway up to deadrise angles $\beta \geq 4^\circ$. The peak impact pressure for $\beta = 4^\circ$ was almost identical (0.31% difference) to the value given by Wagner's theory.

• *Slamming theories including air trapping*

So far slamming theories have neglected the density of air, i.e. if a deformation of the, free surface was considered at all it occurred only after the body penetrated the water surface. The reality is different. The body is preceded by an air cushion that displaces water already before the actual body entry. The density of air plays an even bigger role if air trapping occurs. This is especially the case for breaking wave impacts. In the 1930s, Bagnold performed pioneering work in the development of theories that consider this effect. Bagnold's impact model is simply constructed from added mass, a rigid wall, and a non-linear air cushion between them (Fig. 4.22). This model allows qualitative predictions of the relation between impact velocity, air cushion thickness, and peak impact pressure. For example, the peak impact pressure is proportional to V and \sqrt{H} for slight impact and weak non-linearity of the air cushion; but for severe impact, the peak impact pressure is proportional to V^2 and H . These scaling laws were validated by subsequent experiments.

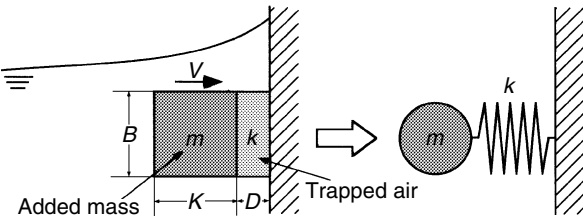


Figure 4.22 Bagnold's model

Trapped air bottom slamming is another typical impact with air cushion effect. For two-dimensional bodies, air trapping occurs for deadrise angles $\beta \leq 3^\circ$. Chuang's (1967) experiment for 2-d wedges gave peak impact pressures as in Table 4.3. The impact velocity V is given in m/s.

Table 4.3 Chuang's (1967) relation for peak impact pressures

β	0°	1°	3°	6°	10°	15°	$\geq 18^\circ$
P_{peak} (kPa)	$102 V$	$115 V^{1.4}$	$189 V^{1.6}$	$64.5 V^2$	$31 V^2$	$17.8 V^2$	Wagner's theory

For $\beta = 0^\circ$ air trapping is significant and the peak impact pressure is proportional to V . Increasing the deadrise angle reduces the amount of air trapping and thus the non-linearity. For practical use, the peak impact pressure is usually assumed to be proportional to V^2 for all β . This results in a conservative estimate.

Johnson and Verhagen developed 2-d theories for bottom impact with air trapping considering 1-d air flow between water surface and bottom to estimate the water surface distortion and the trapped air volume (Fig. 4.23).

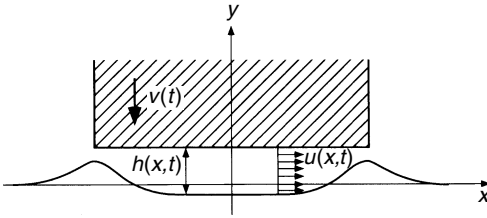


Figure 4.23 One-dimensional air flow model of Verhagen

The peak impact pressure thus estimated was much higher than measured. This disagreement results from the boundary condition at the edge of the flat bottom, where a jet emits to the open air. The theory assumes that the pressure at the edge is atmospheric pressure. This lets the air between water surface and bottom escape too easily, causing an underestimated trapped air volume. Experiments showed that the pressure is higher than atmospheric. Yamamoto has therefore proposed a modified model using a different boundary condition.

Experiments at the Japanese Ship Research Institute have observed the trapped air impact with high-speed cameras and measured the initial thickness of air trapping. It was much thicker than the estimates of both Verhagen and Yamamoto. The reason is that a mixed area of air and water is formed by the high-speed air flow near the edge. Since the density of this mixed area is much higher than that of air, this area effectively chokes the air flow increasing air trapping.

The mechanism of wave impact with air trapping is in reality much more complicated. Viscosity of air, the effect of air leakage during compression, shock waves inside the air flow, and the complicated deformation of the free surface are all effects that may play an important role. Computational fluid dynamics may be the key to significant success here, but has not yet progressed sufficiently yet as discussed below.

- *Effect of water compressibility*

When a blunt body drops on calm water or a flat bottom drops on a smooth wave crest, usually no air trapping occurs. Nevertheless, one cannot simply use Wagner's theory, because at the top of such a blunt body or wave crest the relative angle between body and free surface becomes zero. Then both Wagner's and Watanabe's theories give infinite impact pressure. In reality, compressibility of liquid is important for a very short time at the initial stage of impact, when the expansion velocity of the wet surface dc/dt exceeds the speed of sound for water $c_w \approx 1500$ m/s producing a finite impact pressure. Korobkin (1996) developed two-dimensional theories which consider compressibility and free-surface deformation. For parabolic bodies dropping on the calm-water surface, he derived the impact pressure simply to $P = \rho c_w V$. Korobkin's theory is far more sophisticated yielding also the time history of the pressure decay, but will not be treated here.

- *3-d slamming theories*

All slamming theories treated so far were two dimensional, i.e. they were limited to cross-sections (of infinite cylinders). In reality slamming for ships is a strongly three-dimensional phenomenon due to, e.g., pitch motion and cross-sections in the foreship changing rapidly in the longitudinal direction.

For practical purposes, one tries to obtain quasi three-dimensional solutions based on strip methods or high-speed strip methods. At the University of Michigan, Troesch developed a three-dimensional boundary element method for slamming. However, the method needs to simplify the physics of the process and the geometry of body and free surface and failed to show significant improvement over simpler strip-method approaches when compared to experiments.

Limiting oneself to axisymmetric bodies dropping vertically into the water makes the problem *de facto* two dimensional. The study of 3-d water impact started from the simple extension of Wagner's theory to such cases. The water impact of a cone with small deadrise angle can then be treated in analogy to Wagner's theory as an expanding circular disk. A straightforward extension of Wagner's theory by Chuang overpredicts the peak impact pressure. Subsequent refinements of the theory resulted in a better estimate of the peak impact pressure:

$$p(r) = \frac{1}{2} \rho V^2 \left(\frac{2}{\pi} \right)^2 \left[\frac{4 \cot \beta}{\sqrt{1 - r^2/c^2}} - \frac{r^2/c^2}{1 - r^2/c^2} \right]$$

r and c correspond to x and c in Fig. 4.19. This equation gives about 14% lower peak impact pressures than a straightforward extension of Wagner's theory. Experiments confirmed that the impact pressure on a cone is lower than that on a 2-d wedge of same deadrise angle. So the 3-d effect reduces the impact pressure at least for convex bodies. This indicates that Wagner's theory gives conservative estimates for practical purpose. Since the impact on a ship hull is usually a very local phenomenon, Wagner's equation has been used also for 3-d surfaces using local relative velocity and angle between ship hull and water surface.

Watanabe (1986) extended his two-dimensional slamming theory to three-dimensional oblique impact of flat-bottomed ships. This theory was validated in experiments observing three-dimensional bottom slamming with a high-speed video camera and transparent models. Watanabe classified the slamming of flat-bottomed ships into three types:

1. Slamming due to inclined re-entry of the bottom. The impact pressure runs from stern to bow. No air trapping occurs.
2. Slamming due to vertical (orthogonal) re-entry of the bottom to a wave trough with large-scale air trapping.
3. Slamming due to vertical (orthogonal) re-entry of the bottom to a wave crest with only small-scale, local air trapping.

Type 1 (typical bottom impact observed for low ship speed) can be treated by Watanabe's 3-d theory. Type 3 (typical for short waves and high ship speed) corresponds to Chuang's theory for very small deadrise angle. Type 2 (also typical for short waves and high ship speed) corresponds to Bagnolds' approach, but the air trapping and escaping mechanisms are different to simple 2-d models.

The three-dimensional treatment of slamming phenomena is still subject to research. It is reasonable to test and develop first numerical methods for two-dimensional slamming, before one progresses to computationally more challenging three-dimensional simulations. Until such methods are available with appropriate response times on engineering workstations, in practice

computations will be limited to two-dimensional estimates combined with empirical corrections.

- *Hydro-elastic approaches in slamming*

It is important to evaluate not only peak impact pressures but also structural responses to the impact, to consider the impact pressure in the design of marine structures. Whipping (large-scale, weakly dampened oscillations of the longitudinal bending moment) is a typical elastic response to impact. In the late 1960s and 1970s, slamming and whipping resulted in some spectacular ship wrecks, e.g. bulkers and container ships breaking amidships. The disasters triggered several research initiatives, especially in Japan, which eventually contributed considerably to the development of experimental and numerical techniques for the investigation of slamming and whipping.

Let us denote the slamming impact load as $Z(t)$ and the elastic response of a ship as $S(t)$. Assuming a linear relation between them, we can write:

$$S(t) = \int_0^{\infty} h(t - \tau)Z(\tau) d\tau$$

$h(\tau)$ is the impulse response function of the structure. An appropriate modelling of the structure is indispensable to compute $h(\tau)$. For example, the large-scale (whipping) response can be modelled by a simple beam, whereas small-scale (local) effects can be modelled as panel responses. For complicated structures, FEM analyses determine $h(\tau)$.

When the duration of the impact load is of the same order as the natural period of the structure, the hydro-elastic interaction is strong. The impact load on the flexible bottom can be about twice that on the rigid bottom. Various theories have been developed, some including the effect of air trapping, but these theories are not powerful enough to explain experimental data quantitatively. However, numerical methods either based on FEM or FVM could be used to analyse both fluid and structure simultaneously and should improve considerably our capability to analyse hydro-elastic slamming problems.

- *CFD for slamming*

For most practical impact problems, the body shape is complex, the effect of gravity is considerable, or the body is elastic. In such cases, analytical solutions are very difficult or even impossible. This leaves CFD as a tool. Due to the required computer resources, CFD applications to slamming appeared only since the 1980s. While the results of boundary element methods for water entry problems agree well with analytical results, it is doubtful whether they are really suited to this problem. Real progress is more likely to be achieved with field methods like FEM, FDM, or FVM. Various researchers have approached slamming problems, usually employing surface-capturing methods, e.g. marker-and-cell methods or level-set techniques. Often the Euler equations are solved as viscosity plays a less important role than for many other problems in ship hydrodynamics. But also RANSE solutions including surface tension, water surface deformation, interaction of air and water flows etc. have been presented. The numerical results agree usually well with experimental results for two-dimensional problems. Due to the large required computer resources, few really three-dimensional applications to ships have been presented.

4.6 Exercises: seakeeping

Solutions to the exercises will be posted on the internet (www.bh.com/companions/0750648511)

1. Solve the following two problems for seakeeping:

- A surfboard travels with Froude number $F_n = 0.4$ on a deep water wave of 4 m length. How long must the surfboard be to 'ride' on the wave, i.e. have the same speed as the wave?
- Wavebreaking occurs theoretically when the particle velocity in the x direction is larger than the celerity c of the wave. In practice, wavebreaking occurs for wave steepness h/λ exceeding $\frac{1}{14}$. What are the theoretical and practical limits for h concerning wavebreaking in a deep water wave of $\lambda = 100$ m?

The potential of a regular wave on shallow water is given by:

$$\phi = \operatorname{Re} \left(\frac{-ich}{\sinh(kH)} \cosh(k(z-H)) e^{i(\omega t - kx)} \right)$$

The following parameters are given:

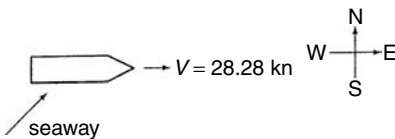
wave length $\lambda = 100$ m

wave amplitude $h = 3$ m

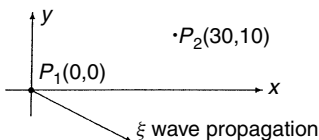
water depth $H = 30$ m

Determine velocity and acceleration field at a depth of $z = 20$ m below the water surface!

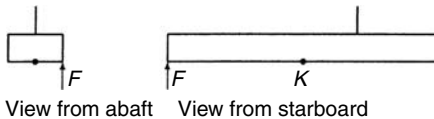
- A ship travels at 28.28 knots in deep sea in regular sea waves. The ship travels east, the waves come from the southwest. The wave length is estimated to be between 50 m and 300 m. The encounter period T_e is measured at 31.42 seconds.
 - What is the wave length of the seaway?
 - There has been a storm for one day in an area 1500 km southwest of the ship's position. Can the waves have their origin in this storm area?



- The position of two buoys is given by their (x, y) coordinates in metres as sketched below. The buoys are excited by a regular wave of $\lambda = 62.8$ m, amplitude $h = 1$ m, and angle $\mu = -30^\circ$ to the x -axis.
 - What is the maximum vertical relative motion between the two buoys if they follow the waves exactly?
 - What is the largest wave length λ to achieve maximum vertical relative motion of twice the wave amplitude?

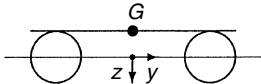


4. Derive the potential of a regular wave on finite water of depth H and the dispersion relation coupling ω and k . Start with the Laplace equation, the kinematic and dynamic conditions on the free surface, the condition of wave celerity, and no-penetration condition at water depth H . Use an x - z -coordinate system with z pointing down. The origin lies in the calm-water surface. A coordinate transformation into a quasi-steady coordinate system moving with wave celerity c is useful. Assume a solution for the potential in this transformed coordinate system of the form $\Phi = f(x) \cdot h(z)$. Assume small wave height h and linearize all expressions (potential and surface elevation) accordingly. Use $\omega = k \cdot c$.
5. Derive the potential and the dispersion relation (coupling between k and ω) of a regular wave on *deep* water as the limit of $H \rightarrow \infty$ for the finite-water expressions.
6. A wavemaker is to be designed for a towing tank of width $B = 4$ m and depth $H = 2.5$ m. The wavemaker shall be designed for a wave of 5 m length and 0.2 m amplitude.
 - (a) What is the power requirement for the motor of the wavemaker, if we assume 30% total efficiency between motor and wave. (For the considered wave length, the depth can be regarded as 'deep'. The power requirement of the wave is energy/length \cdot group velocity, as the energy in a wave is transported with group velocity.)
 - (b) After switching the wavemaker off, for a long time there is still a wave motion with period 40 s observed in the tank. How long is the tank, if the motion is due to the lowest eigenfrequency of the tank?
7. Consider a pontoon with a heavy-lift derrick as sketched. The pontoon has $L = 100$ m, $B = 20$ m, $D = 10$ m, $m_p = 10^7$ kg. The load at the derrick has mass $m_l = 10^6$ kg. The height of the derrick over deck is 10 m. This is where the load can be considered to be concentrated in one point. The longitudinal position of the derrick is 20 m before amidships. A force $F = 10^6$ N acts on the forward corner. We assume homogeneous mass distribution in the pontoon.
 - (a) Consider the pontoon 'in air' (without hydrodynamic masses) and determine the acceleration vector \ddot{u} !
 - (b) Consider the pontoon statically in water and determine u !



8. An infinite cylinder of width $B = 2$ m, draft $T = 1$ m and cross-section coefficient $C_m = 0.8$ with Lewis cross-section floats in equilibrium. Then a harmonic force per length with period $T_e = 3.14$ s and amplitude $F_a = 1$ kN/m is applied. What motion results after a long time (when the initial start-up has decayed)?
9. A cylinder of Lewis cross-section ($L = 10$ m, $B = 1$ m, $T = 0.4$ m, $C_m = 0.8$) floats parallel to the wave crests of regular waves ($\lambda = 5$ m, $h = 0.25$ m) which excite heave motions. Assume that the form of the free surface is not changed by the cylinder. What is the amplitude of relative motion between cylinder and free surface?

10. A raft consists of two circular cylinders with $D = 1$ m diameter and $L = 10$ m length. The two cylinders have a distance of 3 m from centre to centre. The raft has no speed and is located in regular waves coming directly from abeam. The waves have $\lambda = 3\pi$ m and wave amplitude $h = 0.5$ m. Assume the two cylinders to be hydrodynamically independent. The raft has a draft of 0.5 m, centre of gravity in the centre of the connecting plate, radius of moment of inertia for rolling is $ik_x = 1$ m. The C_m is close enough to 0.8 to use the Lewis section curves for this C_m . Help: The centre of gravity of a semicircle is $4/(3\pi)$ its radius from the flat baseline. What is the maximum roll angle?



11. A ship sails in a natural seaway of approximately $T_e = 6$ s encounter period between ship and waves. The bridge of the ship is located forward near the bow. During 1 hour, a downward acceleration exceeding gravity acceleration g was observed 6 times. For downward accelerations exceeding $1.5g$, severe injuries to the crew have to be expected. What is the probability for this happening if the ship continues sailing with same speed in the same seaway for 12 hours?

Discourse: hydrodynamic mass

A body oscillating in water encounters hydrodynamic forces that in turn influence its motion behaviour. For ideal fluids for some simple geometries this hydrodynamic interaction can be computed analytically. For real ship geometries, it is usually determined by panel methods.

For constant velocity there is no force on a deeply submerged body. However, for instationary motions there is a resulting force even in ideal fluids. As an example we consider a circular cylinder of infinite length, i.e. a two-dimensional problem (Fig. 4.24.)

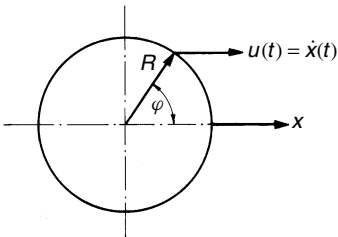


Figure 4.24 Cylinder in harmonic oscillation

The cylinder moves with $u(t) = \dot{x}(t)$. In a body-fixed coordinate system we describe the potential in cylindrical coordinates as:

$$\phi(r, \varphi, t) = -A \frac{\cos \varphi}{r}$$

The free constant A is determined by the boundary condition: no water penetrates the cylinder wall. In other words, the radial velocity of a particle at the cylinder wall must equal the velocity of the cylinder in this direction:

$$\left. \frac{\partial \phi}{\partial r} \right|_{r=R} = A \frac{\cos \varphi}{r^2} \bigg|_{r=R} = u(t) \cos \varphi \longrightarrow A = u(t)R^2 = \dot{x}(t)R^2$$

The pressure is given by the linearized Bernoulli equation:

$$p_{\text{inst}} = -\rho \left. \frac{\partial \phi}{\partial t} \right|_{r=R} = \rho \dot{u} R \cos \varphi$$

This antisymmetric pressure distribution on the body surface results in a force in the x direction (per unit length) which is directed opposite to the acceleration $\dot{u} = \ddot{x}$:

$$f_x = - \int_0^{2\pi} p_{\text{inst}} \cos \varphi R d\varphi = -\rho \dot{u} R^2 \int_0^{2\pi} \cos^2 \varphi d\varphi = -\rho \dot{u} R^2 \pi = -\rho \ddot{x} R^2 \pi$$

The hydrodynamic force is proportional to the acceleration. In essence, the body becomes 'more sluggish' than in air, just as if its mass has increased. The factor of proportionality has the dimension of mass per length:

$$f_x = -\frac{m''}{l} \dot{u} \quad \text{with } m'' = \rho R^2 \pi l$$

m'' is the added mass, also called hydrodynamic or virtual mass. In this case it is of the same magnitude as the displacement of the cylinder. For reasons of symmetry the hydrodynamic mass for this body is the same for all accelerations normal to cylinder axis.

For two-dimensional cross-sections, analytical solutions exist for semicircles. Conformal mapping then also yields solutions for Lewis sections which resemble ship sections (Lewis (1929)). Usually added mass and damping are given as non-dimensional coefficients, e.g. the heave added mass m_{33} (per length of an infinite cylinder) is divided by the mass displaced by a semicircle of the same width as the section:

$$m_{33} = C_z \frac{\pi B^2}{8} \rho$$

m_{22} correspondingly denotes the sway added mass. The cause for the damping lies in the radiated waves. The energy per time and cylinder length of the radiated waves of complex amplitude h is:

$$2 \cdot \rho g \frac{1}{2} |h|^2 \cdot c_{gr} = \rho g |h|^2 \frac{1}{2} \sqrt{\frac{g}{k}} = \frac{\rho g}{2\omega_e} |h|^2$$

The initial factor 2 accounts for waves radiated to both sides. This energy must be supplied by the motion of the cylinder:

$$\text{time average of } n_{33} \dot{u}_3 \dot{u}_3 = \frac{1}{2} n_{33} \omega_e |u_3|^2$$

\bar{A}_z denotes the ratio of amplitude of the radiated waves and the motion amplitude:

$$\bar{A}_z^2 = \frac{|h|^2}{|u_3|^2} = \frac{\omega_e^3}{\rho g^2} n_{33}$$

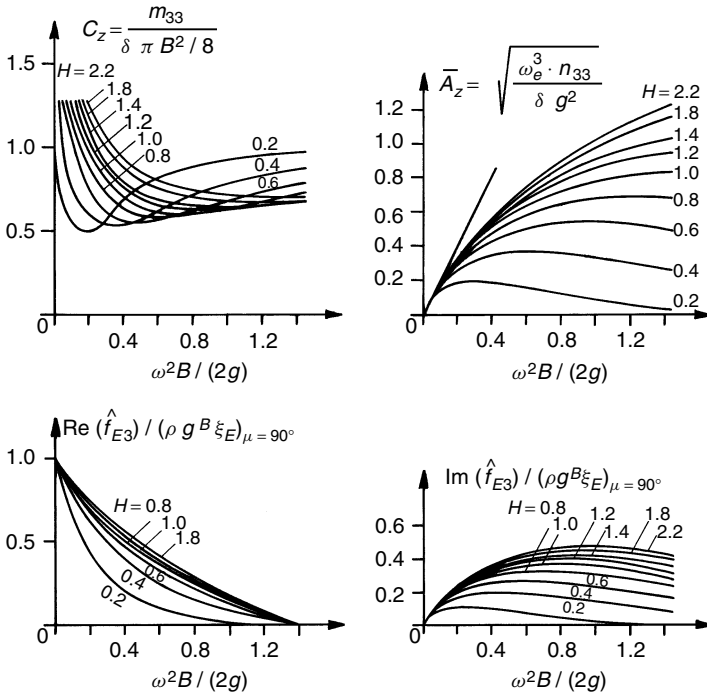


Figure 4.25 Coefficient C_z of hydrodynamic mass, ratio of amplitudes A_z and coefficients of exciting force for Lewis section of fullness $C_m = 0.8$ for various ratios of width to draft. The coefficients are given for vertical force and motion

This ratio is used for the non-dimensional description of the damping constant n_{33} and in similar form for n_{22} . Figure 4.25 gives curves for hydrodynamic coefficients for vertical force and motions over a non-dimensional frequency parameter $\omega_e B / 2g$ for Lewis sections of fullness $C_m = 0.8$ for a parameter variation of $H = B/2T$. The hydrodynamic mass tends to infinity for frequency going towards zero. This is no problem as the accelerations in this case go faster towards zero. So the force (mass times acceleration) vanishes in the limiting case of zero frequency. The real part of the exciting force \hat{f}_{E3} tends towards the hydrostatic expression $\rho g B h$ which is used to non-dimensionalize \hat{f}_{E3} .

Ship manoeuvring

5.1 Introduction

Ship manoeuvring comprises

- course keeping (this concerns only the direction of the ship's longitudinal axis)
- course changing
- track keeping (important in restricted waters)
- speed changing (especially stopping)

Manoeuvring requirements are a standard part of the contract between shipyard and shipowner. IMO regulations specify minimum requirements for all ships, but shipowners may introduce additional or more severe requirements for certain ship types, e.g. tugs, ferries, dredgers, exploration ships. Important questions for the specification of ship manoeuvrability may include:

- Does the ship keep a reasonably straight course (in autopilot or manual mode)?
- Under what conditions (current, wind) can the ship berth without tug assistance?
- Up to what ratio of wind speed to ship speed can the ship still be kept on all courses?
- Can the ship lay rudder in acceptable time from one side to the other?

Ship manoeuvrability is described by the following main characteristics:

- initial turning ability: ability to initiate a turn (rather quickly)
- sustained turning ability: ability for sustained (rather high) turning speed
- yaw checking ability: ability to stop turning motion (rather quickly)
- stopping ability: ability to stop (in rather short distance and time)
- yaw stability: ability to move straight ahead in the absence of external disturbances (e.g. wind) at one rudder angle (so-called neutral rudder angle)

The sustained turning ability appears to be the least important, since it describes the ship behaviour only for a time long after initiating a manoeuvre. The stopping ability is of interest only for slow speeds. For avoiding obstacles at high ship speed, it is far more effective to change course than to stop. (Course changes require less distance than stopping manoeuvres for full speed.)

Understanding ship manoeuvring and the related numerical and experimental tools is important for the designer for the choice of manoeuvring equipment of a ship. Items of the manoeuvring equipment may be:

- rudders
- fixed fins (e.g. above the rudder; skeg)
- jet thrusters
- propellers (including fixed pitch, controllable pitch, slewable, and cycloidal (e.g. Voith–Schneider propellers))
- adjustable ducts for propellers, steering nozzles
- waterjets

Both manoeuvring and seakeeping of ships concern time-dependent ship motions, albeit with some differences:

- The main difficulty in both fields is to determine the fluid forces on the hull (including propeller and rudder) due to ship motions (and possibly waves).
- At least a primitive model of the manoeuvring forces and motions should be part of any seakeeping simulation in oblique waves.
- Contrary to seakeeping, manoeuvring is often investigated in shallow (and usually calm) water and sometimes in channels.
- Linear relations between velocities and forces are reasonable approximations for many applications in seakeeping; in manoeuvring they are applicable only for rudder angles of a few degrees. This is one reason for the following differences.
- Seakeeping is mostly investigated in the frequency domain; manoeuvring investigations usually employ time-domain simulations.
- In seakeeping, motion equations are written in an inertial coordinate system; in manoeuvring simulations a ship-fixed system is applied. (This system, however, typically does not follow heel motions.)
- For fluid forces, viscosity is usually assumed to be of minor importance in seakeeping computations. In manoeuvring simulations, the free surface is often neglected. Ideally, both free surface and viscous effects should be considered for both seakeeping and manoeuvring.

Here we will focus on the most common computational methods for manoeuvring flows. Far more details, especially on manoeuvring devices, can be found in Brix (1993).

5.2 Simulation of manoeuvring with known coefficients

5.2.1 Introduction and definitions

The hydrodynamic forces of main interest in manoeuvring are:

- the longitudinal force (resistance) X
- the transverse force Y
- the yaw moment N

depending primarily on:

- the longitudinal speed u and acceleration \dot{u}
- transverse speed v at midship section and acceleration \dot{v}

- yaw rate (rate of rotation) $r = \dot{\psi}$ (rad/time) and yaw acceleration $\dot{r} = \ddot{\psi}$, where ψ is the yaw angle
- the rudder angle δ (positive to port)

For heel angles exceeding approximately 10° , these relations are influenced substantially by heel. The heel may be caused by wind or, for Froude numbers exceeding approximately 0.25, by the manoeuvring motions themselves. Thus at least for fast ships we are interested also in

- the heeling moment K
- the heel angle ϕ

For scaling these forces and moments from model to full scale, or for estimating them from results in similar ships, X , Y , K , and N are made non-dimensional in one of the following ways:

$$\begin{pmatrix} X' \\ Y' \\ K' \\ N' \end{pmatrix} = \frac{1}{q \cdot L^2} \begin{pmatrix} X \\ Y \\ K/L \\ N/L \end{pmatrix} \quad \text{or} \quad \begin{pmatrix} C_X \\ C_Y \\ C_K \\ C_N \end{pmatrix} = \frac{1}{q \cdot L \cdot T} \begin{pmatrix} X \\ Y \\ K/L \\ N/L \end{pmatrix}$$

with $q = \rho \cdot u^2/2$, ρ water density. Note that here we use the instantaneous longitudinal speed u (for $u \neq 0$) as reference speed. Alternatively, the ship speed at the begin of the manoeuvre may be used as reference speed. L is the length between perpendiculars. The term ‘forces’ will from now on include both forces and moments unless otherwise stated.

The motion velocities and accelerations are made non-dimensional also by suitable powers of u and L :

$$v' = v/u; \quad r' = r \cdot L/u; \quad u' = \dot{u} \cdot L/u^2; \quad \dot{v}' = \dot{v} \cdot L/u^2; \quad \dot{r}' = \dot{r} \cdot L^2/u^2$$

5.2.2 Force coefficients

CFD may be used to determine some of the coefficients, but is not yet established to predict all necessary coefficients. Therefore the body forces are usually determined in model experiments, either with free-running or captured models, see section 5.3. The results of such measurements may be approximated by expressions like:

$$\begin{aligned} Y' = & Y'_v \cdot v' + Y'_r \cdot r' + Y'_v \cdot v' + Y'_{v^3} \cdot (v')^3 + Y'_{vr^2} \cdot v'(r')^2 + Y'_{v\delta^2} \cdot v'\delta^2 \\ & + Y'_r \cdot r' + Y'_{r^3} \cdot (r')^3 + \dots \end{aligned}$$

where $Y'_v \dots$ are non-dimensional coefficients. Unlike the above formula, such expressions may also involve terms like $Y'_{ru} \cdot r' \cdot \Delta u'$, where $\Delta u' = (u - V)/u$. V is a reference speed, normally the speed at the begin of the manoeuvre. Comprehensive tables of such coefficients have been published, e.g. Wolff (1981) for models of five ship types (tanker, Series 60 $C_B = 0.7$, mariner, container ship, ferry) (Tables 5.1 and 5.2). The coefficients for u are based on $\Delta u = u - V$ in these tables. Corresponding to the small Froude numbers, the values do not contain heeling moments and the dependency of coefficients on heel angle. Such tables together with the formulae for X , Y , and N as

Table 5.1 Data of four models used in manoeuvring experiments (Wolff (1981))

	<i>Tanker</i>	<i>Series 60</i>	<i>Container</i>	<i>Ferry</i>
Scale	1:35	1:26	1:34	1:16
L_{pp}	8.286 m	7.034 m	8.029 m	8.725 m
B	1.357 m	1.005 m	0.947 m	1.048 m
T_{fp}	0.463 m	0.402 m	0.359 m	0.369 m
T_m	0.459 m	0.402 m	0.359 m	0.369 m
T_{ap}	0.456 m	0.402 m	0.359 m	0.369 m
C_B	0.805	0.700	0.604	0.644
Coord. origin aft of FP	4.143 m	3.517 m	4.014 m	4.362
LCG	-0.270 m	0.035 m	-0.160 m	-0.149 m
Radius of gyration i_z	1.900 m	1.580 m	1.820 m	1.89 m
No. of propellers	1	1	2	2
Propeller turning	right	right	outward	outward
Propeller diameter	0.226 m	0.279 m	0.181 m	0.215
Propeller P/D	0.745	1.012	1.200	1.135
Propeller A_E/A_0	0.60	0.50	0.86	0.52
No. of blades	5	4	5	4

given above may be used for time simulations of motions of such ships for an arbitrary time history of the rudder angle.

Wolff's results are deemed to be more reliable than other experimental results because they were obtained in large-amplitude, long-period motions of relatively large models (L between 6.4 and 8.7 m). Good accuracy in predicting the manoeuvres of sharp single-screw ships in full scale from coefficients obtained from experiments with such models has been demonstrated. For full ships, for twin-screw ships, and for small models, substantial differences between model and full-scale manoeuvring motions are observed. Correction methods from model to full scale need still further improvement.

For small deviations of the ship from a straight path, only linear terms in the expressions for the forces need to be retained. In addition we neglect heel and all those terms that vanish for symmetrical ships to obtain the equations of motion:

$$\begin{aligned}
 (X'_u - m')\dot{u}' + X'_u \Delta u' + X'_n \Delta n' &= 0 \\
 (Y'_v - m')\dot{v}' + (Y'_r - m'x'_G)\dot{r}' + Y'_v v' + (Y'_r - m')r' &= -Y'_\delta \delta \\
 (N'_v - m'x'_G)\dot{v}' + (N'_r - I'_{xx})\dot{r}' + N'_v v' + (N'_r - m'x'_G)r' &= -N'_\delta \delta
 \end{aligned}$$

I_{zz} is the moment of inertia with respect to the z -axis:

$$I_{zz} = \int (x^2 + y^2) dm$$

$m' = m/(\frac{1}{2}\rho L^3)$ is the non-dimensional mass, $I'_{zz} = I_{zz}/(\frac{1}{2}\rho L^5)$ the non-dimensional moment of inertia coefficient.

If we just consider the linearized equations for side forces and yaw moments, we may write:

$$M'\ddot{u}' + D'\dot{u}' = \vec{r}'\delta$$

Table 5.2 Non-dimensional hydrodynamic coefficient of four ship models (Wolff (1981)); values to be multiplied by 10^{-6}

Model of Initial F_n	Tanker 0.145	Series 60 0.200	Container 0.159	Ferry 0.278
m'	14 622	11 432	6 399	6 765
$x'_G m'$	365	57	-127	-116
I'_{zz}	766	573	329	319
$X'_{\dot{y}}$	-1 077	-1 064	0	0
$X'_{\dot{y}u^2}$	-5 284	0	0	0
$X'_{\dot{y}u}$	-2 217	-2 559	-1 320	-4 336
$X'_{\dot{y}^2}$	1 510	0	1 179	-2 355
$X'_{\dot{y}^3}$	0	-2 851	0	-2 594
$X'_{\dot{y}^2}$	-889	-3 908	-1 355	-3 279
$X'_{\dot{y}^2}$	237	-838	-151	-571
$X'_{\dot{y}^2}$	-1 598	-1 346	-696	-2 879
$X'_{\dot{y}^2u}$	0	-1 833	-2 463	-2 559
$X'_{\dot{y}^2u}$	2 001	2 536	0	3 425
$X'_{\dot{y}^2u}$	0	0	-470	-734
$X'_{\dot{y}^2u}$	9 478	7 170	3 175	4 627
$X'_{\dot{y}^2}$	1 017	942	611	877
$X'_{\dot{y}^2}$	-482	-372	-340	-351
X'_{vu}	745	0	0	0
$X'_{\dot{y}u^2}$	0	0	-207	0
X'_{ru}	0	-270	0	0
$X'_{\dot{y}^2}$	48	0	0	-19
$X'_{\dot{y}^2}$	166	0	0	0
$X'_{\dot{y}^2u}$	0	150	0	0
$X'_{\dot{y}^2\delta}$	-4 717	0	0	0
$X'_{\dot{y}^2\delta}$	-365	0	0	0
$X'_{\dot{y}^3}$	1 164	2 143	0	0
$X'_{\dot{y}^3}$	-118	0	0	0
$X'_{\dot{y}^3u}$	-278	0	0	0
$X'_{\dot{y}^4}$	0	621	213	2 185
$X'_{\dot{y}^3u}$	0	0	-3 865	0
X'_{r^3u}	0	0	-447	0

Longitudinal forces X

Model of	Tanker	Series 60	Container	Ferry
$N'_{\dot{y}}$	-523	326	239	426
$N'_{\dot{y}u^2}$	2 311	1 945	5 025	10 049
$N'_{\dot{y}^2}$	-576	-461	-401	-231
$N'_{\dot{y}^2}$	-130	-250	132	0
$N'_{\dot{y}^2}$	67	9	0	0
$N'_{\dot{y}^2}$	-144	37	8	-36
$N'_{\dot{y}^2}$	-5 544	-6 570	-3 800	-3 919
$N'_{\dot{y}^2}$	-132	0	0	0
$N'_{\dot{y}^3}$	-2 718	-16 602	-23 865	-33 857
N'_{vu}	0	-1 146	-2 179	-3 666
$N'_{\dot{y}^2}$	3 448	4 421	-4 586	0
$N'_{\dot{y}^2}$	2 317	0	1 418	570
$N'_{\dot{y}^2}$	-3 074	-2 900	-1 960	-2 579
$N'_{\dot{y}^2}$	0	-45	0	0
$N'_{\dot{y}^3}$	-865	-1 919	-729	-2 253
N'_{ru}	0	0	-473	0
$N'_{\dot{y}^2}$	913	0	0	0
N'_{rv^2}	-16 196	-20 530	-27 858	-60 110

Model of	Tanker	Series 60	Container	Ferry
$Y'_{\dot{y}}$	-11 420	-12 608	-6 755	-7 396
$Y'_{\dot{y}u^2}$	-21 560	-34 899	-10 301	0
$Y'_{\dot{y}^2}$	-714	-771	-222	-600
$Y'_{\dot{y}^2}$	-468	166	-63	0
$Y'_{\dot{y}^2}$	-244	26	0	0
$Y'_{\dot{y}^2}$	263	-69	-33	57
$Y'_{\dot{y}^2}$	-15 338	-16 630	-8 470	-12 095
$Y'_{\dot{y}^2}$	-36 832	-45 034	0	-137 302
$Y'_{\dot{y}^2}$	-19 040	-37 169	-31 214	-44 365
$Y'_{\dot{y}^2}$	0	0	-4 668	2 199
$Y'_{\dot{y}^2}$	4 842	4 330	2 840	1 901
$Y'_{\dot{y}^2}$	0	152	85	0
$Y'_{\dot{y}^2}$	1 989	2 423	-1 945	-1 361
Y'_{ru}	0	-1 305	2 430	-1 297
$Y'_{\dot{y}u^2}$	0	0	4 769	0
$Y'_{\dot{y}u^2}$	22 878	10 230	-33 237	-36 490
$Y'_{\dot{y}^2}$	1 492	0	0	-2 752
$Y'_{\dot{y}^2}$	3 168	2 959	1 660	3 587
$Y'_{\dot{y}^2}$	0	0	0	98
$Y'_{\dot{y}^2}$	3 621	-7 494	0	0
$Y'_{\dot{y}^2}$	1 552	613	-99	0
$Y'_{\dot{y}^2}$	-5 526	4 344	-1 277	-6 262
$Y'_{\dot{y}u^2}$	0	0	13 962	0
$Y'_{\dot{y}^2}$	1 637	0	2 438	0
$Y'_{\dot{y}^2}$	-4 562	-4 096	0	-5 096
$Y'_{\dot{y}u^2}$	0	974	0	0
$Y'_{\dot{y}^2u}$	2 640	4 001	0	3 192
$Y'_{v v }$	-11 513	-19 989	-47 566	0
$Y'_{r r }$	-351	0	1 731	0
$Y'_{\dot{y} \delta }$	-889	2 029	0	0
$Y'_{\dot{y}^2 \delta }$	12 398	0	0	0
Y'_{r^3u}	0	2 070	0	0

Transverse forces Y

Model of	Tanker	Series 60	Container	Ferry
$N'_{\dot{y}^2}$	-324	0	-404	237
$N'_{\dot{y}^2}$	-1 402	-1 435	-793	-1 621
$N'_{\dot{y}^2}$	0	-138	0	-73
$N'_{\dot{y}^2}$	-1 641	3 907	0	0
$N'_{\dot{y}^2}$	-536	0	0	0
$N'_{\dot{y}^2}$	2 220	-2 622	652	2 886
$N'_{\dot{y}^2}$	0	0	-6 918	-2 950
$N'_{\dot{y}^2}$	-855	0	-1 096	-329
$N'_{\dot{y}^2}$	2 321	1 856	0	2 259
$N'_{\dot{y}^2}$	0	-568	0	0
$N'_{\dot{y}^2u}$	316	0	0	0
$N'_{\dot{y}^2u}$	-1 538	-1 964	0	-1 382
$N'_{\dot{y}^2u}$	0	5 328	8 103	0
$N'_{v v }$	0	0	-1 784	0
$N'_{r r }$	-394	0	0	0
$N'_{\dot{y} \delta }$	384	-1 030	0	0
$N'_{\dot{y}^2 \delta }$	-27 133	-13 452	0	0
N'_{r^3u}	0	-476	0	-1 322

with:

$$M' = \begin{bmatrix} -Y'_v + m' & -Y'_r + m'x_G \\ -N'_v + m'x_G & -N'_r + I_{zz} \end{bmatrix}; \quad \vec{u}' = \begin{Bmatrix} v' \\ r' \end{Bmatrix}$$

$$D' = \begin{bmatrix} -Y'_v & -Y'_r + m' \\ -N'_v & -N'_r + m'x'_G \end{bmatrix}; \quad \vec{r}' = \begin{Bmatrix} Y'_\delta \\ N'_\delta \end{Bmatrix}$$

M' is the mass matrix, D' the damping matrix, \vec{r}' the rudder effectiveness vector, and \vec{u}' the motion vector. The terms on the right-hand side thus describe the steering action of the rudder. Some modifications of the above equation of motion are of interest:

1. If in addition a side thruster at location x_t is active with thrust T , the (non-dimensional) equation of motion modifies to:

$$M'\dot{\vec{u}}' + D'\vec{u}' = \vec{r}'\delta + \begin{Bmatrix} T' \\ T'x'_t \end{Bmatrix}$$

2. For steady turning motion ($\dot{\vec{u}}' = 0$), the original linearized equation of motion simplifies to:

$$D'\vec{u}' = \vec{r}'\delta$$

Solving this equation for r' yields:

$$r' = \frac{Y'_\delta N'_v - Y'_v N'_\delta}{Y'_v(Y'_r - m')C'}\delta$$

C' is the yaw stability index:

$$C' = \frac{N'_r - m'x'_g}{Y'_r - m'} - \frac{N'_v}{Y'_v}$$

$Y'_v(Y'_r - m')$ is positive, the nominator (almost) always negative. Thus C' determines the sign of r' . Positive C' indicate yaw stability, negative C' yaw instability. Yaw instability is the tendency of the ship to increase the absolute value of an existing drift angle. However, the formula is numerically very sensitive and measured coefficients are often too inaccurate for predictions. Therefore, usually more complicated analyses are necessary to determine yaw stability.

3. If the transverse velocity in the equation of motion is eliminated, we obtain a differential equation of second order of the form:

$$T_1 T_2 \ddot{r} + (T_1 + T_2) \cdot \dot{r} + r = -K(\delta + T_2 \dot{\delta})$$

The T_i are time constants. $|T_2|$ is much smaller than $|T_1|$ and thus may be neglected, especially since linearized equations are anyway a (too) strong simplification of the problem, yielding the simple 'Nomoto' equation:

$$T\dot{r} + r = -K\delta$$

T and K denote here time constants. K is sometimes called rudder effectiveness. This simplified equation neglects not only all non-linear effects,

but also the influence of transverse speed, longitudinal speed and heel. As a result, the predictions are too inaccurate for most practical purposes. The Nomoto equation allows, however, a quick estimate of rudder effects on course changes. A slightly better approximation is the 'Norrbin' equation:

$$T\dot{r} + r + \alpha r^3 = -K\delta$$

α is here a non-linear 'damping' factor of the turning motions. The constants are determined by matching measured or computed motions to fit the equations best. The Norrbin equation still does not contain any unsymmetrical terms, but for single-screw ships the turning direction of the propeller introduces an unsymmetry, making the Norrbin equation questionable.

The following regression formulae for linear velocity and acceleration coefficients have been proposed (Clarke *et al.* (1983)):

$$Y'_v = -\pi(T/L)^2 \cdot (1 + 0.16C_B \cdot B/T - 5.1(B/L)^2)$$

$$Y'_r = -\pi(T/L)^2 \cdot (0.67B/L - 0.0033(B/T)^2)$$

$$N'_v = -\pi(T/L)^2 \cdot (1.1B/L - 0.041B/T)$$

$$N'_r = -\pi(T/L)^2 \cdot (1/12 + 0.017C_B \cdot B/T - 0.33B/L)$$

$$Y'_v = -\pi(T/L)^2 \cdot (1 + 0.40C_B \cdot B/T)$$

$$Y'_r = -\pi(T/L)^2 \cdot (-0.5 + 2.2B/L - 0.08B/T)$$

$$N'_v = -\pi(T/L)^2 \cdot (0.5 + 2.4T/L)$$

$$N'_r = -\pi(T/L)^2 \cdot (0.25 + 0.039B/T - 0.56B/L)$$

T is the mean draft. These formulae apply to ships on even keel. For ships with draft difference $t = T_{ap} - T_{fp}$, correction factors may be applied to the linear even-keel velocity coefficients (Inoue and Kijima (1978)):

$$Y'_v(t) = Y'_v(0) \cdot (1 + 0.67t/T)$$

$$Y'_r(t) = Y'_r(0) \cdot (1 + 0.80t/T)$$

$$N'_v(t) = N'_v(0) \cdot (1 - 0.27t/T \cdot Y'_v(0)/N'_v(0))$$

$$N'_r(t) = N'_r(0) \cdot (1 + 0.30t/T)$$

These formulae were based both on theoretical considerations and on model experiments with four 2.5 m models of the Series 60 with different block coefficients for $-0.2 < t/T < 0.6$.

In cases where u and/or the propeller turning rate n vary strongly during a manoeuvre or even change sign as in a stopping manoeuvre, the above coefficients will vary widely. Therefore, the so-called four-quadrant equations, e.g. Sharma (1986), are better suited to represent the forces. These equations are based on a physical explanation of the forces due to hull, rudder and propeller, combined with coefficients to be determined in experiments.

5.2.3 Physical explanation and force estimation

In the following, forces due to non-zero rudder angles are not considered. If the rudder at the midship position is treated as part of the ship's body, only the difference between rudder forces at the actual rudder angle δ and those at $\delta = 0^\circ$ have to be added to the body forces treated here. The gap between ship stern and rudder may be disregarded in this case. Propeller forces and hull resistance in straightforward motion are neglected here.

We use a coordinate system with origin fixed at the midship section on the ship's centre plane at the height of the centre of gravity (Fig. 5.1). The x -axis points forward, y to starboard, z vertically downward. Thus the system participates in the motions u , v , and r of the ship, but does not follow the ship's heeling motion. This simplifies the integration in time (e.g. by a Runge–Kutta scheme) of the ship's position from the velocities u , v , r and eliminates several terms in the force formulae.

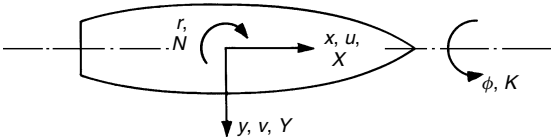


Figure 5.1 Coordinates x , y ; direction of velocities u , v , r , forces X , Y , and moments K , N

Hydrodynamic body forces can be imagined to result from the change of momentum ($=\text{mass} \cdot \text{velocity}$) of the water near to the ship. Most important in manoeuvring is the transverse force acting upon the hull per unit length (e.g. metre) in the x -direction. According to the slender-body theory, this force is equal to the time rate of change of the transverse momentum of the water in a 'strip' between two transverse planes spaced one unit length. In such a 'strip' the water near to the ship's side mostly follows the transverse motion of the respective ship section, whereas water farther from the hull is less influenced by transverse ship motions. The total effect of this water motion on the transverse force is the same as if a certain 'added mass' per length m' moved exactly like the ship section in transverse direction. (This approach is thus similar to the strip method approach in ship seakeeping.)

The added mass m' may be determined for any ship section as:

$$m' = \frac{1}{2} \pi \cdot \rho \cdot T_x^2 \cdot c_y$$

T_x is the section draft and c_y a coefficient. c_y may be calculated:

- analytically if we approximate the actual ship section by a 'Lewis section' (conformal mapping of a semicircle); Fig. 5.2 shows such solutions for parameters (T_x/B) and $\beta = \text{immersed section area}/(B \cdot T_x)$
- for arbitrary shape by a close-fit boundary element method as for 'strips' in seakeeping strip methods, but for manoeuvring the free surface is generally neglected
- by field methods including viscosity effects

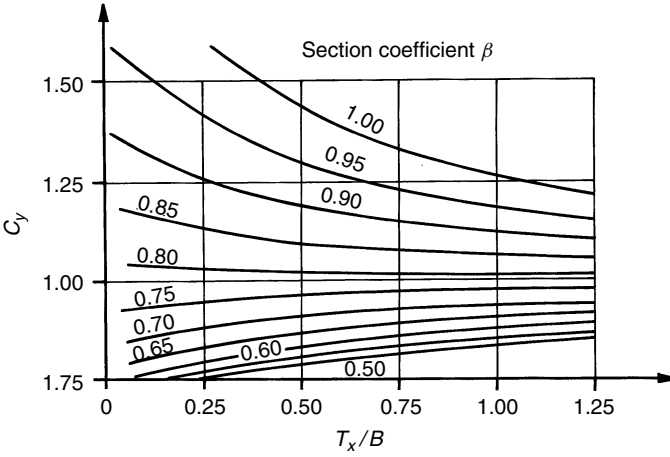


Figure 5.2 Section added mass coefficient C_y for low-frequency, low-speed horizontal acceleration

Neglecting influences due to heel velocity p and heel acceleration \dot{p} , the time rate of change of the transverse momentum of the ‘added mass’ per length is:

$$\left(\frac{\partial}{\partial t} - u \cdot \frac{\partial}{\partial x} \right) [m'(v + x \cdot r)]$$

$\partial/\partial t$ takes account of the local change of momentum (for fixed x) with time t . The term $u \cdot \partial/\partial x$ results from the convective change of momentum due to the longitudinal motion of the water ‘strip’ along the hull with appropriate velocity $-u$ (i.e. from bow to stern). $v + x \cdot r$ is the transverse velocity of the section in the y -direction resulting from both transverse speed v at midship section and the yaw rate r . The total transverse force is obtained by integrating the above expression over the underwater ship length L . The yaw moment is obtained by multiplying each force element with the respective lever x , and the heel moment is obtained by using the vertical moment $z_y m'$ instead of m' , where z_y is the depth coordinate of the centre of gravity of the added mass. For Lewis sections, this quantity can be calculated theoretically (Fig. 5.3). For CFD approaches the corresponding vertical moment is computed directly as part of the numerical solution. Söding gives a short Fortran subroutine to determine c_y and z_y for Lewis sections in Brix (1993), p. 252.

Based on these considerations we obtain the ‘slender-body contribution’ to the forces as:

$$\begin{aligned} \begin{Bmatrix} X \\ Y \\ K \\ N \end{Bmatrix} &= \int_L \begin{Bmatrix} 0 \\ 1 \\ 1 \\ x \end{Bmatrix} \cdot \left(\frac{\partial}{\partial t} - u \cdot \frac{\partial}{\partial x} \right) (m'(v + x \cdot r)) \\ &\quad \cdot \left(\begin{Bmatrix} 0 \\ m' \\ -z_y m' \\ m' \end{Bmatrix} (v + x \cdot r) \right) dx \end{aligned}$$

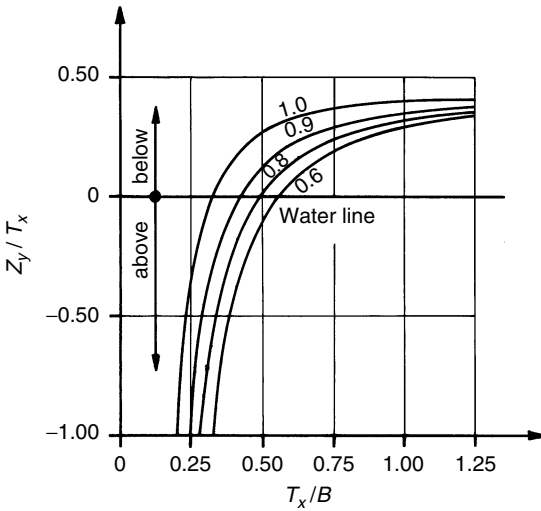


Figure 5.3 Height coordinate Z_y of section added mass m'

The 'slender-body contribution' to X is zero. Several modifications to this basic formula are necessary or at least advisable:

1. For terms involving $-\partial/\partial t$, i.e. for the acceleration dependent parts of the forces, correction factors k_1 , k_2 should be applied. They consider the lengthwise flow of water around bow and stern which is initially disregarded in determining the sectional added mass m' . The acceleration part of the above basic formula then becomes:

$$\begin{Bmatrix} X_1 \\ Y_1 \\ K_1 \\ N_1 \end{Bmatrix} = \int_L \begin{Bmatrix} 0 \\ -k_1 m' \\ z_y m' \\ -k_2 x m' \end{Bmatrix} \cdot (k_1 \dot{v} + k_2 x \cdot \dot{r}) dx$$

k_1 and k_2 are approximated here by regression formulae which were derived from the results of three-dimensional flow calculations for accelerated ellipsoids:

$$k_1 = \sqrt{1 - 0.245\varepsilon - 1.68\varepsilon^2}$$

$$k_2 = \sqrt{1 - 0.76\varepsilon - 4.41\varepsilon^2}$$

with $\varepsilon = 2T_x/L$.

2. For parts in the basic formula due to $u \cdot \partial/\partial x$, one should distinguish terms where $\partial/\partial x$ is applied to the first factor containing m' from terms where the second factor $v + x \cdot r$ is differentiated with respect to x (which results in r). For the former terms, it was found by comparison with experimental values that the integral should be extended only over the region where dm'/dx is negative, i.e. over the forebody. This may be understood as the effect of flow separation in the aftbody. The flow separation causes the water to retain most of its transverse momentum behind the position of maximum added mass which for ships without trim may be taken to be the midship

section. The latter terms, however, should be integrated over the full length of the ship. This results in:

$$\begin{pmatrix} X_2 \\ Y_2 \\ K_2 \\ N_2 \end{pmatrix} = u \begin{pmatrix} 0 \\ -m'_m \\ z_{ym}m'_m \\ -x_m m'_m \end{pmatrix} \cdot (v + x_m \cdot r) \\ + u \cdot r \int_{x_a}^{x_m} \begin{pmatrix} 0 \\ m' \\ -z_y m' \\ x m' \end{pmatrix} dx - u \int_{x_m}^{x_f} \begin{pmatrix} 0 \\ 0 \\ 0 \\ m' \end{pmatrix} (v + x \cdot r) dx$$

x_a is the x coordinate of the aft end, x_f of the forward end of the ship. The index m refers to the x coordinate where m' is maximum. For negative u the differences in treating the fore- and aftbody are interchanged.

3. The slender-body theory disregards longitudinal forces associated with the added mass of the ship in the longitudinal direction. These additional terms are taken from potential-flow theory without flow separation (Newman (1977)):

$$\begin{pmatrix} X_3 \\ Y_3 \\ K_3 \\ N_3 \end{pmatrix} = \begin{pmatrix} -m_x \cdot \dot{u} \\ -m_x \cdot u \cdot r \\ 0 \\ m_x \cdot u \cdot v \end{pmatrix}$$

m_x is the added mass for longitudinal motion; it may be approximated by a formula which was also fitted to theoretical values for ellipsoids:

$$m_x = \frac{m}{\pi \sqrt{L^3 / \nabla - 14}}$$

∇ denotes here the volume displacement. Theoretically additional terms proportional to $r \cdot v$ and r^2 should appear in the formula for X . According to experiments with ship models, however, the $r \cdot v$ term is much smaller and the r^2 term may even have a different sign than the theoretical expression. Therefore these terms which are influenced substantially by flow separation have been omitted. Further, some theoretical terms of small magnitude involving heeling motion or referring to the heeling moment have also been omitted in the above formula for X_3 etc.

4. Because slender-body theory neglects flow separation in transverse flow around ship sections (only longitudinal flow separation is roughly taken into account), an additional 'cross-flow resistance' of the ship sections has to be added. The absolute value of this resistance per unit length is:

$$\frac{1}{2} \rho \cdot T_x \cdot v_x^2 \cdot C_D$$

$v_x = v + x \cdot r$ is the transverse velocity of the section. C_D is a cross-flow resistance coefficient. The direction of the resistance is opposite to the direction of v_x . Thus for arbitrary direction of motion, the term $-v_x |v_x|$ is required instead of v_x^2 . Therefore the cross-flow resistance adds the

following contributions to the body forces:

$$\begin{Bmatrix} X_4 \\ Y_4 \\ K_4 \\ N_4 \end{Bmatrix} = \frac{1}{2}\rho \int_L \begin{Bmatrix} 0 \\ -1 \\ z_D \\ -x \end{Bmatrix} (v + x \cdot r)|v + x \cdot r| T_x C_D dx$$

z_D is the z coordinate (measured downward from the centre of gravity G of ship's mass m) of the action line of the cross-flow resistance. For typical cargo ship hull forms, this force acts about 65% of the draft above the keel line. Thus a constant (mean) value over ship length of:

$$z_D = \overline{KG} - 0.65T$$

may be applied to the formula for X_4 etc. For tug models values of 1.0 ± 0.1 instead of the above 0.65 were found.

C_D is estimated as 1.0 averaged over the whole ship length for cargo vessels like container ships with bilge keels. For fuller hulls values between 0.5 and 0.7 may be suitable. The C_D values are generally higher in the aftbody than in the forebody due to stronger flow separation in the aftbody.

Results of transverse towing tests (at zero speed) with and without heel with large models are presented in Table 5.3. These results differ from the situation at considerable forward speed.

Table 5.3 Results of transverse towin tests with large models upright and with 10° heel; models were equipped with rudder and propeller but without bilge keels

	<i>Cargo ship</i>	<i>Tanker</i>	<i>Tanker</i>	<i>Container ship</i>	<i>Twin-screw salvage tug</i>
L/B	6.66	5.83	6.11	7.61	5.21
B/T	2.46	2.43	2.96	2.93	2.25
C_B	0.66	0.84	0.81	0.58	0.58
C_D	0.562	0.983	0.594	0.791	0.826
C_{D10°	0.511	1.151	–	1.014	–

The sum of contributions 1 to 4 constitutes the total body force:

$$\begin{Bmatrix} X \\ Y \\ K \\ N \end{Bmatrix} = \begin{Bmatrix} X_1 \\ Y_1 \\ K_1 \\ N_1 \end{Bmatrix} + \begin{Bmatrix} X_2 \\ Y_2 \\ K_2 \\ N_2 \end{Bmatrix} + \begin{Bmatrix} X_3 \\ Y_3 \\ K_3 \\ N_3 \end{Bmatrix} + \begin{Bmatrix} X_4 \\ Y_4 \\ K_4 \\ N_4 \end{Bmatrix}$$

For steady traversing or pure yaw motion without forward speed, only terms listed under 4 above are relevant.

The yaw stability is very sensitive to small changes in the body forces. Therefore a reliable prediction of yaw stability based on the slender-body theory or regression analysis of model tests is not possible. Substantial improvements of theoretical calculations seem possible only if the flow separation around the hull is determined in detail by computational simulation of the viscous, turbulent flow in a RANSE code or even LES simulations. RANSE simulations were in the late 1990s subject to research and not yet established for practical applications. Three-dimensional boundary element

methods have been applied to achieve improvements over the slender-body approach, especially capturing free-surface effects (waves, trim and sinkage). However, the slender-body approach described here appears to be useful and sufficient in most cases in deep water. Extensions of the theory to shallow water exist.

5.2.4 Influence of heel

For exact motion predictions including the coupling of manoeuvring motions with heel one should take account of:

- the heeling moments due to weight and mass moments, hydrostatic and hydrodynamic moments on hull, rudder and propeller, and possibly wind heeling moments or other external influences
- the dependence of X , Y and N on heel angle, heel velocity and heel acceleration

Details may be drawn from Bohlmann's (1989, 1990) work on submarine manoeuvring.

By choosing our coordinate origin at the height of the ship's centre of gravity, many of these influences are zero, others are small in cargo ships. For example, the dependence of X , Y and N on the heel rate and heel acceleration can be neglected if the interest is not in the rolling motions themselves, but only in their influence on manoeuvring motions. In this case, the heel angle may be determined by the equilibrium resulting from the manoeuvring heel moment K as stated before, the hydrostatic righting moment, and possibly the wind- and propeller-induced moments. However, the dependence of X , Y and N on the heel angle may be substantial.

The following procedure is recommended to evaluate the influence of heel:

1. In the equations for X_1 etc., m' is determined taking into account the heel angle. This leads to larger m' values in the midship range due to increase of draft with heel for the full midship sections. Capturing the influence of heel in the computations of m' is straightforward in CFD computations, but also a Lewis transformation approach can be extended to include heel (Söding (1984)).
2. In the equations for X_1 , instead of v the expression $v - u \cdot \partial y_B / \partial x$ should be used, where y_B is the y coordinate of the centre of gravity of the immersed section area due to heel. The term takes account of the curvature of the 'centreline' of the heeled hull.
3. The cross-flow resistance coefficient C_D depends on the heel angle. C_D may decrease by 1% to 3% per degree of heel in the direction of drift motion. Due to the increase of section draft (at least in the midship region) with heel, however, the actual cross-flow resistance may increase with heel angle.
4. For larger heel angles exceeding approximately 25° , the cross-flow velocity in the equation for X_4 etc. should be determined with respect to the curved line being composed of the points of maximum draft of the ship sections. If this line has transverse coordinate $y_T(x)$, instead of $v + x \cdot r$ the expression $v + x \cdot r - \partial y_T / \partial x \cdot u$ has to be used in the equation for X_4 etc. for heel angles exceeding 25° . For smaller heel, a linear interpolation of the correction term $-\partial y_T / \partial x \cdot u$ over heel is recommended.

This procedure improves predictions, but still has substantial deficiencies for larger heel angles.

5.2.5 Shallow water and other influences

Body forces not only depend on the actual acceleration, speed and (in case of heel) state of the vessel, but also on the previous time history of body motion. This is due to vortex shedding and waves generated by the ship. However, these ‘memory effects’ are very small in ordinary manoeuvring motions. Exceptions where memory effects may be important are:

- PMM experiments with the usual too small amplitudes
- self-induced motions of a moored ship

Shallow water, non-uniform current and interactions with other ships may substantially influence the body forces as discussed in detail in Brix (1993). The influence of shallow water can be roughly described as follows. If the ship keel is just touching the sea bottom, the effective side ratio of the ship hull is increased from approximately 0.1 (namely $2T/L$; factor 2 due to mirror image at waterplane) to ∞ . This increases the transverse forces approximately by a factor 40 (following the simple estimate formula for rudder lift in section 5.4). The rudder itself increases its effective side ratio from approximately 2 for deep water to ∞ for extremely shallow water. The rudder forces are then increased by a factor of approximately 2.5. The hull forces for a yaw stable ship decrease the course-changing ability, the rudder forces increase the course-changing ability. Since the hull forces increase more than the rudder forces on shallow water, the net result for yaw stable ships is

- increased radius of turning circle
- increased turning time
- increased yaw checking time

For yaw instable ships, this may be different, especially if the yaw stability changes drastically. Shallow water may increase or decrease yaw stability. One of several effects is the change of trim. Boundary element methods, namely ‘wave resistance’ codes may be used to predict trim and sinkage of real ship geometries with usually good accuracy on shallow water. The results of such computations have been used to estimate the amount of yaw instability.

5.2.6 Stopping

The rudder behind a reverse turning propeller is almost without effect. The track of a stopping ship is thus largely determined by the manoeuvring forces of the propeller(s) and wind. For yaw instable ships, the track can be largely influenced by small initial port or starboard motions. For sister ships (large tankers) under ‘same’ conditions, stopping times vary between 12 and 22 minutes with largely differing tracks. The differences are attributed to such small (random) initial differences in yaw motions.

For low speeds, the stopping times and distances can be determined as follows. One assumes that between two points in time t_1 and t_2 the reverse thrust (minus thrust deduction) T is approximately constant and that the

resistance R is proportional to speed u :

$$\frac{R}{u^2} = \frac{R_0}{U_0^2} = k$$

k is the stopping constant. The index 0 denotes the values at the beginning of the manoeuvre. If we assume a straight stopping track, the fundamental equation of motion is:

$$m \cdot u = -(u^2 + u_T^2)$$

The mass m includes the hydrodynamic added mass m'' for longitudinal motion which may be estimated by the empirical formula:

$$\frac{m''}{m_0} = \frac{1}{\pi \sqrt{(L^3/\nabla) - 14}}$$

Here ∇ is the volume displacement. $u_T = U_0 \sqrt{T/R_0}$ is the speed the ship would have after a long time if the thrust T would be directed forward. The above differential equation can be solved (by separation of variables) to yield:

$$\Delta t = t_2 - t_1 = \frac{m}{ku_T} \left[\arctan \frac{u_1}{u_T} - \arctan \frac{u_2}{u_T} \right]$$

The distance is given by multiplying the above differential equation by $u = ds/dt$ and solving again (by separation of variables) to yield:

$$\Delta s = s_2 - s_1 = \frac{m}{2k} \ln \left(\frac{u_1^2 + u_T^2}{u_2^2 + u_T^2} \right)$$

These two equations for Δt and Δs can be used to compute stepwise the stopping process by splitting the process into time intervals where the thrust T can be assumed to be constant. The reverse thrust is best determined by using four-quadrant diagrams for the propellers, if these diagrams are available.

5.2.7 Jet thrusters

Transverse jet thrusters consist of a transverse pipe through the ship hull located usually at the bow or at the stern. The pipe contains a screw propeller which pumps water either to port or starboard thus creating a side thrust (and moment). The purpose of a jet thruster is to increase manoeuvrability at low speeds, allowing the ship to manoeuvre with no or less tug assistance. As the rudder astern already supplies manoeuvring forces, jet thrusters are more effective at the bow and usually placed there ('bow thrusters'). Also stern jets need to cope with potential collision problems in arranging both jet pipe and propeller shaft. Jet thrusters may also serve as an emergency backup for the main rudder. Backups for rudders are needed for ships with dangerous cargo. Jet thrusters are less attractive for ships on long-distance routes calling at few ports. The savings in tug fees may be less than the additional expense for fuel.

For ocean going ships, side thrusts of 0.08–0.12 kN per square metre under-water lateral area are typical values. These values relate to zero forward speed

of the ship. Installed power P , cross-section area of the pipe A , and flow velocity v in the jet thruster are related by:

$$T = \rho \cdot A \cdot v^2$$

$$P = \frac{1}{\eta} \cdot \frac{1}{2} \rho A v^2$$

η is here the efficiency of the thruster propeller. These equations yield:

$$\frac{P}{T} = \frac{v}{2\eta}$$

$$\frac{T}{A} = \rho v^2$$

$\eta = 0.8$ and $v = 11$ m/s yield typical relations: approximately 120 kN/m² thrust per thruster cross-section area and 7 kW power per kN thrust.

With increasing speed, jet thrusters become less effective and rudders become more effective. The reason is that the jet is bent backwards and may reattach to the ship hull. The thrust is then partially compensated by an opposite suction force. This effect may be reduced by installing a second (passive) pipe without a propeller downstream of the thruster (Brix (1993)).

5.2.8 CFD for ship manoeuvring

For most ships, the linear system of equations determining the drift and yaw velocity in steady turning motion is nearly singular. This produces large relative errors in the predicted steady turning rate especially for small rudder angles and turning rates. For large rudder angle and turning rate, non-linear forces alleviate these problems somewhat. But non-linear hull forces depend crucially on the cross-flow resistance or the direction of the longitudinal vortices, i.e. on quantities which are determined empirically and which vary widely. In addition, extreme rudder forces depend strongly on the rudder stall angle which – for a rudder behind the hull and propeller – requires at least two-dimensional RANSE simulations. Thus large errors are frequently made in predicting both the ship's path in hard manoeuvres and the course-keeping qualities. (The prediction of the full ship is fortunately easier as at the higher Reynolds numbers stall rarely occurs). In spite of that, published comparisons between predictions and measurements almost always indicate excellent accuracy. A notable exception is Söding (1993a). The difference is that Söding avoids all information which would not be available had the respective model not been tested previously. The typical very good agreement published by others is then suspected to be either chosen as best results from a larger set of predictions or due to empirical corrections of the calculation method based on experiments which include the ship used for demonstrating the attained accuracy. Naturally, these tricks are not possible for a practical prediction where no previous test results for the ship design can be used. Thus the accuracy of manoeuvring predictions is still unsatisfactory, but differences between alternative designs and totally unacceptable designs may be easily detected using the available methods for manoeuvring prediction. With appropriate validation, it may also be possible to predict full-scale ship motions with sufficient

accuracy, but the experience published so far is insufficient to establish this as state of the art.

The simplest approach to body force computations is the use of regression formulae based on slender-body theory, but with empirical coefficients found from analysing various model experiments, e.g. Clarke *et al.* (1983). The next more sophisticated approach would be to apply slender-body methods directly, deriving the added mass terms for each strip from analytical (Lewis form) or BEM computations. These approaches are still state of the art in ship design practice and have been discussed in the previous chapters.

The application of three-dimensional CFD methods, using either lift-generating boundary elements (vortex or dipole) or field methods (Euler or RANSE solvers) is still predominantly a matter of research, although the boundary element methods are occasionally applied in practical design. The main individual CFD approaches are ranked in increasing complexity:

- *Lifting surface methods*

An alternative to slender-body theory, applicable to rudder and hull (separately or in combination), is the lifting surface model. It models the inviscid flow about a plate (centre plane), satisfying the Kutta condition (smooth flow at the trailing edge) and usually the free-surface condition for zero F_n (double-body flow). The flow is determined as a superposition of horseshoe vortices which are symmetrical with respect to the water surface (mirror plane). The strength of each horseshoe vortex is determined by a collocation method from Biot–Savart’s law. For stationary flow conditions, in the ship’s wake there are no vertical vortex lines, whereas in instationary flow vertical vortex lines are required also in the wake. The vortex strength in the wake follows from three conditions:

1. Vortex lines in the wake flow backwards with the surrounding fluid velocity, approximately with the ship speed u .
2. If the sum of vertical (‘bound’) vortex strength increases over time within the body (due to larger angles of attack), a corresponding negative vorticity leaves the trailing edge, entering into the wake.
3. The vertical vortex density is continuous at the trailing edge.

Except for a ship in waves, it seems accurate enough to use the stationary vortex model for manoeuvring investigations.

Vortex strengths within the body are determined from the condition that the flow is parallel to the midship (or rudder) plane at a number of collocation points. The vortices are located at 1/4 of the chord length from the bow, the collocation points at 3/4 of the chord length from the bow. This gives a system of linear equations to determine the vortex strengths. Transverse forces on the body may then be determined from the law of Kutta–Joukowski, i.e. the body force is the force exerted on all ‘bound’ (vertical) vortices by the surrounding flow.

Alternatively one can smooth the bound vorticity over the plate length, determine the pressure difference between port and starboard of the plate, and integrate this pressure difference. For shallow water, reflections of the vortices are necessary both at the water surface and at the bottom. This produces an infinite number of reflections, a subset of which is used in numerical approximations. If the horizontal vortex lines are arranged in the ship’s centre plane, only transverse forces depending linearly on v and r are generated. The equivalent to the non-linear cross-flow forces in slender-body

theory is found in the vortex models if the horizontal vortex lines are oblique to the centre plane. Theoretically the position of the vortex lines could be determined iteratively to ensure that they move with the surrounding fluid flow which is influenced by all other vortices. But practically this procedure is usually not applied because of the high computing effort and convergence problems. According to classical foil theory, the direction of the horizontal vortices should be halfway between the ship longitudinal direction and the motion direction in deep water. More modern procedures arrange the vortices in longitudinal direction within the ship length, but in an oblique plane (for steady motion at a constant yaw angle) or on a circular cylinder (for steady turning motion) in the wake. The exact direction of the vortices is determined depending on water depth. Also important is the arrangement of vortex lines and collocation points on the material plate. Collocation points should be about halfway between vortex lines both in longitudinal and vertical directions. High accuracy with few vortex lines is attained if the distance between vertical vortices is smaller at both ends of the body, and if the distance between horizontal vortices is small at the keel and large at the waterline.

- *Lifting body methods*

A body with finite thickness generates larger lift forces than a plate. This can be taken into account in different ways:

1. by arranging horseshoe vortices (or dipoles) on the hull on both sides
2. by arranging a source and a vortex distribution on the centre plane
3. by arranging source distributions on the hull and a vortex distribution on the centre plane

In the third case, the longitudinal distribution of bound vorticity can be prescribed arbitrarily, whereas the vertical distribution has to be determined from the Kutta condition along the trailing edge. The Kutta condition can be approximated in different ways. One suitable formulation is: the pressure (determined from the Bernoulli equation) should be equal at port and starboard along the trailing edge. If the ship has no sharp edge at the stern (e.g. below the propeller's axis for a stern bulb), it is not clear where the flow separation (and thus the Kutta condition) should be assumed. This may cause large errors for transverse forces for the hull alone, but when the rudder is modelled together with the hull, the uncertainty is much smaller.

Forces can be determined by integrating the pressure over the hull surface. For a very thin body, the lifting surface and lifting body models should result in similar forces. In practice, however, large differences are found. The lifting-body model with source distributions on both sides of the body has difficulties if the body has a sharp bow. Assuming a small radius at the bow waterline produces much better results. For a ship hull it seems difficult to obtain more accurate results from lifting-body theory than using slender-body theory. For the rudder and for the interaction between rudder and hull, however, lifting surface or lifting body theory is the method of choice for angles of attack where no stall is expected to occur. Beyond the stall angle, only RANSE methods (or even more sophisticated viscous flow computations) may be used.

By the early 1990s research applications for lifting body computations including free surface effects appeared for steady drift motions. The approach of Zou (1990) is typical. First the wave resistance problem is solved including dynamic trim and sinkage. Assuming small asymmetry,

the difference between symmetrical and asymmetrical flow is linearized. The asymmetrical flow is then determined by a lifting body method with an additional source distribution above the free surface.

- *Field methods*

In spite of the importance of viscosity for manoeuvring, viscous hull force calculations appeared in the 1990s only as research applications and were mostly limited to steady flow computations around a ship with a constant yaw angle. Difficulties in RANSE computations for manoeuvring are:

- The number of computational cells is much higher than for resistance computations, because both port and starboard sides must be discretized and because vortices are shed over nearly the full ship length.
- The large-scale flow separation makes wall functions (e.g. in the standard k - ε turbulence model) dubious. But avoiding wall functions increases the necessary cell numbers further and deteriorates the convergence of the numerical solution methods.

State of the art computations for ship hulls at model scale Reynolds numbers were capable of predicting transverse forces and moments reasonably well for steady flow cases with moderately constant yaw angle, but predicted the longitudinal force (resistance) with large relative errors. Flow details such as the wake in the aftbody were usually captured only qualitatively. Either insufficient grid resolutions or turbulence models were blamed for the differences with model tests. By the late 1990s, RANSE results with free-surface deformation (waves) were also presented, but with the exception of Japanese research groups, none of the computations included dynamic trim and sinkage, although for shallow water these play an important role in manoeuvring.

Despite these shortcomings, RANSE computations including free-surface effects will grow in importance and eventually also drift into practical applications. They are expected to substantially improve the accuracy of manoeuvring force predictions over the next decade.

5.3 Experimental approaches

5.3.1 Manoeuvring tests for full-scale ships in sea trials

The main manoeuvring characteristics as listed in the introduction to manoeuvring are quantified in sea trials with the full-scale ship. Usually the design speed is chosen as initial speed in the manoeuvre. Trial conditions should feature deep water (water depth > 2.5 ship draft), little wind (less than Beaufort 4) and ‘calm’ water to ensure comparability to other ships. Trim influences the initial turning ability and yaw stability more than draft. For comparison with other ships, the results are made non-dimensional with ship length and ship length travel time (L/V).

The main manoeuvres used in sea trials follow recommendations of the Manoeuvring Trial Code of ITTC (1975) and the IMO circular MSC 389 (1985). IMO also specifies the display of some of the results in bridge posters and a manoeuvring booklet on board ships in the IMO resolution A.601(15) (1987) (Provision and display of manoeuvring information on board ships). These can also be found in Brix (1993).

The main manoeuvres in sea trials are:

1. *Turning circle test*

Starting from straight motion at constant speed, the rudder is turned at maximum speed to an angle δ (usually maximum rudder angle) and kept at this angle, until the ship has performed a turning circle of at least 540° . The trial is performed for both port and starboard side. The essential information obtained from this manoeuvre (usually by GPS) consists of (Fig. 5.4):

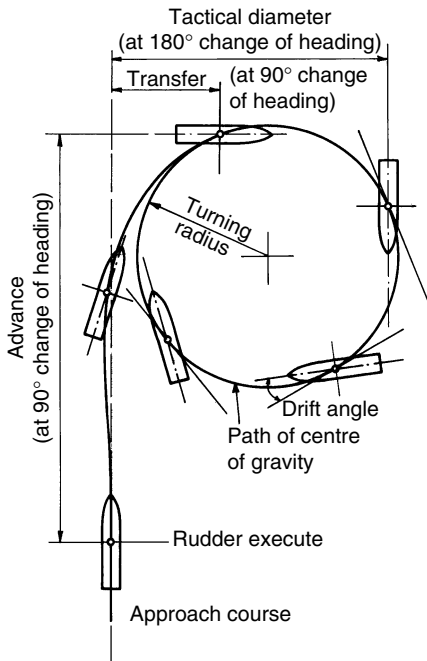


Figure 5.4 Definitions used on turning circle

- tactical diameter
- maximum advance
- transfer at 90° change of heading
- times to change heading 90° and 180°
- transfer loss of steady speed

Typical values are tactical diameter of $4.5\text{--}7L$ for slender, $2.4\text{--}4$ for short and full ships. Decisive is the slenderness ratios $L/\sqrt[3]{\nabla}$, where ∇ is the volume displacement.

Fast displacement ships with $F_n > 0.25$ may feature dangerously large heel angles in turning circles. The heel is always outwards, i.e. away from the centre of the turning circle. (Submarines and boats with dynamic lift like hydrofoils are exceptional in that they may heel inwards.) The heel is induced by the centrifugal force $m \cdot u \cdot r$ acting outwards on the ship's centre of gravity, the hull force $Y_v v + Y_r r$ acting inwards, and the much smaller rudder force $Y_\delta \delta$ acting outwards. For manoeuvring predictions

it is important to consider that the ship is faster at the beginning of the turning circle and slower at sustained turning. The heeling angle exceeds dynamically the statical heel angle due to forces listed above.

The turning circle test is used to evaluate the turning ability of the ship.

2. *Spiral manoeuvres*

We distinguish between:

– ‘Direct’ spiral manoeuvre (*Dieudonne*)

With the ship on an initial straight course, the rudder is put hard to one side until the ship has reached a constant rate of change of heading. The rudder angle is then decreased in steps (typically 5° , but preferably less near zero rudder angle) and again held until a steady condition is reached. This process is repeated until the rudder has covered the whole range to the maximum rudder angle on the other side. The rate of turn is noted for each rudder angle. The test should be performed at least for yaw unstable ships going both from port to starboard and from starboard to port.

– ‘Indirect’ (reverse) spiral manoeuvre (*Bech*)

The ship is steered at a constant rate of turn and the mean rudder angle required to produce this yaw rate is measured. This way, points on the curve rate of turn vs. rudder angle may be taken in any order.

The spiral test results in a curve as shown in Fig. 5.5. The spiral test is used to evaluate the turning ability and the yaw stability of the ship. For yaw unstable ships, there may be three possible rates of turn for one given rudder angle as shown in Fig. 5.5. The one in the middle (dotted line) represents an instable state which can only be found by the indirect method. In the direct method, the rate of turn ‘switches’ at the vertical sections of the curve suddenly to the other part of the curve if the rudder angle is changed. This is indicated by the dotted arrows in Fig. 5.5.

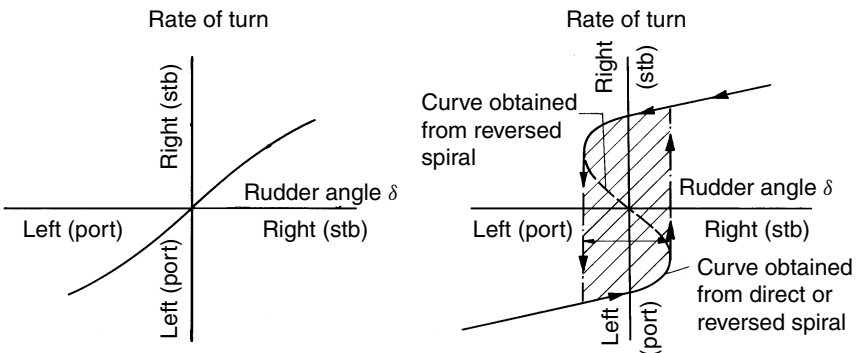


Figure 5.5 Results of spiral tests for yaw stable and yaw unstable ship

The spiral test, especially with the direct method, is time consuming and sensitive to external influences. The results show that a linearization of the body force equations is acceptable only for small $|r|$ (Fig. 5.5). For yaw stable ships, the bandwidth of acceptable rudder angles to give small $|r|$ is small, e.g. $\pm 5^\circ$. For yaw unstable ships, large $|r|$ may result for any δ .

3. Pull-out manoeuvre

After a turning circle with steady rate of turn the rudder is returned to midship. If the ship is yaw stable, the rate of turn will decay to zero for turns both port and starboard. If the ship is yaw unstable, the rate of turn will reduce to some residual rate of turn (Fig. 5.6).

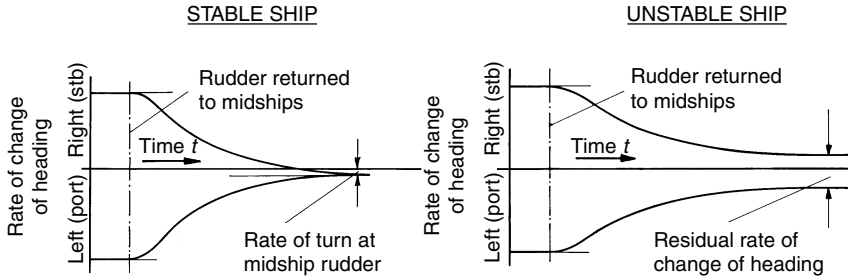


Figure 5.6 Results of pull-out manoeuvre

The pull-out manoeuvre is a simple test to give a quick indication of a ship's yaw stability, but requires very calm weather. If the yaw rate in a pull-out manoeuvre tends towards a finite value in single-screw ships, this is often interpreted as yaw instability, but it may be at least partially due to the influence of unsymmetries induced by the propeller in single-screw ships or wind.

4. Zigzag manoeuvre

The rudder is reversed alternately by a rudder angle δ to either side at a deviation ψ_e from the initial course. After a steady approach the rudder is put over to starboard (first execute). When the heading is ψ_e off the initial course, the rudder is reversed to the same rudder angle to port at maximum rudder speed (second execute). After counter rudder has been applied, the ship continues turning in the original direction (overshoot) with decreasing turning speed until the yaw motion changes direction. In response to the rudder the ship turns to port. When the heading is ψ_e off the initial course to port, the rudder is reversed again at maximum rudder speed to starboard (third execute). This process continues until a total of, e.g., five rudder executes have been completed. Typical values for ψ_e are 10° and 20° . The test was especially developed for towing tank tests, but it is also popular for sea trials. The test yields initial turning time, yaw checking time and overshoot angle (Fig. 5.7).

For the determination of body force coefficients a modification of the zigzag manoeuvre is better suited: the incremental zigzag test. Here, after each period other angles δ and ψ_e are chosen to cover the whole range of rudder angles. If the incremental zigzag test is properly executed it may substitute all other tests as the measured coefficients should be sufficient for an appropriate computer simulation of all other required manoeuvring quantities.

Figure 5.8 shows results of many model zigzag tests as given by Brix (1993). These yield the following typical values:

- initial turning time t_a : 1–1.5 ship length travel time
- time to check starboard yaw t_s : 0.5–2 ship travel length time (more for fast ships)

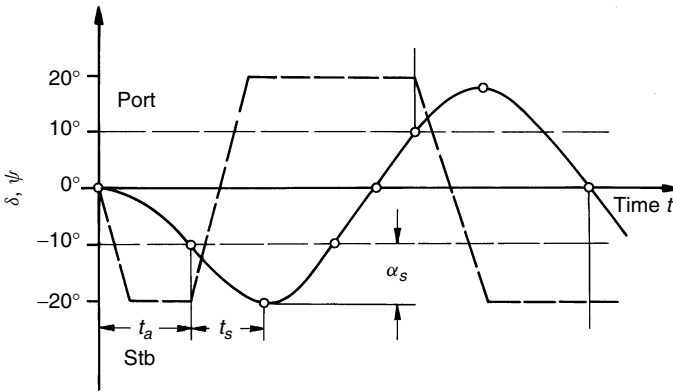


Figure 5.7 Scheme of zigzag manoeuvre; t_u initial turning time, t_s yaw checking time, α_s overshoot angle; ———— rudder angle δ , - - - - - course angle ψ

- starboard overshoot angle α_s : 5° – 15°
- turning speed to port r (yaw rate): 0.2–0.4 per ship travel length time

5. Stopping trial

The most common manoeuvre in stopping trials is the crash-stop from full ahead speed. For ships equipped with fixed-pitch propellers, the engine is stopped and then as soon as possible reversed at full astern. Controllable-pitch propellers (CPP) allow a direct reversion of the propeller pitch. Sometimes the rudder is kept midships, sometimes one tries to keep the ship on a straight course which is difficult as the rudder effectiveness usually decreases drastically during the stopping manoeuvre and because the reversing propeller induces substantial transverse forces on the afterbody. The reaction to stopping manoeuvres is strongly non-linear. Thus environmental influences (e.g. wind) and slight changes in the initial conditions (e.g. slight deviation of the heading to either port or starboard) may change the resulting stopping track considerably.

The manoeuvre ends when $u = 0$. Results of the stopping manoeuvre are (Fig. 5.9):

- head reach (distance travelled in the direction of the ship's initial course)
- lateral deviation (distance to port or starboard measured normal to the ship's initial course)
- stopping time

Crash-stops from full speed are nautically not sensible as turning usually offers better avoidance strategies involving shorter distances. Therefore stopping manoeuvres are recommended also at low speed, because then the manoeuvre is of practical interest for navigation purposes.

Single-screw ships with propellers turning right (seen from abaft clockwise) will turn to starboard in a stopping manoeuvre. For controllable-pitch propellers, the propeller pitch is reversed for stopping. Since according to international nautical conventions, collision avoidance manoeuvres should be executed with starboard evasion, single-screw ships should be equipped with right-turning fixed-pitch propellers or left-turning CPPs.

Simulations of stopping manoeuvres use typically the four-quadrant diagrams for propellers to determine the propeller thrust also in astern operation, see section 2.2, Chapter 2.

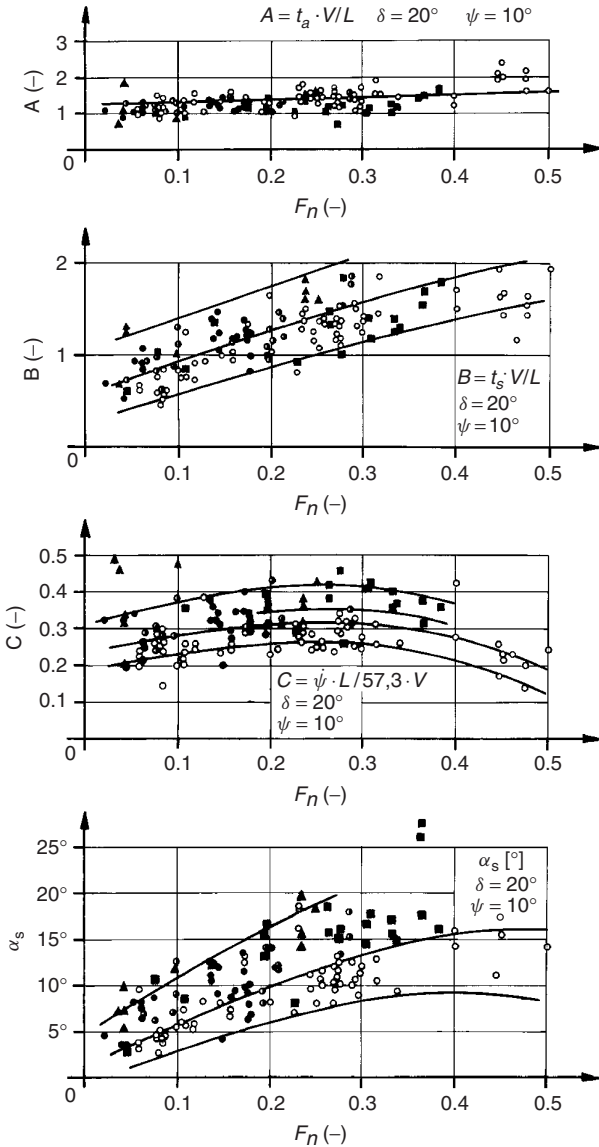


Figure 5.8 Non-dimensional data obtained from zigzag model tests (Brix (1993))
 A = non-dimensional initial turing times $\beta = B$ = non-dimensional times to check starboard yaw C = non-dimensional turning speed to port α_s starboard overshoot angle

6. Hard rudder test

With the ship on an initially straight course, the rudder is put hard to 35° port. As soon as this rudder angle is reached (i.e. without waiting for a specific heading or rate of turning), the rudder is reversed to hard starboard. The time for changing the rudder angle from 35° on one side to 30° on the other side must not exceed 28 seconds according to IMO

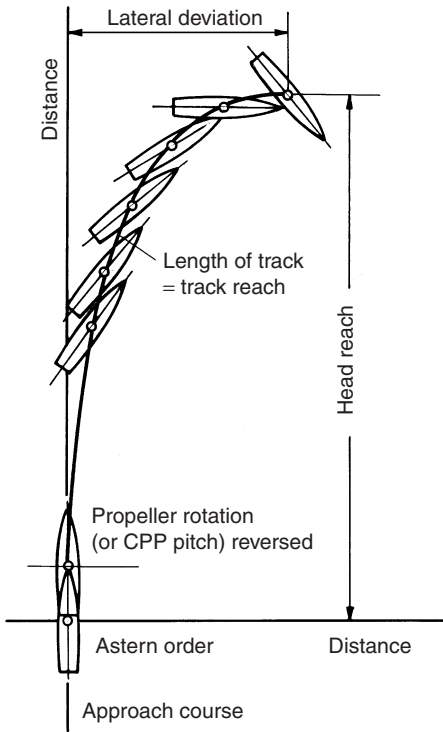


Figure 5.9 Results of stopping trial

regulations (SOLAS 1960). This regulation is rightfully criticized as the time limit is independent of ship size. The IMO regulation is intended to avoid underdimensioning of the rudder gear.

7. *Man-overboard manoeuvre (Williamson turn)*

This manoeuvre brings the ship in minimum time on opposite heading and same track as at the beginning of the manoeuvre, e.g. to search for a man overboard. The rudder is laid initially hard starboard, at, e.g., 60° (relative to the initial heading) hard port, and at, e.g., -130° to midship position again (Fig. 5.10). The appropriate angles (60° , -130°) vary with each ship and loading condition and have to be determined individually such that at the end of the manoeuvre the deviation in heading is approximately 180° and in track approximately zero. This is determined in trial-and-error tests during ship trials. However, an approximate starting point is determined in computational simulations beforehand.

5.3.2 Model tests

Model tests to evaluate manoeuvrability are usually performed with models ranging between 2.5 m and 9 m in length. The models are usually equipped with propeller(s) and rudder(s), electrical motor and rudder gear. Small models are subject to considerable scaling errors and usually do not yield satisfactory agreement with the full-scale ship, because the too small model Reynolds

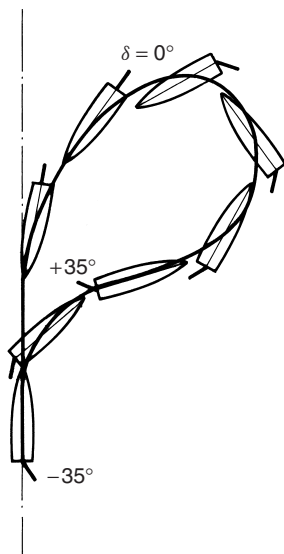


Figure 5.10 Man-overboard manoeuvre (Williamson turn)

number leads to different flow separation at model hull and rudder and thus different non-dimensional forces and moments, especially the stall angle (angle of maximum lift force shortly before the flow separates completely on the suction side), which will be much smaller in models (15° to 25°) than in the full-scale ship ($>35^\circ$). Another scaling error also contaminates tests with larger models: the flow velocity at the rudder outside the propeller slipstream is too small (due to a too large wake fraction in model scale) and the flow velocity inside the propeller slipstream is too large (because the too large model resistance requires a larger propeller thrust). The effects cancel each other partially for single-screw ships, but usually the propeller effect is stronger. This is also the case for twin-screw twin-rudder ships, but for twin-screw midship-rudder ships the wake effect dominates for free-running models. For a captured model, propeller thrust minus thrust deduction does not have to equal resistance. Then the propeller loading may be chosen lower such that scale effects are minimized. However, the necessary propeller loading can only be estimated.

Model tests are usually performed at Froude similarity. For small Froude numbers, hardly any waves are created and the non-dimensional manoeuvring parameters become virtually independent of the Froude number. For $F_n < 0.3$, e.g., the body forces Y and N may vary with speed only by less than 10% for deep water. For higher speeds the wave resistance changes noticeably and the propeller loading increases, as does the rudder effectiveness if the rudder is placed in the propeller slipstream. Also, in shallow water, trim and sinkage change with F_n influencing Y and N . If the rudder pierces the free surface or is close enough for ventilation to occur, the Froude number is always important.

Model tests with free-running models are usually performed indoors to avoid wind effects. The track of the models is recorded either by cameras (two or more) or from a carriage following the model in longitudinal and transverse directions. Turning circle tests can only be performed in broad basins and even then usually only with rather small models. Often, turning circle tests are

also performed in towing tanks with an adjacent round basin at one end. The manoeuvre is then initiated in the towing tank and ends in the round basin. Spiral tests and pull-out manoeuvres require more space than usually available in towing tanks. However, towing tanks are well suited for zigzag manoeuvres. If the ship's track is precisely measured in these tests, all necessary body force coefficients can be determined and the other manoeuvres can be numerically simulated with sufficient accuracy.

Model tests with captured models determine the body force coefficients by measuring the forces and moments for prescribed motions. The captured models are also equipped with rudders, propellers, and electric motors for propulsion.

- Oblique towing tests can be performed in a regular towing tank. For various yaw and rudder angles, resistance, transverse force, and yaw moment are measured, sometimes also the heel moment.
- Rotating arm tests are performed in a circular basin. The carriage is then typically supported by an island in the centre of the basin and at the basin edge. The carriage then rotates around the centre of the circular basin. The procedure is otherwise similar to oblique towing tests. Due to the disturbance of the water by the moving ship, only the first revolution should be used to measure the desired coefficients. Large non-dimensional radii of the turning circle are only achieved for small models (inaccurate) or large basins (expensive). The technology is today largely obsolete and replaced by planar motion mechanisms which can also generate accelerations, not just velocities.
- Planar motion mechanisms (PMMs) are installed on a towing carriage. They superimpose sinusoidal transverse or yawing motions (sometimes also sinusoidal longitudinal motions) to the constant longitudinal speed of the towing carriage. The periodic motion may be produced mechanically from a circular motion via a crankshaft or by computer-controlled electric motors (computerized planar motion carriage (CPMC)). The CPMC is far more expensive and complicated, but allows the extension of model motions over the full width of the towing tank, arbitrary motions and a precise measuring of the track of a free-running model.

5.4 Rudders

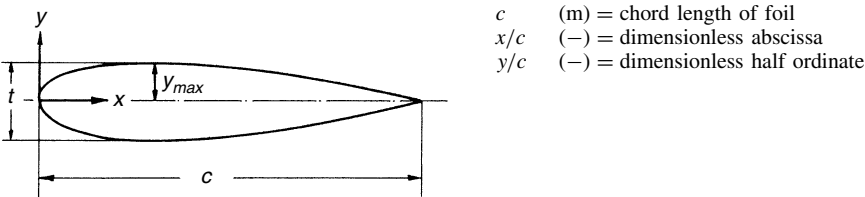
5.4.1 General remarks and definitions

Rudders are hydrofoils pivoting on a vertical or nearly vertical axis. They are normally placed at the ship's stern behind the propeller(s) to produce a transverse force and a steering moment about the ship's centre of gravity by deflecting the water flow to a direction of the foil plane. Table 5.4 gives offsets of several profiles used for rudders depicted in Fig. 5.11. Other profile shapes and hydrodynamic properties are available from Abbott and Doenhoff (1959), and Whicker and Fehlner (1958).

Rudders are placed at the ship's stern for the following reasons:

- The rudder moment turning the ship is created by the transverse force on the rudder and an oppositely acting transverse force on the ship hull acting near the bow. This moment increases with distance between the rudder force and the hull force.

Table 5.4 Offsets of rudder profiles



Note: last digits of profile designation correspond to the thickness form e.g. 25 for $t/c = 0.25$.
For differing thickness t' the half ordinates y' to be obtained by multiplication

$$\frac{y'}{c} = \frac{t'}{t} \cdot \frac{y}{c}$$

	<i>IFS62- TR 25</i>	<i>IFS61- TR 25</i>	<i>IFS58- TR 15</i>	<i>HSVA- MP71-20</i>	<i>HSVA- MP73-20</i>	<i>NACA 00-20</i>	<i>NACA 64₃-018</i>
x/c	y/c	y/c	y/c	y/c	y/c	y/c	y/c
0.0000	0.0000	0.0000	0.0000	0.0000	0.04420*	0.04420*	0.02208*
0.0125	0.0553	0.0553	0.0306	0.0230	0.03156	0.03156	0.02177
0.0250	0.0732	0.0732	0.0409	0.0306	0.04356	0.04356	0.03005
0.0500	0.0946	0.0946	0.0530	0.0419	0.05924	0.05924	0.04186
0.1000	0.1142	0.1142	0.0655	0.0583	0.07804	0.07804	0.05803
0.1500	0.1226	0.1226	0.0715	0.0706	0.08910	0.08910	0.06942
0.2000	0.1250	0.1250	0.0743	0.0801	0.09562	0.09562	0.07782
0.2500	0.1234	0.1226	0.0750	0.0881	0.09902	0.09902	0.08391
0.3000	0.1175	0.1176	0.0740	0.0939	0.10000	0.10000	0.08789
0.4000	0.0993	0.1002	0.0669	0.0996	0.09600	0.09672	0.08952
0.4500	–	–	–	0.1000	–	–	0.08630
0.5000	0.0742	0.0766	0.0536	0.0965	0.08300	0.08824	0.08114
0.6000	0.0480	0.0533	0.0377	0.0766	0.06340	0.07606	0.06658
0.7000	0.0263	0.0357	0.0239	0.0546	0.04500	0.06106	0.04842
0.8000	0.0123	0.0271	0.0168	0.0335	0.02740	0.04372	0.02888
0.9000	0.0080	0.0250	0.0150	0.0140	0.01200	0.02414	0.01101
1.0000	0.0075	0.0250	0.0150	0.0054	0.00540	0.00210	0.00000

*radius

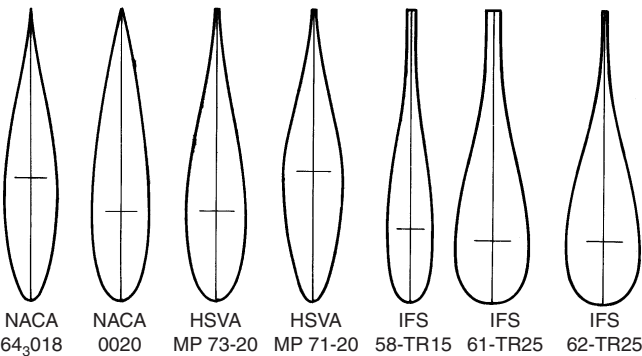


Figure 5.11 Some rudder profiles, offsets given in Table 5.4

- Rudders outside of the propeller slipstream are ineffective at small or zero ship speed (e.g. during berthing). In usual operation at forward speed, rudders outside of the propeller slipstream are far less effective. Insufficient rudder effectiveness at slow ship speed can be temporarily increased by increasing the propeller rpm, e.g. when passing other ships. During stopping, rudders in the propeller slipstream are ineffective.
- Bow rudders not exceeding the draft of the hull are ineffective in ahead motion, because the oblique water flow generated by the turned rudder is redirected longitudinally by the hull. Thus, transverse forces on a bow rudder and on the forward moving hull cancel each other. The same generally applies to stern rudders in backward ship motion. The yaw instability of the backward moving ship in one example could not be compensated by rudder actions if the drift angle exceeded $\beta = 1.5^\circ$. To improve the manoeuvrability of ships which frequently have to move astern (e.g. car ferries), bow rudders may be advantageous. In reverse flow, maximum lift coefficients of rudders range between 70% and 100% of those in forward flow. This force is generally not effective for steering the ship astern with a stern rudder, but depending on the maximum astern speed it may cause substantial loads on the rudder stock and steering gear due to the unsuitable balance of normal rudders for this condition.

The rudder effectiveness in manoeuvring is mainly determined by the maximum transverse force acting on the rudder (within the range of rudder angles achievable by the rudder gear). Rudder effectiveness can be improved by:

- rudder arrangement in the propeller slipstream (especially for twin-screw ships)
- increasing the rudder area
- better rudder type (e.g. spade rudder instead of semi-balanced rudder)
- rudder engine which allows larger rudder angles than the customary 35°
- shorter rudder steering time (more powerful hydraulic pumps in rudder engine)

Figure 5.12 defines the parameters of main influence on rudder forces and moments generated by the dynamic pressure distribution on the rudder surface. The force components in flow direction α and perpendicular to it are termed drag D and lift L , respectively. The moment about a vertical axis through the leading edge (nose) of the rudder (positive clockwise) is termed Q_N . If the leading edge is not vertical, the position at the mean height of the rudder is used as a reference point.

The moment about the rudder stock at a distance d behind the leading edge (nose) is:

$$Q_R = Q_N + L \cdot d \cdot \cos \alpha + D \cdot d \cdot \sin \alpha$$

The stagnation pressure:

$$q = \frac{\rho}{2} \cdot V^2$$

and the mean chord length $c_m = A_R/b$ are used to define the following non-dimensional force and moment coefficients:

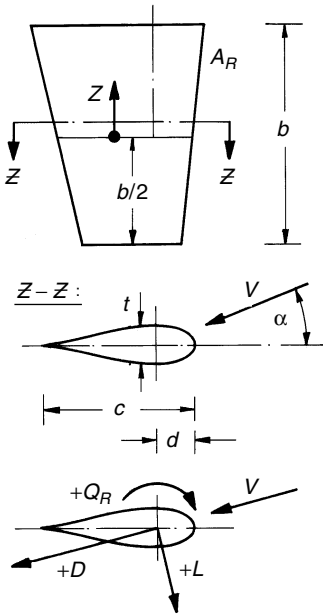


Figure 5.12 Definition sketch of rudder geometry and rudder forces A_R = rudder area; b = rudder height; c = chord length; d = rudder stock position; D = drag; L = lift; Q_R = rudder stock torque; t = rudder thickness v = flow velocity; z = vertical rudder coordinate at $b/2$; α = angle of attack; $\delta = b/2/A_R$ = aspect ratio

lift coefficient	$C_L = L/(q \cdot A_R)$
drag coefficient	$C_D = D/(q \cdot A_R)$
nose moment coefficient	$C_{QN} = Q_N/(q \cdot A_R \cdot c_m)$
stock moment coefficient	$C_{QR} = Q_R/(q \cdot A_R \cdot c_m)$

The stock moment coefficient is coupled to the other coefficients by:

$$C_{QR} = C_{QN} + \frac{d}{c_m}(C_L \cdot \cos \alpha + C_D \cdot \sin \alpha)$$

For low fuel consumption of the ship (for constant rudder effectiveness), we want to minimize the ratio C_L/C_D for typical small angle of attacks as encountered in usual course-keeping mode. Due to the propeller slipstream, angles of attack of typically 10° to 15° (with opposing sign below and above the propeller shaft) occur for zero-deflected rudders. Reducing the rudder resistance by 10% in this range of angles of attack improves the propulsive efficiency by more than 1%. Various devices to improve ship propulsion by partial recovery of the propeller's rotative energy have been proposed in the course of time, e.g. Schneekluth and Bertram (1998). However, the major part of this energy, which accounts only for a few per cent of the total engine power, is recovered anyhow by the rudder in the propeller slipstream.

Size and thus cost of the rudder engine are determined by the necessary maximum torque at the rudder stock. The stock moment is zero if the centre of effort for the transverse rudder force lies on the rudder stock axis. As the centre of effort depends on the angle of attack, this is impossible to achieve for all angles of attack. Rudder shapes with strongly changing centres of effort require therefore larger rudder engines. The position of the centre of effort

behind the leading edge (nose) is:

$$c_s = \frac{c \cdot C_{QN}}{C_L \cos \alpha + C_D \sin \alpha}$$

The denominator in this formula is the non-dimensional force coefficient for the normal force on the rudder.

5.4.2 Fundamental hydrodynamic aspects of rudders and simple estimates

C_L , C_D and C_{QN} can be determined in wind tunnel tests or computations. Extensive wind tunnel measurements have been published by Thieme (1992), and Whicker and Fehlner (1958).

Figure 5.13 shows an example. Practically these data allow rough estimates only of rudder forces and moments of ships, because in reality the flow to the rudder is irregular and highly turbulent and has a higher Reynolds number than the experiments, and because interactions with the ship's hull influence the rudder forces. For angles of attack smaller than stall angle α_s (i.e. the angle of maximum C_L) the force coefficients may be approximated with ample accuracy by the following formulae:

$$C_L = C_{L1} + C_{L2} = 2\pi \frac{\Lambda \cdot (\Lambda + 0.7)}{(\Lambda + 1.7)^2} \cdot \sin \alpha + C_Q \cdot \sin \alpha \cdot |\sin \alpha| \cdot \cos \alpha$$

$$C_D = C_{D1} + C_{D2} + C_{D0} = \frac{C_L^2}{\pi \cdot \Lambda} + C_Q |\sin \alpha|^3 + C_{D0}$$

$$C_{QN} = -(C_{L1} \cdot \cos \alpha + C_{D1} \cdot \sin \alpha) \cdot \left(0.47 - \frac{\Lambda + 2}{4(\Lambda + 1)}\right) - 0.75 \cdot (C_{L2} \cdot \cos \alpha + C_{D2} \cdot \sin \alpha)$$

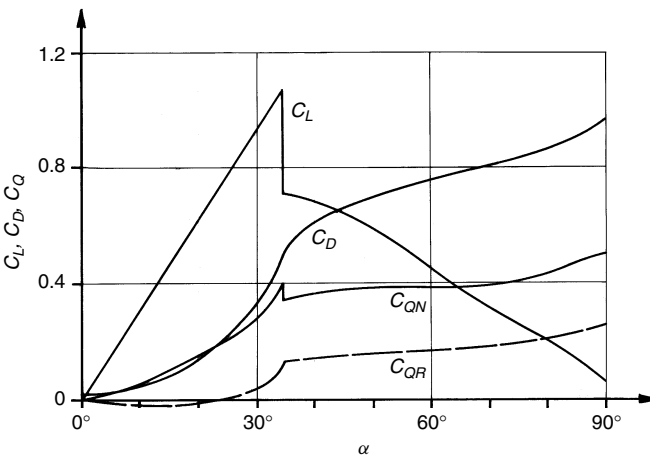


Figure 5.13 Force and moment coefficients of a hydrofoil $\lambda = 1$; rudder stock position $d/c_m = 0.25$; NACA-0015; $R_n = 0.79c \cdot 10^6$; Q_N = nose moment; Q_R = rudder stock torque

Figure 5.14 illustrates the C_L formula. The first term in the C_L formula follows from potential thin-foil theory for the limiting aspect ratios $\Lambda = 0$ and $\Lambda = \infty$. For other aspect ratios it is an approximation to theoretical and experimental results. The first term in the C_D formula is the induced resistance due to the generation of trailing vortices behind the foil. The equation includes a 10% increase of the minimum induced drag which occurs for an elliptical load distribution over the rudder height. The first term in the C_{QN} formula would be a good approximation of the theoretical moment in ideal fluid if 0.5 were used instead of the empirical value 0.47. The second terms in the formulae for C_L and C_D follow from the assumption of an additional resistance-like force depending quadratically on the velocity component $V \cdot \sin \alpha$ which is perpendicular to the rudder plane. A resistance coefficient $C_Q \approx 1$ may be used for rudders with a sharp upper and lower edge. Rounding the edges (which is difficult in practice) would lead to much smaller C_Q values. The second term in the C_{QN} formula follows from the assumption that this force component acts at 75% chord length from the leading edge. C_{D0} in the formula for C_D approximates the surface friction. We may approximate:

$$C_{D0} = 2.5 \cdot \frac{0.075}{(\log R_n - 2)^2}$$

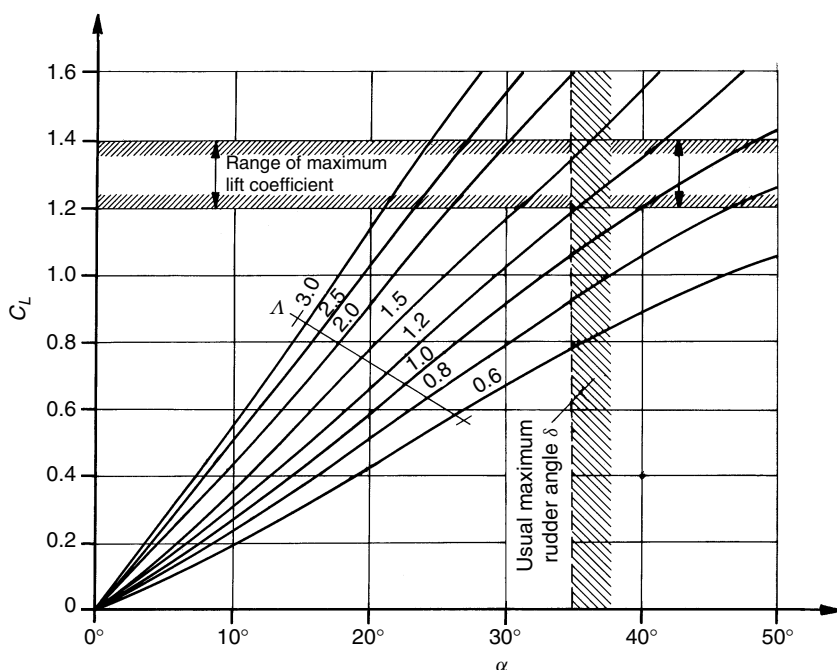


Figure 5.14 Lift coefficient C_L versus angle of attack α with the aspect ratio λ as parameter

This is 2.5 times the frictional resistance coefficient following the ITTC 1957 formula. C_{D0} refers to the rudder area which is about half the wetted area of

the rudder. In addition a form factor has to be taken into account to yield the factor 2.5.

For hydrofoils the Reynolds number is defined as:

$$R_n = \frac{V \cdot c}{\nu}$$

where V is the inflow velocity (for rudders usually V_A), c the mean chord length and $\nu \approx 1.35 \cdot 10^{-6} \text{ m}^2/\text{s}$ the kinematic viscosity of water at 10°C .

Table 5.5 shows the good agreement of the approximate formulae with model test measurements of Whicker and Fehlner (1958) (columns 1 to 6) and Thieme (1958) (other columns). Thieme's results suffer somewhat from small Reynolds numbers. Rudder Reynolds numbers behind a large ship are in the vicinity of $R_n = 5 \cdot 10^7$. Too small Reynolds numbers result in larger drag coefficients, a backward shift of the centre of effort of the rudder force and smaller stall angles α_s (by up to a factor of 2) than in reality. The Reynolds number of column 13 corresponds approximately to the conditions in model manoeuvring experiments. However, the strong turbulence behind a ship model and its propeller act similarly to a larger Reynolds number in these experiments.

Table 5.5 Measured (M) and computed (C) force and moment coefficients of different profiles (Thieme (1958), Whicker and Fehlner (1958)); +: independent from profile shape; *: uncertain values, probably due to experimental technique

Profile	−+	NACA 0015	−+	NACA 0015	−+	NACA 0015
\wedge	1	1	2	2	3	3
$(t/c)_{\max}$	+	15	+	15	+	15
at x/c		30		30		30
$R_n/10^6$	2.7	2.7	2.7	2.7	2.7	2.7
C_L at $\alpha = 10^\circ$	0.27	0.27	0.44	0.44	0.55	0.55
C_L at $\alpha = 20^\circ$	0.59	0.60	0.92	0.93	1.14	1.10
C_L at $\alpha = \alpha_s$	1.17	1.26	1.33	1.33	1.32	1.25
$\alpha_s [^\circ]$		38.5		28.7		23.0
C_L/C_D at $\alpha = 10^\circ$	8.11	7.26	10.45	10.35	12.28	12.40
C_L/C_D at $\alpha = 20^\circ$	4.62	4.25	5.70	5.79	6.63	7.05
C_L/C_D at $\alpha = \alpha_s$	2.28	2.20	3.88	4.00	5.76	6.00
c_s/c at $\alpha = 10^\circ$	0.17	0.16	0.18	0.19	0.19	0.18
c_s/c at $\alpha = \alpha_s$	0.30	0.31	0.24	0.25	0.23	0.23

Profile	NACA 0015	NACA 0025	IFS62 TR 25	IFS61 TR 25	IFS58 TR 15	Plate $t/c = 0.03$	NACA 0015
\wedge	1	1	1	1	1	1	1
$(t/c)_{\max}$	15	25	25	25	15	3	15
at x/c	30	30	20	20	25	−	30
$R_n/10^6$	0.79	0.78	0.78	0.79	0.79	0.71	0.20
C_L at $\alpha = 10^\circ$	0.29	0.27	0.33	0.32	0.32	0.34	0.35
C_L at $\alpha = 20^\circ$	0.62	0.59	0.71	0.69	0.67	0.72	0.55
C_L at $\alpha = \alpha_s$	1.06	1.34	1.48	1.34	1.18	1.14	0.72
$\alpha_s [^\circ]$	33.8	46.0*	46.0*	41.0*	33.5	40*	35.0
C_L/C_D at $\alpha = 10^\circ$	7.20	5.40	4.70	4.00	6.40	3.80	2.80
C_L/C_D at $\alpha = 20^\circ$	4.40	4.20	3.60	3.60	3.90	2.50	1.75
C_L/C_D at $\alpha = \alpha_s$	2.30	1.70	1.50	1.80	2.40	1.30	1.19
c_s/c at $\alpha = 10^\circ$	0.18	0.20	0.27	0.26	0.25	0.28	0.28
c_s/c at $\alpha = \alpha_s$	0.35	0.35	0.36	0.25	0.33	0.41	0.43

The formulae for C_L , C_D , and C_{QN} do not take into account the profile shape. The profile shape affects mainly the stall angle α_s , the maximum lift and the cavitation properties of the rudder, but hardly the lift at a given angle of attack below α_s . Table 5.5 shows that, compared to the 'standard' NACA profiles, concave profiles with thickness maximum in front of the standard value of 30% of the chord length (measured from the leading edge) produce larger maximum lift and less change of the centre of effort of the rudder force. The latter fact allows a smaller steering gear if the rudder is properly balanced. On the other hand, these profiles have higher drag coefficients, thus requiring more propulsive power for the same ship speed. (For a rudder behind a propeller, the slipstream rotation causes angles of attack of typically 10° to 15° . A 10% increase of the rudder resistance in this angle-of-attack range accounts for approximately 1% increase in the necessary propulsion power). For ship speeds exceeding 22 knots and the rudder in the propeller slipstream, profiles with the opposite tendency (backward-shifted maximum thickness) are preferred because they are less prone to cavitation.

Greater profile thickness produces greater maximum lift at the (correspondingly greater) stall angle α_s , but it increases the rudder drag, and in most cases the danger of cavitation in high-speed ships. Thus, the smallest thickness possible to accommodate the rudder post and bearing is normally used. For rudders of small aspect ratio, the greater maximum lift of thick rudders is realized only in yaw checking, but not at all if the steering gear allows the normal $\delta = 35^\circ$ rudder angle only (Fig. 5.14). A trailing edge of substantial thickness decreases the change of the centre of effort c_s with angle of attack α , but it causes substantially increased drag; thus, because of too large drag, the application of these profiles should be avoided at least in long-range vessels.

The approximate formulae for the force coefficients are only valid for angles of attack $\alpha < \alpha_s$. Beyond the stall angle α_s the flow separates near the profile leading edge (nose) on the suction side of the profile without reattachment. Then the lift decreases strongly and the drag increases (Fig. 5.13). The sudden drop in lift beyond the stall angle α_s is not found for certain other profiles and in rudders behind a propeller.

The stall angle α_s depends primarily on:

- the aspect ratio Λ
- the profile shape and thickness
- the Reynolds number
- probably the surface roughness
- the turbulence of the inflow
- the spatial distribution of the inflow velocity

Because of the last four parameters, an exact prediction of maximum rudder lift from wind tunnel or towing tank experiments is impossible. Whereas a greater aspect ratio Λ (height-to-chord ratio b/c_m) increases the lift for a given angle of attack $\alpha < \alpha_s$, the maximum lift coefficient (typically $1.2 < C_{L,\max} < 1.4$) is practically independent of the aspect ratio (Fig. 5.14). Thus increasing the rudder area by increasing the chord length is of equal effect as by increasing the rudder height with respect to the maximum rudder force if the stall angle is reached by the steering gear; otherwise, an increase in rudder height is much more effective than a corresponding increase in chord length. (A rudder angle $\delta = 35^\circ$ relative to the ship's longitudinal axis corresponds to angles of

attack α of nearly the same size in initial turning, of smaller size during steady turning and of larger size in the yaw checking phase.)

Because of the different stall angles α_s and lift curve slopes of rudders of different aspect ratios it would be advantageous to use an effective rudder angle δ_{eff} instead of the geometrical rudder angle δ for rules, e.g., about the maximum rudder angle and the rudder rate of the steering gear, as well as for nautical use. This would be 'fairer' for rudders of different aspect ratio; it would also make better use of rudders of smaller aspect ratio (today their greater stall angle α_s is frequently not realized because of a too small maximum rudder angle δ) and would lead to more equal response of different ships on (effective) rudder angles. If geometric and effective rudder angles are defined to coincide for a normal aspect ratio of $\Lambda = 2$, their relationship is (Fig. 5.15):

$$\delta_{\text{eff}} = \frac{2.2 \cdot \Lambda}{\Lambda + 2.4} \cdot \delta$$

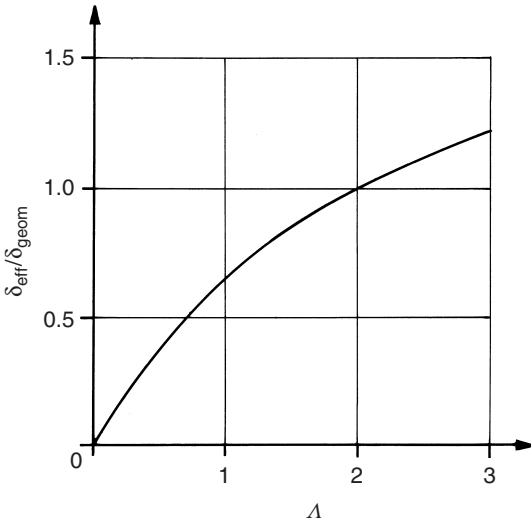


Figure 5.15 Ratio between effective and geometrical angle of attack

For aspect ratios $\Lambda < 3$ which are typical for ship rudders, the vertical distribution of the lift force in homogeneous, unbounded flow is practically elliptic:

$$\text{lift per length} = \frac{L}{b} \cdot \frac{4}{\pi} \cdot \sqrt{1 - \left(\frac{z}{b/2}\right)^2}$$

Here z is the vertical distance from the mean height between the lower and upper edge of the rudder. The distribution is hardly influenced by the rudder shape if the usual trapezoidal shape with a taper ratio $0.5 < c_{\text{min}}/c_{\text{max}} < 1.0$. Thus, for a free-running rudder of trapezoidal shape the lift centre is nearly at half the rudder height, not at the centre of gravity of the shape. This effect is even more pronounced for lower aspect ratios. If there is only a small gap between the upper edge of the rudder and fixed parts of the hull (at the rudder

angles concerned), the centre of effort moves up a little, but never more than 7.5% of b , the value for a rudder without a gap at its upper edge.

Air ventilation may occur on the suction side of the rudder if the rudder pierces or comes close to the water surface. The extent of the ventilation may cover a large part of the rudder (even the whole rudder height) decreasing the rudder effectiveness drastically. This is important for manoeuvres at ballast draft for full speed, e.g. at ship trials.

The dynamic pressure along the profile of a rudder depends on the local velocity v according to Bernoulli's law:

$$p_{\text{dyn}} = \frac{\rho}{2} \cdot (V^2 - v^2) = q \cdot \left(1 - \frac{v^2}{V^2}\right)$$

For the usual straight profiles v/V is decomposed into two components:

1. Component v_t/V due to the profile thickness t . This component is equal on both sides of the profile. v_t/V may be taken from Table 5.6. For different profile thickness t , the velocity ratio v_t/V must be corrected by

$$\left[\left(\frac{v_t}{V}\right)_{\text{actual}} - 1\right] = \left[\left(\frac{v_t}{V}\right)_{\text{table}} - 1\right] \cdot \frac{t_{\text{actual}}}{t_{\text{table}}}$$

Table 5.6 v_t/V ; flow speed v_t along the profile over inflow velocity V as a function of the profile abscissa x , $\alpha = 0^\circ$

x/c (%)	NACA 643-018	NACA 0020	HSVA MP73-20	HSVA MP71-20	IFS58 TR15	IFS61 TR25	IFS62 TR25
0	0.00	0.00	0.00	0.00	0.00	0.00	0.00
0.75	0.77	0.69	0.69	0.57	0.79	0.67	0.68
1.25	0.96	0.91	0.91	0.88	1.06	0.95	0.94
2.5	1.05	1.03	1.08	1.00	1.20	1.09	1.18
5.0	1.11	1.17	1.22	1.10	1.29	1.47	1.48
7.5	1.15	1.25	1.27	1.12	1.30	1.52	1.53
10	1.17	1.27	1.29	1.14	1.28	1.50	1.52
15	1.20	1.30	1.31	1.18	1.26	1.47	1.48
20	1.22	1.29	1.30	1.20	1.23	1.43	1.44
30	1.25	1.26	1.27	1.24	1.20	1.31	1.33
40	1.26	1.21	1.24	1.28	1.16	1.18	1.21
50	1.20	1.17	1.17	1.30	1.08	1.06	1.08
60	1.13	1.13	1.07	1.14	1.00	0.96	0.97
70	1.06	1.08	1.01	1.04	0.94	0.90	0.90
80	0.98	1.03	0.95	0.96	0.93	0.90	0.87
90	0.89	0.96	0.88	0.87	0.96	0.94	0.90
95	0.87	0.91	0.89	0.87	0.97	0.95	0.93

Information on other profiles may be found in Abbott and Doenhoff (1959) or computed by CFD (e.g. boundary element method).

2. Component v_a/V due to the angle of attack α . This component has opposite sign on both sides of the profile. It is practically independent from the profile shape. Only in the front part does it depend on the profile nose radius. Figure 5.16 illustrates this for a lift coefficient $C_L \approx 1$. The values given

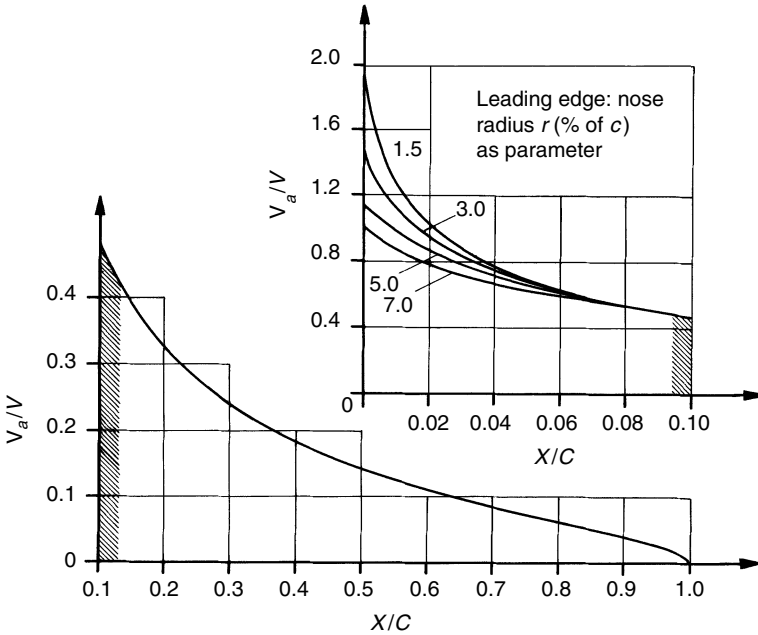


Figure 5.16 Relative change of velocity V_a/V on the surface due to the angle of attack α for $C_{L1} \approx 1$

in the Fig. 5.16 have to be multiplied by the actual local lift coefficient:

$$C_{Ll} = \frac{\text{lift per length}}{c \cdot q} = C_L \cdot \frac{4}{\pi} \cdot \sqrt{1 - \left(\frac{z}{b/2}\right)^2}$$

where $C_L(\Lambda)$ is estimated by the usual formula for the force coefficients as given at the beginning of this chapter.

The dynamic pressure is then:

$$p_{\text{dyn}} = \left[1 - \left(\frac{v_t}{V} \pm \frac{v_a}{V} \cdot C_{Ll} \right)^2 \right] \cdot q$$

Due to the quadratic relationship in this equation, the pressure distribution will generate the given C_{Ll} only approximately. For better accuracy, the resulting local lift coefficient should be integrated from the pressure difference between both sides of the profile. If it differs substantially from the given value, the pressure distribution is corrected by superimposing the v_a/V distribution in the above formula for p_{dyn} with a factor different from C_{Ll} such that the correct C_{Ll} is attained by the integration of the pressure difference.

The dynamic pressure is negative over most of the profile length, for moderate lift coefficients even on the pressure side of the rudder. This is illustrated in Fig. 5.17 for an NACA0021 profile. The curve for $C_{Ll} = 0$ corresponds to the component due to the profile thickness alone. For other C_{Ll} values, the upper and lower curves refer to the pressure and suction

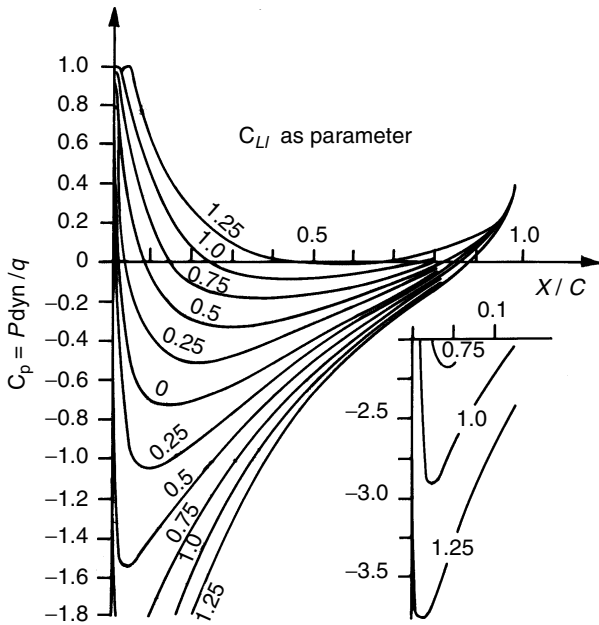


Figure 5.17 Distribution of the non-dimensional dynamic pressure along a NACA0021 profile as a function of the local lift coefficient C_{Li} (Riegels (1958))

sides, respectively. For profiles with a curved mean line, an additional velocity component has to be added. It may be taken from Abbott and Doenhoff (1959), pp. 77ff and App. II, or it may be determined by a two-dimensional potential-flow calculation for which various methods and codes are available. Brix (1993), p. 84, gives a sample calculation for the NACA64₃-018 profile for $\alpha = 15^\circ$.

5.4.3 Rudder types

Various rudder types have been developed over the years (Fig. 5.18):

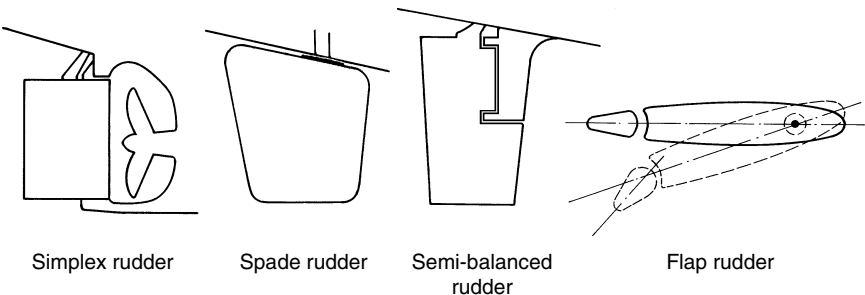


Figure 5.18 Various rudder types

- *Rudder with heel bearing (simplex)*

The most common rudder type formerly built was a rectangular profile rudder with heel bearing. The heel has to have considerable width to withstand the horizontal forces. Flow separation at the heel increases resistance and the non-homogeneity of the wake field at the propeller plane which in turn increases propeller-induced vibrations. Therefore modern single-screw ships are usually equipped with other rudder types, but the rudder with heel bearing is still popular for small craft and some fishery vessels, because it is cheap.

- *Spade rudder*

This type of rudder is commonly applied, especially on ferries, ro-ro ships, and special craft. The rudder stock is subject to high bending moments, especially for high ship speed and large rudder height. For stock diameters larger than 1 m, this design becomes impractical.

- *Semi-balanced rudders*

For semi-balanced rudders, a fixed guide-head (sometimes called rudder horn) extends over the upper part of the rudder. This type of rudder has the following properties:

- decreased rudder bending moment compared to spade rudders
- reduced rudder effectiveness compared to spade rudders. For steady turning circles, the semi-balanced rudder produces only approximately half the transverse force than a spade rudder of the same area (including the area of the rudder horn). The reasons for the reduced transverse force are:
 - * The horizontal gap between horn and rudder opens wide for large rudder angles. Sometimes horizontal plates are attached at the horn along the gap as a remedy for this problem (rudder scissors).
 - * Unfavourable angle of attack for the rudder horn (fixed guide-head).
- drag/lift ratio of the rudder about twice as high as for spade rudders

- *Flap rudders*

Flap rudders (e.g. Becker rudders) consist of a movable rudder with a trailing edge flap activated by a mechanical or hydraulic system, thus producing a variable flap angle as a function of the rudder angle. This system works like an airfoil with a flap. Flap rudders give a much higher lift per rudder angle and a 60% to 70% higher maximum lift compared to a conventional rudder of same shape, size and area.

Less frequently, the following rudder types are employed:

- *Rudders with rotating cylinders*

These rudders have a rotating cylinder at the leading edge. Whereas the freely arranged rotating cylinder works according to the Magnus effect, the combination of a rotating cylinder and a conventional rudder shifts the stall to a much higher angle of attack by eliminating the boundary layer at the separation-prone leading edge. However, at full scale the stall angle of conventional rudders is often so high that the added complexity of this rudder is not justified.

- *Active rudder/rudder propellers*

Rudder propellers are azimuthing ducted or free-running propellers in a fixed or hinged vertical position. They are active control devices with directed thrust. The 'active propeller' is a special solution of a motor-driven ducted

propeller integrated in the main rudder. Thus besides auxiliary propulsion qualities, a directed thrust is available within the range of the main rudder angles. This increases the manoeuvring qualities of the ship especially at low speeds.

- *Steering nozzle with rudder*

Steering nozzle may be fitted with flapped or unflapped rudders. This highly effective steering device is sometimes fitted to tugs, research or fishery ships.

A fixed fin above the rudder improves the yaw checking stability as much as if the area of the fixed fin would be included in the movable rudder. However, for course-changing ability only the movable rudder is decisive. In fact, a fixed fin has a course-stabilizing property and increases, e.g., the turning circle diameter. A gap between the rudder top and the hull increases the rudder resistance at centre position due to the induced resistance of the oblique inflow of the propeller slipstream and the resistance of the rudder.

Twin-screw ships may be fitted with spade or semi-balanced rudders, either behind the propellers or as midship rudders. For fast ships with a rudder arrangement on the centreplane cavitation problems are avoided, but this arrangement is less effective than rudders in the propeller slipstream especially on shallow water.

5.4.4 Interaction of rudder and propeller

Rudders are normally placed in the propeller slipstream for the following reasons:

- A profiled rudder increases the propulsive efficiency by utilizing a part of the rotational energy contained in the propeller slipstream.
- In steady ahead motion, the rudder forces are typically more than twice those of a rudder outside of the propeller slipstream.
- Even for a stationary or slowly moving ship, substantial rudder forces may be generated by increasing the propeller rpm (especially to provide increased rudder effectiveness during transient manoeuvres).

Because the rudder forces are proportional to the flow speed squared at the rudder, an accurate determination of the speed in the propeller slipstream at the rudder position is required to correctly predict rudder forces. According to the momentum theory of the propeller, the mean axial speed of the slipstream far behind the propeller is

$$V_{\infty} = V_A \sqrt{1 + C_{Th}}$$

where C_{Th} is the thrust loading coefficient:

$$C_{Th} = \frac{8}{\pi} \cdot \frac{K_T}{J^2} = \frac{T}{\frac{\rho}{2} V_A^2 A_P}$$

V_A is the mean axial speed of inflow to the propeller, A_P the propeller area. The theoretical slipstream radius r_{∞} far behind the propeller flows from the law of continuity, assuming that the mean axial speed at the propeller is the

average between V_A and V_∞ :

$$r_\infty = r_0 \sqrt{\frac{1}{2} \left(1 + \frac{V_A}{V_\infty} \right)}$$

Here r_0 is half the propeller diameter D .

Normally the rudder is in a position where the slipstream contraction is not yet completed. The slipstream radius and axial velocity may be approximated by (Söding (1982)):

$$r_x = r_0 \cdot \frac{0.14(r_\infty/r_0)^3 + r_\infty/r_0 \cdot (x/r_0)^{1.5}}{0.14(r_\infty/r_0)^3 + (x/r_0)^{1.5}}$$

and:

$$V_x = V_\infty \cdot \left(\frac{r_\infty}{r} \right)^2$$

Here x is the distance of the respective position behind the propeller plane. To determine rudder force and moment, it is recommended to use the position of the centre of gravity of the rudder area within the propeller slipstream.

The above expression for r_x is an approximation of a potential-flow calculation. Compared to the potential flow result, the slipstream will increase in diameter with increasing the distance x from the propeller plane due to turbulent mixing with the surrounding fluid. This may be approximated (Söding (1986)) by adding:

$$\Delta r = 0.15x \cdot \frac{V_x - V_A}{V_x + V_A}$$

to the potential slipstream radius and correcting the slipstream speed according to the momentum theorem:

$$V_{\text{corr}} = (V_x - V_A) \left(\frac{r}{r + \Delta r} \right)^2 + V_A$$

The results of applying this procedure are shown in Fig. 5.19. V_{corr} is the mean value of the axial speed component over the slipstream cross-section.

The rudder generates a lift force by deflecting the water flow up to considerable lateral distances from the rudder. Therefore the finite lateral extent of the propeller slipstream diminishes the rudder lift compared to a uniform inflow velocity. This is approximated (Söding (1982)) (based on two-dimensional potential flow computations for small angles of attack) by multiplying the rudder lift determined from the velocity within the rudder plane by the correction factor λ determined from:

$$\lambda = \left(\frac{V_A}{V_{\text{corr}}} \right)^f \quad \text{with} \quad f = 2 \cdot \left(\frac{2}{2 + d/c} \right)^8$$

Here V_A is the speed outside of the propeller slipstream laterally from the rudder. d is the half-width of the slipstream. For practical applications, it is recommended to transform the circular cross-section (radius $r + \Delta r$) of the

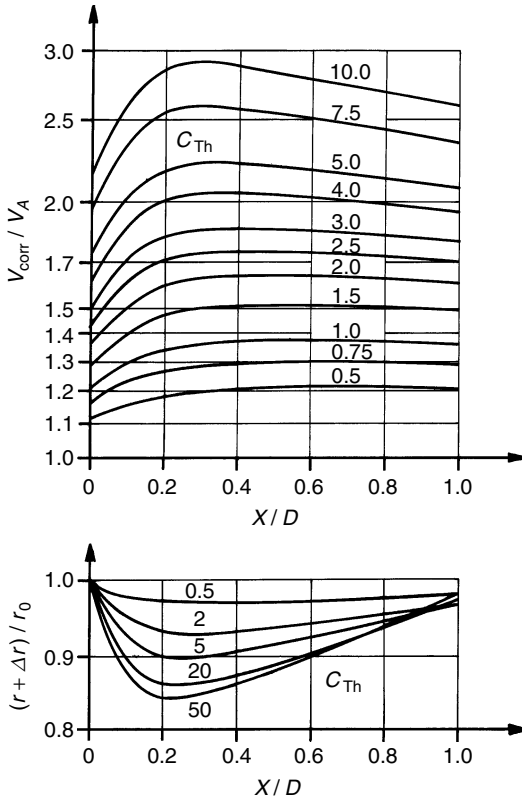


Figure 5.19 Mean axial slipstream speed as a function of propeller approach speed V_A and slipstream radius $(r + \Delta r)/r_0$ due to potential flow and turbulent mixing at different positions x/D behind the propeller

propeller slipstream to a quadratic one (edge length $2d$) of equal area. This leads to the relation:

$$d = \sqrt{\frac{\pi}{4}}(r + \Delta r) = 0.886 \cdot (r + \Delta r)$$

The inflow velocity in the rudder plane varies along the rudder height due to the wake distribution and the propeller slipstream. The effect of this variation may be approximated by using the mean squared velocity:

$$\overline{V^2} = \frac{1}{A_R} \int_0^b V^2 \cdot c \cdot dz$$

for the determination of the rudder lift. However, lifting-surface calculations show that, compared to a uniform distribution, the lift coefficient (defined with reference to $\overline{V^2}$) is some 5% higher for rudders extending downward beyond the lower edge of the propeller slipstream (Fig. 5.20). Hence it is recommended to extend the rudder as far to the base line of the ship as possible.

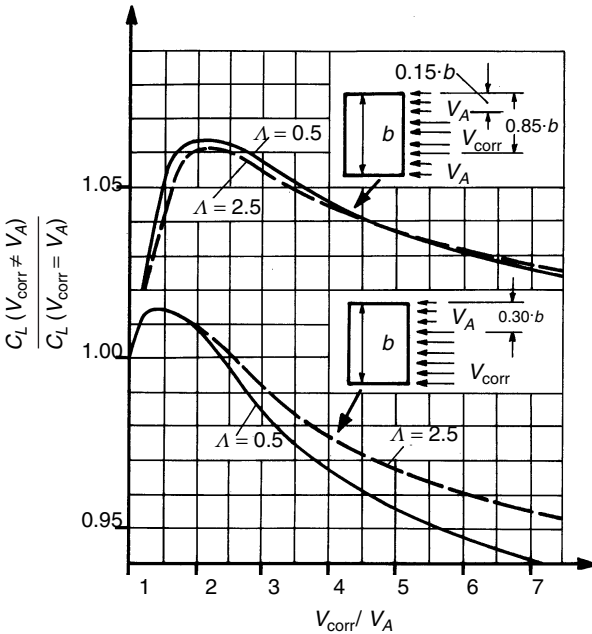


Figure 5.20 Lift coefficients as a function of the vertical distribution of flow and the aspect ratio λ

A simple global correction for the lift force of a rudder behind a propeller (to be added to the lift computed by the usual empirical formulae for rudders in free stream) is (Söding (1998a, b)):

$$\Delta L = T \cdot \left(1 + \frac{1}{\sqrt{1 + C_{Th}}} \right) \cdot \sin \delta$$

The additional drag (or decrease in propeller thrust) is:

$$\Delta D = T \cdot \left(1 + \frac{1}{\sqrt{1 + C_{Th}}} \right) \cdot (1 - \cos \delta)$$

5.4.5 Interaction of rudder and ship hull

If the hull above the rudder is immersed, it suppresses the flow from the pressure to the suction side around the upper edge of the rudder. This has effects similar to an increase of the rudder aspect ratio Λ :

- It decreases the induced drag.
- It increases the slope of the lift curve versus angle of attack α .
- It hardly influences the maximum lift at the stall angle α_s .

The magnitude of this effect depends on the size of the gap between the upper edge of the rudder and the hull. For very small gaps, the aspect ratio Λ_{eff} is theoretically twice the nominal value, in practice $\Lambda_{\text{eff}} \approx 1.6 \cdot \Lambda_{\text{geom}}$. To close

the gap between hull and rudder at least for small rudder angles δ – and thus increasing the rudder effectiveness – a fixed fin above the rudder is advantageous for small-rudder angles. If the hull above the rudder is not immersed or if the rudder intersects the water surface, the free surface may also increase somewhat the effective aspect ratio Λ_{eff} . However, this effect decreases with increasing ship speed and may turn to the opposite at higher speed by rudder ventilation drawn from the surface along the suction side of the rudder. To decrease rudder ventilation, a broad stern shape sufficiently immersed into the water especially above the front part of the rudder is advantageous.

The wake of the hull decreases the inflow velocity to the rudder and increases the propeller load. Differences in wake and propeller load between model and ship are the main cause of scale effects in model manoeuvring experiments. Whereas the wake due to hull surface friction will be similar at the rudder and at the propeller, the potential wake – at least for small Froude numbers, i.e. without influence of the free surface – is nearly zero at the rudder, but typically amounts to 10% to 25% of the ship's speed at the propeller of usual single-screw ships. It amounts nearly to the thrust deduction fraction t . Thus the flow outside of the propeller slipstream is accelerated between the propeller and the rudder by about $t \cdot V$. This causes a pressure drop which also accelerates the propeller slipstream to approximately:

$$V_x = (V_{\text{corr}}^2 + t \cdot V^2) / V_{\text{corr}}$$

The corresponding slipstream contraction is:

$$r_x = (r + \Delta r) \cdot \sqrt{V_{\text{corr}} / V_x}$$

For non-zero rudder angle and forward ship speed, an interaction between the flow around rudder and hull occurs which decreases the lift force at the rudder; however, an additional transverse force of equal direction is generated at the aftbody. Compared to the rudder lift without hull interaction, the total transverse force is increased by the factor $1 + a_H \cdot a_H$ may be approximated (Söding (1982)):

$$a_H = \frac{1}{1 + (4.9 \cdot e/T + 3 \cdot c/T)^2}$$

Here T is the draft of the ship, e the mean distance between the front edge of the rudder and the aft end of the hull, and c the mean rudder chord length. Compared to the free-running rudder, the centre of effort of the total transverse force is shifted forward by approximately:

$$\Delta x = \frac{0.3T}{e/T + 0.46}$$

Potential flow computations show that Δx may increase to up half the ship's length in shallow water if the gap length e between rudder and hull tends to zero, as may be the case for twin-screw ships with a centre rudder. This would decrease the ship's turning ability on shallow water. For a non-zero drift velocity v (positive to starboard, measured amidships) and a non-zero yaw rate r (positive clockwise if seen from above) of the ship, the hull in front of the rudder influences the flow direction at the rudder position. Without

hull influence, the transverse flow velocity v relative to the hull at the rudder position x_R is:

$$v_R = -(v + x_R \cdot r)$$

where x_R is the distance between rudder and midship section, negative for stern rudders. However, experiments of Kose (1982) with a freely rotating, unbalanced rudder behind a ship model without propeller indicated a mean transverse velocity at the rudder's position of only:

$$v_R = -(0.36 \cdot v + 0.66 \cdot x_R \cdot r)$$

From the rudder angle δ (positive to port side), the mean longitudinal flow speed V_x (positive backward) and the mean transverse flow speed v_R at the rudder position, the angle of attack follows:

$$\alpha = \delta + \arctan \frac{v_R}{V_{\text{corr}}}$$

5.4.6 Rudder cavitation

Rudder cavitation may occur even at small rudder angles for ship speed's exceeding 22 knots with rudder(s) in the propeller slipstream and:

$$\frac{P}{D^2 \pi / 4} > 700 \text{ kW/m}^2$$

Here P is the delivered power, D the propeller diameter.

Rudder cavitation – as with propeller cavitation – is caused by water evaporation where at points of high flow velocity the pressure locally drops below the vapour pressure of the water. Cavitation erosion (loss of material by mechanical action) occurs when small bubbles filled with vapour collapse on or near to the surface of the body. During the collapse a microscopic high-velocity jet forms, driven by surface tension and directed onto the body surface. It causes small cracks and erosion, which in seawater may be magnified by corrosion (galvanic loss of material). Paint systems, rubber coatings, enamel etc. offer no substantial resistance to cavitation, but austenitic steel and some types of bronze seem to retard the erosion compared to the mild steel normally used for rudders.

The cavitation number σ (Fig. 5.21) is a non-dimensional characteristic value for studying cavitation problems in model experiments:

$$\sigma = \frac{p - p_v}{\frac{\rho}{2} V^2}$$

where p is the pressure in undisturbed flow, i.e. atmospheric pressure plus hydrostatic pressure, p_v vaporization pressure, V ship speed, ρ density of water.

There are different types of rudder cavitation:

1. *Bubble cavitation on the rudder side plating*

For large rudder angles, cavitation is unavoidable in ships of more than about 10 knots. It will decrease the rudder lift substantially if the cavitation

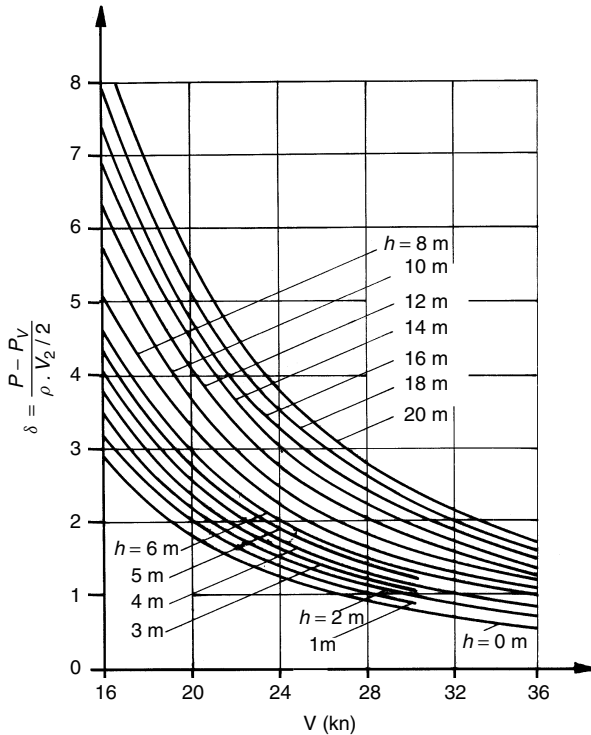


Figure 5.21 Cavitation numbers σ as a function of the ship speed V with the submersion h (depth below water surface) as parameter

causes a complete separation of flow from the suction side. Otherwise its influence on rudder forces is small (Kracht (1987)). Cavitation erosion is of interest only if it occurs within the range of rudder angles $\delta = \pm 5^\circ$ used for course keeping. Evaluation of model experiments shows that the onset of cavitation is indeed observed if the pressure determined by potential-flow theory is smaller than the water vaporization pressure p_v . p_v lies typically between 1% and 3% of the atmospheric pressure. It may therefore (not in model tests, but for full-scale ships) simply be taken as zero. Thus, to test for blade side cavitation in the design stage of ships, one may proceed as follows:

- Determine the slipstream radius $r + \Delta r$ and the inflow speed to the rudder V_{corr} from Fig. 5.19 or the corresponding formulae at about 80% of the propeller tip radius above and below the propeller axis.
- Correct these values to obtain V_x and r_x by (see above):

$$V_x = (V_{\text{corr}}^2 + t \cdot V^2) / V_{\text{corr}}$$

$$r_x = (r + \Delta r) \cdot \sqrt{V_{\text{corr}} / V_x}$$

- Because of non-uniform distribution of the slipstream velocity, add 12% of V to obtain the maximum axial speed at the rudder:

$$V_{\text{max}} = V_x + 0.12 \cdot (V_{\text{corr}} - V_A)$$

- Estimate the inflow angle α to the rudder due to the rotation of the propeller slipstream by

$$\alpha = \arctan \left(4.3 \cdot \frac{K_Q}{J^2} \cdot \sqrt{\frac{1 - \bar{w}}{1 - w_{\text{local}}}} \cdot \frac{V_A}{V_{\text{max}}} \right)$$

\bar{w} is the mean wake number and w_{local} the wake number at the respective position. The equation is derived from the momentum theorem with an empirical correction for the local wake. It is meant to apply about 0.7 to 1.0 propeller diameter behind the propeller plane. The position relevant to the pressure distribution is about 1/2 chord length behind the leading edge of the rudder.

- Add $\delta = 3^\circ = 0.052 \text{ rad}$ as an allowance for steering rudder angles.
- Determine the maximum local lift coefficient $C_{Ll \text{ max}}$ from Fig. 5.22, where $\alpha + \delta$ are to be measured in radians. c is the chord length of the rudder at the respective height, r_x the propeller slipstream radius (see above):

$$r_x = r_o \cdot \sqrt{\frac{1}{2} \left(1 + \frac{V_A}{V_\infty} \right)}$$

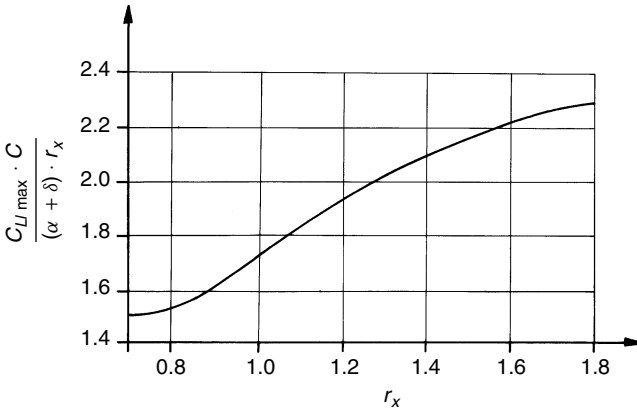


Figure 5.22 Diagram for determining the local values, of maximum lift coefficient $C_{Ll \text{ max}}$

Figure 5.22 is based on lifting-line calculations of a rudder in the propeller slipstream. It takes into account the dependence of the local lift coefficient on the vertical variation of inflow velocity and direction.

- Determine the extreme negative non-dimensional pressure on the suction side depending on profile and local lift coefficient $C_{Ll \text{ max}}$. For this we use Fig. 5.23 derived from potential flow calculations.
- Add to p_{dyn} (negative) the static pressure $p_{\text{stat}} = 103 \text{ kPa} + \rho \cdot g \cdot h$. h is the distance between the respective point on the rudder and the water surface, e.g. 80% of the propeller radius above the propeller axis.

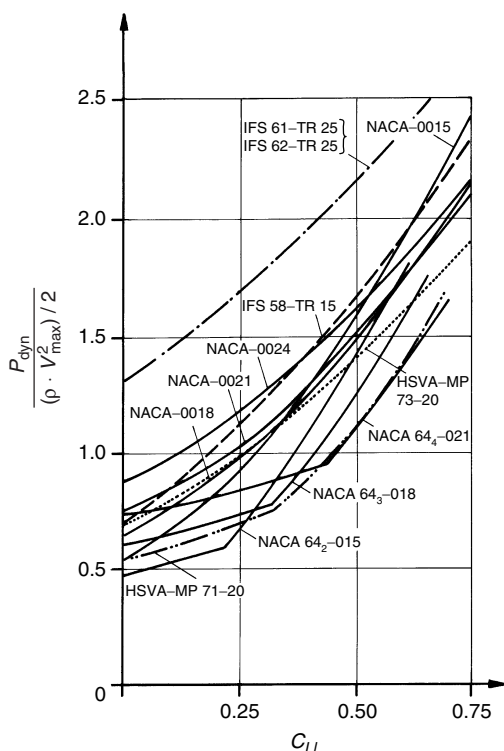


Figure 5.23 Extreme negative dynamic pressure of the suction side as a function of the local lift coefficient C_{Li} and the profile

If the resulting minimum pressure on the suction side is negative or slightly positive (less than 3 kPa), the side plating of the rudder is prone to cavitation. For a right-turning propeller (turning clockwise looking forward) the cavitation will occur:

- on the starboard side in the upper part of the rudder relative to the propeller axis
- on the port side in the lower part of the rudder relative to the propeller axis

Brix (1993), pp. 91–92, gives an example for such a computation. Measures to decrease rudder side cavitation follow from the above prediction method:

- Use profiles with small p_{dyn} at the respective local lift coefficient. These profiles have their maximum thickness at approximately 40% behind the leading edge.
- Use profiles with an inclined (relative to the mean rudder plane) or curved mean line to decrease the angle of attack (Brix *et al.* (1971)). For a right-turning propeller, the rudder nose should be on the port side above the propeller axis, on the starboard side below it.

2. Rudder sole cavitation

Due to the pressure difference between both sides of the rudder caused, e.g., by the rotation of the propeller slipstream, a flow component around the rudder sole from the pressure to the suction side occurs. It causes a

rudder tip vortex (similar to propeller tip vortices) which may be filled by a cavitation tube. This may cause damage if it attaches to the side of the rudder. However, conditions for this are not clear at present. If the rudder has a sharp corner at the front lower edge, even for vanishing angles of attack the flow cannot follow the sharp bend from the leading edge to the base plate, causing cavitation in the front part of the rudder sole. As a precaution the base plate is bent upward at its front end (Brix *et al.* (1971)). This lowers the cavitation number below which sole cavitation occurs (Fig. 5.24). For high ship speeds exceeding, e.g., 26 knots cavitation has still been reported. However, it is expected that a further improvement could be obtained by using a smoothly rounded lower face or a baffle plate at the lower front end (Kracht (1987)). No difficulties have been reported at the rudder top plate due to the much lower inflow velocity.

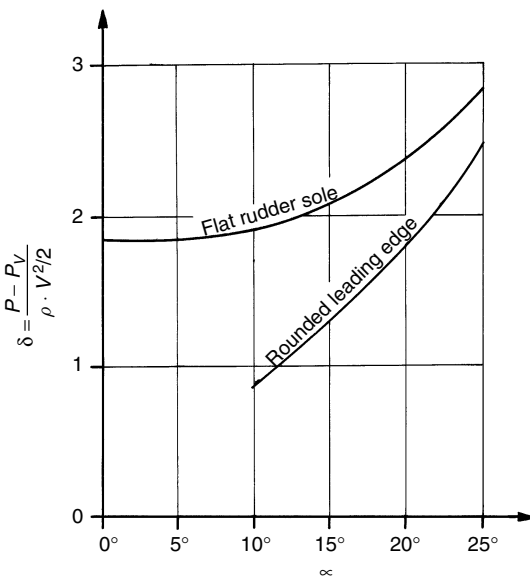


Figure 5.24 Cavitation number σ below which rudder sole cavitation occurs as a function of the angle of attack α and the rudder sole construction

3. Propeller tip vortex cavitation

Every propeller causes tip vortices. These are regions of low pressure, often filled with cavitation tubes. Behind the propeller they form spirals which are intersected by the rudder. Therefore, cavitation erosion frequently occurs at the rudder at the upper and sometimes lower slipstream boundaries, mainly (for right-turning propellers) on the upper starboard side of the rudder. This problem is not confined to high-speed ships. The best means to reduce these effects is to decrease gradually the propeller loading to the blade tips by appropriately reduced pitch, and to use a high propeller skew. These methods also reduce propeller-induced vibrations.

4. Propeller hub cavitation

Behind the propeller hub a vortex is formed which is often filled by a cavitation tube. However, it seems to cause fewer problems at the rudder

than the tip vortices, possibly due to the lower axial velocity behind the propeller hub.

5. Cavitation at surface irregularities

Surface irregularities disturbing the smooth flow cause high flow velocities at convex surfaces and edges, correspondingly low pressures and frequently cavitation erosion. At the rudder, such irregularities may be zinc anodes and shaft couplings. It is reported that also behind scoops, propeller bossings etc. cavitation erosion occurred, possibly due to increased turbulence of the flow. Gaps between the horn and the rudder blade in semi-balanced rudders are especially prone to cavitation, leading to erosion of structurally important parts of the rudder. For horizontal and vertical gaps (also in flap rudders) the rounding of edges of the part behind the gap is recommended.

5.4.7 Rudder design

There are no regulations for the rating of the rudder area. The known recommendations give the rudder area as a percentage of the underwater lateral area $L \cdot T$. Det Norske Veritas recommends:

$$\frac{A_R}{L \cdot T} \geq 0.01 \cdot \left(1 + 25 \left(\frac{B}{L} \right)^2 \right)$$

This gives a rudder area of approximately 1.5% of the underwater lateral area for ships of usual width; for unusually broad ships (large mass, low yaw stability) a somewhat larger value is given. This corresponds to typical rudder designs and can serve as a starting point for further analyses of the steering qualities of a ship.

Recommended minimum criteria for the steering qualities of a ship are:

- Non-dimensional initial turning time in Z 20°/10° manoeuvres: $t'_a = 1 + 1.73F_n$.
- Non-dimensional yaw checking time in Z 20°/10° manoeuvres: $t'_s = 0.78 + 2.12F_n$.
- The rudder should be able to keep the ship on a straight course with a rudder angle of maximum 20° for wind from arbitrary direction and $v_w/V = 5$. v_w is the wind speed, V the ship speed.
- The ship must be able to achieve a turning circle of less than $5 \cdot L$ at the same v_w/V for maximum rudder angle.

The criteria for initial turning time and yaw checking time were derived by Brix using regression analysis for 20°/10° zigzag test results for many ships (Fig. 5.8). The time criteria are critical for large ships (bulklers, tankers), while the wind criteria are critical for ships with a large lateral area above the water (ferries, combatants, container ships). An additional criterion concerning yaw stability would make sense, but this would be difficult to check computationally.

The rudder design can be checked against the above criteria using computations (less accurate) or model tests (more expensive). A third option would be the systematically varied computations of Wagner, described in Brix (1993), pp. 95–102. This approach yields a coefficient $C_{Y\delta}$ for rudder effectiveness which inherently meets the above criteria. The method described in Brix

(1993) uses design diagrams. For computer calculations, empirical formulae also derived by Wagner exist.

5.4.8 CFD for rudder flows and conclusions for rudder design

The determination of forces on the rudder is important for practical design purposes:

- The transverse force is needed to evaluate the manoeuvrability of ships already in the design stage as required by IMO.
- The longitudinal force influences noticeably the propulsive efficiency.
- The shaft torsional moment is decisive for selecting a suitable rudder gear.

In principle, there are three sources of information for these forces:

- Model experiments which produce accurate forces at model Reynolds numbers, but suffer from severe scale effects when predicting the maximum lift at full scale.
- RANSE computations appear to be the most reliable source of information and should gain in importance also for practical design of rudders.
- BEM computations can often give sufficiently accurate results with a minimum of effort if some empirical relationships and corrections are applied.

Söding (1998a, b) described the state of the art for BEM comparing the results to RANSE and experimental results. The RANSE computations used for comparison were finite-volume methods employing a standard $k-\varepsilon$ turbulence model with wall function.

Söding's BEM approach for rudder flows introduces some special features:

- Special adaptations of the BEM take the irrotational inflow to the rudder induced by hull and propeller into account.
- The propeller slipstream is averaged in circumferential direction. The radial thrust distribution is assumed such that it approaches gradually zero at the outer limit and is zero in the hub region.
- The ship hull above the rudder can either be modelled as horizontal mirror plane or as a separate body discretized by boundary elements.

The BEM results were compared to RANSE and experimental results for various rudders. According to potential theory, a thin foil in two-dimensional flow (i.e. for aspect ratio $\Lambda = \infty$) at a small angle of attack α produces lift nearly linearly increasing with α corresponding to:

$$\frac{dC_L}{d\alpha} = 2\pi$$

In three-dimensional flow, the lift gradient is decreased by a reduction factor $r(\Lambda)$ which is well approximated by:

$$r(\Lambda) = \Lambda \frac{\Lambda + 0.7}{(\Lambda + 1.7)^2}$$

Except for Λ , details of the rudder shape in side view (e.g. rectangular or trapezoidal) have hardly any influence on $dC_L/d\alpha$. However, the profile thickness and shape have some influence. Computations and measurements of the lift coefficient corrected for infinite aspect ratio by the formula above yield the following conclusions:

- All values differ from the theoretical value 2π by less than $\pm 17\%$.
- For the same profile, measurements and computations by any method differ generally by only a few per cent, except for NACA profiles with thickness ratio greater than 25%.
- Two-dimensional and three-dimensional RANSE computations hardly differ from each other except for thick NACA profiles.
- The Reynolds number based on axial inflow velocity and mean rudder chord length has relatively little effect on the lift gradient.
- The BEM fails to predict the low lift gradient of profiles with large opening angle of the trailing edge. For such profiles, the Kutta condition used in potential flow is a poor approximation.
- Substantial thickness at the trailing edge increases the lift slope.

Further detailed investigations based on RANSE computations produced the following insight into the effect of profile thickness:

- Thick profiles produce more lift than thinner ones if they have a sharp end (concave sides), and a lower lift if they end in a larger angle (convex or flat sides).
- The mostly used NACA00 profiles are worse than the other profiles investigated, both with respect to lift slope and to the ratio between lift and drag.
- For all profiles, the lift/drag ratio decreases with increasing thickness. Therefore, for a good propulsive efficiency, one should use the thinnest possible profile.
- The IFS profile generates the largest lift. However, when compared to the HSVA MP73-25 profile the difference is small and the lift/drag ratio is worse than for the HSVA profile. The IFS profile is also more liable to suffer from cavitation due to its very uneven pressure distribution on the suction side.

BEM is not capable of predicting the stall angle because stall is inherently a viscous phenomenon. For hard-over manoeuvres, the stall angle and its associated maximum lift may be more important than $dC_L/d\alpha$. RANSE computations show that higher Reynolds numbers produce larger maximum C_L . Thus experimental values without extrapolation to actual Reynolds numbers are misleading with respect to maximum lift forces. Other conclusions for the maximum lift at stall angle from RANSE computations are:

- The maximum C_L ranges between 1.2 and more than 2. This upper limit is substantially larger than assumed in classification rules.
- The aspect ratio Λ is of minor influence only. Larger aspect ratio produces somewhat smaller $C_{L,\max}$.
- Small Λ yield large stall angles. (They also yield small $dC_L/d\alpha$, hence little change in the maximum C_L .)
- The taper ratio of the rudder has practically no influence on the maximum C_L .

- Profiles with concave sides produce larger $C_{L,\max}$ than those with flat or convex sides.

Three-dimensional RANSE computation give slightly lower maximum C_L than two-dimensional RANSE computations. The relation between the two-dimensional and three-dimensional values approximately determines the maximum lift while avoiding the complexities (and cost) of three-dimensional RANSE computations especially for complex configurations and non-uniform inflow.

The recommended procedure is then:

- Perform a two-dimensional RANSE computation for the actual profile and Reynolds number in uniform flow to determine the maximum C_L .
- Perform a panel calculation for the three-dimensional arrangement.
- Convert the computed lift to C_L using an average inflow velocity. The averaged velocity is the root mean square axial velocity averaged over the rudder height.
- Determine the approximate stall angle as that where the three-dimensional C_L in potential flow amounts to 95% of the maximum $C_{L,2d}$ in the two-dimensional RANSE computation.
- Truncate the computed lift forces at that angle, but not drag and stock moment.

In practice, the aftbody arrangement with propeller and rudder is rather more complicated and may even involve additional complexities such as nozzles, fins and bulbs. These make grid generation for field methods (and even BEM) complicated. No RANSE computations for such complex arrangements were known by 1999 and only few BEM attempted.

5.5 Exercise: manoeuvring

Solutions to the exercises will be posted on the internet (www.bh.com/companions/0750648511)

1. A motor yacht of 10 000 kg displacement is equipped with a 1 m^2 profile rudder with $\Lambda = 1.2$. The yacht is a twin-screw ship with central rudder. The rudder lies outside the propeller slipstream. The yacht has a speed of 13.33 m/s. For the central position of the rudder we can assume a velocity of 0.75 ship speed due to the wake. The ‘glide ratio’ (ratio of propeller thrust to ship weight) is $\varepsilon = 0.15$.

The yacht is to be converted to waterjet propulsion. For this purpose propeller and rudder will be dismantled and waterjets installed. Waterjets are used to manoeuvre the ship by turning the jets a maximum of 35° , just as previously the maximum rudder angle was 35° . The speed may be assumed to be unaffected by the conversion.

Will the yacht react faster or slower after its conversion? Why?

2. A tanker of 250 000 t displacement sails at 15 knots at a delivered power $P_D = 15\,000\text{ kW}$. The overall efficiency is

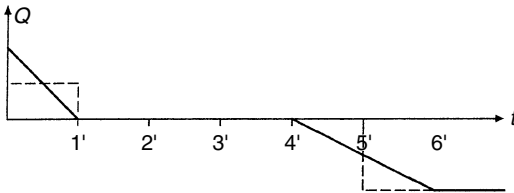
$$\eta = \frac{R \cdot U}{P_D} = 0.7$$

The tanker performs a soft stop manoeuvre. The engine is reducing linearly the torque Q within one minute to zero. The next three minutes are used to brake the shaft and to prepare the engine for reverse operation. During the following two minutes the engine is started and accelerated again linearly to full reverse torque.

How long will be the stopping distance for the tanker if it sails exactly straight ahead? Quantities not given are to be estimated!

Hints:

- (a) During the short periods of acceleration and deceleration of the engine, the ship speed is virtually constant.
- (b) The linear deceleration and acceleration shall be approximated by step functions covering the same 'area' of $Q \cdot t$, where t is the time:



- (c) The added mass in longitudinal motion may be approximated by

$$\frac{m''}{m} = \frac{1}{\pi \sqrt{(L^3/\nabla) - 14}}$$

where L is the length, ∇ the displacement of the ship.

- (d) In reverse propeller operation the ratio of thrust to resistance shall be $|T/R| = 0.945$.
3. (a) A ship lays rudder according to sine function over time alternating between port and starboard with amplitude 10° and 2 minutes period. The ship performs course changes of $\pm 20^\circ$. The maximum course deviation to port occurs 45 seconds after the maximum rudder angle to port has been reached. Determine from these data the parameters of the Nomoto equation:

$$T\ddot{\psi} + \dot{\psi} = -K\delta$$

The ship is yaw stable for $K > 0$. Is the ship yaw stable?

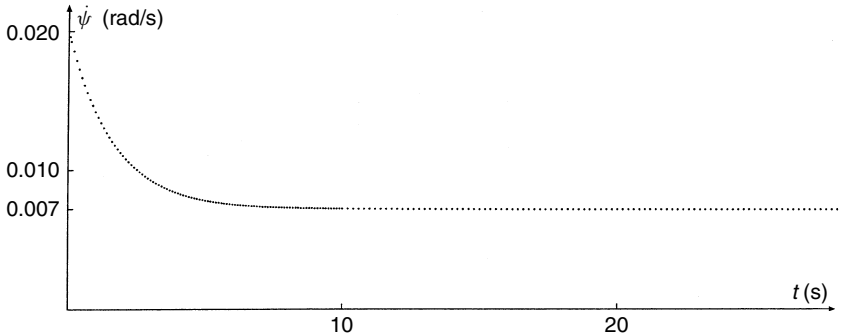
- (b) The ship speed is reduced to 50% of the value in (a). The rudder action is the same as in (a). How large is the amplitude of course changes and what is the delay between maximum rudder angle and maximum course deviation?
- (c) The rudder height is kept constant at 6 m. The rudder area is increased from 18 m^2 in (a) to 24 m^2 . The speed is kept as in (a). How large now is the course amplitude and the delay between maximum rudder angle and maximum course deviation?

Hint: For constant rudder angle, the Nomoto equation has the solution: $\dot{\psi} = ae^{\alpha t} + b$.

4. A ship follows the 'Norrbin' equation:

$$T\ddot{\psi} + \dot{\psi} + \alpha\dot{\psi}^3 = -K\delta$$

The ship performs a pull-out manoeuvre and the following curve for $\dot{\psi}$ is recorded:



- (a) Determine the constants T and α !
 - (b) Sketch a corresponding curve of $\dot{\psi}$ for the case that at $t = 0$, $\dot{\psi} = 0.002$ rad/s instead of $\dot{\psi} = 0.02$ rad/s.
5. Determine the rudder lift at 10° rudder angle for the semi-balanced rudder behind a propeller and hull of a ferry as shown below. The ship speed is 30 kn, the propeller thrust 4000 kN. The wake fraction is $w = 0.25$. Correct the rudder lift for the propeller loading according to Söding (1998a, b).

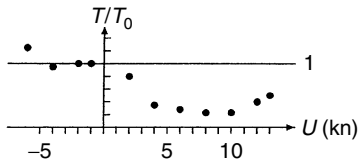
Following Goodrich and Mooland (1979) we may assume that at 10° rudder angle a semi-balanced rudder as the one depicted may have 79.2% of the lift of a 'normal' rudder.

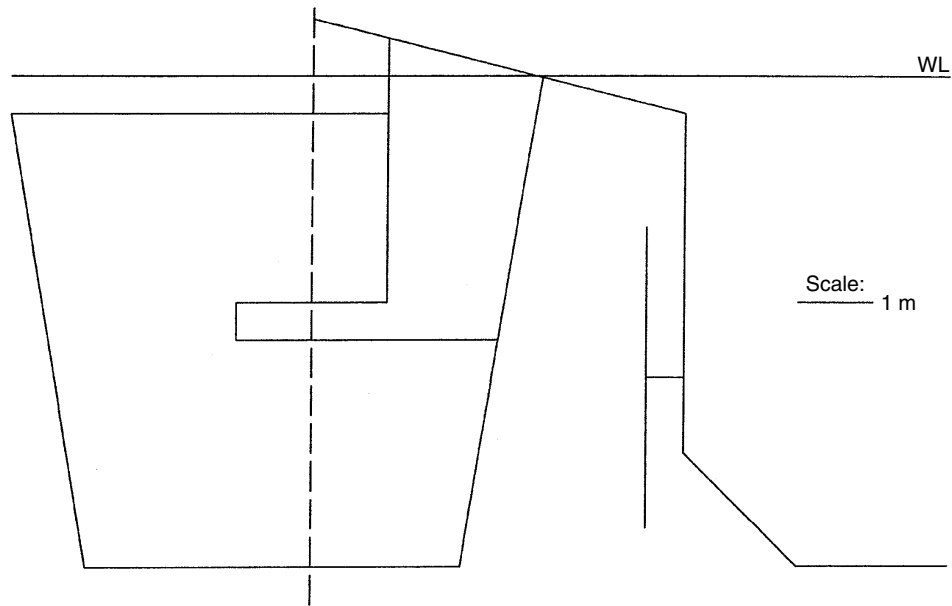
Dimensions are to be taken from the sketch (see p. 206).

6. The container ship in Tables 5.1 and 5.2 sails in a turning circle with rudder in the centre position using just its bow thruster at maximum power. The bow thruster is located 4 m aft of the forward perpendicular. The power of the thruster is 4000 kW. The pipe diameter is 2.5 m. The ship speed is 5 kn. The efficiency of the bow thruster is $\eta = 0.8$.

Compute the radius of the turning circle R assuming linear correlation between hull forces and motions. The radius of the turning circle follows from the relation $U = r \cdot R$, where r is the yaw rate.

Forward speed changes the thrust of a bow thruster T from the value at zero speed T_0 :





Boundary element methods

6.1 Introduction

The Laplace equation is a *linear* differential equation, i.e. arbitrary linear combinations (superpositions) of elementary solutions of the Laplace equation will again form a possible solution. This chapter is devoted to various elementary solutions used in the computation of ship flows. It is not really necessary to understand the given formulae, but the concepts should be understood. Fortran subroutines for elements are public domain and may be obtained on the internet, see Preface.

Consider the case if still water is seen from a passing airplane with speed V , or from a razor blade ship not disturbing the flow. Here the water appears to flow uniformly in the negative direction x with the speed V . The water has no velocity component in the y or z direction, and everywhere uniformly the velocity $-V$ in the x direction. The corresponding potential is:

$$\phi = -Vx$$

Another elementary potential is that of an undisturbed incident wave as given in section 4.3.1, Chapter 4.

Various elements (elementary solutions) exist to approximate the disturbance effect of the ship. These more or less complicated mathematical expressions are useful to model displacement ('sources') or lift ('vortices', 'dipoles'). The common names indicate a graphical physical interpretation of the abstract mathematical formulae and will be discussed in the following.

The basic idea of all the related boundary element methods is to superimpose elements in an unbounded fluid. Since the flow does not cross a streamline just as it does not cross a real fluid boundary (such as the hull), any unbounded flow field in which a streamline coincides with the actual flow boundaries in the bounded problem can be interpreted as a solution for the bounded flow problem in the limited fluid domain. Outside this fluid domain, the flow cannot (and should not) be interpreted as a physical flow, even though the computation can give velocities, pressures, etc. everywhere.

The velocity at a field point \vec{x} induced by some typical panel types and some related formula work is given in the following. Expressions are often derived in a local coordinate system. The derivatives of the potential are transformed from the local x - y - z system to a global \bar{x} - \bar{y} - \bar{z} system. In two dimensions, we limit ourselves to x and z as coordinates, as these are the typical coordinates for a

strip in a strip method. $\vec{n} = (n_x, n_z)$ is the outward unit normal in global coordinates, coinciding with the local z vector. \vec{t} and \vec{s} are unit tangential vectors, coinciding with the local x and y vectors, respectively. The transformation from the local to the global system is as follows:

1. Two-dimensional case

$$\phi_{\bar{x}} = n_z \cdot \phi_x + n_x \cdot \phi_z$$

$$\phi_{\bar{z}} = -n_x \cdot \phi_x + n_z \cdot \phi_z$$

$$\phi_{\bar{xx}} = (n_z^2 - n_x^2) \cdot \phi_{xx} + (2n_x n_z) \cdot \phi_{xz}$$

$$\phi_{\bar{xz}} = (n_z^2 - n_x^2) \cdot \phi_{xz} - (2n_x n_z) \cdot \phi_{xx}$$

$$\phi_{\bar{xxz}} = n_z(1 - 4n_x^2) \cdot \phi_{xxz} - n_x(1 - 4n_z^2) \cdot \phi_{xzz}$$

$$\phi_{\bar{xzz}} = n_x(1 - 4n_z^2) \cdot \phi_{xxz} + n_z(1 - 4n_x^2) \cdot \phi_{xzz}$$

2. Three-dimensional case

$$\phi_{\bar{x}} = t_1 \cdot \phi_x + s_1 \cdot \phi_y + n_1 \cdot \phi_z$$

$$\phi_{\bar{y}} = t_2 \cdot \phi_x + s_2 \cdot \phi_y + n_2 \cdot \phi_z$$

$$\phi_{\bar{z}} = t_3 \cdot \phi_x + s_3 \cdot \phi_y + n_3 \cdot \phi_z$$

$$\phi_{\bar{x}\bar{x}} = t_1^2 \phi_{xx} + s_1^2 \phi_{yy} + n_1^2 \phi_{zz} + 2(s_1 t_1 \phi_{xy} + n_1 t_1 \phi_{xz} + n_1 s_1 \phi_{yz})$$

$$\phi_{\bar{x}\bar{y}} = t_1 t_2 \phi_{xx} + t_1 s_2 \phi_{xy} + t_1 n_2 \phi_{xz} + s_1 t_2 \phi_{xy} + s_1 s_2 \phi_{yy} + s_1 n_2 \phi_{yz} \\ + n_1 t_2 \phi_{xz} + n_1 s_2 \phi_{yz} + n_1 n_2 \phi_{zz}$$

$$\phi_{\bar{x}\bar{z}} = t_1 t_3 \phi_{xx} + t_1 s_3 \phi_{xy} + t_1 n_3 \phi_{xz} + s_1 t_3 \phi_{xy} + s_1 s_3 \phi_{yy} + s_1 n_3 \phi_{yz} \\ + n_1 t_3 \phi_{xz} + n_1 s_3 \phi_{yz} + n_1 n_3 \phi_{zz}$$

$$\phi_{\bar{y}\bar{y}} = t_2^2 \phi_{xx} + s_2^2 \phi_{yy} + n_2^2 \phi_{zz} + 2(s_2 t_2 \phi_{xy} + n_2 t_2 \phi_{xz} + n_2 s_2 \phi_{yz})$$

$$\phi_{\bar{y}\bar{z}} = t_2 t_3 \phi_{xx} + t_2 s_3 \phi_{xy} + t_2 n_3 \phi_{xz} + s_2 t_3 \phi_{xy} + s_2 s_3 \phi_{yy} + s_2 n_3 \phi_{yz} \\ + n_2 t_3 \phi_{xz} + n_2 s_3 \phi_{yz} + n_2 n_3 \phi_{zz}$$

$$\phi_{\bar{x}\bar{x}\bar{z}} = t_1^2(t_3 \phi_{xxx} + s_3 \phi_{xxy} + n_3 \phi_{xxz}) + s_1^2(t_3 \phi_{xyy} + s_3 \phi_{yyy} + n_3 \phi_{yyz}) \\ + n_1^2(t_3 \phi_{xzz} + s_3 \phi_{yzz} + n_3 \phi_{zzz}) + 2(s_1 t_1(t_3 \phi_{xxy} + s_3 \phi_{xyy} + n_3 \phi_{xyz}) \\ + n_1 t_1(t_3 \phi_{xxz} + s_3 \phi_{xyz} + n_3 \phi_{xzz}) + n_1 s_1(t_3 \phi_{xyy} + s_3 \phi_{yyz} + n_3 \phi_{yzz}))$$

$$\phi_{\bar{x}\bar{y}\bar{z}} = t_1 t_2(t_3 \phi_{xxx} + s_3 \phi_{xxy} + n_3 \phi_{xxz}) + (t_1 s_2 + s_1 t_2) \\ \times (t_3 \phi_{xxy} + s_3 \phi_{xyy} + n_3 \phi_{xyz}) + s_1 s_2(t_3 \phi_{xyy} + s_3 \phi_{yyy} + n_3 \phi_{yyz}) \\ + (t_1 n_2 + n_1 t_2)(t_3 \phi_{xxz} + s_3 \phi_{xyz} + n_3 \phi_{xzz}) \\ + n_1 n_2(t_3 \phi_{xzz} + s_3 \phi_{yzz} + n_3 \phi_{zzz}) + (s_1 n_2 + n_1 s_2) \\ \times (t_3 \phi_{xyy} + s_3 \phi_{yyz} + n_3 \phi_{yzz})$$

$$\phi_{\bar{x}\bar{z}\bar{z}} = t_1 t_3(t_3 \phi_{xxx} + s_3 \phi_{xxy} + n_3 \phi_{xxz}) + (t_1 s_3 + s_1 t_3) \\ \times (t_3 \phi_{xxy} + s_3 \phi_{xyy} + n_3 \phi_{xyz}) + s_1 s_3(t_3 \phi_{xyy} + s_3 \phi_{yyy} + n_3 \phi_{yyz})$$

$$\begin{aligned}
& + (t_1 n_3 + n_1 t_3)(t_3 \phi_{xxz} + s_3 \phi_{xyz} + n_3 \phi_{xzz}) \\
& + n_1 n_3 (t_3 \phi_{xzz} + s_3 \phi_{yzz} + n_3 \phi_{zzz}) + (s_1 n_3 + n_1 s_3) \\
& \times (t_3 \phi_{xyz} + s_3 \phi_{yyz} + n_3 \phi_{yzz}) \\
\phi_{\bar{y}\bar{y}\bar{z}} &= t_2^2 (t_3 \phi_{xxx} + s_3 \phi_{xxy} + n_3 \phi_{xxz}) + s_2^2 (t_3 \phi_{xyy} + s_3 \phi_{yyy} + n_3 \phi_{yyz}) \\
& + n_2^2 (t_3 \phi_{xzz} + s_3 \phi_{yzz} + n_3 \phi_{zzz}) + 2(s_2 t_2 (t_3 \phi_{xxy} + s_3 \phi_{xyy} + n_3 \phi_{xyz}) \\
& + n_2 t_2 (t_3 \phi_{xxz} + s_3 \phi_{xyz} + n_3 \phi_{xzz}) + n_2 s_2 (t_3 \phi_{xyy} + s_3 \phi_{yyz} + n_3 \phi_{yzz})) \\
\phi_{\bar{y}\bar{z}\bar{z}} &= t_2 t_3 (t_3 \phi_{xxx} + s_3 \phi_{xxy} + n_3 \phi_{xxz}) + (t_2 s_3 + s_2 t_3) \\
& \times (t_3 \phi_{xxy} + s_3 \phi_{xyy} + n_3 \phi_{xyz}) + s_2 s_3 (t_3 \phi_{xyy} + s_3 \phi_{yyy} + n_3 \phi_{yyz}) \\
& + (t_2 n_3 + n_2 t_3)(t_3 \phi_{xxz} + s_3 \phi_{xyz} + n_3 \phi_{xzz}) \\
& + n_2 n_3 (t_3 \phi_{xzz} + s_3 \phi_{yzz} + n_3 \phi_{zzz}) + (s_2 n_3 + n_2 s_3) \\
& \times (t_3 \phi_{xyz} + s_3 \phi_{yyz} + n_3 \phi_{yzz})
\end{aligned}$$

6.2 Source elements

The most common elements used in ship flows are source elements which are used to model the displacement effect of a body. Elements used to model the lift effect such as vortices or dipoles are in addition employed if lift plays a significant role, e.g. in yawed ships for manoeuvring.

6.2.1 Point source

1. Two-dimensional case

The coordinates of the source are (x_q, z_q) . The distance between source point and field point (x, y) is $r = \sqrt{(x - x_q)^2 + (z - z_q)^2}$. The potential induced at the field point is then:

$$\phi = \frac{\sigma}{2\pi} \ln r = \frac{\sigma}{4\pi} \ln((x - x_q)^2 + (z - z_q)^2)$$

This yields the velocities:

$$\vec{v} = \begin{Bmatrix} \phi_x \\ \phi_z \end{Bmatrix} = \frac{\sigma}{2\pi r^2} \begin{Bmatrix} x - x_q \\ z - z_q \end{Bmatrix}$$

The absolute value of the velocity is then:

$$v = \frac{\sigma}{2\pi r^2} \sqrt{(x - x_q)^2 + (z - z_q)^2} = \frac{\sigma}{2\pi r}$$

The absolute value of the velocity is thus the same for all points on a radius r around the point source. The direction of the velocity is pointing radially away from the source point and the velocity decreases with distance as $1/r$. Thus the flow across each concentric ring around the source point is constant. The element can be physically interpreted as a source of water which constantly pours water flowing radially in all directions. σ is the strength of this source. For negative σ , the element acts like a sink with

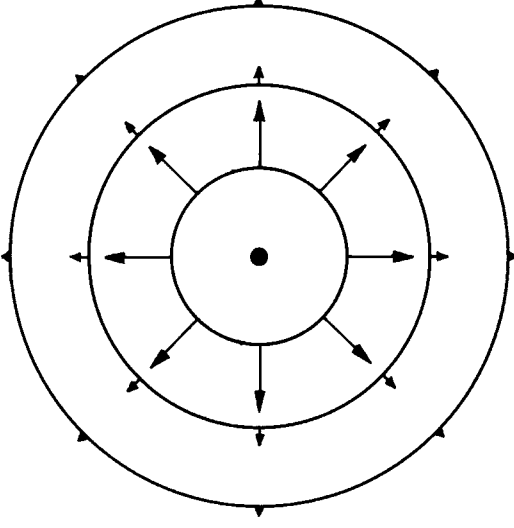


Figure 6.1 Effect of a point source

water flowing from all directions into the centre. Figure 6.1 illustrates the effect of the element.

Higher derivatives are:

$$\phi_{xx} = -\phi_{zz} = \frac{\sigma}{2\pi} \frac{1}{r^2} - \phi_x \cdot \frac{2(x - x_q)}{r^2}$$

$$\phi_{xz} = -\phi_x \cdot \frac{2(z - z_q)}{r^2}$$

$$\phi_{xxz} = -\phi_{zzz} = -2 \cdot \left(\frac{(x - x_q)}{r^2} \phi_{xz} + \frac{(z - z_q)}{r^2} \phi_{xx} \right)$$

$$\phi_{xzz} = -2 \cdot \left(\frac{(x - x_q)}{r^2} \phi_{zz} + \frac{(z - z_q)}{r^2} \phi_{xz} \right)$$

2. Three-dimensional case

The corresponding expressions in three dimensions are:

$$r = \sqrt{(x - x_q)^2 + (y - y_q)^2 + (z - z_q)^2}$$

$$\phi = -\sigma \frac{1}{4\pi r}$$

$$\phi_x = \sigma \frac{1}{2\pi r^3} (x - x_q)$$

$$\phi_y = \sigma \frac{1}{2\pi r^3} (y - y_q)$$

$$\phi_z = \sigma \frac{1}{2\pi r^3} (z - z_q)$$

$$\begin{aligned}
\phi_{xx} &= (-3\phi_x(x - x_q) - \phi)/r^2 \\
\phi_{xy} &= (-3\phi_x(y - y_q))/r^2 \\
\phi_{xz} &= (-3\phi_x(z - z_q))/r^2 \\
\phi_{yy} &= (-3\phi_y(y - y_q) - \phi)/r^2 \\
\phi_{yz} &= (-3\phi_y(z - z_q))/r^2 \\
\phi_{xxz} &= -(2(\phi/r^2) + 5\phi_{xx})dz/r^2 \\
\phi_{xyz} &= -5\phi_{xy}dz/r^2 \\
\phi_{xzz} &= -5\phi_{xz}dz/r^2 - 3\phi_x/r^2 \\
\phi_{yyz} &= -(2(\phi/r^2) + 5\phi_{yy})dz/r^2 \\
\phi_{yzz} &= -5\phi_{yz}dz/r^2 - 3\phi_y/r^2
\end{aligned}$$

6.2.2 Regular first-order panel

1. Two-dimensional case

For a panel of constant source strength we formulate the potential in a local coordinate system. The origin of the local system lies at the centre of the panel. The panel lies on the local x -axis, the local z -axis is perpendicular to the panel pointing outward. The panel extends from $x = -d$ to $x = d$. The potential is then

$$\phi = \int_{-d}^d \frac{\sigma}{2\pi} \cdot \ln \sqrt{(x - x_q)^2 + z^2} dx_q$$

With the substitution $t = x - x_q$ this becomes:

$$\begin{aligned}
\phi &= \frac{1}{2} \int_{x-d}^{x+d} \frac{\sigma}{2\pi} \cdot \ln(t^2 + z^2) dt \\
&= \frac{\sigma}{4\pi} \left[t \ln(t^2 + z^2) + 2z \arctan \frac{t}{z} - 2t \right]_{x-d}^{x+d}
\end{aligned}$$

Additive constants can be neglected, giving:

$$\phi = \frac{\sigma}{4\pi} \left(x \ln \frac{r_1}{r_2} + d \ln(r_1 r_2) + 2z \arctan \frac{2dz}{x^2 + z^2 - d^2} + 4d \right)$$

with $r_1 = (x + d)^2 + z^2$ and $r_2 = (x - d)^2 + z^2$. The derivatives of the potential (still in local coordinates) are:

$$\begin{aligned}
\phi_x &= \frac{\sigma}{2\pi} \cdot \frac{1}{2} \ln \frac{r_1}{r_2} \\
\phi_z &= \frac{\sigma}{2\pi} \cdot \arctan \frac{2dz}{x^2 + z^2 - d^2}
\end{aligned}$$

$$\phi_{xx} = \frac{\sigma}{2\pi} \cdot \left(\frac{x+d}{r_1} - \frac{x-d}{r_2} \right)$$

$$\phi_{xz} = \frac{\sigma}{2\pi} \cdot z \cdot \left(\frac{1}{r_1} - \frac{1}{r_2} \right)$$

$$\phi_{xxz} = \frac{\sigma}{2\pi} \cdot (-2z) \cdot \left(\frac{x+d}{r_1^2} - \frac{x-d}{r_2^2} \right)$$

$$\phi_{xzz} = \frac{\sigma}{2\pi} \cdot \left(\frac{(x+d)^2 - z^2}{r_1^2} - \frac{(x-d)^2 - z^2}{r_2^2} \right)$$

ϕ_x cannot be evaluated (is singular) at the corners of the panel. For the centre point of the panel itself ϕ_z is:

$$\phi_z(0, 0) = \lim_{z \rightarrow 0} \phi_z(0, z) = \frac{\sigma}{2}$$

If the ATAN2 function in Fortran is used for the general expression of ϕ_z , this is automatically fulfilled.

2. Three-dimensional case

In three dimensions the corresponding expressions for an arbitrary panel are rather complicated. Let us therefore consider first a simplified case, namely a plane rectangular panel of constant source strength, (Fig. 6.2). We denote the distances of the field point to the four corner points by:

$$r_1 = \sqrt{x^2 + y^2 + z^2}$$

$$r_2 = \sqrt{(x-\ell)^2 + y^2 + z^2}$$

$$r_3 = \sqrt{x^2 + (y-h)^2 + z^2}$$

$$r_4 = \sqrt{(x-\ell)^2 + (y-h)^2 + z^2}$$

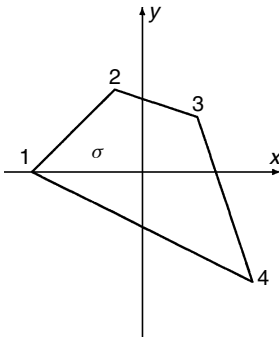


Figure 6.2 Simple rectangular flat panel of constant strength; origin at centre of panel

The potential is:

$$\phi = -\frac{\sigma}{4\pi} \int_0^h \int_0^\ell \frac{1}{\sqrt{(x-\xi)^2 + (y-\eta)^2 + z^2}} d\xi d\eta$$

The velocity in the x direction is:

$$\begin{aligned}
 \frac{\partial \phi}{\partial x} &= \frac{\sigma}{4\pi} \int_0^h \int_0^\ell \frac{x - \xi}{\sqrt{(x - \xi)^2 + (y - \eta)^2 + z^2}^3} d\xi d\eta \\
 &= \frac{\sigma}{4\pi} \int_0^h -\frac{1}{\sqrt{(x - \ell)^2 + (y - \eta)^2 + z^2}} + \frac{1}{\sqrt{x^2 + (y - \eta)^2 + z^2}} d\eta \\
 &= \frac{\sigma}{4\pi} \ln \frac{(r_3 - (y - h))(r_1 - y)}{(r_2 - y)(r_4 - (y - h))}
 \end{aligned}$$

The velocity in the y direction is in similar fashion:

$$\frac{\partial \phi}{\partial y} = \frac{\sigma}{4\pi} \ln \frac{(r_2 - (x - \ell))(r_1 - x)}{(r_3 - x)(r_4 - (x - \ell))}$$

The velocity in the z direction is:

$$\begin{aligned}
 \frac{\partial \phi}{\partial z} &= \frac{\sigma}{4\pi} \int_0^h \int_0^\ell \frac{z}{\sqrt{(x - \xi)^2 + (y - \eta)^2 + z^2}^3} d\xi d\eta \\
 &= \frac{\sigma}{4\pi} \int_0^h -\frac{z(x - \ell)}{((y - \eta)^2 + z^2)\sqrt{(x - \ell)^2 + (y - \eta)^2 + z^2}} \\
 &\quad + \frac{zx}{((y - \eta)^2 + z^2)\sqrt{x^2 + (y - \eta)^2 + z^2}} d\eta
 \end{aligned}$$

Substituting:

$$t = \frac{\eta - y}{\sqrt{x^2 + (\eta - y)^2 + z^2}}$$

yields:

$$\begin{aligned}
 \frac{\partial \phi}{\partial z} &= \frac{\sigma}{4\pi} \left[\int_{-y/r_2}^{(h-y)/r_4} \frac{-z(x - \ell)}{z^2 + (x - \ell)^2 t^2} dt + \int_{-y/r_1}^{(h-y)/r_3} \frac{zx}{z^2 + x^2 t^2} dt \right] \\
 &= \frac{\sigma}{4\pi} \left[-\arctan \frac{x - \ell}{z} \frac{h - y}{r_4} + \arctan \frac{x - \ell - y}{z} \frac{y}{r_2} \right. \\
 &\quad \left. - \arctan \frac{x - y}{z} \frac{y}{r_1} + \arctan \frac{x}{z} \frac{h - y}{r_3} \right]
 \end{aligned}$$

The derivation used:

$$\begin{aligned}
 \int \frac{1}{\sqrt{x^2 + a^2}} dx &= \ln(x + \sqrt{x^2 + a^2}) + C \\
 \int \frac{x}{\sqrt{x^2 + a^2}^3} dx &= -\frac{1}{\sqrt{x^2 + a^2}} + C
 \end{aligned}$$

$$\int \frac{1}{\sqrt{x^2 + a^2}^3} dx = \frac{x}{a^2 \sqrt{x^2 + a^2}} + C$$

$$\int \frac{1}{a + bx^2} dx = \frac{1}{\sqrt{ab}} \arctan \frac{bx}{\sqrt{ab}} \quad \text{for } b > 0$$

The numerical evaluation of the induced velocities has to consider some special cases. As an example: the finite accuracy of computers can lead to problems for the above given expression of the x component of the velocity, when for small values of x and z the argument of the logarithm is rounded off to zero. Therefore, for $(\sqrt{x^2 + z^2} \ll y)$ the term $r_1 - y$ must be substituted by the approximation $(x^2 + z^2)/2x$. The other velocity components require similar special treatment.

Hess and Smith (1964) pioneered the development of boundary element methods in aeronautics, thus also laying the foundation for most subsequent work for BEM applications to ship flows. Their original panel used constant source strength over a plane polygon, usually a quadrilateral. This panel is still the most popular choice in practice.

The velocity is again given in a local coordinate system (Fig. 6.3). For quadrilaterals of unit source strength, the induced velocities are:

$$\frac{\partial \phi}{\partial x} = \frac{y_2 - y_1}{d_{12}} \ln \left(\frac{r_1 + r_2 - d_{12}}{r_1 + r_2 + d_{12}} \right) + \frac{y_3 - y_2}{d_{23}} \ln \left(\frac{r_2 + r_3 - d_{23}}{r_2 + r_3 + d_{23}} \right)$$

$$+ \frac{y_4 - y_3}{d_{34}} \ln \left(\frac{r_3 + r_4 - d_{34}}{r_3 + r_4 + d_{34}} \right) + \frac{y_1 - y_4}{d_{41}} \ln \left(\frac{r_4 + r_1 - d_{41}}{r_4 + r_1 + d_{41}} \right)$$

$$\frac{\partial \phi}{\partial y} = \frac{x_2 - x_1}{d_{12}} \ln \left(\frac{r_1 + r_2 - d_{12}}{r_1 + r_2 + d_{12}} \right) + \frac{x_3 - x_2}{d_{23}} \ln \left(\frac{r_2 + r_3 - d_{23}}{r_2 + r_3 + d_{23}} \right)$$

$$+ \frac{x_4 - x_3}{d_{34}} \ln \left(\frac{r_3 + r_4 - d_{34}}{r_3 + r_4 + d_{34}} \right) + \frac{x_1 - x_4}{d_{41}} \ln \left(\frac{r_4 + r_1 - d_{41}}{r_4 + r_1 + d_{41}} \right)$$

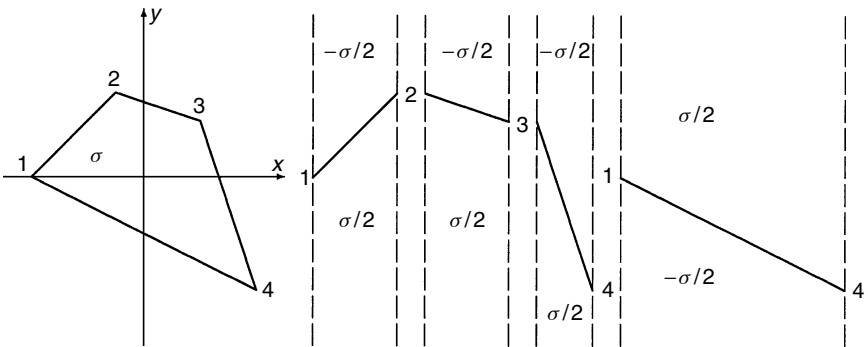


Figure 6.3 A quadrilateral flat panel of constant strength is represented by Hess and Smith as superposition of four semi-infinite strips

$$\begin{aligned}
\frac{\partial \phi}{\partial z} = & \arctan \left(\frac{m_{12}e_1 - h_1}{zr_1} \right) - \arctan \left(\frac{m_{12}e_2 - h_2}{zr_2} \right) \\
& + \arctan \left(\frac{m_{23}e_2 - h_2}{zr_2} \right) - \arctan \left(\frac{m_{23}e_3 - h_3}{zr_3} \right) \\
& + \arctan \left(\frac{m_{34}e_3 - h_3}{zr_3} \right) - \arctan \left(\frac{m_{34}e_4 - h_4}{zr_4} \right) \\
& + \arctan \left(\frac{m_{41}e_4 - h_4}{zr_4} \right) - \arctan \left(\frac{m_{41}e_1 - h_1}{zr_1} \right)
\end{aligned}$$

x_i, y_i are the local coordinates of the corner points i , r_i the distance of the field point (x, y, z) from the corner point i , d_{ij} the distance of the corner point i from the corner point j , $m_{ij} = (y_j - y_i)/(x_j - x_i)$, $e_i = z^2 + (x - x_i)^2$ and $h_i = (y - y_i)(x - x_i)$. For larger distances between field point and panel, the velocities are approximated by a multipole expansion consisting of a point source and a point quadrupole. For large distances the point source alone approximates the effect of the panel.

For real ship geometries, four corners on the hull often do not lie in one plane. The panel corners are then constructed to lie within one plane approximating the four points on the actual hull: the normal on the panel is determined from the cross-product of the two 'diagonal' vectors. The centre of the panel is determined by simple averaging of the coordinates of the four corners. This point and the normal define the plane of the panel. The four points on the hull are projected normally on this plane. The panels thus created do not form a closed body. As long as the gaps are small, the resulting errors are negligible compared to other sources of errors, e.g. the assumption of constant strength, constant pressure, constant normal over each panel, or enforcing the boundary condition only in one point of the panel. Hess and Smith (1964) comment on this issue:

'Nevertheless, the fact that these openings exist is sometimes disturbing to people hearing about the method for the first time. It should be kept in mind that the elements are simply devices for obtaining the surface source distribution and that the polyhedral body... has no direct physical significance, in the sense that the flow eventually calculated is not the flow about the polyhedral-type body. Even if the edges of the adjacent elements are coincident, the normal velocity is zero at only one point of each element. Over the remainder of the element there is flow through it. Also, the computed velocity is infinite on the edges of the elements, whether these are coincident or not.'

6.2.3 Jensen panel

Jensen (1988) developed a panel of the same order of accuracy, but much simpler to program, which avoids the evaluation of complicated transcendental functions and in its implementation relies largely on just a repeated evaluation of point source routines. As the original publication is little known and difficult to obtain internationally, the theory is repeated here. The approach requires, however, closed bodies. Then the velocities (and higher derivatives) can be

computed by simple numerical integration if the integrands are transformed analytically to remove singularities. In the formulae for this element, \vec{n} is the unit normal pointing outward from the body into the fluid, \oint the integral over S excluding the immediate neighbourhood of \vec{x}_q , and ∇ the Nabla operator with respect to \vec{x} .

1. Two-dimensional case

A Rankine source distribution on a closed body induces the following potential at a field point \vec{x} :

$$\phi(\vec{x}) = \int_S \sigma(\vec{x}_q) G(\vec{x}, \vec{x}_q) dS$$

S is the surface contour of the body, σ the source strength, $G(\vec{x}, \vec{x}_q) = (1/2\pi) \ln |\vec{x} - \vec{x}_q|$ is the Green function (potential) of a unit point source. Then the induced normal velocity component is:

$$v_n(\vec{x}) = \vec{n}(\vec{x}) \nabla \phi(\vec{x}) = \oint_S \sigma(\vec{x}_q) \vec{n}(\vec{x}) \nabla G(\vec{x}, \vec{x}_q) dS + \frac{1}{2} \sigma(\vec{x}_q)$$

Usually the normal velocity is given as boundary condition. Then the important part of the solution is the tangential velocity on the body:

$$v_t(\vec{x}) = \vec{t}(\vec{x}) \nabla \phi(\vec{x}) = \oint_S \sigma(\vec{x}_q) \vec{t}(\vec{x}) \nabla G(\vec{x}, \vec{x}_q) dS$$

Without further proof, the tangential velocity (circulation) induced by a distribution of point sources of the same strength at point \vec{x}_q vanishes:

$$\oint_{S(\vec{x})} \nabla G(\vec{x}, \vec{x}_q) \vec{t}(\vec{x}) dS = 0$$

Exchanging the designations \vec{x} and \vec{x}_q and using $\nabla G(\vec{x}, \vec{x}_q) = -\nabla G(\vec{x}_q, \vec{x})$, we obtain:

$$\oint_S \nabla G(\vec{x}, \vec{x}_q) \vec{t}(\vec{x}_q) dS = 0$$

We can multiply the integrand by $\sigma(\vec{x})$ – which is a constant as the integration variable is \vec{x}_q – and subtract this zero expression from our initial integral expression for the tangential velocity:

$$\begin{aligned} v_t(\vec{x}) &= \oint_S \sigma(\vec{x}_q) \vec{t}(\vec{x}) \nabla G(\vec{x}, \vec{x}_q) dS - \underbrace{\oint_S \sigma(\vec{x}) \nabla G(\vec{x}, \vec{x}_q) \vec{t}(\vec{x}_q) dS}_{=0} \\ &= \oint_S [\sigma(\vec{x}_q) \vec{t}(\vec{x}) - \sigma(\vec{x}) \vec{t}(\vec{x}_q)] \nabla G(\vec{x}, \vec{x}_q) dS \end{aligned}$$

For panels of constant source strength, the integrand in this formula tends to zero as $\vec{x} \rightarrow \vec{x}_q$, i.e. at the previously singular point of the integral. Therefore this expression for v_t can be evaluated numerically. Only the length ΔS of the contour panels and the first derivatives of the source potential for each \vec{x}, \vec{x}_q combination are required.

2. Three-dimensional case

The potential at a field point \vec{x} due to a source distribution on a closed body surface S is:

$$\phi(\vec{x}) = \int_S \sigma(\vec{x}_q) G(\vec{x}, \vec{x}_q) dS$$

σ the source strength, $G(\vec{x}, \vec{x}_q) = -(4\pi|\vec{x} - \vec{x}_q|)^{-1}$ is the Green function (potential) of a unit point source. Then the induced normal velocity component on the body is:

$$v_n(\vec{x}) = \vec{n}(\vec{x}) \nabla \phi(\vec{x}) = \oint_S \sigma(\vec{x}_q) \vec{n}(\vec{x}) \nabla G(\vec{x}, \vec{x}_q) dS + \frac{1}{2} \sigma(\vec{x}_q)$$

Usually the normal velocity is prescribed by the boundary condition. Then the important part of the solution is the velocity in the tangential directions \vec{t} and \vec{s} . \vec{t} can be chosen arbitrarily, \vec{s} forms a right-handed coordinate system with \vec{n} and \vec{t} . We will treat here only the velocity in the t direction, as the velocity in the s direction has the same form. The original, straightforward form is:

$$v_t(\vec{x}) = \vec{t}(\vec{x}) \nabla \phi(\vec{x}) = \oint_S \sigma(\vec{x}_q) \vec{t}(\vec{x}) \nabla G(\vec{x}, \vec{x}_q) dS$$

A source distribution of constant strength on the surface S of a sphere does not induce a tangential velocity on S :

$$\oint_S \vec{t}(\vec{x}) \nabla G(\vec{x}, \vec{k}) dS = 0$$

for \vec{x} and \vec{k} on S . The sphere is placed touching the body tangentially at the point \vec{x} . The centre of the sphere must lie within the body. (The radius of the sphere has little influence on the results within wide limits. A rather large radius is recommended.) Then every point \vec{x}_q on the body surface can be projected to a point \vec{k} on the sphere surface by passing a straight line through \vec{k} , \vec{x}_q , and the sphere's centre. This projection is denoted by $\vec{k} = P(\vec{x}_q)$. dS on the body is projected on dS on the sphere. \mathcal{R} denotes the relative size of these areas: $dS = \mathcal{R} dS$. Let R be the radius of the sphere and \vec{c} be its centre. Then the projection of \vec{x}_q is:

$$P(\vec{x}_q) = \frac{\vec{x}_q - \vec{c}}{|\vec{x}_q - \vec{c}|} \mathcal{R} + \vec{c}$$

The area ratio \mathcal{R} is given by:

$$\mathcal{R} = \frac{\vec{n} \cdot (\vec{x}_q - \vec{c})}{|\vec{x}_q - \vec{c}|} \left(\frac{\mathcal{R}}{|\vec{x}_q - \vec{c}|} \right)^2$$

With these definitions, the contribution of the sphere ('fancy zero') can be transformed into an integral over the body surface:

$$\oint_S \vec{t}(\vec{x}) \nabla G(\vec{x}, P(\vec{x}_q)) \mathcal{R} dS = 0$$

We can multiply the integrand by $\sigma(\vec{x})$ – which is a constant as the integration variable is \vec{x}_q – and subtract this zero expression from our original expression for the tangential velocity:

$$\begin{aligned} v_t(\vec{x}) &= \oint_S \sigma(\vec{x}_q) \vec{l}(\vec{x}) \nabla G(\vec{x}, \vec{x}_q) \, dS - \underbrace{\oint_S \sigma(\vec{x}) \vec{l}(\vec{x}) \nabla G(\vec{x}, P(\vec{x}_q)) \mathcal{R} \, dS}_{=0} \\ &= \oint_S [\sigma(\vec{x}_q) \vec{l}(\vec{x}) \nabla G(\vec{x}, \vec{x}_q) - \sigma(\vec{x}) \vec{l}(\vec{x}) \nabla G(\vec{x}, P(\vec{x}_q)) \mathcal{R}] \, dS \end{aligned}$$

For panels of constant source strength, the integrand in this expression tends to zero as $\vec{x} \rightarrow \vec{x}_q$, i.e. at the previously singular point of the integral. Therefore this expression for v_i can be evaluated numerically.

6.2.4 Higher-order panel

The panels considered so far are ‘first-order’ panels, i.e. halving the grid spacing will halve the error in approximating a flow (for sufficiently fine grids). Higher-order panels (these are invariably second-order panels) will quadratically decrease the error for grid refinement. Second-order panels need to be at least quadratic in shape and linear in source distribution. They give much better results for simple geometries which can be described easily by analytical terms, e.g. spheres or Wigley parabolic hulls. For real ship geometries, first-order panels are usually sufficient and may even be more accurate for the same effort, as higher-order panels require more care in grid generation and are prone to ‘overshoot’ in regions of high curvature as in the aftbody. For some applications, however, second derivatives of the potential are needed on the hull and these are evaluated simply by second-order panels, but not by first-order panels.

1. Two-dimensional case

We want to compute derivatives of the potential at a point (x, y) induced by a given curved portion of the boundary. It is convenient to describe the problem in a local coordinate system (Fig. 6.4). The x - or ξ -axis is tangent to the curve and the perpendicular projections on the x -axis of the ends of the curve lie equal distances d to the right and the left of the origin. The y - or η -axis is normal to the curve. The arc length along the curve is denoted by s , and a general point on the curve is (ξ, η) . The distance between (x, y)

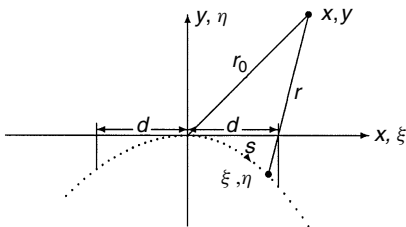


Figure 6.4 Coordinate system for higher-order panel (two dimensional)

and (ξ, η) is:

$$r = \sqrt{(x - \xi)^2 + (y - \eta)^2}$$

The velocity induced at (x, y) by a source density distribution $\sigma(s)$ along the boundary curve is:

$$\nabla\phi = \frac{1}{2\pi} \int_{-d}^d \left\{ \begin{matrix} x - \xi \\ y - \eta \end{matrix} \right\} \frac{\sigma(s) ds}{r^2} d\xi$$

The boundary curve is defined by $\eta = \eta(\xi)$. In the neighbourhood of the origin, the curve has a power series:

$$\eta = c\xi^2 + d\xi^3 + \dots$$

There is no term proportional to ξ , because the coordinate system lies tangentially to the panel. Similarly the source density has a power series:

$$\sigma(s) = \sigma^{(0)} + \sigma^{(1)}s + \sigma^{(2)}s^2 + \dots$$

Then the integrand in the above expression for $\nabla\phi$ can be expressed as a function of ξ and then expanded in powers of ξ . The resulting integrals can be integrated to give an expansion for $\nabla\phi$ in powers of d . However, the resulting expansion will not converge if the distance of the point (x, y) from the origin is less than d . Therefore, a modified expansion is used for the distance r :

$$r^2 = [(x - \xi)^2 + y^2] - 2y\eta + \eta^2 = r_f^2 - 2y\eta + \eta^2$$

$r_f = \sqrt{(x - \xi)^2 + y^2}$ is the distance (x, y) from a point on the flat element. Only the latter terms in this expression for r^2 are expanded:

$$r^2 = r_f^2 - 2yc\xi^2 + O(\xi^3)$$

Powers $O(\xi^3)$ and higher will be neglected from now on.

$$\frac{1}{r^2} = \frac{1}{r_f^2 - 2yc\xi^2} \cdot \frac{r_f^2 + 2yc\xi^2}{r_f^2 + 2yc\xi^2} = \frac{1}{r_f^2} + \frac{2yc\xi^2}{r_f^4}$$

$$\frac{1}{r^4} = \frac{1}{r_f^4} + \frac{4yc\xi^2}{r_f^6}$$

The remaining parts of the expansion are straightforward:

$$\begin{aligned} s &= \int_0^\xi \sqrt{1 + \left(\frac{d\eta}{d\xi}\right)^2} d\xi = \int_0^\xi \sqrt{1 + (2c\xi)^2} d\xi \\ &\approx \int_0^\xi 1 + 2c^2\xi^2 d\xi = \xi + \frac{2}{3}c^2\xi^3 \end{aligned}$$

Combine this expression for s with the power series for $\sigma(s)$:

$$\sigma(s) = \sigma^{(0)} + \sigma^{(1)}\xi + \sigma^{(2)}\xi^2$$

Combine the expression of s with the above expression for $1/r^2$:

$$\frac{1}{r^2} \frac{ds}{d\xi} = \left(\frac{1}{r_f^2} + \frac{2cy\xi^2}{r_f^4} \right) (1 + 2c^2\xi^2) = \left(\frac{1}{r_f^2} + \frac{2cy\xi^2}{r_f^4} + \frac{2c^2\xi^2}{r_f^2} \right)$$

Now the integrands in the expression for $\nabla\phi$ can be evaluated.

$$\begin{aligned} \phi_x &= \frac{1}{2\pi} \int_{-d}^d \sigma \frac{(x-\xi)}{r^2} \frac{ds}{d\xi} d\xi \\ &= \frac{1}{2\pi} \int_{-d}^d (\sigma^{(0)} + \sigma^{(1)}\xi + \sigma^{(2)}\xi^2)(x-\xi) \left(\frac{1}{r_f^2} + \frac{2cy\xi^2}{r_f^4} + \frac{2c^2\xi^2}{r_f^2} \right) d\xi \\ &= \frac{1}{4\pi} [\phi_x^{(0)}\sigma^{(0)} + \phi_x^{(1)}\sigma^{(1)} + c\phi_x^{(c)}\sigma^{(0)} + \phi_x^{(2)}(\sigma^{(2)} + 2c^2\sigma^{(0)})] \\ \phi_x^{(0)} &= \int_{-d}^d \frac{2(x-\xi)}{r_f^2} d\xi = \int_{x-d}^{x+d} \frac{2t}{t^2+y^2} dt = [\ln(t^2+y^2)]_{x-d}^{x+d} = \ln(r_1^2/r_2^2) \end{aligned}$$

$$\text{with } r_1 = \sqrt{(x+d)^2+y^2} \quad \text{and} \quad r_2 = \sqrt{(x-d)^2+y^2}$$

$$\begin{aligned} \phi_x^{(1)} &= \int_{-d}^d \frac{2\xi(x-\xi)}{r_f^2} d\xi = 2 \int_{x-d}^{x+d} \frac{t(x-t)}{t^2+y^2} dt = x\phi_x^{(0)} + y\phi_y^{(0)} - 4d \\ \phi_x^{(c)} &= \int_{-d}^d \frac{4(x-\xi)y\xi^2}{r_f^4} d\xi = 4y \int_{x-d}^{x+d} \frac{t(t-x)^2}{(t^2+y^2)^2} dt - 2\phi_y^{(1)} + \frac{(2d)^3xy}{r_1^2r_2^2} \\ \phi_x^{(2)} &= \int_{-d}^d \frac{2(x-\xi)\xi^2}{r_f^2} d\xi = 2 \int_{x-d}^{x+d} \frac{t(t-x)^2}{t^2+y^2} dt = x\phi_x^{(1)} + y\phi_y^{(1)} \end{aligned}$$

Here the integrals were transformed with the substitution $t = (x - \xi)$.

$$\begin{aligned} \phi_y &= \frac{1}{2\pi} \int_{-d}^d \sigma \frac{(y-\eta)}{r^2} \frac{ds}{d\xi} d\xi \\ &= \frac{1}{2\pi} \int_{-d}^d (\sigma^{(0)} + \sigma^{(1)}\xi + \sigma^{(2)}\xi^2)(y - c\xi^2) \\ &\quad \times \left(\frac{1}{r_f^2} + \frac{2cy\xi^2}{r_f^4} + \frac{2c^2\xi^2}{r_f^2} \right) d\xi \\ &= \frac{1}{4\pi} [\phi_y^{(0)}\sigma^{(0)} + \phi_y^{(1)}\sigma^{(1)} + c\phi_y^{(c)}\sigma^{(0)} + \phi_y^{(2)}(\sigma^{(2)} + 2c^2\sigma^{(0)})] \\ \phi_y^{(0)} &= \int_{-d}^d \frac{2y}{r_f^2} d\xi = 2 \int_{x-d}^{x+d} \frac{y}{t^2+y^2} dt \\ &= 2 \left[\arctan \frac{t}{y} \right]_{x-d}^{x+d} = 2 \arctan \frac{2dy}{x^2+y^2-d^2} \end{aligned}$$

$$\begin{aligned}
\phi_y^{(1)} &= \int_{-d}^d \frac{2\xi y}{r_f^2} d\xi = 2y \int_{x-d}^{x+d} \frac{(x-t)}{t^2 + y^2} dt = x\phi_y^{(0)} - y\phi_x^{(0)} \\
\phi_y^{(c)} &= \int_{-d}^d 4y^2 \frac{\xi^2}{r_f^4} - \frac{2\xi^2}{r_f^2} d\xi \\
&= 4y^2 \int_{x-d}^{x+d} \frac{(t-x)^2}{(t^2 + y^2)^2} dt - 2 \int_{x-d}^{x+d} \frac{(t-x)^2}{t^2 + y^2} dt \\
&= 2\phi_x^{(1)} - 4d^3 \frac{x^2 - y^2 - d^2}{r_1^2 r_2^2} \\
\phi_y^{(2)} &= \int_{-d}^d \frac{2y\xi^2}{r_f^2} d\xi = 2y \int_{x-d}^{x+d} \frac{(t-x)^2}{t^2 + y^2} dt = x\phi_y^{(1)} - y\phi_x^{(1)}
\end{aligned}$$

The original formulae for the first derivatives of these higher-order panels were analytically equivalent, but less suited for programming involving more arithmetic operations than the formulae given here. Higher derivatives of the potential are, e.g., given in Bertram (1999).

2. Three-dimensional case

The higher-order panels are parabolic in shape with a bi-linear source distribution on each panel. The original procedure of Hess was modified by Hughes and Bertram (1995) to include also higher derivatives of the potential. The complete description of the formulae used to determine the velocity induced by the higher-order panels would be rather lengthy. So only the general procedure is described here. The surface of the ship is divided into panels as in a first-order panel method. However, the surface of each panel is approximated by a parabolic surface, as opposed to a flat surface. The geometry of a panel in the local panel coordinate system is described as:

$$\zeta = C + A\xi + B\eta + P\xi^2 + 2Q\xi\eta + R\eta^2$$

The ξ -axis and η -axis lie in the plane tangent to the panel at the panel control point, and the ζ -axis is normal to this plane. This equation can be written in the form:

$$\zeta - \zeta_o = P(\xi - \xi_o)^2 + 2Q(\xi - \xi_o)(\eta - \eta_o) + R(\eta - \eta_o)^2$$

The point (ξ_o, η_o, ζ_o) is used as a collocation point and origin of the local panel coordinate system. In the local panel coordinate system, terms depending on A , B , and C do not appear in the formulae for the velocity induced by a source distribution on the panel. R and P represents the local curvatures of the ship in the two coordinate directions, Q the local 'twist' in the ship form.

The required input consists of the coordinates of panel corner points lying on the body surface and information concerning how the corner points are connected to form the panels. In our implementation, each panel is allowed to have either three or four sides. The first and third sides of the panel should be (nearly) parallel. Otherwise, the accuracy of the panels deteriorates. For a given panel, the information available to determine the coefficients $A \dots R$ consists of the three or four panel corner points of the panel and the corner

points of the panels which border the panel in question. For a quadrilateral panel with neighbouring panels on all sides, eight 'extra' vertex points are provided by the corner points of the adjacent panels (Fig. 6.5). For triangular panels and panels lying on the edges of the body, fewer extra vertex points will be available. The panel corner points will be listed as $x_i, y_i, z_i, i = 1 \dots 4$, and the extra vertex points as $\tilde{x}_j, \tilde{y}_j, \tilde{z}_j, j = 1 \dots N_v$, where N_v is the number of extra vertex points ($3 < N_v < 8$). For triangular panels four corner points are also specified, but either the first and second or the third and fourth corner points are identical (i.e. the first or third side of the panel has zero length). The curved panel is required to pass exactly through all of its corner points and to pass as closely as possible to the extra vertex points of the neighbouring panels. The order in which the corner points are specified is important, in that this determines whether the normal vector points into the fluid domain or into the body. In our method, the corner points should be ordered clockwise when viewed from the fluid domain, so that the normal vector points into the fluid domain.

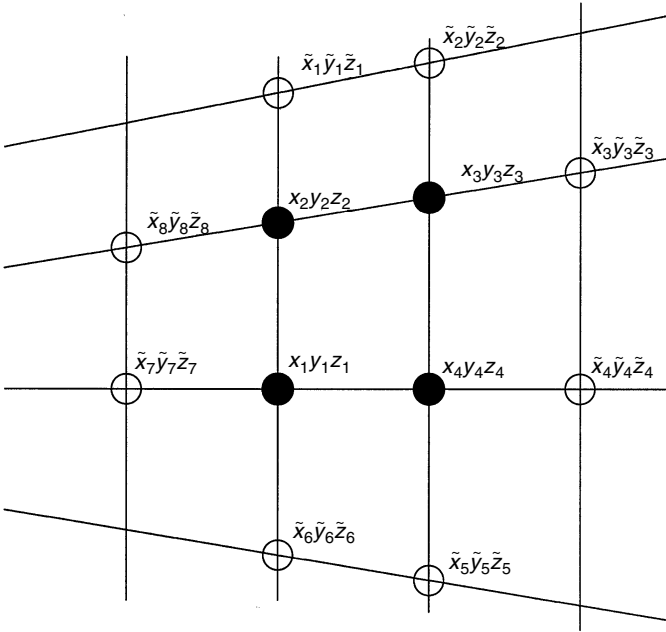


Figure 6.5 Additional points used for computing the local surface curvature of a panel (seen from the fluid domain)

The source strength on each panel is represented by a bi-linear distribution, as opposed to a constant distribution as in a first-order method:

$$\sigma(\xi, \eta) = \sigma_0 + \sigma_x(\xi - \xi_o) + \sigma_y(\eta - \eta_o)$$

σ_x and σ_y are the slopes of the source strength distribution in the ξ and η directions respectively. In the system of linear equations set up in this method, only the value of the source strength density at the collocation point on each panel, the σ_0 term, is solved for directly. The derivatives of

the source density (σ_x and σ_y terms) are expressed in terms of the source strength density at the panel collocation point and at the collocation points of panels bordering the panel in question. First the collocation points of the adjacent panels are transformed into the local coordinate system of the panel in question. Then the above equation for the source strength is fitted in a least squares sense to the values of source density at the collocation points of the adjacent panels to determine σ_0 , σ_x , and σ_y . For a four-sided panel which does not lie on a boundary of the body, four adjacent panel collocation points will be available for performing the least squares fit, (Fig. 6.6). In

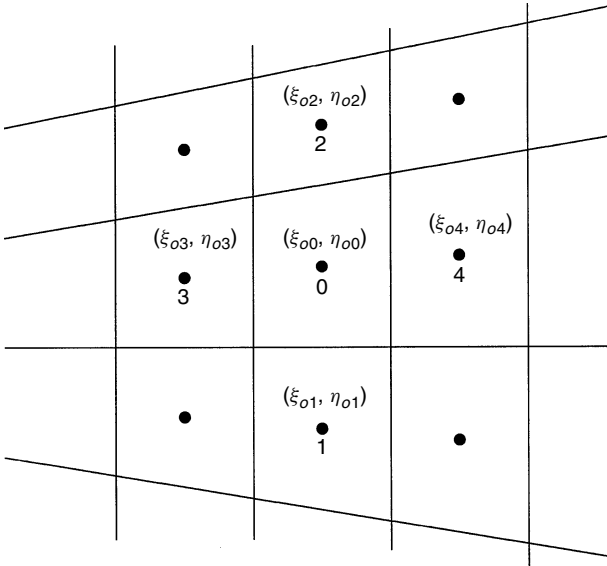


Figure 6.6 Adjacent panels used in the least-squares fit for the source density derivatives

other cases only three or possibly two adjacent panels will be available. The procedure expresses the unknown source strength derivatives in terms of the source density at the collocation point of the adjacent panels. If the higher-order terms are set to zero, the element reduces to the regular first-order panel. A corresponding option is programmed in our version of the panel.

6.3 Vortex elements

Vortex elements are useful to model lifting flows, e.g. in the lifting-line method for propellers and foils, see section 2.3, Chapter 2.

1. Two-dimensional case

Consider a vortex of strength Γ at x_w, z_w and a field point x, z . Denote $\Delta x = x - x_w$ and $\Delta z = z - z_w$. The distance between the two points is $r = \sqrt{\Delta x^2 + \Delta z^2}$. The potential and velocities induced by this vortex are:

$$\phi = -\frac{\Gamma}{2\pi} \arctan \frac{z - z_w}{x - x_w}$$

$$\phi_x = \frac{\Gamma}{2\pi} \frac{\Delta z}{r^2}$$

$$\phi_z = -\frac{\Gamma}{2\pi} \frac{\Delta x}{r^2}$$

The absolute value of the velocity is then $(\Gamma/2\pi)1/r$, i.e. the same for each point on a concentric ring around the centre x_w, z_w . The velocity decays with distance to the centre. So far, the vortex has the same features as the source. The difference is the direction of the velocity. The vortex induces velocities that are always tangential to the concentric ring (Fig. 6.7), while the source produced radial velocities. The formulation given here produces counter-clockwise velocities for positive Γ .

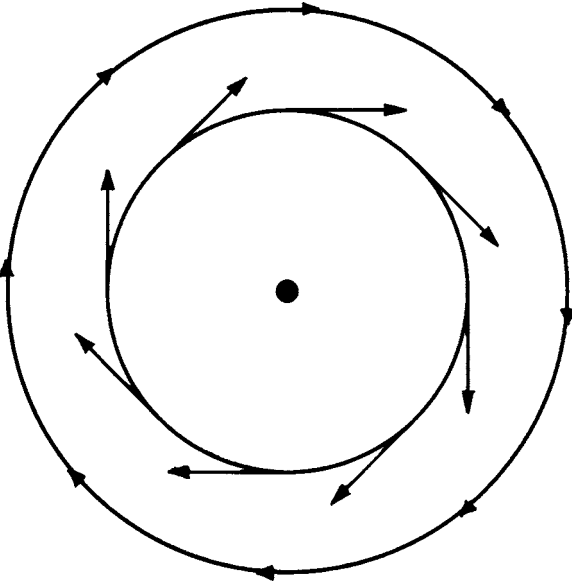


Figure 6.7 Velocities induced by vortex

The strength of the vortex is the ‘circulation’. In general, the circulation is defined as the integral of the tangential velocities about any closed curve. For the definition given above, this integral about any concentric ring will indeed yield Γ as a result.

This point vortex of strength Γ leads to similar expressions for velocities and higher derivatives as a point source of strength σ . One can thus express one by the other as follows:

$$\frac{2\pi}{\Gamma} \Phi_x = \frac{2\pi}{\sigma} \phi_z$$

$$\frac{2\pi}{\Gamma} \Phi_z = -\frac{2\pi}{\sigma} \phi_x$$

$$\frac{2\pi}{\Gamma} \Phi_{xx} = \frac{2\pi}{\sigma} \phi_{xz}$$

$$\frac{2\pi}{\Gamma} \Phi_{xz} = -\frac{2\pi}{\sigma} \phi_{xx}$$

$$\frac{2\pi}{\Gamma} \Phi_{xxz} = \frac{2\pi}{\sigma} \phi_{xzz}$$

$$\frac{2\pi}{\Gamma} \Phi_{xzz} = -\frac{2\pi}{\sigma} \phi_{xxz}$$

Φ is the potential of the vortex, ϕ the potential of the source. The same relations hold for converting between vortex panels and source panels of constant strength. It is thus usually not necessary to program vortex elements separately. One can rather call the source subroutines with a suitable rearrangement of the output parameters in the call of the subroutine.

A vortex panel of constant strength – i.e. all panels have the same strength – distributed on the body coinciding geometrically with the source panels (of individual strength), enforces automatically a Kutta condition, e.g. for a hydrofoil.

2. Three-dimensional case

The most commonly used three-dimensional vortex element is the horseshoe vortex. A three-dimensional vortex of strength Γ , lying on a closed curve C , induces a velocity field:

$$\vec{v} = \nabla\phi = \frac{\Gamma}{4\pi} \int_C \frac{d\vec{s} \times \vec{D}}{D^3}$$

We use the special case that a horseshoe vortex lies in the plane $y = y_w = \text{const.}$, from $x = -\infty$ to $x = x_w$. Arbitrary cases may be derived from this case using a coordinate transformation. The vertical part of the horseshoe vortex runs from $z = z_1$ to $z = z_2$, (Fig. 6.8). Consider a field point (x, y, z) . Then: $\Delta x = x - x_w$, $\Delta y = y - y_w$, $\Delta z_1 = z - z_1$, $\Delta z_2 = z - z_2$, $t_1 = \sqrt{\Delta x^2 + \Delta y^2 + \Delta z_1^2}$ and $t_2 = \sqrt{\Delta x^2 + \Delta y^2 + \Delta z_2^2}$.

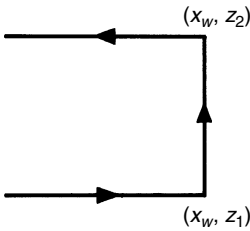


Figure 6.8 Horseshoe vortex

The horseshoe vortex then induces the following velocity:

$$\begin{aligned} \vec{v} = & \frac{\Gamma}{4\pi} \left[\left(\frac{\Delta z_1}{t_1} - \frac{\Delta z_2}{t_2} \right) \frac{1}{\Delta x^2 + \Delta y^2} \begin{Bmatrix} -\Delta y \\ \Delta x \\ 0 \end{Bmatrix} + \left(1 - \frac{\Delta x}{t_1} \right) \right. \\ & \times \frac{1}{\Delta y^2 + \Delta z_1^2} \begin{Bmatrix} 0 \\ -\Delta z_1 \\ \Delta y \end{Bmatrix} i - \left(1 - \frac{\Delta x}{t_2} \right) \frac{1}{\Delta y^2 + \Delta z_2^2} \begin{Bmatrix} 0 \\ s\Delta z_2 \\ \Delta y \end{Bmatrix} \left. \right] \end{aligned}$$

The derivation used $\int (t^2 + a^2)^{-3/2} dt = t/(a^2\sqrt{t^2 + a^2})$. For $\Delta x^2 + \Delta y^2 \ll |\Delta z_1||\Delta z_2|$ or $\Delta y^2 + \Delta z_1^2 \ll \Delta x^2$ special formulae are used. Bertram (1992) gives details and expressions for higher derivatives.

6.4 Dipole elements

6.4.1 Point dipole

The dipole (or doublet) is the limit of a source and sink of equal strength brought together along some direction (usually x) keeping the product of distance and source strength constant. The result is formally the same as differentiating the source potential in the required direction. The strength of a dipole is usually denoted by m . Again, r denotes the distance between field point \vec{x} and the dipole at \vec{x}_d . We consider a dipole in the x direction here. We define $\Delta \vec{x} = \vec{x} - \vec{x}_d$.

1. Two-dimensional case

The potential and derivatives for a dipole in the x direction are:

$$\begin{aligned}\phi &= \frac{m}{2\pi r^2} \Delta x \\ \phi_x &= \frac{m}{2\pi r^2} - 2\phi \frac{\Delta x}{r^2} \\ \phi_z &= -2\phi \frac{\Delta z}{r^2} \\ \phi_{xx} &= \left(-6 + 8 \frac{\Delta x^2}{r^2} \right) \cdot \frac{\phi}{r^2} \\ \phi_{xz} &= -2 \frac{\Delta z \cdot \phi_x + \Delta x \cdot \phi_z}{r^2}\end{aligned}$$

The streamlines created by this dipole are circles, (Fig. 6.9).

2. Three-dimensional case

The three-dimensional point dipole in the x direction is correspondingly given by:

$$\begin{aligned}\phi &= -\frac{m}{4\pi r^3} \Delta x \\ \phi_x &= -\frac{m}{4\pi r^3} - 3\phi \frac{\Delta x}{r^2} \\ \phi_y &= -3\phi \frac{\Delta y}{r^2} \\ \phi_z &= -3\phi \frac{\Delta z}{r^2}\end{aligned}$$

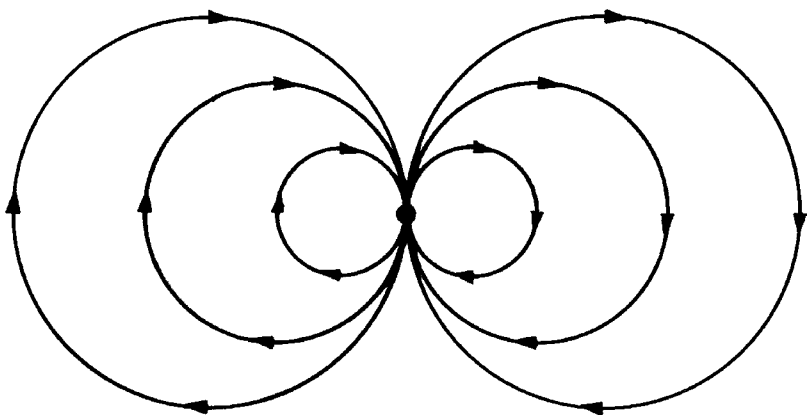


Figure 6.9 Velocities induced by point dipole

$$\begin{aligned}\phi_{xx} &= \frac{-5\phi_x \Delta x - 4\phi}{r^2} \\ \phi_{xy} &= \frac{-5\phi_x \Delta y + 2\Delta y \cdot (-m/4\pi r^3)}{r^2} \\ \phi_{xz} &= \frac{-5\phi_x \Delta z + 2\Delta z \cdot (-m/4\pi r^3)}{r^2} \\ \phi_{yy} &= \frac{-5\phi_y \Delta y - 3\phi}{r^2} \\ \phi_{yz} &= \frac{-5\phi_z \Delta y}{r^2} \\ \phi_{zx} &= \frac{-5\phi_x \Delta x - 4\phi}{r^2}\end{aligned}$$

The expressions for the dipole can be derived formally by differentiation of the corresponding source expression in x . Therefore usually source subroutines (also for distributed panels) are used with a corresponding redefinition of variables in the parameter list of the call. This avoids double programming. Dipoles like vortices can be used (rather equivalently) to generate lift in flows.

6.4.2 Thiart element

The ship including the rudder can be considered as a vertical foil of considerable thickness and extremely short span. For a steady yaw angle, i.e. a typical manoeuvring application, one would certainly enforce a Kutta condition at the trailing edge, either employing vortex or dipole elements. For harmonic motions in waves, i.e. a typical seakeeping problem, one should

similarly employ a Kutta condition, but this is often omitted. If a Kutta condition is employed in frequency-domain computations, the wake will oscillate harmonically in strength. This can be modelled by discrete dipole elements of constant strength, but for high frequencies this approach requires many elements. The use of special elements which consider the oscillating strength analytically is more efficient and accurate, but also more complicated. Such a 'Thiart element' has been developed by Professor Gerhard Thiart of Stellenbosch University and is described in detail in Bertram (1998b), and Bertram and Thiart (1998). The oscillating ship creates a vorticity. The problem is similar to that of an oscillating airfoil. The circulation is assumed constant within the ship. Behind the ship, vorticity is shed downstream with ship speed V . Then:

$$\left(\frac{\partial}{\partial t} - V \frac{\partial}{\partial x} \right) \gamma(x, z, t) = 0$$

γ is the vortex density, i.e. the strength distribution for a continuous vortex sheet. The following distribution fulfils the above condition:

$$\gamma(x, z, t) = \text{Re}(\hat{\gamma}_a(z) \cdot e^{i(\omega_e/V)(x-x_a)} \cdot e^{i\omega_e t}) \quad \text{for } x \leq x_a$$

Here $\hat{\gamma}_a$ is the vorticity density at the trailing edge x_a (stern of the ship). We continue the vortex sheet inside the ship at the symmetry plane $y = 0$, assuming a constant vorticity density:

$$\gamma(x, z, t) = \text{Re}(\hat{\gamma}_a(z) \cdot e^{i\omega_e t}) \quad \text{for } x_a \leq x \leq x_f$$

x_f is the leading edge (forward stem of the ship). This vorticity density is spatially constant within the ship.

A vortex distribution is equivalent to a dipole distribution if the vortex density γ and the dipole density m are coupled by:

$$\gamma = \frac{dm}{dx}$$

The potential of an equivalent semi-infinite strip of dipoles is then obtained by integration. This potential is given (except for a so far arbitrary 'strength' constant) by:

$$\Phi(x, y, z) = \text{Re} \left(\int_{-\infty}^{x_f} \int_{z_u}^{z_o} \hat{m}(\xi) \frac{y}{r^3} d\xi d\zeta e^{i\omega_e t} \right) = \text{Re}(\varphi(x, y, z) \cdot e^{i\omega_e t})$$

with $r = \sqrt{(x - \xi)^2 + y^2 + (z - \zeta)^2}$ and:

$$\hat{m}(\xi) = \begin{cases} x_f - \xi & \text{for } x_a \leq \xi \leq x_f \\ \frac{V}{i\omega_e} (1 - e^{i(\omega_e/V)(\xi-x_a)}) + (x_f - x_a) & \text{for } -\infty \leq \xi \leq x_a \end{cases}$$

It is convenient to write φ as:

$$\begin{aligned}\varphi(x, y, z) = & y \int_{z_u}^{z_o} \int_{x_a}^{x_f} \frac{x - \xi}{r^3} d\xi d\zeta + (x_f - x) \int_{z_u}^{z_o} \int_{x_a}^{x_f} \frac{y}{r^3} d\xi d\zeta \\ & + \left(\frac{V}{i\omega_e} + (x_f - x_a) \right) \int_{z_u}^{z_o} \int_{-\infty}^{x_a} \frac{y}{r^3} d\xi d\zeta \\ & - \left(\frac{V}{i\omega_e} e^{-i\omega_e x_a/V} \right) y \int_{z_u}^{z_o} \int_{-\infty}^{x_a} e^{i\omega_e \xi/V} \frac{1}{r^3} d\xi d\zeta\end{aligned}$$

The velocity components and higher derivatives are then derived by differentiation of Φ , which can be reduced to differentiation of φ . The exact formulae are given in Bertram (1998b), and Bertram and Thiaert (1998). The expressions involve integrals with integrands of the form ‘arbitrary smooth function’ · ‘harmonically oscillating function’. These are accurately and efficiently evaluated using a modified Simpson’s method developed by Söding:

$$\begin{aligned}\int_{x_1}^{x_1+2h} f(x) e^{ikx} dx = & \frac{e^{ikx_1}}{k} \left[e^{2ikh} \left(\frac{0.5f_1 - 2f_2 + 1.5f_3}{kh} - i \left(f_3 - \frac{\Delta^2 f}{k^2 h^2} \right) \right) \right. \\ & \left. + \frac{1.5f_1 - 2f_2 + 0.5f_3}{kh} + i \left(f_1 - \frac{\Delta^2 f}{h^2 k^2} \right) \right]\end{aligned}$$

where $f_1 = f(x_1)$, $f_2 = f(x_1 + h)$, $f_3 = f(x_1 + 2h)$, $\Delta^2 f = f_1 - 2f_2 + f_3$.

6.5 Special techniques

6.5.1 Desingularization

The potential and its derivatives become singular directly on a panel, i.e. infinite terms appear in the usual formulae which prevent straightforward evaluation. For the normal velocity, this singularity can be removed analytically for the collocation point on the panel itself, but the resulting special treatment makes parallelization of codes difficult. When the element is placed somewhat outside the domain of the problem, (Fig. 6.10), it is ‘desingularized’, i.e. the singularity is removed. This has several advantages:

- In principle the same expression can be evaluated everywhere. This facilitates parallel algorithms in numerical evaluation and makes the code generally shorter and easier.
- Numerical experiments show that desingularization improves the accuracy as long as the depth of submergence is not too large.

The last point surprised some mathematicians. Desingularization results in a Fredholm integral equation of the first kind. (Otherwise a Fredholm equation

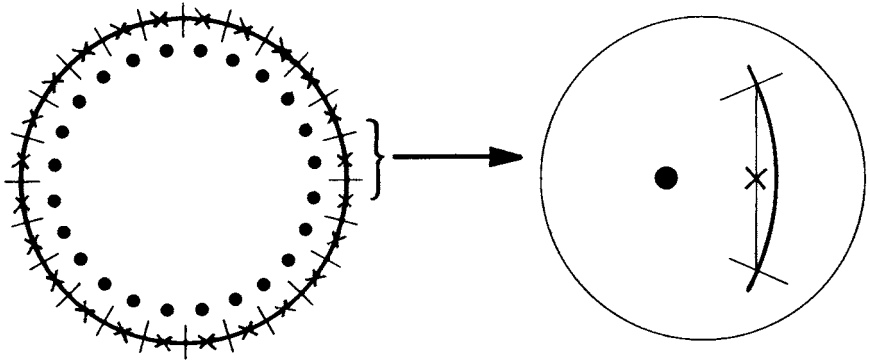


Figure 6.10 Desingularization

of second kind results.) This can lead in principle to problems with uniqueness and existence of solutions, which in practice manifest themselves first by an ill-conditioned matrix for the unknowns (source strengths or directly potential). For engineers, the problems are directly apparent without going into mathematical classification:

- If the individual elements (sources) are too far from the collocation points, they will all have almost the same influence. Then they will not be able to represent arbitrary local flow patterns.
- If the individual elements are somewhat removed, the individual sharp local steepness in flow pattern (singularity) will smooth out rapidly forming a relatively smooth flow distribution which can relatively smoothly approximate arbitrary flows.
- If the individual elements are very close, an uneven cobblestone flow distribution results due to the discontinuity between the individual elements.

Thus the desingularization distance has to be chosen appropriately within a bandwidth to yield acceptable results. The distance should be related to the grid size. As the grid becomes finer, the desingularized solution approaches the conventional singular-element solution. Fortunately, several researchers have shown that the results are relatively insensitive to the desingularization distance, as long as this ranges between 0.5 and 2 typical grid spacings.

The historical development of desingularization of boundary element methods is reviewed in Cao *et al.* (1991), and Raven (1998).

Desingularization is used in many ‘fully non-linear’ wave resistance codes in practice for the free-surface elements. Sometimes it is also used for the hull elements, but here narrow pointed bows introduce difficulties requiring often special effort in grid generation. Some close-fit routines for two-dimensional seakeeping codes (strip-method modules) also employ desingularization.

6.5.2 Patch method

Traditional boundary element methods enforce the kinematic condition (no-penetration condition) on the hull exactly at one collocation point per panel,

usually the panel centre. The resistance predicted by these methods is for usual discretizations insufficient for practical requirements, at least if conventional pressure integration on the hull is used. Söding (1993b) proposed therefore a variation of the traditional approach which differs in some details from the conventional approach. Since his approach uses also flat segments on the hull, but not as distributed singularities, he called the approach 'patch' method to distinguish it from the usual 'panel' methods.

For double-body flows the resistance in an ideal fluid should be zero. This allows the comparison of the accuracy of various methods and discretizations as the non-zero numerical resistance is then purely due to discretization errors. For double-body flows, the patch method reduces the error in the resistance by one order of magnitude compared to ordinary first-order panel methods, without increasing the computational time or the effort in grid generation. However, higher derivatives of the potential or the pressure directly on the hull cannot be computed as easily as for a regular panel method.

The patch method introduces basically three changes to ordinary panel methods:

- 'patch condition'
Panel methods enforce the no-penetration condition on the hull exactly at one collocation point per panel. The 'patch condition' states that the integral of this condition over one patch of the surface is zero. This averaging of the condition corresponds to the techniques used in finite element methods.
- pressure integration
Potentials and velocities are calculated at the patch corners. Numerical differentiation of the potential yields an average velocity. A quadratic approximation for the velocity using the average velocity and the corner velocities is used in pressure integration. The unit normal is still considered constant.
- desingularization
Single point sources are submerged to give a smoother distribution of the potential on the hull. As desingularization distance between patch centre and point source, the minimum of (10% of the patch length, 50% of the normal distance from patch centre to a line of symmetry) is recommended.

Söding (1993) did not investigate the individual influence of each factor, but the higher-order pressure integration and the patch condition contribute approximately the same.

The patch condition states that the flow through a surface element (patch) (and not just at its centre) is zero. Desingularized Rankine point sources instead of panels are used as elementary solutions. The potential of the total flow is:

$$\phi = -Vx + \sum_i \sigma_i \varphi_i$$

σ is the source strength, φ is the potential of a Rankine point source. r is the distance between source and field point. Let M_i be the outflow through a patch (outflow = flow from interior of the body into the fluid) induced by a point source of unit strength.

1. *Two-dimensional case*

The potential of a two-dimensional point source is:

$$\varphi = \frac{1}{4\pi} \ln r^2$$

The integral zero-flow condition for a patch is:

$$-V \cdot n_x \cdot l + \sum_i \sigma_i M_i = 0$$

n_x is the x component of the unit normal (from the body into the fluid), l the patch area (length). The flow through a patch is invariant of the coordinate system. Consider a local coordinate system x, z , (Fig. 6.11). The patch extends in this coordinate system from $-s$ to s . The flow through the patch is:

$$M = - \int_{-s}^s \phi_z dx$$

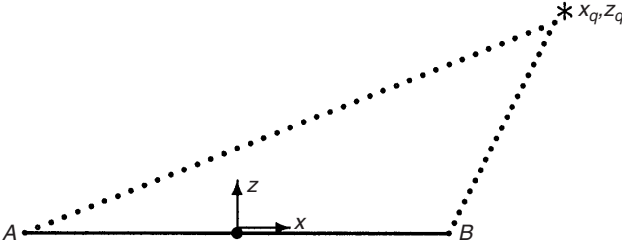


Figure 6.11 Patch in 2d

A Rankine point source of unit strength induces at x, z the vertical velocity:

$$\phi_z = \frac{1}{2\pi} \frac{z - z_q}{(x - x_q)^2 + (z - z_q)^2}$$

Since $z = 0$ on the patch, this yields:

$$M = \int_{-s}^s \frac{1}{2\pi} \frac{z_q}{(x - x_q)^2 + z_q^2} dx = \frac{1}{2\pi} \arctan \frac{l z_q}{x_q^2 + z_q^2 - s^2}$$

The local z_q transforms from the global coordinates:

$$z_q = -n_x \cdot (\bar{x}_q - \bar{x}_c) - n_z \cdot (\bar{z}_q - \bar{z}_c)$$

\bar{x}_c, \bar{z}_c are the global coordinates of the patch centre, \bar{x}_q, \bar{z}_q of the source.

From the value of the potential ϕ at the corners A and B , the average velocity within the patch is found as:

$$\bar{v} = \frac{\phi_B - \phi_A}{|\vec{x}_B - \vec{x}_A|} \cdot \frac{\vec{x}_B - \vec{x}_A}{|\vec{x}_B - \vec{x}_A|}$$

i.e. the absolute value of the velocity is:

$$\frac{\Delta\phi}{\Delta s} = \frac{\phi_B - \phi_A}{|\vec{x}_B - \vec{x}_A|}$$

The direction is tangential to the body, the unit tangential is $(\vec{x}_B - \vec{x}_A)/|\vec{x}_B - \vec{x}_A|$. The pressure force on the patch is:

$$\Delta\vec{f} = \vec{n} \int p \, dl = \vec{n} \frac{\rho}{2} \left(V^2 \cdot l - \int \vec{v}^2 \, dl \right)$$

\vec{v} is not constant! To evaluate this expression, the velocity within the patch is approximated by:

$$\vec{v} = a + bt + ct^2$$

t is the tangential coordinate directed from A to B . \vec{v}_A and \vec{v}_B are the velocities at the patch corners. The coefficients a , b , and c are determined from the conditions:

- The velocity at $t = 0$ is \vec{v}_A : $a = \vec{v}_A$.
 - The velocity at $t = 1$ is \vec{v}_B : $a + b + c = \vec{v}_B$.
 - The average velocity (integral over one patch) is \bar{v} : $a + \frac{1}{2}b + \frac{1}{3}c = \bar{v}$
- This yields:

$$a = \vec{v}_A$$

$$b = 6\bar{v} - 4\vec{v}_A - 2\vec{v}_B$$

$$c = -6\bar{v} + 3\vec{v}_A + 3\vec{v}_B$$

Using the above quadratic approximation for \vec{v} , the integral of \vec{v}^2 over the patch area is found after some lengthy algebraic manipulations as:

$$\begin{aligned} \int \vec{v}^2 \, dl &= l \int_0^1 \vec{v}^2 \, dt = l \cdot \left(a^2 + ab + \frac{1}{3}(2ac + b^2) + \frac{1}{2}bc + \frac{1}{5}c^2 \right) \\ &= l \cdot \left(\bar{v}^2 + \frac{2}{15}((\vec{v}_A - \bar{v}) + (\vec{v}_B - \bar{v}))^2 - \frac{1}{3}(\vec{v}_A - \bar{v})(\vec{v}_B - \bar{v}) \right) \end{aligned}$$

Thus the force on one patch is

$$\begin{aligned} \Delta\vec{f} &= -\vec{n} \cdot l \cdot \left((\bar{v}^2 - V^2) + \frac{2}{15}((\vec{v}_A - \bar{v}) + (\vec{v}_B - \bar{v}))^2 \right. \\ &\quad \left. - \frac{1}{3}(\vec{v}_A - \bar{v})(\vec{v}_B - \bar{v}) \right) \end{aligned}$$

2. *Three-dimensional case*

The potential of a three-dimensional source is:

$$\varphi = -\frac{1}{4\pi|\vec{x} - \vec{x}_q|} \quad (1)$$

Figure 6.12 shows a triangular patch ABC and a source S. Quadrilateral patches may be created by combining two triangles. The zero-flow condition for this patch is

$$-V\frac{(\vec{a} \times \vec{b})_1}{2} + \sum_i \sigma_i M_i = 0$$

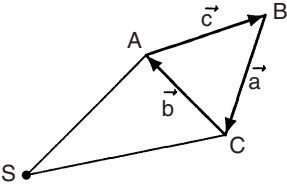


Figure 6.12 Source point S and patch ABC

The first term is the volume flow through ABC due to the uniform flow; the index 1 indicates the x component (of the vector product of two sides of the triangle). The flow M through a patch ABC induced by a point source of unit strength is $-\alpha/(4\pi)$. α is the solid angle in which ABC is seen from S. The rules of spherical geometry give α as the sum of the angles between each pair of planes SAB, SBC, and SCA minus π :

$$\alpha = \beta_{SAB,SBC} + \beta_{SBC,SCA} + \beta_{SCA,SAB} - \pi$$

where, e.g.,

$$\beta_{SAB,SBC} = \arctan \frac{-(\vec{A} \times \vec{B}) \times (\vec{B} \times \vec{C}) \cdot \vec{B}}{(\vec{A} \times \vec{B}) \cdot (\vec{B} \times \vec{C})|\vec{B}|}$$

Here \vec{A} , \vec{B} , \vec{C} are the vectors pointing from the source point S to the panel corners A, B, C. The solid angle may be approximated by A^*/d^2 if the distance d between patch centre and source point exceeds a given limit. A^* is the patch area projected on a plane normal to the direction from the source to the patch centre:

$$\vec{d} = \frac{1}{3}(\vec{A} + \vec{B} + \vec{C})$$

$$A^* = \frac{1}{2}(\vec{a} \times \vec{b}) \cdot \frac{\vec{d}}{d}$$

With known source strengths σ_i , one can determine the potential ϕ and its derivatives $\nabla\phi$ at all patch corners. From the ϕ values at the corners A, B, C, the average velocity within the triangle is found as:

$$\bar{v} = \overline{\nabla\phi} = \frac{\phi_A - \phi_C}{n_{AB}^2} \vec{n}_{AB} + \frac{\phi_B - \phi_A}{n_{AC}^2} \vec{n}_{AC}$$

with:

$$\vec{n}_{AB} = \vec{b} - \frac{\vec{c} \cdot \vec{b}}{\vec{c}^2} \vec{c} \quad \text{and} \quad \vec{n}_{AC} = \vec{c} - \frac{\vec{b} \cdot \vec{c}}{\vec{b}^2} \vec{b}$$

With known \vec{v} and corner velocities $\vec{v}_A, \vec{v}_B, \vec{v}_C$, the pressure force on the triangle can be determined:

$$\Delta \vec{f} = \vec{n} \int p \, dA = \vec{n} \frac{\rho}{2} \left(V^2 \cdot A - \int \vec{v}^2 \, dA \right)$$

where \vec{v} is *not* constant! $A = \frac{1}{2} |\vec{a} \times \vec{b}|$ is the patch area. To evaluate this equation, the velocity within the patch is approximated by:

$$\vec{v} = \vec{v} + (\vec{v}_A - \vec{v})(2r^2 - r) + (\vec{v}_B - \vec{v})(2s^2 - s) + (\vec{v}_C - \vec{v})(2t^2 - t)$$

r is the ‘triangle coordinate’ directed to patch corner A: $r = 1$ at A, and $r = 0$ at the line BC. s and t are the corresponding ‘triangle coordinates’ directed to B resp. C. Using this quadratic \vec{v} formula, the integral of \vec{v}^2 over the triangle area is found after some algebraic manipulations as:

$$\begin{aligned} \int \vec{v}^2 \, dA = A \cdot & \left[\vec{v}^2 + \frac{1}{30} (\vec{v}_A - \vec{v})^2 + \frac{1}{30} (\vec{v}_B - \vec{v})^2 + \frac{1}{30} (\vec{v}_C - \vec{v})^2 \right. \\ & - \frac{1}{90} (\vec{v}_A - \vec{v})(\vec{v}_B - \vec{v}) - \frac{1}{90} (\vec{v}_B - \vec{v})(\vec{v}_C - \vec{v}) \\ & \left. - \frac{1}{90} (\vec{v}_C - \vec{v})(\vec{v}_A - \vec{v}) \right] \end{aligned}$$

Numerical example for BEM

7.1 Two-dimensional flow around a body in infinite fluid

One of the most simple applications of boundary element methods is the computation of the potential flow around a body in an infinite fluid. The inclusion of a rigid surface is straightforward in this case and leads to the double-body flow problem which will be discussed at the end of this chapter.

7.1.1 Theory

We consider a submerged body of arbitrary (but smooth) shape moving with constant speed V in an infinite fluid domain. For inviscid and irrotational flow, this problem is equivalent to a body being fixed in an inflow of constant speed. For testing purposes, we may select a simple geometry like a circle (cylinder of infinite length) as a body.

For the assumed ideal fluid, there exists a velocity potential ϕ such that $\vec{v} = \nabla\phi$. For the considered ideal fluid, continuity gives Laplace's equation which holds in the whole fluid domain:

$$\Delta\phi = \phi_{xx} + \phi_{zz} = 0$$

In addition, we require the boundary condition that water does not penetrate the body's surface (hull condition). For an inviscid fluid, this condition can be reformulated requiring just vanishing normal velocity on the body:

$$\vec{n} \cdot \nabla\phi = 0$$

\vec{n} is the inward unit normal vector on the body hull. This condition is mathematically a Neumann condition as it involves only derivatives of the unknown potential.

Once a potential and its derivatives have been determined, the forces on the body can be determined by direct pressure integration:

$$f_1 = \int_S p n_1 dS$$

$$f_2 = \int_S p n_2 dS$$

S is the wetted surface. p is the pressure determined from Bernoulli's equation:

$$p = \frac{\rho}{2}(V^2 - (\nabla\phi)^2)$$

The force coefficients are then:

$$C_x = \frac{f_1}{\frac{\rho}{2}V^2S}$$

$$C_z = \frac{f_2}{\frac{\rho}{2}V^2S}$$

7.1.2 Numerical implementation

The velocity potential ϕ is approximated by uniform flow superimposed by a finite number N of elements. These elements are in the sample program DOUBL2D desingularized point sources inside the body (Fig. 6.10). The choice of elements is rather arbitrary, but the most simple elements are selected here for teaching purposes.

We formulate the potential ϕ as the sum of parallel uniform flow (of speed V) and a residual potential which is represented by the elements:

$$\phi = -Vx + \sum \sigma_i \varphi$$

σ_i is the strength of the i th element, φ the potential of an element of unit strength. The index i for φ is omitted for convenience but it should be understood in the equations below that φ refers to the potential of only the i th element.

Then the Neumann condition on the hull becomes:

$$\sum_{i=1}^N \sigma_i (\vec{n} \cdot \nabla \varphi) = V n_1$$

This equation is fulfilled on N collocation points on the body forming thus a linear system of equations in the unknown element strengths σ_i . Once the system is solved, the velocities and pressures are determined on the body.

The pressure integral for the x force is evaluated approximately by:

$$\int_S p n_1 dS \approx \sum_{i=1}^N p_i n_{1,i} s_i$$

The pressure, p_i , and the inward normal on the hull, n_i , are taken constant over each panel. s_i is the area of one segment.

For double-body flow, an 'element' consists of a source at $z = z_q$ and its mirror image at $z = -z_q$. Otherwise, there is no change in the program.

7.2 Two-dimensional wave resistance problem

The extension of the theory for a two-dimensional double-body flow problem to a two-dimensional free surface problem with optional shallow-water effect introduces these main new features:

- ‘fully non-linear’ free-surface treatment
- shallow-water treatment
- treatment of various element types in one program

While the problem is purely academical as free surface steady flows for ships in reality are always strongly three dimensional, the two-dimensional problem is an important step in understanding the three-dimensional problem. Various techniques have in the history of development always been tested and refined first in the much faster and easier two-dimensional problem, before being implemented in three-dimensional codes. The two-dimensional problem is thus an important stepping stone for researchers and a useful teaching example for students.

7.2.1 Theory

We consider a submerged body of arbitrary (but smooth) shape moving with constant speed V under the free surface in water of constant depth. The depth may be infinite or finite. For inviscid and irrotational flow, this problem is equivalent to a body being fixed in an inflow of constant speed.

We extend the theory given in section 7.1 simply repeating the previously discussed conditions and focusing on the new conditions. Laplace’s equation holds in the whole fluid domain. The boundary conditions are:

- Hull condition: water does not penetrate the body’s surface.
- Kinematic condition: water does not penetrate the water surface.
- Dynamic condition: there is atmospheric pressure at the water surface.
- Radiation condition: waves created by the body do not propagate ahead.
- Decay condition: far ahead and below of the body, the flow is undisturbed.
- Open-boundary condition: waves generated by the body pass unreflected any artificial boundary of the computational domain.
- Bottom condition (shallow-water case): no water flows through the sea bottom.

The decay condition replaces the bottom condition if the bottom is at infinity, i.e. in the usual infinite fluid domain case.

The wave resistance problem features two special problems requiring an iterative solution:

1. A non-linear boundary condition appears on the free surface.
2. The boundaries of water (waves) are not *a priori* known.

The iteration starts with approximating:

- the unknown wave elevation by a flat surface
- the unknown potential by the potential of uniform parallel flow

In each iterative step, wave elevation and potential are updated yielding successively better approximations for the solution of the non-linear problem.

The equations are formulated here in a right-handed Cartesian coordinate system with x pointing forward towards the 'bow' and z pointing upward. For the assumed ideal fluid, there exists a velocity potential ϕ such that $\vec{v} = \nabla\phi$. The velocity potential ϕ fulfils Laplace's equation in the whole fluid domain:

$$\Delta\phi = \phi_{xx} + \phi_{zz} = 0$$

The hull condition requires vanishing normal velocity on the body:

$$\vec{n} \cdot \nabla\phi = 0$$

\vec{n} is the inward unit normal vector on the body hull.

The kinematic condition (no penetration of water surface) gives at $z = \zeta$:

$$\nabla\phi \cdot \nabla\zeta = \phi_z$$

For simplification, we write $\zeta(x, y, z)$ with $\zeta_z = \partial\zeta/\partial z = 0$.

The dynamic condition (atmospheric pressure at water surface) gives at $z = \zeta$:

$$\frac{1}{2}(\nabla\phi)^2 + gz = \frac{1}{2}V^2$$

with $g = 9.81 \text{ m/s}^2$. Combining the dynamic and kinematic boundary conditions eliminates the unknown wave elevation $z = \zeta$:

$$\frac{1}{2}\nabla\phi \cdot \nabla(\nabla\phi)^2 + g\phi_z = 0$$

This equation must still be fulfilled at $z = \zeta$. If we approximate the potential ϕ and the wave elevation ζ by arbitrary approximations Φ and $\bar{\zeta}$, linearization about the approximated potential gives at $z = \zeta$:

$$\nabla\Phi \cdot \nabla(\frac{1}{2}(\nabla\Phi)^2 + \nabla\Phi \cdot \nabla(\phi - \Phi)) + \nabla(\phi - \Phi) \cdot \nabla(\frac{1}{2}(\nabla\Phi)^2) + g\phi_z = 0$$

Φ and $\phi - \Phi$ are developed in a Taylor expansion about $\bar{\zeta}$. The Taylor expansion is truncated after the linear term. Products of $\zeta - \bar{\zeta}$ with derivatives of $\phi - \Phi$ are neglected. This yields at $z = \zeta$:

$$\begin{aligned} \nabla\Phi \cdot \nabla(\frac{1}{2}(\nabla\Phi)^2 + \nabla\Phi \cdot \nabla(\phi - \Phi)) + \nabla(\phi - \Phi) \cdot \nabla(\frac{1}{2}(\nabla\Phi)^2) + g\phi_z \\ + [\frac{1}{2}\nabla\Phi \cdot \nabla(\nabla\Phi)^2 + g\Phi_z]_{\zeta}(\zeta - \bar{\zeta}) = 0 \end{aligned}$$

A consistent linearization about Φ and $\bar{\zeta}$ substitutes ζ by an expression depending solely on $\bar{\zeta}$, $\Phi(\bar{\zeta})$ and $\phi(\bar{\zeta})$. For this purpose, the original expression for ζ is also developed in a truncated Taylor expansion and written at $z = \bar{\zeta}$:

$$\begin{aligned} \zeta &= -\frac{1}{2g}(-(\nabla\Phi)^2 + 2\nabla\Phi \cdot \nabla\phi + 2\nabla\Phi \cdot \nabla\Phi_z(\zeta - \bar{\zeta}) - V^2) \\ \zeta - \bar{\zeta} &= \frac{-\frac{1}{2}(2\nabla\Phi \cdot \nabla\phi - (\nabla\Phi)^2 - V^2) - g\bar{\zeta}}{g + \nabla\Phi \cdot \nabla\Phi_z} \end{aligned}$$

Substituting this expression in our equation for the free-surface condition gives the consistently linearized boundary condition at $z = \bar{\zeta}$:

$$\nabla\Phi\nabla[-(\nabla\Phi)^2 + \nabla\Phi \cdot \nabla\phi] + \frac{1}{2}\nabla\phi\nabla(\nabla\Phi)^2 + g\phi_z + \frac{[\frac{1}{2}\nabla\Phi\nabla(\nabla\Phi)^2 + g\Phi_z]_z}{g + \nabla\Phi \cdot \nabla\Phi_z} \\ \times (-\frac{1}{2}[-(\nabla\Phi)^2 + 2\nabla\Phi \cdot \nabla\phi - V^2] - g\bar{\zeta}) = 0$$

The denominator in the last term becomes zero when the vertical particle acceleration is equal to gravity. In fact, the flow becomes unstable already at 0.6 to 0.7g both in reality and in numerical computations.

It is convenient to introduce the following abbreviations:

$$\vec{a} = \frac{1}{2}\nabla((\nabla\Phi)^2) = \left\{ \begin{array}{l} \Phi_x\Phi_{xx} + \Phi_z\Phi_{xz} \\ \Phi_x\Phi_{xz} + \Phi_z\Phi_{zz} \end{array} \right\} \\ B = \frac{[\frac{1}{2}\nabla\Phi\nabla(\nabla\Phi)^2 + g\Phi_z]_z}{g + \nabla\Phi \cdot \nabla\Phi_z} = \frac{[\nabla\Phi\vec{a} + g\Phi_z]_z}{g + a_2} \\ = \frac{1}{g + a_2}(\Phi_x^2\Phi_{xxz} + \Phi_z^2\Phi_{zzz} + g\Phi_{zz} \\ + 2[\Phi_x\Phi_z\Phi_{xzz} + \Phi_{xz} \cdot a_1 + \Phi_{zz} \cdot a_2])$$

Then the boundary condition at $z = \bar{\zeta}$ becomes:

$$2(\vec{a}\nabla\phi + \Phi_x\Phi_z\phi_{xz}) + \Phi_x^2\phi_{xx} + \Phi_z^2\phi_{zz} + g\phi_z - B\nabla\Phi\nabla\phi \\ = 2\vec{a}\nabla\Phi - B(\frac{1}{2}((\nabla\Phi)^2 + V^2) - g\bar{\zeta})$$

The non-dimensional error in the boundary condition at each iteration step is defined by:

$$\varepsilon = \max(|\vec{a}\nabla\Phi + g\Phi_z|)/(gV)$$

Where ‘max’ means the maximum value of all points at the free surface.

For given velocity, Bernoulli’s equation determines the wave elevation:

$$z = \frac{1}{2g}(V^2 - (\nabla\phi)^2)$$

The first step of the iterative solution is the classical linearization around uniform flow. To obtain the classical solutions for this case, the above equation should also be linearized as:

$$z = \frac{1}{2g}(V^2 + (\nabla\Phi)^2 - 2\nabla\Phi\nabla\phi)$$

However, it is computationally simpler to use the non-linear equation.

The bottom, radiation, and open-boundary conditions are fulfilled by the proper arrangement of elements as described below. The decay condition – like the Laplace equation – is automatically fulfilled by all elements.

Once a potential has been determined, the force on the body in the x direction can be determined by direct pressure integration:

$$f_1 = \int_S p n_1 dS$$

S is the wetted surface. p is the pressure determined from Bernoulli's equation:

$$p = \frac{\rho}{2}(V^2 - (\nabla\phi)^2)$$

The force in the x direction, f_1 , is the (negative) wave resistance. The non-dimensional wave resistance coefficient is:

$$C_W = -f_1 / \left(\frac{\rho}{2} V^2 S \right)$$

7.2.2 Numerical implementation

The velocity potential ϕ is approximated by uniform flow superimposed by a finite number of elements. These elements are in the sample program SHAL2D:

- desingularized point source clusters above the free surface
- desingularized point sources inside the body

The choice of elements is rather arbitrary, but very simple elements have been selected for teaching purposes.

The height of the elements above the free surface is not corrected in SHAL2D. For usual discretizations (10 elements per wave length) and moderate speeds, this procedure should work without problems. For finer discretizations (as often found for high speeds), problems occur which require a readjustment of the panel layer. However, in most cases it is sufficient to adjust the source layer just once after the first iteration and then 'freeze' it.

We formulate the potential ϕ as the sum of parallel uniform flow (of speed V) and a residual potential which is represented by the elements:

$$\phi = -Vx + \sum \sigma_i \varphi$$

σ_i is the strength of the i th element, φ the potential of an element of unit strength. The expression 'element' refers to one source (cluster) and all its mirror images. If the collocation point and source centre are sufficiently far from each other, e.g. three times the grid spacing, the source cluster may be substituted by a single point source. This accelerates the computation without undue loss of accuracy.

Then the no-penetration boundary condition on the hull becomes:

$$\sum \sigma_i (\vec{n} \cdot \nabla \varphi) = V n_1$$

The linearized free-surface condition becomes:

$$\begin{aligned} & \sum \sigma_i (2(\vec{a} \nabla \varphi + \Phi_x \Phi_z \varphi_{xz}) + \Phi_x^2 \varphi_{xx} + \Phi_z^2 \varphi_{zz} + g \varphi_z - B \nabla \Phi \nabla \varphi) \\ &= 2(\vec{a} \nabla \Phi + a_1 V) - B(\frac{1}{2}((\nabla \Phi)^2 + V^2) - g \bar{\xi} + V \Phi_x) \end{aligned}$$

These two equations form a linear system of equations in the unknown element strengths σ_i . Once the system is solved, the velocities (and higher derivatives of the potential) are determined on the water surface. Then the error ε is determined.

For shallow water, mirror images of elements at the ocean bottom are used. This technique is similar to the mirror imaging at the still waterplane used for double-body flow in section 7.1.

The radiation and open-boundary conditions are fulfilled using ‘staggered grids’. This technique adds an extra row of panels at the downstream end of the computational domain and an extra row of collocation points at the upstream end (Fig. 3.11). For equidistant grids, this can also be interpreted as shifting or staggering the grid of collocation points vs. the grid of elements, hence the name ‘staggered grid’. However, this name is misleading as for non-equidistant grids or three-dimensional grids with quasi-streamlined grid lines, adding an extra row at the ends is not the same as shifting the whole grid.

The pressure integral for the x force is evaluated approximately by

$$\int_S p n_1 dS \approx \sum_{i=1}^{N_B} p_i n_{1,i} s_i$$

N_B is the number of elements on the hull. The pressure, p_i , and the inward normal on the hull, n_i , are taken constant over each panel. s_i is the area of one segment.

7.3 Three-dimensional wave resistance problem

The extension of the theory for a two-dimensional submerged body to a three-dimensional surface-piercing ship free to trim and sink introduces these main new features:

- surface-piercing hulls
- dynamic trim and sinkage
- transom stern
- Kutta condition for multihulls

The theory outlined here is the theory behind the STEADY code (Hughes and Bertram (1995)). The code is a typical representative of a state of the art ‘fully non-linear’ wave resistance code of the 1990s.

7.3.1 Theory

We consider a ship moving with constant speed V in water of constant depth. The depth and width may be infinite and is in fact assumed to be so in most cases. For inviscid and irrotational flow, this problem is equivalent to a ship being fixed in an inflow of constant speed.

For the considered ideal fluid, continuity gives Laplace’s equation which holds in the whole fluid domain. A unique description of the problem requires further conditions on all boundaries of the fluid resp. the modelled fluid domain:

- Hull condition: water does not penetrate the ship’s surface.

- Transom stern condition: for ships with a transom stern, we assume that the flow separates and the transom stern is dry. Atmospheric pressure is then enforced at the edge of the transom stern.
- Kinematic condition: water does not penetrate the water surface.
- Dynamic condition: there is atmospheric pressure at the water surface.
- Radiation condition: waves created by the ship do not propagate ahead. (This condition is not valid for transcritical depth Froude numbers when the flow becomes unsteady and soliton waves are pulsed ahead. But ships are never designed for such speeds.)
- Decay condition: far away from the ship, the flow is undisturbed.
- Open-boundary condition: waves generated by the ship pass unreflected any artificial boundary of the computational domain.
- Equilibrium: the ship is in equilibrium, i.e. trim and sinkage are changed such that the dynamic vertical force and the trim moment are counteracted.
- Bottom condition (shallow-water case): no water flows through the sea bottom.
- Kutta condition (for multihulls): at the end of each side floater the flow separates smoothly. This is approximated by setting the y velocity to zero.

The decay condition replaces the bottom condition if the bottom is at infinity, i.e. in the usual infinite fluid domain case.

The problem is solved using boundary elements (in the case of STEADY higher-order panels on the ship hull, point source clusters above the free surface). The wave resistance problem features two special problems requiring an iterative solution approach:

1. A non-linear boundary condition appears on the free surface.
2. The boundaries of water (waves) and ship (trim and sinkage) are not *a priori* known.

The iteration starts with approximating:

- the unknown wave elevation by a flat surface
- the unknown potential by the potential of uniform parallel flow
- the unknown position of the ship by the position of the ship at rest

In each iterative step, wave elevation, potential, and position are updated yielding successively better approximations for the solution of the non-linear problem (Fig. 7.1).

The equations are formulated here in a right-handed Cartesian coordinate system with x pointing forward towards the bow and z pointing upward. The moment about the y -axis (and the trim angle) are positive clockwise (bow immerses for positive trim angle).

For the assumed ideal fluid, there exists a velocity potential ϕ such that $\vec{v} = \nabla\phi$. The velocity potential ϕ fulfils Laplace's equation in the whole fluid domain:

$$\Delta\phi = \phi_{xx} + \phi_{yy} + \phi_{zz} = 0$$

A unique solution requires the formulation of boundary conditions on all boundaries of the modelled fluid domain.

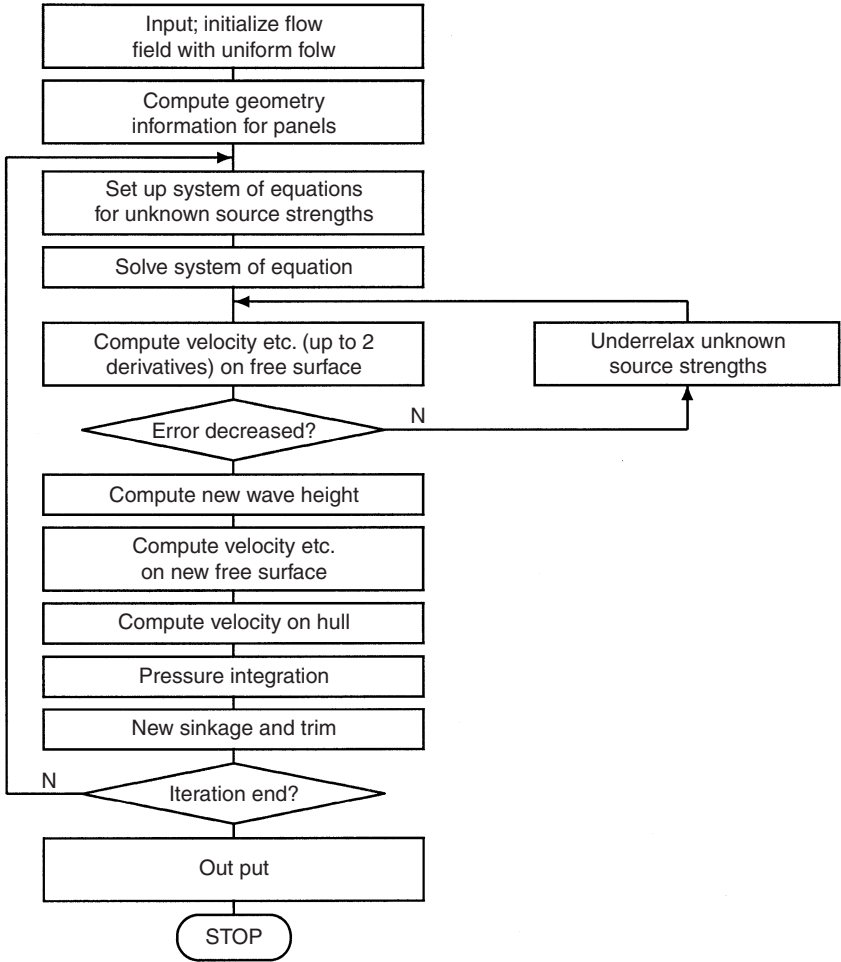


Figure 7.1 Flow chart of iterative solution

The hull condition (no penetration of ship hull) requires that the normal velocity on the hull vanishes:

$$\vec{n} \cdot \nabla \phi = 0$$

\vec{n} is the inward unit normal vector on the ship hull.

The transom stern condition (atmospheric pressure at the edge of the transom stern $z = z_T$) is derived from Bernoulli's equation:

$$\frac{1}{2}(\nabla \phi)^2 + gz_T = \frac{1}{2}V^2$$

with $g = 9.81 \text{ m/s}^2$. This condition is non-linear in the unknown potential. We assume that the water flows at the stern predominantly in the x direction, such

that the y and z components are negligible. This leads to the linear condition:

$$\phi_x + \sqrt{V^2 - 2gz_T} = 0$$

For points above the height of stagnation $V^2/2g$, this condition leads to a negative term in the square root. For these points, stagnation of horizontal flow is enforced instead. Both cases can be combined as:

$$\phi_x + \sqrt{\max(0, V^2 - 2gz_T)} = 0$$

The Kutta condition is originally a pressure condition, thus also non-linear. However, the obliqueness of the flow induced at the end of each side floater is so small that a simplification can be well justified. We then enforce just zero y velocity (Joukowski condition):

$$\phi_y = 0$$

The kinematic condition (no penetration of water surface) gives at $z = \zeta$:

$$\nabla\phi \cdot \nabla\zeta = \phi_z$$

For simplification, we write $\zeta(x, y, z)$ with $\zeta_z = \partial\zeta/\partial z = 0$.

The dynamic condition (atmospheric pressure at water surface) gives at $z = \zeta$:

$$\frac{1}{2}(\nabla\phi)^2 + gz = \frac{1}{2}V^2$$

Combining the dynamic and kinematic boundary conditions and linearizing consistently yields again at $z = \bar{\zeta}$, see section 7.2:

$$2(\bar{a}\nabla\phi + \Phi_x\Phi_y\phi_{xy} + \Phi_x\Phi_z\phi_{xz} + \Phi_y\Phi_z\phi_{yz}) + \Phi_x^2\phi_{xx} + \Phi_y^2\phi_{yy} + \Phi_z^2\phi_{zz} + g\phi_z - B\nabla\Phi\nabla\phi = 2\bar{a}\nabla\Phi - B(\frac{1}{2}((\nabla\Phi)^2 + V^2) - g\bar{\zeta})$$

with

$$\begin{aligned} \bar{a} &= \frac{1}{2}\nabla((\nabla\Phi)^2) = \begin{Bmatrix} \Phi_x\Phi_{xx} + \Phi_y\Phi_{xy} + \Phi_z\Phi_{xz} \\ \Phi_x\Phi_{xy} + \Phi_y\Phi_{yy} + \Phi_z\Phi_{yz} \\ \Phi_x\Phi_{xz} + \Phi_y\Phi_{yz} + \Phi_z\Phi_{zz} \end{Bmatrix} \\ B &= \frac{[\frac{1}{2}\nabla\Phi\nabla(\nabla\Phi)^2 + g\Phi_z]_z}{g + \nabla\Phi \cdot \nabla\Phi_z} = \frac{[\nabla\Phi\bar{a} + g\Phi_z]_z}{g + a_3} \\ &= \frac{1}{g + a_3}(\Phi_x^2\Phi_{xxz} + \Phi_y^2\Phi_{yyz} + \Phi_z^2\Phi_{zzz} + g\Phi_{zz} + 2[\Phi_x\Phi_y\Phi_{xyz} \\ &\quad + \Phi_x\Phi_z\Phi_{xzz} + \Phi_y\Phi_z\Phi_{yzz} + \Phi_{xz} \cdot a_1 + \Phi_{yz} \cdot a_2 + \Phi_{zz} \cdot a_3]) \end{aligned}$$

The bottom, radiation, and open-boundary conditions are fulfilled by the proper arrangement of elements as described below. The decay condition – like the Laplace equation – is automatically fulfilled by all elements.

Once a potential has been determined, the forces can be determined by direct pressure integration on the wetted hull. The forces are corrected by the hydrostatic forces at rest. (The hydrostatic x force and y moment should be zero, but are non-zero due to discretization errors. The discretization error is hoped to be reduced by subtracting the value for the hydrostatic force):

$$f_1 = \int_S p n_1 dS - \int_{S_0} p_s n_1 dS$$

$$f_3 = \int_S p n_3 dS - \int_{S_0} p_s n_3 dS$$

$$f_5 = \int_S p(z n_1 - x n_3) dS - \int_{S_0} p_s(z n_1 - x n_3) dS$$

S is the actually wetted surface. S_0 is the wetted surface of the ship at rest. $p_s = -\rho g z$ is the hydrostatic pressure, where ρ is the density of water. p is the pressure determined from Bernoulli's equation:

$$p = \frac{\rho}{2}(V^2 - (\nabla\phi)^2) - \rho g z$$

The force in the x direction, f_1 , is the (negative) wave resistance. The non-dimensional wave resistance coefficient is:

$$C_W = -f_1 / \left(\frac{\rho}{2} V^2 S \right)$$

The z force and y moments are used to adjust the position of the ship. We assume small changes of the position of the ship. Δz is the deflection of the ship (positive, if the ship surfaces) and $\Delta\theta$ is the trim angle (positive if bow immerses) (Fig. 7.2).

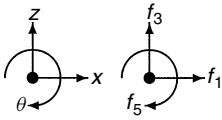


Figure 7.2 Coordinate system; x points towards bow, origin is usually amidships in still waterline; relevant forces and moment

For given Δz and $\Delta\theta$, the corresponding z force and y moment (necessary to enforce this change of position) are:

$$\begin{Bmatrix} f_3 \\ f_5 \end{Bmatrix} = \begin{bmatrix} A_{WL} \cdot \rho \cdot g & -A_{WL} \cdot \rho \cdot g \cdot x_{WL} \\ -A_{WL} \cdot \rho \cdot g \cdot x_{WL} & I_{WL} \cdot \rho \cdot g \end{bmatrix} \begin{Bmatrix} \Delta z \\ \Delta\theta \end{Bmatrix}$$

A_{WL} is the area, I_{WL} the moment of inertia, and x_{WL} the centre of the still waterplane. I_{WL} and x_{WL} are taken relative to the origin which we put amidships. Inversion of this matrix gives an equation of the form:

$$\begin{Bmatrix} \Delta z \\ \Delta\theta \end{Bmatrix} = \begin{bmatrix} a_{11} & a_{12} \\ a_{21} & a_{22} \end{bmatrix} \begin{Bmatrix} f_3 \\ f_5 \end{Bmatrix}$$

The coefficients a_{ij} are determined once in the beginning by inverting the matrix for the still waterline. Then during each iteration the position of the ship

is changed by Δz and $\Delta\theta$ giving the final sinkage and trim when converged. The coefficients should actually change as the ship trims and sinks and thus its actual waterline changes from the still waterline. However, this error just slows down the convergence, but (for convergence) does not change the final result for trim and sinkage.

7.3.2 Numerical implementation

The velocity potential ϕ is approximated by parallel flow superimposed by a finite number of elements. These elements are for STEADY higher-order panels lying on the ship surface, linear panels (constant strength) in a layer above part of the free surface, and vortex elements lying on the local centre plane of any side floater. However, the choice of elements is rather arbitrary. If just wave resistance computations are performed, first-order elements are sufficient and actually preferable due their greater robustness.

The free-surface elements are again usually ‘desingularized’. We place them approximately one panel length above the still-water plane ($z = 0$).

We formulate the potential ϕ as the sum of parallel uniform flow (of speed V) and a residual potential which is represented by the elements:

$$\phi = -Vx + \sum \sigma_i \varphi$$

σ_i is the strength of the i th element, φ the potential of an element of unit strength. The index i for φ is omitted for convenience but it should be understood in the equations below that φ refers to the potential of only the i th element. The expression ‘element’ refers to one panel or vortex and all its mirror images.

Then the no-penetration boundary condition on the hull becomes:

$$\sum \sigma_i (\vec{n} \cdot \nabla \varphi) = V n_1$$

The Kutta condition becomes:

$$\sum \sigma_i \varphi_y = 0$$

The transom stern condition becomes:

$$\sum \sigma_i \varphi_x = V - \sqrt{\max(0, V^2 - 2gz_T)}$$

The linearized free surface condition becomes then:

$$\begin{aligned} & \sum \sigma_i (2(\vec{a} \nabla \varphi + \Phi_x \Phi_y \varphi_{xy} + \Phi_x \Phi_z \varphi_{xz} + \Phi_y \Phi_z \varphi_{yz}) + \Phi_x^2 \varphi_{xx} \\ & + \Phi_y^2 \varphi_{yy} + \Phi_z^2 \varphi_{zz} + g\varphi_z - B \nabla \Phi \nabla \varphi) \\ & = 2(\vec{a} \nabla \Phi + a_1 V) - B(\frac{1}{2}((\nabla \Phi)^2 + V^2) - g\bar{\zeta} + V \Phi_x) \end{aligned}$$

These four equations form a linear system of equations in the unknown element strengths σ_i . Once the system is solved, the velocities (and higher derivatives of the potential) are determined on the water surface and the error ε is determined. A special refinement accelerates and stabilizes to some extent the iteration

process: if the error ε_{i+1} in iteration step $i + 1$ is larger than the error ε_i in the previous i th step the source strengths are underrelaxed:

$$\sigma_{i+1,\text{new}} = \frac{\sigma_{i+1,\text{old}} \cdot \varepsilon_i + \sigma_i \cdot \varepsilon_{i+1}}{\varepsilon_i + \varepsilon_{i+1}}$$

Velocities and errors are evaluated again with the new source strengths. If the error is decreased the computation proceeds, otherwise the underrelaxation is repeated. If four repetitions still do not improve the error compared to the previous step, the computation is stopped. In this case, no converged non-linear solution can be found. This is usually the case if breaking waves appear in the real flow at a location of a collocation point.

Mirror images of panels are used (Fig. 7.3):

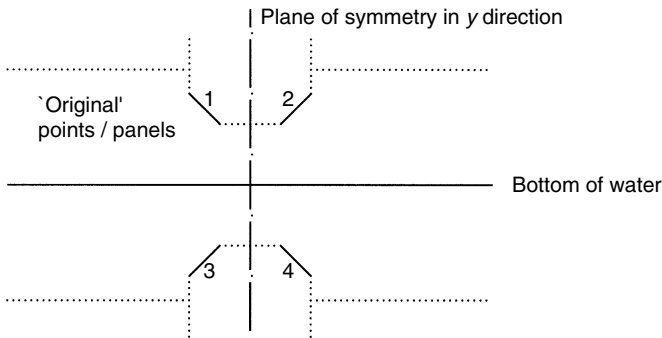


Figure 7.3 Mirror images of panels are used

1. In the y direction with respect to the centre plane $y = 0$.
2. For shallow water in the z direction with respect to the water bottom $z = z_{\text{bottom}}$: $z' = -2|z_{\text{bottom}}| - z$.

The computation of the influence of one element on one collocation point uses the fact that the influence of a panel at A on a point at B has the same absolute value and opposite sign as a panel at B on a point at A. Actually, mirror images of the collocation point are produced and the influence of the original panel is computed for all mirror points. Then the sign of each influence is changed according to Table 7.1.

The radiation and open-boundary conditions are fulfilled using ‘staggered grids’ as for the two-dimensional case. No staggering in the y direction is necessary.

For equidistant grids and collocation points along lines of $y = \text{const.}$, this can also be interpreted as shifting or staggering the grid of collocation points vs. the grid of elements, hence the name ‘staggered grid’. However, for three-dimensional grids around surface-piercing ships the grids are not staggered in a strict sense as, with the exception of the very ends, collocation points always lie directly under panel centres.

The pressure integral for the x force – the procedure for the z force and the y moment are corresponding – is evaluated approximately by

Table 7.1 Sign for derivatives of potential due to interchanging source and collocation point; mirror image number as in Fig. 7.4

	1	2	3	4
ϕ_x	+	+	+	+
ϕ_y	+	-	+	-
ϕ_z	+	+	+	+
ϕ_{xx}	+	+	+	+
ϕ_{xy}	+	-	+	-
ϕ_{xz}	+	+	+	+
ϕ_{yy}	+	+	+	+
ϕ_{yz}	+	-	+	-
ϕ_{xxz}	+	+	+	+
ϕ_{xyz}	+	-	+	-
ϕ_{xzz}	+	+	+	+
ϕ_{yyz}	+	+	+	+
ϕ_{yzz}	+	-	+	-

$$\int_S p n_1 dS \approx 2 \sum_{i=1}^{N_B} p_i n_{1,i} s_i$$

N_B is the number of elements on the hull. The pressure, p_i , and the inward normal on the hull, n_i , are taken constant over each panel. The factor 2 is due to the port/starboard symmetry.

The non-linear solution makes it necessary to discretize the ship above the still waterline. The grid can then be transformed (regenerated) such that it always follows the actually wetted surface of the ship. However, this requires fully automatic grid generation which is difficult on complex ship geometries prefer to discretize a ship initially to a line $z = \text{const.}$ above the free waterline. Then the whole grid can trim and sink relative to the free surface, as the grids on free surface and ship do not have to match. Then in each step, the actually wetted part of the ship grid has to be determined. The wetted area of each panel can be determined as follows.

A panel is subdivided into triangles. Each triangle is formed by one side of the panel and the panel centre. Bernoulli's equation correlates the velocity in a panel to a height z_w where the pressure would equal atmospheric pressure:

$$z_w = \frac{1}{2g}(V^2 - (\nabla\phi)^2)$$

If z_w lies above the highest point of the triangle, s_i is taken as the triangle area. If z_w lies below the lowest point of the triangle, $s_i = 0$. If z_w lies between the highest and the lowest point of the triangle, the triangle is partially submerged and pierces the water surface (Fig. 7.4).

In this case, the line z_w divides the triangle into a subtriangle ABC and the remaining trapezoid. If the triangle ABC is submerged (left case) s_i is taken to the area of ABC, otherwise to the triangle area minus ABC. The value of z in the pressure integral (e.g. for the hydrostatic contribution) is taken from the centre of the submerged partial area.

If a panel at the upper limit of discretization is completely submerged, the discretization was chosen too low. The limit of upper discretization is given

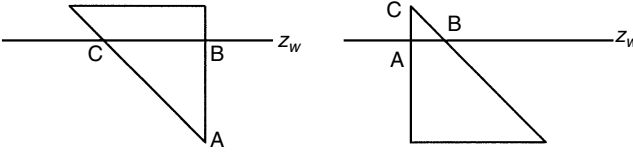


Figure 7.4 Partially submerged triangle with subtriangle ABC submerged (left) or surfaced (right)

for the trimmed ship by:

$$z = m_{\text{sym}}x + n_{\text{sym}}$$

7.4 Strip method module (two dimensional)

Strip methods as discussed in section 4.4.2, Chapter 4, are the standard tool in evaluating ship seakeeping. An essential part of each strip method is the computation of hydrodynamic masses, damping, and exciting forces for each strip. This computation was traditionally based on conformal mapping techniques, where an analytical solution for a semicircle was transformed to a shape resembling a ship section. This technique is not capable of reproducing complex shapes as found in the forebody of modern ships where possibly cross-section may consist of unconnected parts for bulbous bow and upper stem. Numerical ‘close-fit’ methods became available with the advent of computers in naval architecture and are now widely used in practice. In the following, one example of such a close-fit method to solve the two-dimensional strip problem is presented. The Fortran source code for the method is available on the internet (www.bh.com/companions/0750648511).

We compute the radiation and diffraction problems for a two-dimensional cross-section of arbitrary shape in harmonic, elementary waves. As usual, we assume an ideal fluid. Then there exists a velocity potential ϕ such that the partial derivatives of this potential in an arbitrary direction yield the velocity component of the flow in that direction. We neglect all non-linear effects in our computations. The problem is formulated in a coordinate system as shown in Fig. 7.5. Indices y , z , and t denote partial derivatives with respect to these variables.

We solve the problem in the frequency domain. The two-dimensional seakeeping potentials will then be harmonic functions oscillating with encounter frequency ω_e :

$$\phi(y, z, t) = \text{Re}(\hat{\phi}(y, z)e^{i\omega_e t})$$

The potential must fulfil the Laplace equation:

$$\phi_{yy} + \phi_{zz} = 0$$

in the whole fluid domain ($z < 0$) subject to following boundary conditions:

1. Decaying velocity with water depth:

$$\lim_{z \rightarrow -\infty} \nabla \phi = 0$$

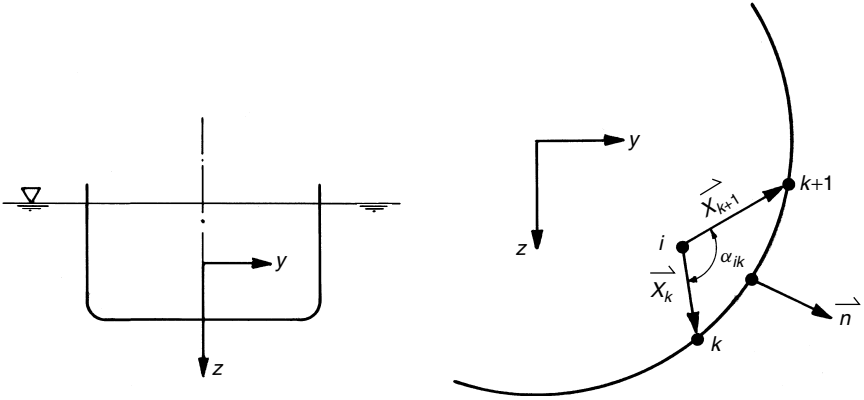


Figure 7.5 Coordinate system used; sources i are located inside contour

2. There is atmospheric pressure everywhere on the free surface $z = \zeta$ (dynamic condition). Then Bernoulli's equation yields

$$\phi_t + \frac{1}{2}(\nabla\phi)^2 - g\zeta = 0$$

3. There is no flow through the free surface (kinematic condition), i.e. the local vertical velocity of a particle coincides with the rate of change of the surface elevation in time:

$$\phi_z = \zeta_t$$

4. Differentiation of the dynamic condition with respect to time and combination with the kinematic condition yields

$$\phi_{tt} + \phi_y\phi_{yt} + \phi_z\phi_{zt} - g\phi_z = 0$$

This expression can be developed in a Taylor expansion around $z = 0$. Omitting all non-linear terms yields then

$$\phi_{tt} - g\phi_z = 0$$

5. There is no flow through the body contour, i.e. the normal velocity of the water on the body contour coincides with the normal velocity of the hull (or, respectively, the relative normal velocity between body and water is zero):

$$\vec{n} \cdot \nabla\phi = \vec{n} \cdot \vec{v}$$

Here \vec{v} is the velocity of the body, \vec{n} is the outward unit normal vector.

6. Waves created by the body must radiate away from the body:

$$\lim_{|y| \rightarrow \infty} \phi = \text{Re}(\hat{\phi} e^{-kz} e^{i(\omega_e t - k|y|)})$$

$\hat{\phi}$ is here a yet undetermined, but constant, amplitude.

Using the harmonic time dependency of the potential, we can reformulate the Laplace equation and all relevant boundary conditions such that only the time-independent complex amplitude of the potential $\hat{\phi}$ appears:

Laplace equation:

$$\hat{\phi}_{yy} + \hat{\phi}_{zz} = 0 \quad \text{for } z < 0$$

Decay condition:

$$\lim_{z \rightarrow \infty} \nabla \hat{\phi} = 0$$

Combined free surface condition:

$$\frac{\omega_e^2}{g} \hat{\phi} + \hat{\phi}_z = 0 \quad \text{at } z = 0$$

The body boundary condition is here explicitly given for the radiation problem of the body in heave motion. This will serve as an example. The other motions (sway, roll) and the diffraction problem are treated in a very similar fashion. The body boundary condition for heave is then:

$$\vec{n} \nabla \hat{\phi} = i\omega_e n_2$$

n_2 is the z component of the (two-dimensional) normal vector \vec{n} .

The radiation condition for $\hat{\phi}$ is derived by differentiation of the initial radiation condition for ϕ with respect to y and z , respectively. The resulting two equations allow the elimination of the unknown constant amplitude $\hat{\phi}$ yielding:

$$i\hat{\phi}_z = \text{sign}(y) \cdot \hat{\phi}_y$$

$\hat{\phi}$ can be expressed as the superposition of a finite number n of point source potentials, see section 6.2.1, Chapter 6. The method described here uses desingularized sources located (a small distance) inside the body and above the free surface. The grid on the free surface extends to a sufficient distance to both sides depending on the wavelength of the created wave. Due to symmetry, sources at y_i, z_i should have the same strength as sources at $-y_i, z_i$. (For sway and roll motion, we have anti-symmetrical source strength.) We then exploit symmetry and use source pairs as elements to represent the total potential:

$$\hat{\phi}(y, z) = \sum_{i=1}^n \sigma_i \varphi_i$$

$$\varphi_i = \frac{1}{4\pi} \ln[(y - y_i)^2 + (z - z_i)^2] + \frac{1}{4\pi} \ln[(y + y_i)^2 + (z - z_i)^2]$$

This formulation automatically fulfils the Laplace equation and the decay condition. The body, free surface, and radiation conditions are fulfilled numerically by adjusting the element strengths σ_i appropriately. We enforce these conditions only on points $y_i > 0$. Due to symmetry, they will then also be fulfilled automatically for $y_i < 0$.

The method described here uses a patch method to numerically enforce the boundary conditions, see section 6.5.2, Chapter 6. The body boundary condition is then integrated over one patch, e.g. between the points k and $k + 1$ on

the contour (Fig. 7.5):

$$\sum_{i=1}^n \sigma_i \int_{p_k}^{p_{k+1}} \nabla \varphi_i \vec{n}_k dS = i\omega_e \int_{p_k}^{p_{k+1}} n_2 dS$$

As n_2 can be expressed as $n_2 = dy/ds$, this yields:

$$\sum_{i=1}^n \sigma_i \int_{p_k}^{p_{k+1}} \nabla \varphi_i \vec{n}_k dS = i\omega_e (y_{k+1} - y_k)$$

The integral on the l.h.s. describes the flow per time (flux) through the patch (contour section) under consideration due to a unit source at y_i, z_i and its mirror image. The flux for just the source without its image corresponds to the portion of the angle α_{ik} (Fig. 7.5):

$$\int_{p_k}^{p_{k+1}} \nabla \varphi_i \vec{n}_k dS = \frac{\alpha_{ik}}{2\pi}$$

Correspondingly we write for the elements formed by a pair of sources:

$$\int_{p_k}^{p_{k+1}} \nabla \varphi_i \vec{n}_k dS = \frac{\alpha_{ik}^+}{2\pi} + \frac{\alpha_{ik}^-}{2\pi}$$

The angle α_{ik}^+ is determined by:

$$\alpha_{ik} = \arctan \left(\frac{\vec{x}_{k+1} \times \vec{x}_k}{\vec{x}_{k+1} \cdot \vec{x}_k} \right)_1$$

The index 1 denotes here the x component of the vector.

The other numerical conditions can be formulated in an analogous way. The number of patches corresponds to the number of elements. The patch conditions form then a system of linear equations for the unknown element strengths σ_i which can be solved straightforwardly. Once the element strengths are known, the velocity can be computed everywhere. The pressure integration for the patch method described in section 6.5.2, Chapter 6, then yields the forces on the section. The forces can then again be decomposed into exciting forces (for diffraction) and radiation forces expressed as added mass and damping coefficients analogous to the decomposition described in section 4.4, Chapter 4. The method has been encoded in the Fortran routines HMASSE and WERREG (see www.bh.com/companions/0750648511).

7.5 Rankine panel method in the frequency domain

7.5.1 Theory

The seakeeping method is limited theoretically to $\tau > 0.25$. In practice, accuracy problems may occur for $\tau < 0.4$. The method does not treat transom sterns. The theory given is that behind the FREDDY code (Bertram (1998)).

We consider a ship moving with mean speed V in a harmonic wave of small amplitude h with $\tau = V\omega_e/g > 0.25$. ω_e is the encounter frequency,

$g = 9.81 \text{ m/s}^2$. The resulting (linearized) seakeeping problems are similar to the steady wave resistance problem described previously and can be solved using similar techniques.

The fundamental field equation for the assumed potential flow is again Laplace's equation. In addition, boundary conditions are postulated:

1. No water flows through the ship's surface.
2. At the trailing edge of the ship, the pressures are equal on both sides. (Kutta condition.)
3. A transom stern is assumed to remain dry. (Transom condition.)
4. No water flows through the free surface. (Kinematic free surface condition.)
5. There is atmospheric pressure at the free surface. (Dynamic free surface condition.)
6. Far away from the ship, the disturbance caused by the ship vanishes.
7. Waves created by the ship move away from the ship. For $\tau > 0.25$, waves created by the ship propagate only downstream. (Radiation condition.)
8. Waves created by the ship should leave artificial boundaries of the computational domain without reflection. They may not reach the ship again. (Open-boundary condition.)
9. Forces on the ship result in motions. (Average longitudinal forces are assumed to be counteracted by corresponding propulsive forces, i.e. the average speed V remains constant.)

Note that this verbal formulation of the boundary conditions coincides virtually with the formulation for the steady wave resistance problem.

All coordinate systems here are right-handed Cartesian systems. The inertial $Oxyz$ system moves uniformly with velocity V . x points in the direction of the body's mean velocity V , z points vertically upwards. The \underline{Oxyz} system is fixed at the body and follows its motions. When the body is at rest position, \underline{x} , \underline{y} , \underline{z} coincide with x , y , z . The angle of encounter μ between body and incident wave is defined such that $\mu = 180^\circ$ denotes head sea and $\mu = 90^\circ$ beam sea.

The body has 6 degrees of freedom for rigid body motion. We denote corresponding to the degrees of freedom:

- u_1 surge motion of \underline{O} in the x direction, relative to O
- u_2 heave motion of \underline{O} in the y direction, relative to O
- u_3 heave motion of \underline{O} in the z direction, relative to O
- u_4 angle of roll = angle of rotation around the x -axis
- u_5 angle of pitch = angle of rotation around the y -axis
- u_6 angle of yaw = angle of rotation around the z -axis

The motion vector is \vec{u} and the rotational motion vector $\vec{\alpha}$ are given by:

$$\vec{u} = \{u_1, u_2, u_3\}^T \quad \text{and} \quad \vec{\alpha} = \{u_4, u_5, u_6\}^T = \{\alpha_1, \alpha_2, \alpha_3\}^T$$

All motions are assumed to be small of order $O(h)$. Then for the three angles α_i , the following approximations are valid: $\sin(\alpha_i) = \tan(\alpha_i) = \alpha_i$, $\cos(\alpha_i) = 1$.

The relation between the inertial and the hull-bound coordinate system is given by the linearized transformation equations:

$$\vec{x} = \underline{\vec{x}} + \vec{\alpha} \times \underline{\vec{x}} + \vec{u}$$

$$\underline{\vec{x}} = \vec{x} - \vec{\alpha} \times \vec{x} - \vec{u}$$

Let $\vec{v} = \vec{v}(\vec{x})$ be any velocity relative to the $Oxyz$ system and $\vec{v} = \vec{v}(\underline{x})$ the velocity relative to the $O\underline{x}\underline{y}\underline{z}$ system where \vec{x} and \underline{x} describe the same point. Then the velocities transform:

$$\vec{v} = \underline{v} + \vec{\alpha} \times \underline{v} + (\vec{\alpha}_t \times \underline{x} + \vec{u}_t)$$

$$\underline{v} = \vec{v} - \vec{\alpha} \times \vec{v} - (\vec{\alpha}_t \times \vec{x} + \vec{u}_t)$$

The differential operators ∇_x and $\nabla_{\underline{x}}$ transform:

$$\nabla_x = \{\partial/\partial x, \partial/\partial y, \partial/\partial z\}^T = \nabla_{\underline{x}} + \vec{\alpha} \times \nabla_{\underline{x}}$$

$$\nabla_{\underline{x}} = \{\partial/\partial \underline{x}, \partial/\partial \underline{y}, \partial/\partial \underline{z}\}^T = \nabla_x - \vec{\alpha} \times \nabla_x$$

Using a three-dimensional truncated Taylor expansion, a scalar function transforms from one coordinate system into the other:

$$f(\vec{x}) = f(\underline{x}) + (\vec{\alpha} \times \underline{x} + \vec{u}) \nabla_{\underline{x}} f(\underline{x})$$

$$f(\underline{x}) = f(\vec{x}) - (\vec{\alpha} \times \vec{x} + \vec{u}) \nabla_x f(\vec{x})$$

Correspondingly we write:

$$\nabla_x f(\vec{x}) = \nabla_{\underline{x}} f(\underline{x}) + ((\vec{\alpha} \times \underline{x} + \vec{u}) \nabla_{\underline{x}}) \nabla_{\underline{x}} f(\underline{x})$$

$$\nabla_{\underline{x}} f(\underline{x}) = \nabla_x f(\vec{x}) - ((\vec{\alpha} \times \vec{x} + \vec{u}) \nabla_x) \nabla_x f(\vec{x})$$

A perturbation formulation for the potential is used:

$$\phi^{\text{total}} = \phi^{(0)} + \phi^{(1)} + \phi^{(2)} + \dots$$

$\phi^{(0)}$ is the part of the potential which is independent of the wave amplitude h . It is the solution of the steady wave resistance problem described in the previous section (where it was denoted by just ϕ). $\phi^{(1)}$ is proportional to h , $\phi^{(2)}$ proportional to h^2 etc. Within a theory of first order (linearized theory), terms proportional to h^2 or higher powers of h are neglected. For reasons of simplicity, the equality sign is used here to denote equality of low-order terms only, i.e. $A = B$ means $A = B + O(h^2)$.

We describe both the z -component of the free surface ζ and the potential in a first-order formulation. $\phi^{(1)}$ and $\zeta^{(1)}$ are time harmonic with ω_e , the frequency of encounter:

$$\begin{aligned} \phi^{\text{total}}(x, y, z; t) &= \phi^{(0)}(x, y, z) + \phi^{(1)}(x, y, z; t) \\ &= \phi^{(0)}(x, y, z) + \text{Re}(\hat{\phi}^{(1)}(x, y, z) e^{i\omega_e t}) \end{aligned}$$

$$\begin{aligned} \zeta^{\text{total}}(x, y; t) &= \zeta^{(0)}(x, y) + \zeta^{(1)}(x, y; t) \\ &= \zeta^{(0)}(x, y) + \text{Re}(\hat{\zeta}^{(1)}(x, y) e^{i\omega_e t}) \end{aligned}$$

Correspondingly the symbol $\hat{\cdot}$ is used for the complex amplitudes of all other first-order quantities, such as motions, forces, pressures etc.

The superposition principle can be used within a linearized theory. Therefore the radiation problems for all 6 degrees of freedom of the rigid-body motions

and the diffraction problem are solved separately. The total solution is a linear combination of the solutions for each independent problem.

The harmonic potential $\phi^{(1)}$ is divided into the potential of the incident wave ϕ^w , the diffraction potential ϕ^d , and 6 radiation potentials:

$$\phi^{(1)} = \phi^d + \phi^w + \sum_{i=1}^6 \phi^i u_i$$

It is convenient to decompose ϕ^w and ϕ^d into symmetrical and antisymmetrical parts to take advantage of the (usual) geometrical symmetry:

$$\phi^w(x, y, z) = \underbrace{\frac{\phi^w(x, y, z) + \phi^w(x, -y, z)}{2}}_{\phi^{w,s}} + \underbrace{\frac{\phi^w(x, y, z) - \phi^w(x, -y, z)}{2}}_{\phi^{w,a}}$$

$$\phi^d = \phi^{d,s} + \phi^{d,a} = \phi^7 + \phi^8$$

Thus:

$$\phi^{(1)} = \phi^{w,s} + \phi^{w,a} + \sum_{i=1}^6 \phi^i u_i + \phi^7 + \phi^8$$

The conditions satisfied by the steady flow potential $\phi^{(0)}$ are repeated here from section 7.3 without further comment.

The particle acceleration in the steady flow is: $\vec{a}^{(0)} = (\nabla\phi^{(0)}\nabla)\nabla\phi^{(0)}$

We define an acceleration vector \vec{a}^g $\vec{a}^g = \vec{a}^{(0)} + \{0, 0, g\}^T$

For convenience I introduce an abbreviation: $B = \frac{1}{a_3^g} \frac{\partial}{\partial z} (\nabla\phi^{(0)}\vec{a}^g)$

In the whole fluid domain: $\Delta\phi^{(0)} = 0$

At the steady free surface: $\nabla\phi^{(0)}\vec{a}^g = 0$

$$\frac{1}{2}(\nabla\phi^{(0)})^2 + g\zeta^{(0)} = \frac{1}{2}V^2$$

On the body surface: $\vec{n}(\vec{x})\nabla\phi^{(0)}(\vec{x}) = 0$

Also suitable radiation and decay conditions are observed.

The linearized potential of the incident wave on water of infinite depth is expressed in the inertial system:

$$\phi^w = \text{Re} \left(-\frac{igh}{\omega} e^{-ik(x \cos \mu - y \sin \mu) - kz} e^{i\omega_e t} \right) = \text{Re}(\hat{\phi}^w e^{i\omega_e t})$$

$\omega = \sqrt{gk}$ is the frequency of the incident wave, $\omega_e = |\omega - kV \cos \mu|$ the frequency of encounter. k is the wave number. The derivation of the expression for ϕ^w assumes a linearization around $z = 0$. The same formula will be used now in the seakeeping computations, although the average boundary is at the steady wave elevation, i.e. different near the ship. This may be an inconsistency, but the diffraction potential should compensate this 'error'.

We write the complex amplitude of the incident wave as:

$$\hat{\phi}^w = -\frac{igh}{\omega} e^{\vec{\bar{d}}\vec{d}} \quad \text{with } \vec{d} = \{-ik \cos \mu, ik \sin \mu, -kz\}^T$$

At the free surface ($z = \zeta^{\text{total}}$) the pressure is constant, namely atmospheric pressure ($p = p_0$):

$$\frac{D(p - p_0)}{Dt} = \frac{\partial(p - p_0)}{\partial t} + (\nabla\phi^{\text{total}}\nabla)(p - p_0) = 0$$

Bernoulli's equation gives at the free surface ($z = \zeta^{\text{total}}$) the dynamic boundary condition:

$$\phi_t^{\text{total}} + \frac{1}{2}(\nabla\phi^{\text{total}})^2 + g\zeta^{\text{total}} + \frac{p}{\rho} = \frac{1}{2}V^2 + \frac{p_0}{\rho}$$

The kinematic boundary condition gives at $z = \zeta^{\text{total}}$:

$$\frac{D\zeta^{\text{total}}}{Dt} = \frac{\partial}{\partial t}\zeta^{\text{total}} + (\nabla\phi^{\text{total}}\nabla)\zeta^{\text{total}} = \phi_z^{\text{total}}$$

Combining the above three equations yields at $z = \zeta^{\text{total}}$:

$$\phi_{tt}^{\text{total}} + 2\nabla\phi^{\text{total}}\nabla\phi_t^{\text{total}} + \nabla\phi^{\text{total}}\nabla(\frac{1}{2}\nabla\phi^{\text{total}})^2 + g\phi_z^{\text{total}} = 0$$

Formulating this condition in $\phi^{(0)}$ and $\phi^{(1)}$ and linearizing with regard to stationary terms gives at $z = \zeta^{\text{total}}$:

$$\begin{aligned} \phi_{tt}^{(1)} + 2\nabla\phi^{(0)}\nabla\phi_t^{(1)} + \nabla\phi^{(0)}\nabla(\frac{1}{2}(\nabla\phi^{(0)})^2 + \nabla\phi^{(1)}\nabla\phi^{(0)}) \\ + \nabla\phi^{(1)}\nabla(\frac{1}{2}(\nabla\phi^{(0)})^2) + g\phi_z^{(0)} + g\phi_z^{(1)} = 0 \end{aligned}$$

We develop this equation in a linearized Taylor expansion around $\zeta^{(0)}$ using the abbreviations \vec{a} , \vec{a}^g , and B for steady flow contributions. This yields at $z = \zeta^{(0)}$:

$$\begin{aligned} \phi_{tt}^{(1)} + 2\nabla\phi^{(0)}\nabla\phi_t^{(1)} + \nabla\phi^{(0)}\vec{a}^g + \nabla\phi^{(0)}(\nabla\phi^{(0)}\nabla)\nabla\phi^{(1)} \\ + \nabla\phi^{(1)}(\vec{a} + \vec{a}^g) + Ba_3^g\zeta^{(1)} = 0 \end{aligned}$$

The steady boundary condition can be subtracted, yielding:

$$\phi_{tt}^{(1)} + 2\nabla\phi^{(0)}\nabla\phi_t^{(1)} + \nabla\phi^{(0)}(\nabla\phi^{(0)}\nabla)\nabla\phi^{(1)} + \nabla\phi^{(1)}(\vec{a} + \vec{a}^g) + Ba_3^g\zeta^{(1)} = 0$$

$\zeta^{(1)}$ will now be substituted by an expression depending solely on $\zeta^{(0)}$, $\phi^{(0)}(\zeta^{(0)})$ and $\phi^{(1)}(\zeta^{(0)})$. To this end, Bernoulli's equation is also developed in a Taylor expansion. Bernoulli's equation yields at $z = \zeta^{(0)} + \zeta^{(1)}$:

$$\phi_t^{\text{total}} + \frac{1}{2}(\nabla\phi^{\text{total}})^2 + g\zeta^{\text{total}} = \frac{1}{2}V^2$$

A truncated Taylor expansion gives at $z = \zeta^{(0)}$:

$$\phi_t^{(1)} + \frac{1}{2}(\nabla\phi^{\text{total}})^2 + g\zeta^{(0)} - \frac{1}{2}V^2 + (\nabla\phi^{\text{total}}\nabla\phi_z^{\text{total}} + g)\zeta^{(1)} = 0$$

Formulating this condition in $\phi^{(0)}$ and $\phi^{(1)}$, linearizing with regard to stationary terms and subtracting the steady boundary condition yields:

$$\phi_t^{(1)} + \nabla\phi^{(0)}\nabla\phi^{(1)} + a_3^g\zeta^{(1)} = 0$$

This can be reformulated as:

$$\zeta^{(1)} = -\frac{\phi_t^{(1)} + \nabla\phi^{(0)}\nabla\phi^{(1)}}{a_3^g}$$

By inserting this expression in the free-surface condition and performing the time derivatives leaving only complex amplitudes, the free-surface condition at $z = \zeta^{(0)}$ becomes:

$$\boxed{(-\omega_e^2 + Bi\omega_e)\hat{\phi}^{(1)} + ((2i\omega_e + B)\nabla\phi^{(0)} + \vec{a}^{(0)} + \vec{a}^g)\nabla\hat{\phi}^{(1)} + \nabla\phi^{(0)}(\nabla\phi^{(0)}\nabla)\nabla\hat{\phi}^{(1)} = 0}$$

The last term in this condition is explicitly written:

$$\begin{aligned} \nabla\phi^{(0)}(\nabla\phi^{(0)}\nabla)\nabla\hat{\phi}^{(1)} &= (\phi_x^{(0)})^2\phi_{xx}^{(1)} + (\phi_y^{(0)})^2\phi_{yy}^{(1)} + (\phi_z^{(0)})^2\phi_{zz}^{(1)} \\ &\quad + 2 \cdot (\phi_x^{(0)}\phi_y^{(0)}\phi_{xy}^{(1)} + \phi_x^{(0)}\phi_z^{(0)}\phi_{xz}^{(1)} + \phi_y^{(0)}\phi_z^{(0)}\phi_{yz}^{(1)}) \end{aligned}$$

Complications in formulating the kinematic boundary condition on the body's surface arise from the fact that the unit normal vector is conveniently expressed in the body-fixed coordinate system, while the potential is usually given in the inertial system. The body surface is defined in the body-fixed system by the relation $\underline{S}(\underline{\vec{x}}) = 0$.

Water does not penetrate the body's surface, i.e. relative to the body-fixed coordinate system the normal velocity is zero, at $\underline{S}(\underline{\vec{x}}) = 0$:

$$\underline{\vec{n}}(\underline{\vec{x}}) \cdot \underline{\vec{v}}(\underline{\vec{x}}) = 0$$

$\underline{\vec{n}}$ is the inward unit normal vector. The velocity transforms into the inertial system as:

$$\underline{\vec{v}}(\underline{\vec{x}}) = \vec{v}(\vec{x}) - \vec{\alpha} \times \vec{v}(\vec{x}) - (\vec{\alpha}_t \times \vec{x} + \vec{u}_t)$$

where \vec{x} is the inertial system description of the same point as $(\underline{\vec{x}})$. \vec{v} is expressed as the sum of the derivatives of the steady and the first-order potential:

$$\vec{v}(\vec{x}) = \nabla\phi^{(0)}(\vec{x}) + \nabla\phi^{(1)}(\vec{x})$$

For simplicity, the subscript x for the ∇ operator is dropped. It should be understood that from now on the argument of the ∇ operator determines its type, i.e. $\nabla\phi(\vec{x}) = \nabla_x\phi(\vec{x})$ and $\nabla\phi(\underline{\vec{x}}) = \nabla_{\underline{x}}\phi(\underline{\vec{x}})$. As $\phi^{(1)}$ is of first order small, $\phi^{(1)}(\underline{\vec{x}}) = \phi^{(1)}(\vec{x}) = \phi^{(1)}$.

The r.h.s. of the above equation for $\vec{v}(\vec{x})$ transforms back into the hull-bound system:

$$\vec{v}(\vec{x}) = \nabla\phi^{(0)}(\underline{\vec{x}}) + ((\vec{\alpha} \times \underline{\vec{x}} + \vec{u})\nabla)\nabla\phi^{(0)}(\underline{\vec{x}}) + \nabla\phi^{(1)}$$

Combining the above equations and omitting higher-order terms yields:

$$\begin{aligned} \underline{\vec{n}}(\underline{\vec{x}})(\nabla\phi^{(0)}(\underline{\vec{x}}) - \vec{\alpha} \times \nabla\phi^{(0)} + ((\vec{\alpha} \times \underline{\vec{x}} + \vec{u})\nabla)\nabla\phi^{(0)} + \nabla\phi^{(1)} \\ - (\vec{\alpha}_t \times \vec{x} + \vec{u}_t)) = 0 \end{aligned}$$

This boundary condition must be fulfilled at any time. The steady terms give the steady body-surface condition as mentioned above. Because only terms of first order are left, we can exchange \vec{x} and $\vec{\underline{x}}$ at our convenience. Using some vector identities we derive:

$$\vec{n} \nabla \hat{\phi}^{(1)} + \hat{u}[(\vec{n} \nabla) \nabla \phi^{(0)} - i\omega_e \vec{n}] + \hat{\alpha}[\vec{n} \times \nabla \phi^{(0)} + \vec{\underline{x}} \times ((\vec{n} \nabla) \nabla \phi^{(0)} - i\omega_e \vec{n})] = 0$$

where all derivatives of potentials can be taken with respect to the inertial system.

With the abbreviation $\vec{m} = (\vec{n} \nabla) \nabla \phi^{(0)}$ the boundary condition at $\underline{S}(\vec{\underline{x}}) = 0$ becomes:

$$\vec{n} \nabla \hat{\phi}^{(1)} + \hat{u}(\vec{m} - i\omega_e \vec{n}) + \hat{\alpha}(\vec{\underline{x}} \times (\vec{m} - i\omega_e \vec{n}) + \vec{n} \times \nabla \phi^{(0)}) = 0$$

The Kutta condition requires that at the trailing edge the pressures are equal on both sides. This is automatically fulfilled for the symmetric contributions (for monohulls). Then only the antisymmetric pressures have to vanish:

$$-\rho(\phi_t^i + \nabla \phi^{(0)} \nabla \hat{\phi}^i) = 0$$

This yields on points at the trailing edge:

$$i\omega_e \hat{\phi}^i + \nabla \phi^{(0)} \nabla \hat{\phi}^i = 0$$

Diffraction and radiation problems for unit amplitude motions are solved independently as described in the next section. After the potential $\hat{\phi}^i$ ($i = 1 \dots 8$) have been determined, only the motions u_i remain as unknowns.

The forces \vec{F} and moments \vec{M} acting on the body result from the body's weight and from integrating the pressure over the instantaneous wetted surface S . The body's weight \vec{G} is:

$$\vec{G} = \{0, 0, -mg\}^T$$

m is the body's mass. (In addition, a propulsive force counteracts the resistance. This force could be included in a similar fashion as the weight. However, resistance and propulsive force are assumed to be negligibly small compared to the other forces.)

\vec{F} and \vec{M} are expressed in the inertial system (\vec{n} is the inward unit normal vector):

$$\vec{F} = \int_S (p(\vec{x}) - p_0) \vec{n}(\vec{x}) dS + \vec{G}$$

$$\vec{M} = \int_S (p(\vec{x}) - p_0) (\vec{x} \times \vec{n}(\vec{x})) dS + \vec{x}_g \times \vec{G}$$

\vec{x}_g is the centre of gravity. The pressure is given by Bernoulli's equation:

$$p(\vec{x}) - p_0 = -\rho(\frac{1}{2}(\nabla \phi^{\text{total}}(\vec{x}))^2 - \frac{1}{2}V^2 + gz + \phi_t^{\text{total}}(\vec{x}))$$

$$= \underbrace{-\rho(\frac{1}{2}(\nabla\phi^{(0)}(\vec{x}))^2 - \frac{1}{2}V^2 + gz)}_{p^{(0)}} \underbrace{-\rho(\nabla\phi^{(0)}\nabla\phi^{(1)} + \phi_t^{(1)})}_{p^{(1)}}$$

The r.h.s. of the expressions for \vec{F} and \vec{M} are now transformed from the inertial system to the body-fixed system. This includes a Taylor expansion around the steady position of the body. The normal vector \vec{n} and the position \vec{x} are readily transformed as usual:

$$\begin{aligned}\vec{x} &= \vec{\underline{x}} + \vec{\alpha} \times \vec{\underline{x}} + \vec{u} \\ \vec{n}(\vec{x}) &= \vec{\underline{n}}(\vec{\underline{x}}) + \vec{\alpha} \times \vec{\underline{n}}(\vec{\underline{x}})\end{aligned}$$

The steady parts of the equations give:

$$\begin{aligned}\vec{F}^{(0)} &= \int_{\underline{S}^{(0)}} p^{(0)} \vec{\underline{n}} d\underline{S} + \vec{G} = 0 \\ \vec{M}^{(0)} &= \int_{\underline{S}^{(0)}} p^{(0)} (\vec{\underline{x}} \times \vec{\underline{n}}) d\underline{S} + \vec{\underline{x}}_g \times \vec{G} = 0\end{aligned}$$

The ship is in equilibrium for steady flow. Therefore the steady forces and moments are all zero.

The first-order parts give (r.h.s. quantities are now all functions of $\vec{\underline{x}}$):

$$\begin{aligned}\vec{F}^{(1)} &= \int_{\underline{S}^{(0)}} [(p^{(1)} + \nabla p^{(0)}(\vec{\alpha} \times \vec{\underline{x}} + \vec{u})) \vec{\underline{n}} d\underline{S} - \vec{\alpha} \times \vec{G} \\ \vec{M}^{(1)} &= \int_{\underline{S}^{(0)}} [(p^{(1)} + \nabla p^{(0)}(\vec{\alpha} \times \vec{\underline{x}} + \vec{u})) (\vec{\underline{x}} \times \vec{\underline{n}}) d\underline{S} - \vec{\underline{x}}_g \times (\vec{\alpha} \times \vec{G})\end{aligned}$$

where $(\vec{\alpha} \times \vec{\underline{x}}) \times \vec{\underline{n}} + \vec{\underline{x}} \times (\vec{\alpha} \times \vec{\underline{n}}) = \vec{\alpha} \times (\vec{\underline{x}} \times \vec{\underline{n}})$ and the expressions for $\vec{F}^{(0)}$ and $\vec{M}^{(0)}$ have been used. Note: $\nabla p^{(0)} = -\rho \vec{\alpha}^g$. The difference between instantaneous wetted surface and average wetted surface still has not to be considered as the steady pressure $p^{(0)}$ is small in the region of difference.

The instationary pressure is divided into parts due to the incident wave, radiation and diffraction:

$$p^{(1)} = p^w + p^d + \sum_{i=1}^6 p^i u_i$$

Again the incident wave and diffraction contributions can be decomposed into symmetrical and antisymmetrical parts:

$$\begin{aligned}p^w &= p^{w,s} + p^{w,a} \\ p^d &= p^{d,s} + p^{d,a} = p^7 + p^8\end{aligned}$$

Using the unit motion potentials, the pressure parts p^i are derived:

$$\begin{aligned}p^i &= -\rho(\phi_t^i + \nabla\phi^{(0)}\nabla\phi^i) \\ p^w &= -\rho(\phi_t^w + \nabla\phi^{(0)}\nabla\phi^w) \\ p^d &= -\rho(\phi_t^d + \nabla\phi^{(0)}\nabla\phi^d)\end{aligned}$$

The individual terms in the integrals for $\vec{F}^{(1)}$ and $\vec{M}^{(1)}$ are expressed in terms of the motions u_i , using the vector identity $(\vec{\alpha} \times \vec{x})\vec{a}^g = \vec{\alpha}(\vec{x} \times \vec{a}^g)$:

$$\begin{aligned}\vec{F}^{(1)} &= \int_{\underline{S}^{(0)}} (p^w + p^d) \vec{n} \, d\underline{S} + \sum_{i=1}^6 \left(\int_{\underline{S}^{(0)}} p^i \vec{n} \, d\underline{S} \right) u_i \\ &\quad + \int_{\underline{S}^{(0)}} -\rho(\vec{u}\vec{a}^g + \vec{\alpha}(\vec{x} \times \vec{a}^g)) \vec{n} \, d\underline{S} - \vec{\alpha} \times \vec{G} \\ \vec{M}^{(1)} &= \int_{\underline{S}^{(0)}} (p^w + p^d) (\vec{x} \times \vec{n}) \, d\underline{S} + \sum_{i=1}^6 \left(\int_{\underline{S}^{(0)}} p^i (\vec{x} \times \vec{n}) \, d\underline{S} \right) u_i \\ &\quad - \vec{x}_g \times (\vec{\alpha} \times \vec{G}) + \int_{\underline{S}^{(0)}} -\rho(\vec{u}\vec{a}^g + \vec{\alpha}(\vec{x} \times \vec{a}^g)) (\vec{x} \times \vec{n}) \, d\underline{S}\end{aligned}$$

The relation between forces, moments and motion acceleration is:

$$\vec{F}^{(1)} = m(\vec{u}_{tt} + \vec{\alpha}_{tt} \times \vec{x}_g)$$

$$\vec{M}^{(1)} = m(\vec{x}_g \times \vec{u}_{tt}) + I\vec{\alpha}_{tt}$$

I is the matrix of moments of inertia:

$$I = \begin{bmatrix} \Theta_{\underline{x}} & 0 & -\Theta_{\underline{x}\underline{z}} \\ 0 & \Theta_{\underline{y}} & 0 \\ -\Theta_{\underline{x}\underline{z}} & 0 & \Theta_{\underline{z}} \end{bmatrix}$$

where mass distribution symmetrical in y is assumed. $\Theta_{\underline{x}}$ etc. are the moments of inertia and the centrifugal moments with respect to the origin of the body-fixed $\underline{Ox}\underline{y}\underline{z}$ system:

$$\Theta_{\underline{x}} = \int (\underline{y}^2 + \underline{z}^2) \, dm; \quad \Theta_{\underline{xy}} = \int \underline{x}\underline{y} \, dm; \quad \text{etc.}$$

Combining the above equations for $\vec{F}^{(1)}$ and $\vec{M}^{(1)}$ yields a linear system of equations in the unknown u_i that is quickly solved using Gauss elimination.

7.5.2 Numerical implementation

Systems of equations for unknown potentials

The two unknown diffraction potentials and the six unknown radiation potentials are determined by approximating the unknown potentials by a superposition of a finite number of Rankine higher-order panels on the ship and above the free surface. For the antisymmetric cases, in addition Thiert elements, section 6.4.2, Chapter 6, are arranged and a Kutta condition is imposed on collocation points at the last column of collocation points on the stern. Radiation and open-boundary conditions are fulfilled by the ‘staggering’ technique (adding one row of collocation points at the upstream end of the free-surface grid and one row of source elements at the downstream end of the free-surface grid). This technique works only well for $\tau > 0.4$.

Elements use mirror images at $y = 0$ and for shallow water at $z = z_{\text{bottom}}$. For the symmetrical cases, all mirror images have the same strength. For the antisymmetrical case, the mirror images on the negative y sector(s) have negative element strength of the same absolute magnitude.

Each unknown potential is then written as:

$$\hat{\phi}^i = \sum \hat{\sigma}_i \varphi$$

σ_i is the strength of the i th element, φ the potential of an element of unit strength. φ is real for the Rankine elements and complex for the Thiert elements.

The same grid on the hull may be used as for the steady problem, but the grid on the free surface should be created new depending on the wave length of the incident wave. The quantities on the new grid can be interpolated within the new grid from the values on the old grid. Outside the old grid in the far field, all quantities are set to uniform flow on the new grid.

For the boundary condition on the free surface, we introduce the following abbreviations:

$$f_q = -\omega_e^2 + i\omega_e B$$

$$f_{qx} = (2i\omega_e + B)\phi_x^{(0)} + 2a_1$$

$$f_{qy} = (2i\omega_e + B)\phi_y^{(0)} + 2a_2$$

$$f_{qz} = (2i\omega_e + B)\phi_z^{(0)} + 2a_3$$

$$f_{qxx} = \phi_x^{(0)} \cdot \phi_x^{(0)} - \phi_z^{(0)} \cdot \phi_z^{(0)}$$

$$f_{qxy} = 2 \cdot \phi_x^{(0)} \cdot \phi_y^{(0)}$$

$$f_{qxz} = 2 \cdot \phi_x^{(0)} \cdot \phi_z^{(0)}$$

$$f_{qyy} = \phi_y^{(0)} \cdot \phi_y^{(0)} - \phi_z^{(0)} \cdot \phi_z^{(0)}$$

$$f_{qyz} = 2 \cdot \phi_y^{(0)} \cdot \phi_z^{(0)}$$

Then we can write the free surface condition for the radiation cases ($i = 1 \dots 6$):

$$\begin{aligned} \sum \hat{\sigma}_i (f_q \varphi + f_{qx} \varphi_x + f_{qy} \varphi_y + f_{qz} \varphi_z + f_{qxx} \varphi_{xx} + f_{qxy} \varphi_{xy} \\ + f_{qxz} \varphi_{xz} + f_{qyy} \varphi_{yy} + f_{qyz} \varphi_{yz}) = 0 \end{aligned}$$

where it has been exploited that all potentials fulfil Laplace's equation. Similarly, we get for the symmetrical diffraction problem:

$$\begin{aligned} \sum \hat{\sigma}_i (f_q \varphi + f_{qx} \varphi_x + f_{qy} \varphi_y + f_{qz} \varphi_z + f_{qxx} \varphi_{xx} + f_{qxy} \varphi_{xy} + f_{qxz} \varphi_{xz} \\ + f_{qyy} \varphi_{yy} + f_{qyz} \varphi_{yz}) + f_q \hat{\phi}^{w,s} + f_{qx} \hat{\phi}_x^{w,s} + f_{qy} \hat{\phi}_y^{w,s} + f_{qz} \hat{\phi}_z^{w,s} \\ + f_{qxx} \hat{\phi}_{xx}^{w,s} + f_{qxy} \hat{\phi}_{xy}^{w,s} + f_{qxz} \hat{\phi}_{xz}^{w,s} + f_{qyy} \hat{\phi}_{yy}^{w,s} + f_{qyz} \hat{\phi}_{yz}^{w,s} = 0 \end{aligned}$$

The expression for the antisymmetrical diffraction problem is written correspondingly using $\hat{\phi}^{w,a}$ on the r.h.s.

Hull condition

For the hull conditions for the 8 radiation and diffraction problems, we introduce the following abbreviations, where the auxiliary variable h is used as a local variable with different meaning than further below for the system of equations for the motions:

$$\begin{aligned} \{h_1, h_2, h_3\}^T &= \vec{m} - i\omega_e \vec{n} \\ \{h_4, h_5, h_6\}^T &= \vec{x} \times (\vec{m} - i\omega_e \vec{n}) + \vec{n} \times \nabla \phi^{(0)} \\ h_7 &= \nabla \hat{\phi}^{w,s} \cdot \vec{n} \\ h_8 &= \nabla \hat{\phi}^{w,a} \cdot \vec{n} \end{aligned}$$

Then the hull condition can be written for the j th case ($j = 1 \dots 8$):

$$\sum \hat{\sigma}_i(\vec{n} \cdot \varphi) + h_j = 0$$

The Kutta condition is simply written:

$$\begin{aligned} \sum \hat{\sigma}_i(i\omega_e \varphi + \nabla \phi^{(0)} \nabla \varphi) &= 0 \quad \text{for case } j = 2, 4, 6 \\ \sum \hat{\sigma}_i(i\omega_e \varphi + \nabla \phi^{(0)} \nabla \varphi) + i\omega_e \hat{\phi}^{w,s} + \nabla \phi^{(0)} \nabla \hat{\phi}^{w,s} &= 0 \quad \text{for case } j = 8 \end{aligned}$$

The l.h.s. of the four systems of equations for the symmetrical cases and the l.h.s. for the four systems of equations for the antisymmetrical cases share the same coefficients each. Thus four systems of equations can be solved simultaneously using a Gauss elimination procedure.

System of equations for motions

We introduce the abbreviations:

$$\begin{aligned} \{h_1, h_2, h_3\}^T &= -\rho \vec{a}^g \\ \{h_4, h_5, h_6\}^T &= -\rho \vec{x} \times \vec{a}^g \\ h_7 &= p^{w,s} = -\rho(i\omega_e \hat{\phi}^{w,s} + \nabla \phi^{(0)} \nabla \hat{\phi}^{w,s}) \\ h_8 &= p^{w,a} = -\rho(i\omega_e \hat{\phi}^{w,a} + \nabla \phi^{(0)} \nabla \hat{\phi}^{w,a}) \end{aligned}$$

Recall that the instationary pressure contribution is:

$$p^i = -\rho(i\omega_e \hat{\phi}^i + \nabla \phi^{(0)} \nabla \hat{\phi}^i)$$

Then we can rewrite the conditions for $\vec{F}^{(1)}$ and $\vec{M}^{(1)}$:

$$\begin{aligned} -m(\vec{u}_{tt} + \vec{\alpha}_{tt} \times \vec{x}_g) + \sum_{i=1}^8 \left(\int_{\underline{S}^{(0)}} (p^i + h_i) \vec{n} \, d\underline{S} \right) u_i - \vec{\alpha} \times \vec{G} &= 0 \\ -m(\vec{x}_g \times \vec{u}_{tt}) - I \vec{\alpha}_{tt} \sum_{i=1}^8 \left(\int_{\underline{S}^{(0)}} (p^i + h_i) (\vec{x} \times \vec{n}) \, d\underline{S} \right) u_i - \vec{x}_g \times (\vec{\alpha} \times \vec{G}) &= 0 \end{aligned}$$

The weight terms $-\vec{\alpha} \times \vec{G}$ and $-\vec{x}_g \times (\vec{\alpha} \times \vec{G})$ contribute with $W = mg$:

$$\begin{bmatrix} 0 & 0 & 0 & 0 & W & 0 \\ 0 & 0 & 0 & -W & 0 & 0 \\ 0 & 0 & 0 & 0 & 0 & 0 \\ 0 & 0 & 0 & \underline{z}_g W & 0 & 0 \\ 0 & 0 & 0 & 0 & \underline{z}_g W & 0 \\ 0 & 0 & 0 & -\underline{x}_g W & 0 & 0 \end{bmatrix} \begin{Bmatrix} u_1 \\ u_2 \\ u_3 \\ u_4 \\ u_5 \\ u_6 \end{Bmatrix}$$

The mass terms $-m(\vec{u}_{tt} + \vec{\alpha}_{tt} \times \vec{x}_g)$ and $-m(\vec{x}_g \times \vec{u}_{tt}) - I\vec{\alpha}_{tt}$ contribute:

$$-m \frac{\partial^2}{\partial t^2} \begin{bmatrix} 1 & 0 & 0 & 0 & \underline{z}_g & 0 \\ 0 & 1 & 0 & -\underline{z}_g & 0 & \underline{x}_g \\ 0 & 0 & 1 & 0 & -\underline{x}_g & 0 \\ 0 & -\underline{z}_g & 0 & k_{\underline{x}}^2 & 0 & -k_{\underline{x}\underline{z}}^2 \\ \underline{z}_g & 0 & -\underline{x}_g & 0 & k_{\underline{y}}^2 & 0 \\ 0 & \underline{x}_g & 0 & -k_{\underline{x}\underline{z}}^2 & 0 & k_{\underline{z}}^2 \end{bmatrix} \begin{Bmatrix} u_1 \\ u_2 \\ u_3 \\ u_4 \\ u_5 \\ u_6 \end{Bmatrix}$$

where the radii of inertia k have been introduced, e.g. $\Theta_{\underline{x}} = mk_{\underline{x}}^2$ etc.

References

- Abbott, I. and Doenhoff, A. (1959). *A theory of wing sections*. Dover Publ.
- Allison, J. (1993). Marine waterjet propulsion. *Trans. SNAME* **101**, pp. 275–335
- Anep II-I (1983). *Standardized wave and wind environments for NATO operational areas*. Allied Naval Engineering Publication
- Bertram, V. (1992). Wellenwiderstandsberechnung für SWATH-Schiffe und Katamarane. *Jahrbuch Schiffbautechnische Gesellschaft*, Springer, pp. 343–351
- Bertram, V. (1998a). Marching towards the numerical ship model basin. *Euromech Conf.* 374, Poitiers, pp. 3–17
- Bertram, V. (1998b). Numerical investigation of steady flow effects in three-dimensional seakeeping computations. 22. *Symp. Naval Hydrodynamics*, Washington
- Bertram, V. (1999). Panel methods for wave resistance computations. 31. *Wegemt school 'CFD for ship and offshore design'*, WEGEMT, London
- Bertram, V. and Jensen, G. (1994). Recent applications of computational fluid dynamics. *Ship Technology Research* 41/3, pp. 131–134
- Bertram, V. and Thiart, G. (1998). A Kutta condition for ship seakeeping computations with a Rankine panel method. *Ship Technology Research* **45**, pp. 54–63
- Bertram, V. and Yasukawa, H. (1996). Rankine source methods for seakeeping problems. *Jahrbuch Schiffbautechnische Gesellschaft*, Springer, pp. 411–425
- Blendermann, W. (1998). Parameters of the long-term wind conditions above the oceans, *Ship Technology Research* **45**, pp. 99–104
- Bohlmann, H. J. (1989). Vorausberechnung des Bewegungsverhaltens von Ubooten. *Jahrbuch Schiffbautechnische Gesellschaft*, Springer
- Bohlmann, H. J. (1990). Berechnung hydrodynamischer Koeffizienten von Ubooten zur Vorhersage des Bewegungsverhaltens. *IfS Report* **513**, Univ. Hamburg
- Breslin, J. P. and Andersen, P. (1994). *Hydrodynamics of Ship Propellers*. Cambridge University Press
- Brix, J. (ed.) (1993). *Manoeuvring technical manual*. Seehafen-Verlag
- Brix, J., Nolte, A. and Heinzel, S. (1971). Konstruktive Maßnahmen zur Verhinderung der Kavitation an der Rudersohle. *Hansa* **16**, pp. 1579–1587
- Cao, Y., Schultz, W. and Beck, R. F. (1991). Three-dimensional desingularized boundary integral methods for potential problems. *Int. J. Num. Methods in Fluids* **12**, pp. 785–803
- Chang B. C. and Blume, P. (1998). Survivability of damaged ro-ro passenger vessels. *Ship Technology Research* **45**, pp. 105–117
- Chapman, R. B. (1975). Free-surface effects for yawed surface piercing plates. *J. Ship Research* **20**, pp. 125–132
- Chuang, S. L. (1967). Experiments on slamming of wedge-shaped bodies. *J. Ship Research* **11**, pp. 190–198
- Chung, T. J. (1978). *Finite element analysis in fluid dynamics*. McGraw-Hill
- Clarke, D., Gedling, P. and Hine, G. (1983). The application of manoeuvring criteria in hull design using linear theory. *The Naval Architect*, pp. 45–68
- Faltinsen, O. (1993). *Sea loads on ships and offshore structures*. Cambridge University Press
- Ferziger, J. H. and Peric, M. (1996). *Computational methods in fluid dynamics*. 2nd edn, Springer
- Goodrich, G. J. and Molland, A. F. (1979). Wind tunnel investigation of semi-balanced ship skeg rudders. *Naval Architect*, pp. 285–301

- Hess, J. L. (1986). Review of the source panel technique for flow computation. *Innovative Numerical Methods in Engineering*, Springer, pp. 197–210
- Hess, J. L. (1990). Panel methods in computational fluid dynamics. *Annual Rev. Fluid Mech.* **22**, pp. 255–274
- Hess, J. L. and Smith, A. M. O. (1964). Calculation of nonlifting potential flow about arbitrary three-dimensional bodies. *J. Ship Research* **8**, pp. 22–44
- Hughes, M. and Bertram, V. (1995). A higher-order panel method for 3-d free surface flows. *IfS Report* **558**, Univ. Hamburg
- Inoue, S. and Kijima, K. (1978). The hydrodynamic derivatives on ship manoeuvrability in the trimmed condition. *ITTC* **Vol. 2**, pp. 87–92
- Isay, W. H. (1989). *Kavitation*. Hansa-Verlag
- ISSC (1994). Int. Ship and Offshore Structures Congress, Jeffery, N.E.; Kendrick, A.M. (eds), St. John's
- Janson, C. E. (1996). *Potential flow panel methods for the calculation of free surface flows with lift*. PhD Thesis, Chalmers University of Technology
- Jensen, G. (1988). *Berechnung der stationären Potentialströmung um ein Schiff unter Berücksichtigung der nichtlinearen Randbedingung an der freien Wasseroberfläche*. *IfS Report* **484**, Univ. Hamburg
- Kashiwagi, M. (1997). Numerical seakeeping calculations based on slender ship theory. *Ship Technology Research* **44**, pp. 167–192
- Kato, H. (1996). Cavitation. *Advances in Marine Hydrodynamics*. Comp. Mech. Publ., pp. 233–277
- Keller, W. H. auf'm (1973). Extended diagrams for determining the resistance and required power for single-screw ships. *Int. Shipb. Progr.*, p. 253
- Kerwin, J. E. (1986). Marine propellers. *Ann. Rev. Fluid Mech.* **18**, pp. 387–403
- Kerwin, J. E. and Lee, C. S. (1978). Prediction of steady and unsteady marine propeller performance by numerical lifting-surface theory. *Trans. SNAME* **86**, pp. 218–253
- Kerwin, J. E., Kinnas, S. A., Lee, J. T. and Shih, W. Z. (1987). A surface panel method for the hydrodynamic analysis of ducted propellers. *Trans. SNAME* **95**, pp. 93–122
- Kinnas, S. A. (1996). Theory and numerical methods for the hydrodynamic analysis of marine propulsors. *Advances in Marine Hydrodynamics*. Comp. Mech. Publ., pp. 279–322
- Korobkin, A. (1996). Water impact problems in ship hydrodynamics. *Advances in Marine Hydrodynamics*. Comp. Mech. Publ., pp. 323–371
- Kose, K. (1982). On the new mathematical model of manoeuvring motions of a ship and applications. *Int. Shipb. Progr.* **29**, pp. 205–220
- Kracht, A. (1987). Kavitation an Rudern. *Jahrbuch Schiffbautechnische Gesellschaft*. Springer, pp. 167–179
- Kruppa, C. (1994). Wasserstrahlantriebe. *Handbuch der Werften* **XXII**. Hansa-Verlag, pp. 111–136
- Lackenby, H. (1963). The effect of shallow water on ship speed. *Shipbuilder and Marine Engineer* **70**, pp. 446–450
- Lap, A. J. W (1954). Diagrams for determining the resistance of single screw ships. *Int. Shipb. Progr.*, p. 179
- Larsson, L. (1997). CFD in ship design – Prospects and limitations. *Ship Technology Research* **44**, pp. 133–154
- Larsson, L. and Baba, E. (1996). Ship resistance and flow computations. *Advances in marine Hydrodynamics*, M. Ohkusu (ed.), Comp. Mech. Publ., pp. 1–75
- Larsson, L., Regnström, B., Broberg, L., Li, D. Q. and Janson, C. E. (1998). Failures, fantasies, and feats in the theoretical/numerical prediction of ship performance. *22. Symp. Naval Shiphydrodyn.*, Washington
- Lauder, B. E. and Spalding, D. B. (1974). The numerical computation of turbulent flows. *Computer methods in Applied Mechanics and Engineering* **3**
- Lerbs, H. (1952). Moderately loaded propellers with a finite number of blades and an arbitrary distribution of circulation. *Trans. SNAME* **60**, pp. 73–123
- Lerbs, H. (1955). Ergebnisse der angewandten Theorie des Schiffspropellers. *Jahrbuch Schiffbautechnische Gesellschaft*, Springer, pp. 163–206
- Lewis, F. M. (1929). The inertia of the water surrounding a vibrating ship. *Trans. SNAME* **27**, pp. 1–20
- Lewis, E. V. (ed.) (1990). *Principles of Naval Architecture*. Soc. Naval Arch. Marine Eng.
- Mizoguchi, S. and Tanizawa, K. (1996). Impact wave loads due to slamming – A review. *Ship Technology Research* **43**, pp. 139–154

- Morgan, W. B. and Lin, W. C. (1998). Predicting ship hydrodynamic performance in today's world. *Naval Engineers J.*, September, pp. 91–98
- Morino, L. and Kuo, C. C. (1974). Subsonic potential aerodynamics for complex configurations: A general theory. *AIAA J.* **12/2**, pp. 191–197
- Morino, L. (1975). Steady and oscillatory subsonic and supersonic aerodynamics around complex configurations. *AIAA J.* **13/3**, pp. 368–374
- Muzaferija, S. and Peric, M. (1998). Computation of free-surface flows using interface-tracking and interface-capturing methods. *Nonlinear Water Wave Interaction*, Advances in Fluid Mechanics, Comp. Mech. Publ.
- Nakos, D. (1990). Ship wave patterns and motions by a three-dimensional Rankine panel method. Ph.D. thesis, MIT
- Nakos, D. and Sclavounos, P. (1990). Steady and unsteady wave patterns. *J. Fluid Mechanics* **215**, pp. 256–288
- Newman, J. N. (1965). The exciting forces on a moving body in waves. *J. Ship Research* **10**, pp. 190–199
- Newman, J. N. (1977). *Marine hydrodynamics*. MIT Press
- Newman, J. N. (1978). The theory of ship motions. *Adv. Appl. Mech.* **18**, pp. 222–283
- Pereira, R. (1988). Simulation nichtlinearer Seegangslasten, *Schiffstechnik* **35**, pp. 173–193
- Peyret, R. and Taylor, T. D. (1985). *Computational methods for fluid flow*. Springer
- Raven, H. (1996). *A solution method for the nonlinear ship wave resistance problem*. PhD Thesis, TU Delft
- Reich, Y., Bertram, V. and Friesch, J. (1997). The development of a decision support system for propeller design. ICCAS'97, Yokohama, pp. 363–378
- Riegels, F. W. (1958). *Aerodynamische Profile*. R. Oldenbourg
- Salvesen, N., Tuck, E. O. and Faltinsen, O. (1970). Ship motions and sea loads. *Trans. SNAME* **78**, pp. 250–287
- Schlichting, H. (1979). *Boundary layer theory*. 7th edn, McGraw-Hill
- Schneekluth, H. and Bertram, V. (1998). *Ship design for efficiency and economy*. Butterworth-Heinemann
- Sharma, S. D. (1986). Kräfte am Unter- und Überwasserschiff. *Handbuch der Werften XVIII*, pp. 31–43
- Söding, H. (1982). Prediction of ship steering capabilities. *Schiffstechnik*, pp. 3–29
- Söding, H. (1984). Bewertung der Manöviereigenschaften im Entwurfsstadium. *Jahrbuch Schiffbautechnische Gesellschaft*, Springer, pp. 179–201
- Söding, H. (1986). Kräfte am Ruder. *Handbuch der Werften XVIII*, Hansa-Verlag, pp. 47–56
- Söding, H. (1987). Ermittlung der Kentergefahr aus Bewegungssimulationen. *Schiffstechnik* **34**, pp. 28–39
- Söding, H. (1993a). CFD for manoeuvring of ships. *19th WEGEMT School*, Nantes
- Söding, H. (1993b). A method for accurate force calculations in potential flow. *Ship Technology Research* **40**, pp. 176–186
- Söding, H. (1994). Was kann und sollte unsere Forschung im nächsten Jahrzehnt leisten? *Schiff+Hafen* 46/12, pp. 47–51
- Söding, H. (1995). Wave resistance by Michell integral. *Ship Technology Research* **42**, pp. 163–164
- Söding, H. (1996a). Advances in panel methods. *21. Symp. Naval Hydrodyn.*, Trondheim, pp. 997–1006
- Söding, H. (1996b). Discrete Fourier Transformation. *Ship Technology Research* **43**, p. 48
- Söding, H. (1997). Wind wave spectrum. *Ship Technology Research* **44**, pp. 71–72
- Söding, H. (1998a). Limits of potential theory in rudder flow predictions. *Ship Technology Research* **45**, pp. 141–155
- Söding, H. (1998b). Limits of potential theory in rudder flow predictions. *22. Symp. Naval Hydrodynamics*, Washington
- Söding, H. and Bertram, V. (1998). Schiffe im Seegang. *Handbuch der Werften XXIV*, Hansa-Verlag, pp. 151–189
- SSC (1995). *Hydrodynamic impact on displacement ship hulls*. Ship Structure Committee, SSC-385, SSC-385A
- Streckwall, H. (1993). Anwendung auf Propeller. *27. Kontakt-Studium 'Numerische Methoden in der Strömungsmechanik'*. IfS, Univ. Hamburg
- Streckwall, H. (1999). Numerical techniques for propeller design. *31. Wegemt school 'CFD for ship and offshore design'*, WEGEMT, London
- Tanizawa, K. and Bertram, V. (1998). Slamming. *Handbuch der Werften XXIV*, Hansa-Verlag, pp. 191–210

- Terswiga, T. J. C. van (1996). *Waterjet-hull interaction*. Ph.D. Thesis, TU Delft, ISBN 90-75757-01-8.
- Thieme, H. (1962). Zur Formgebung von Schiffsrudern. *Jahrbuch Schiffbautechnische Gesellschaft*, Springer, pp. 381–426
- Thompson, J. F., Warsi, Z. U. A and Mastin, C. W. (1985). *Numerical Grid Generation*. North-Holland
- Tupper, E. (1996). *Introduction to naval architecture*. Butterworth-Heinemann
- Versteeg, H. K. and Malalasekera, W. (1995). *An introduction to computational fluid dynamics – The finite volume method*. Addison Wesley Longman
- Whicker, L. F. and Fehlner, L. F. (1958). *Free stream characteristics of a family of low aspect ratio control surfaces for application to ship design*. DTMB Report 933, David Taylor Model Basin, Washington
- Wolff, K. (1981). *Ermittlung der Manövriereigenschaften fünf repräsentativer Schiffstypen mit Hilfe von CPMC-Modellversuchen*. IfS Report **412**, Univ. Hamburg
- Zou, Z. J. (1990). *Hydrodynamische Kräfte am manövrierenden Schiff auf flachem Wasser bei endlicher Froudezahl*. IfS Report **503**, Univ. Hamburg

Index

- Actuator disk, 44
Added mass, 148–150, 158
Added resistance, 132
Advance number, 40
Air flow, 18
Airy wave, 101
Appendages, 80
- BEM, 14, 43, 49–50, 120, 127–130, 207–264
Bending moment, 132
Body force, 153, 158–163
Boundary layer equations, 12
- Cauchy number, 8
Cavitation, 51–54, 56, 195–200
Cavitation tunnel, 102
Celerity, 102
CFD, 3–4, 9–36, 83–91, 145, 166–169, 201–203
Cost, 19–22
CPMC, 177
- Desingularization, 229–231
Differencing scheme, 32–33
Diffraction, 123
Dipole, 226–229
Dispersion, 32, 102
Downwash, 46
- Efficiency, 40, 64
Euler equations, 12
- Fast ships, 91–95, 130–131
Field methods, 15, 50
- Finite-volume methods, 15
Form factor, 73–74
Four-quadrant diagrams, 40, 157
Froude number, 6
FVM, s. Finite-volume methods
Full-scale trials, 8, 169–175
- Geosim, 75
GFM, s. Green function method
Green function method, 119
Grid, 21–22, 31, 33
Group velocity, 104
- Hughes–Prohaska, 73
- IMO, 151, 169
Induced pressures, 60
ITTC 1957, 71
ITTC 1978, 74, 76–80
- Jensen panel, 215–218
Jet thruster, 156, 165–166
- Laplace equation, 12, 207
LES, 11
Lewis section, 148–149, 158
Lifting body method, 168
Lifting-line theory, 42–43, 45–46
Lifting-surface method, 43, 46–49, 167–168
- Manoeuvring, 3, 16, 151–206
Manoeuvring simulations, 152–169
Model test, 1–4, 54–56, 68–80, 99–101, 175–177

Momentum theory, 43–44

Morino, 50

Multigrid, 31–33

Navier–Stokes equations, 10

Nomoto, 156

Norrbin, 157

Open-water test, 55

Panel method, s. BEM

Patch method, 231–235

Planing hulls, 92

PMM, 177

Power, 62

Propeller, 17–18, 37–61, 94–95

Propulsion, 1–3, 15, 62–97

Radiation, 122

Rankine singularity method, s.BEM

RANSE, 11, 43, 50, 90–91, 117

Resistance, 1–3, 15, 62–97

Reynolds number, 7

Reynolds stress, 11

Roughness, 82

Routing, 98

Rudder, 177–203

Seakeeping, 1–4, 16–17, 98–150,
253–264

Seaway, 82, 106–117

Shallow water, 81, 102, 164

Similarity laws, 4–8

SIMPLE, 29

Simulation, 134–136, 152–169

Slamming, 17, 138–145

Source, 209–223

Spectrum, 107–115, 132–134

Stopping, 164–165

Strip method, 118, 121–126, 250–253

Surface effect ship, 94, 181

Thiart element, 227–229

Thrust, 39, 62–63

Thrust deduction fraction, 63

Torque, 39

Towing tank, 68–69

Turbulence, 23–26

Turning ability, 151

Vortex, 223–226

Vortex-lattice method, 42–43, 47–48

Wageningen B-series, 40

Wake, 2, 63–64

Waterjet, 37, 95

Wave, 28, 101–106

Wave resistance, 66, 83–90, 238–250

Wind, 82, 109–115

Yaw checking ability, 151

Yaw rate, 153

Yaw stability, 151, 156